Degradation of Perovskite Solar Cells Induced by Intrinsic Stress Factors

Zur Erlangung des akademischen Grades einer

DOKTORIN DER INGENIEURWISSENSCHAFTEN
(Dr.-Ing.)

von der KIT-Fakultät für
Elektrotechnik und Informationstechnik des
Karlsruher Instituts für Technologie (KIT)

angenommene

DISSERTATION

von

M.Sc. Roja Singh

geboren in: Kathmandu, Nepal

Tag der mündlichen Prüfung:	18.09.2025
Hauptreferent:	Prof. Dr. Ulrich W. Paetzold
Korreferent:	Prof. Dr. Stefan Weber

Kurzfassung

Der steigende weltweite Energiebedarf und die übermäßige Abhängigkeit von nicht-erneuerbaren Energiequellen haben zur globalen Erwärmung geführt. Unter den nachhaltigen Alternativen hebt sich Solarenergie als tragfähige Lösung zur Abschwächung der Klimakrise hervor, aufgrund ihrer zunehmenden Verbreitung, sinkenden Kosten und kürzeren Genehmigungszeiten für die Netzintegration. Jüngste Fortschritte in der Photovoltaiktechnologie, insbesondere bei Perowskit-Silizium-Tandemsolarzellen (TSCs), zeigen ein bemerkenswertes Potenzial zur Steigerung der Energieumwandlungseffizienz über die Grenzen konventioneller Siliziumsolarzellen hinaus. Durch die Kombination von Absorbern mit komplementären Bandlücken zielen TSCs darauf ab, ein breiteres Spektrum des Sonnenlichts effizienter zu nutzen. Trotz der Erreichung von Rekordwirkungsgraden im Labormaßstab wird die Kommerzialisierung von Perowskit-Silizium-TSCs jedoch durch Herausforderungen im Zusammenhang mit der Langzeitstabilität von Perowskit-Solarzellen (PSCs) eingeschränkt. Stressfaktoren wie Licht, erhöhte Temperaturen, Spannungseinflüsse, Feuchtigkeit und Sauerstoff führen zu schneller Material- und Gerätealterung der PSCs. Eine detaillierte Untersuchung der Degradationsmechanismen unter betrieblichen Bedingungen ist notwendig, um die Ursachen des Versagens zu identifizieren.

Einzelschicht-Perowskit-Solarzellen bieten eine geeignete Plattform, um die Degradation einzelner Subzellen isoliert zu untersuchen, bevor komplexere Gerätearchitekturen wie Perowskit-Silizium-TSCs betrachtet werden, bei denen Stabilitätsprobleme durch zusätzliche Schnittstellen und Materialinteraktionen verstärkt werden. Da Tandemsolarzellen zunehmend an Bedeutung gewinnen, um höhere Wirkungsgrade zu erzielen und die Stromgestehungskosten weiter zu senken, stehen insbesondere zweipolige TSCs vor mehreren kritischen Herausforderungen, die ihre kommerzielle Einführung verzögern. Ein zentrales Problem ist das Stromabgleich (Current Matching) zwischen den Subzellen, das aufgrund der Serienverschaltung erforderlich ist. Spektrale Verschiebungen, nicht-uniforme Beleuchtung oder Degradation einer Subzelle führen zu einem Ungleichgewicht in der Stromerzeugung der oberen und unteren Zelle. Das Tandemsystem arbeitet dann suboptimal, wobei der Gesamtstrom der TSC durch den geringeren Strom einer der beiden Subzellen limitiert wird. Stromungleichgewichte können langfristigen Stress verursachen, der die Degradation, insbesondere an den rekombinierenden Zwischenkontakten, beschleunigt. Als Antwort auf diese Einschränkungen werden alternative Strategien zur effektiveren Nutzung des Sonnenspektrums untersucht. Eine dieser Ansätze ist die Photonenkonversion (Upconversion), bei der Photonen mit niedriger Energie in Photonen höherer Energie umgewandelt werden, die dann vom aktiven Absorbermaterial aufgenommen werden können. Trotz des konzeptionellen Potenzials dieser Methode fehlen bislang umfassende Machbarkeitsstudien zur Integrationsfähigkeit in PSCs und deren Auswirkungen auf die Langzeitstabilität.

In dieser Arbeit wird systematisch der Einfluss von Verarbeitungsparametern – insbesondere der Precursor-Stöchiometrie und der Abschrecktechnik – auf die Dünnschichteigenschaften von Perowskitmaterialien untersucht. Dabei wird aufgezeigt, wie diese Materialeigenschaften die Leistung und die betriebliche Stabilität von PSCs beeinflussen. Es werden Degradationsanalysen durchgeführt, um die Ursachen des Leistungsverlusts von Einzelschicht-PSCs unter verschiedenen Betriebsstressfaktoren zu identifizieren. Unter den untersuchten Parametern hat sich gezeigt, dass die Precursor-Stöchiometrie einen erheblichen Einfluss auf die Stabilität der PSCs unter Betriebsbedingungen hat. Nach erfolgreicher Integration von Perowskitabsorbern in zweipolige Tandemzellen werden die Auswirkungen des Stromabgleichs auf die Geräteleistung und die

Langzeitstabilität untersucht. Ein möglichst präziser Stromabgleich zwischen den Subzellen in zweipoligen Perowskit-Tandemsolarzellen ist entscheidend für eine stabile Betriebsdauer. Zur Überwindung der inhärenten Begrenzungen durch Stromungleichgewichte wird außerdem eine umfassende Machbarkeitsanalyse der Photonenkonversion durchgeführt, mit Fokus auf deren Auswirkungen auf die Langzeitstabilität. Darüber hinaus wird zur Bewertung der praktischen Anwendbarkeit von zweipoligen Perowskit-basierten TSCs deren Leistung unter realen Außenbedingungen untersucht. Die Überbrückung dieser Wissenslücken und die Bewältigung der Stabilitätsprobleme sind entscheidend, um das volle Potenzial der nächsten Generation von Perowskit-Photovoltaiksystemen auszuschöpfen.

Abstract

The rising global energy demand and the overdependence on the non-renewable energy resources has led to global warming. Among the sustainable alternatives, as a viable solution to mitigate the climate crisis, solar energy stands out for its increasing deployment, falling costs and shorter approval timelines for grid integration. Recent advancements in photovoltaic technologies, particularly perovskite-silicon tandem solar cells (TSCs), have shown remarkable potential in enhancing the power conversion efficiencies beyond the limits of the conventional silicon solar cells. By stacking absorbers with complementary bandgaps, TSCs aim to utilize a broader portion of the solar spectrum more efficiently. However, despite achieving record-breaking efficiencies in laboratory scale, the commercialization of perovskite-silicon TSCs is hindered by challenges related to the long-term stability of perovskite solar cells (PSCs).

Stressors such as light, elevated temperature, voltage bias, moisture and oxygen lead to rapid material and device degradation of PSCs. Detailed investigations into degradation mechanisms under the influence of operational factors are necessary in analyzing the root causes of failure. Single junction perovskite solar cells are a platform to study the degradation of individual sub cell independently, before advancing to more complex device configurations, such as perovskite-silicon TSCs, where stability challenges are compounded by additional interfaces and material interactions. As TSCs, become increasingly relevant for achieving high efficiencies and further reducing the levelized cost of electricity, the practical realization of two-terminal TSCs face several critical challenges delaying their commercial deployment. One of the foremost issues is current matching between the subcells, a requirement due to the series-connected subcell configuration. Spectral shifts, non-uniform illumination, or subcell degradation leads to mismatch in the current generated by the top and the bottom cells. The tandem system operates sub-optimally, with the overall current of the TSCs being limited by the lower current of the two subcells. Current mismatch can induce long-term stress that accelerates degradation, particularly at the interconnecting recombination junctions. In response to these limitations, alternative strategies are also being explored to harvest the solar spectrum more effectively. One such approach is photon upconversion, which enables the transformation of sub-bandgap photons into usable higher-energy photons that can be absorbed by the active layer of the solar cell. Despite the conceptual potential of this approach, feasibility studies focusing on the integration compatibility in the PSCs on the long-term stability are largely absent.

This work systematically investigates the influence of processing parameters (mainly precursor stoichiometry and quenching technique) on the thin film properties of perovskite materials and elucidates how these properties affect the performance and operational stability of PSCs. Degradation analyses are conducted to identify the root cause of failure in single junction PSCs, under different the operational stress factors. Among the parameters studied, precursor stoichiometry greatly influences the stability of the PSCs under the operational stress factors. Following the successful integration of perovskite absorbers into the two-terminal TSCs, the effects of current matching between subcells on device efficiency and long-term stability are examined. Close current matching in subcells of the two-terminal all-perovskite tandem solar cells is best for operational stability. To address the inherent limitations associated with current mismatch, a comprehensive feasibility assessment of photon upconversion is conducted, with a focus on its implications for the long-term operational stability. Furthermore, to evaluate the practical viability of the two-terminal perovskite-based TSCs; their performance is assessed under real-world outdoor conditions. Bridging this knowledge gap and overcoming these stability challenges are key to realizing the full potential of the next-generation perovskite photovoltaics.

Abbreviations

PV	Photovoltaic
PSC	Perovskite Solar Cells
PCE	Power Conversion Efficiency
TSC	Tandem Solar Cells
MSP	Minimum Sustainable Price
LED	Light Emitting Diodes
LASER	Light Amplification by Stimulated Emission of Radiation
QFLS	Quasi-Fermi Level Splitting
CTL	Charge Transport Layers
ETL	Electron Transport Layer
HTL	Hole Transport Layer
I_{SC}	Short-circuit Current
J_{SC}	Short-circuit Current Density
V_{OC}	Open-Circuit Voltage
FF	Fill Factor
R_s	Series Resistance
R_{sh}	Shunt Resistance
2T	Two Terminal
4T	Four Terminal
TCO	Transparent Conductive Oxides
NIR	Near-infrared
UV	Ultraviolet
VIS	Visible
IEC	International Electrotechnical Commission

ISOS	International Summit on Organic and hybrid perovskite Solar cell
XRD	X-Ray Diffraction
OM	Optical Microscopy
AFM	Atomic Force Microscopy
AEM	Scanning electron microscopy
CL	Cathodoluminescence
J-*V*	Current density-Voltage
STC	Standard Testing Conditions
MPP	Maximum Power Point
EQE	External Quantum Efficiency
EL	Electroluminescence
CELIV	Charge Extraction by Linearly Increasing Voltage
ASQ	Antisolvent Quenching
VQ	Vacuum Quenching
MR	Molar Ratio
WBG	Wide-Bandgap
NBG	Narrow-Bandgap
UC	Upconversion
SB	Sub-bandgap
TTA	Triplet-Triplet Annihilation
ET	energy transfer
ϕ_{UC}	UC quantum yields
IML	Index Matching Liquid
BB	Broad-band
WVTR	Water Vapor Transmission Rate
DC	Direct Current

Abbreviations

AC	Analog Current
PL	Photoluminescence
DIN	Deutsches Institut für Normung
TCP	Transmission Control Protocol
IP	Internet Protocol
PR	Performance Ratio

Contents

1. Introduction

1.1. Motivation

Since the onset of industrialization in the 1800s and the subsequent rise in energy consumption, the world has grown increasingly reliant on fossil fuels such as coal, oil and natural gas. However, this dependence presents significant challenges. Firstly, these energy sources are non-renewable and will eventually be depleted with continued large-scale use. Secondly, burning fossil fuels emits greenhouse gases, primarily carbon dioxide, which trap heat in the atmosphere and are a leading cause of global warming. As a result, the planet is facing severe climatic adversities. In response, 196 countries signed the 2015 Paris Agreement, aiming to limit the rise in global average temperature to below 1.5 °C above the pre-industrial levels by the end of the century [1]. Achieving this goal requires a global transition toward low-carbon or carbon-neutral energy sources, often referred to as "clean energy." Fortunately, the Earth offers abundant renewable energy options, including solar, wind, geothermal and hydropower. Accelerating the adoption of these sustainable sources is essential to reducing dependence on fossil fuels and meeting the Paris Agreement's targets.

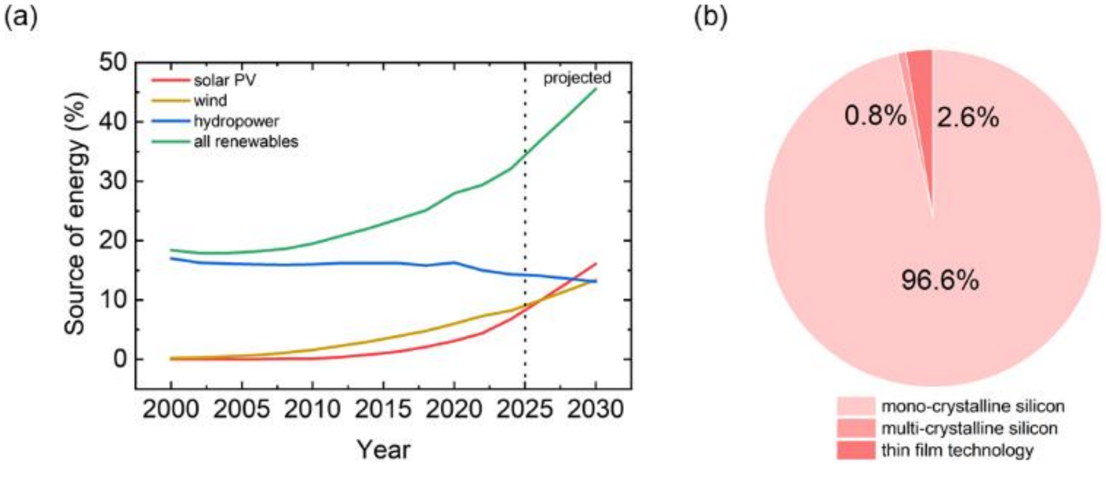

Figure 1.1: (a) Increasing trend in consumption of renewable energy sources (solar, wind, hydropower and others) over time and expected trends in the upcoming years [2]. Adapted with permission from International Energy Agency. (b) Contribution of power generation among different photovoltaics technologies to meet the increasing demand of solar photovoltaics (estimated for 2023) [3]. Adapted with permission from Fraunhofer Institute for Solar Energy Systems.

As the global economy expands, both production and energy consumption continue to rise each year. Since the launch of the Paris Agreement in 2015, reliance on fossil fuels, particularly coal and oil, has begun to decline. According to the International Energy Agency, by 2025, renewable energy sources is accounted for approximately 35% of the total final energy consumption, as illustrated in

Figure 1.1 (a). Notably, wind energy generation has doubled and solar energy production has increased fivefold compared to 2015 levels [2]. This upward trend is expected to continue, with renewables projected to contribute nearly 50% of energy consumption by 2030, driven by increasing demand, falling costs and shorter approval timelines. These developments are promising and highlight the importance of advancing renewable energy technologies to secure a cleaner and more sustainable future for our planet. Thanks to the benefits such as government subsidies, minimal maintenance requirements and reduced energy bills for homeowners, solar energy has emerged as the leading renewable energy source. This rising demand for photovoltaic (PV) installations must be matched by the market supply. In 2023, the estimated power generation from various PV technologies, measured in gigawatt-peak (GW_p), was as follows:

Table 1.1: Estimation of power generation from the different photovoltaics (PV) technologies for the year 2023 [3].

PV technology	Power estimated (GW_p)	Power estimated (%)
Monocrystalline silicon	485	96.6
Multicrystalline silicon	4	0.8
Thin film technology	13	2.6
Total	502	100

As illustrated in **Figure 1.1(b)**, thin-film technologies were estimated to account for approximately 2.6% of the total power generated by PV systems in 2023, with Cadmium Telluride and Copper Indium Gallium Selenide being the primary contributors [3]. While these thin-film PV systems are the alternatives to the dominant silicon PV technology, a promising emerging approach involves perovskite PVs that are being developed to complement, rather than replace, silicon-based PV systems. Although perovskite solar cells (PSCs) are a relatively new technology, they have made impressive progress in improving the power conversion efficiency (PCE), as shown in **Figure 1.2 (a)**. By 2025, the record efficiency of the single junction PSCs reached 27%, closing the gap with the PCE of the monocrystalline silicon solar cells [4]. In addition to their high efficiency, perovskites have a unique property called bandgap tunability, which allows them to be combined with other solar cell technologies in a tandem configuration [5], [6].

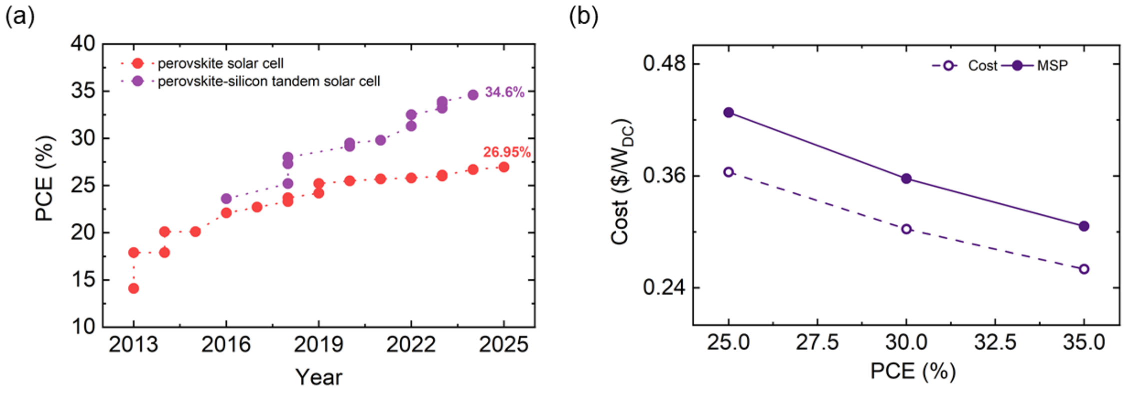

Figure 1.2: (a) Record power conversion efficiency (PCE) reported for perovskite solar cells (PSCs) and perovskite-silicon tandem solar cells (TSCs) over the years [4]. Adapted with permission from National Renewable Energy Laboratory. (b) Estimated decrease in module manufacturing cost and minimum sustainable price (MSP) with increase in reported PCE of perovskite- silicon TSCs (based on production costs) [7]. Adapted with permission from Elsevier.

Tandem solar cells (TSCs) stack absorbers with different bandgaps to capture a wider portion of the solar spectrum. This design allows them to utilize both: (a) high-energy photons more efficiently to minimizing energy loss as heat, and (b) low-energy photons that would otherwise pass through a single junction cell without being absorbed [8]. By leveraging this broader spectral absorption, TSCs can surpass the theoretical efficiency limits of conventional single junction solar cells. As a result, tandem PV technology presents an opportunity to significantly boost power output with only a modest increase in manufacturing costs [9].

There are also alternative strategies to utilize the solar spectrum more efficiently. Spectral convertors are approaches aimed at harvesting low and high-energy photons that would otherwise not be utilized by the solar cell [10],[11]. Spectral convertors are broadly categorized into upconversion, downconversion and downshifting. Upconversion is the process of combining energy of two or more low-energy photons into one high-energy photon that can be absorbed by the active layer of the solar cell [10]. Upconversion also has the potential to enhance the performance of PSCs with cost effective synthesis process [12].

Cost is a critical factor in the advancement of a technology, as it influences both market competitiveness and the price customers ultimately pay. The minimum sustainable price (MSP) is the lowest price at which a manufacturer can sell a product while still covering all costs and remaining financially viable on the long run. **Figure 1.2 (b)** shows the estimated manufacturing costs (in dollars per watt of direct current, $\$/W_{DC}$) and MSPs for perovskite-silicon TSCs, based on current production costs. For the current performance levels of perovskite-silicon TSCs, the MSP is approximately $\$0.27/W_{DC}$. By comparison, in 2025, the projected MSP for conventional monocrystalline silicon modules, with an efficiency of around 23%, is about $\$0.19/W_{DC}$ [7]. Although perovskite-based solar modules are currently more expensive to produce, their steep rise in record PCE, as demonstrated in **Figure 1.2 (a)** can help reduce the levelized cost of electricity, making the energy they generate more cost-effective over time [9].

At the early stages of perovskite PV development, progress in four key areas were essential for accelerating the commercialization of the technology: high efficiency, scalability, toxicity and stability [13]. Challenges in three of these key areas have been effectively addressed:

(i) The efficiency of single junction perovskite solar cells has now surpassed 27% [4]

(ii) Scalable processes like vapor phase deposition, slot-die coating, ink-jet printing, blade coating, etc. have been implemented to manufacture large-scale modules with decent performance [14]–[17]

(iii) Usage of green solvents and replacement of Pb^{2+} with other elements like Sn^{2+} has opened up the possibility of making this technology less toxic and hence more green and sustainable [18]–[20].

One major challenge the perovskite community continues to face is the long-term stability, which remains a significant barrier to the rapid commercialization of the perovskite technology.

1.2. Objective

The stability of a solar cell is its ability to maintain consistent performance, such as power output and PCE, over time when exposed to environmental and operational conditions like light, elevated temperature, voltage bias, humidity and oxygen. A stable solar cell should preserve a substantial portion of its initial PCE after prolonged exposure to intrinsic stress factors such as light, elevated temperature, and electrical bias, conditions inherent to device operation [21]. However, ensuring this level of reliability remains a major hurdle for PSC technology [22]. In contrast, commercial silicon solar cells have already demonstrated excellent long-term durability, often maintaining efficient performance for over 25 years with minimal degradation [23].

Addressing the problem of stability in PSCs requires a deep understanding of the failure mechanisms triggered by the above mentioned intrinsic stress factors (**Objective 1**). Unfortunately, progress is hindered by inconsistent and insufficient reporting of stability data, which obscures the root cause of failure and delays the development of robust solutions (**Objective 2**).

The complexity increases when the PSCs are integrated into the tandem configurations. Achieving optimal performance in serially connected TSCs require precise current matching between the subcells. Maximum efficiency is attained when both subcells generate equal current; otherwise, the total current output of the TSC is constrained by the subcell with the lower current. However, sustaining current matching under real-world operating conditions is inherently difficult (**Objective 3**). Variations in light intensity, spectral distribution, and temperature can cause current mismatch over time, ultimately diminishing the overall efficiency of TSCs [24]–[26]. Spectral converters are also capable of enhancing the solar spectrum utilization by extending the range of the absorbed photons. To harness low-energy photons that would otherwise be lost, upconverters can be integrated into the PSC architecture [10]. However, the stability of such a combination of PSCs and spectral converters remains largely unexplored (**Objective 4**).

Beyond intrinsic stress factors, like for all PV technologies, PSCs must also contend with extrinsic environmental stressors, particularly oxygen and humidity [27]–[29]. These stress factors can degrade the active materials and corrode electrical contacts, significantly shortening the device lifespan [30],[31]. Therefore, implementing a reliable and scalable encapsulation strategy is essential to protect the device from exposure to the real world conditions (**Objective 5**). Operation of PSCs under the outdoor condition makes it susceptible to the variations in temperature and irradiance alongside exposure to extreme weather conditions (**Objective 6**). These parameters are controlled in laboratory conditions. Hence, developing an understanding of the failure mechanisms under these unpredictable outdoor conditions becomes more complex and non-trivial.

Given these concerns, resolving stability issues is paramount for the advancement of perovskite PV and TSC technologies. This work investigates the stability of PSCs and perovskite-based TSCs, aiming to build a comprehensive understanding of the materials, mechanisms and strategies necessary to enhance long-term performance and reliability.

1.3. Outline

Chapter 2 discusses the characteristics of the perovskite PV technology. Explanation of the working principle of PSCs alongside the theoretical efficiency limits and ways to overcome the efficiency limits using TSCs and spectral convertors are discussed. Finally, the stability related issues of the different components of the perovskite-based solar cells under intrinsic (operational) and extrinsic (environmental) stressors are addressed.

Chapter 3 introduces the deposition techniques used for fabrication of perovskite-based solar cells alongside description of the structural, morphological and electrical characterization techniques used to analyze them.

Chapter 4 analyzes the relationship between process parameters and the quality of the perovskite films. The stability of the PSCs fabricated with different film properties are tested separately under the intrinsic stress factors: light, voltage bias and temperature. Segregating the mutual stress factors strengthens analysis of the root cause of degradation under the influence of an individual stressor (addressing **Objective 1**). Dark recovery and post degradation analysis performed on the aged PSCs encourages reporting genuine datasets minimizing discrepancies and addressing **Objective 2**. Intentional current mismatch induced in the subcells of all-perovskite TSC highlights the critical role of current matching between the subcells of a TSC in achieving maximum output power. Compared to the optimized, current-matched condition, any reduction in current from one of the subcells in the all-perovskite TSCs leads to a clear decrease in power output and device stability. This emphasizes the importance of maintaining current matching during operation, directly addressing **Objective 3**.

Chapter 5 deals with an alternative concept of upconversion implemented for harvesting sub-bandgap photons and utilization of a broader part of the solar spectrum. Alongside utilization of upconversion materials for boosting the performance in PSCs, the feasibility of this novel concept in the field of perovskite PV is analyzed, addressing **Objective 4**.

Chapter 6 focuses on the measurement of the state-of-the-art encapsulated perovskite-silicon TSCs under the outdoor condition, giving a more realistic perspective about the operational stability of TSCs. Protecting TSCs from the atmospheric stress factors (**Objective 5**) and monitoring the performance under the operational stress factors helps disentangle the effects of extrinsic vs. intrinsic stress factors. Critical assessment alongside additional characterizations supports speculations about the root cause of failure of the complex perovskite-silicon TSCs under real life conditions (**Objective 6)**.

Chapter 7 summarizes the main findings of this work and motivates ideas for further explorations.

2. Theoretical Background

This chapter presents the theoretical background necessary to understand and assess the results discussed in this dissertation. It introduces perovskite semiconductors and their exceptional structural and optoelectronic characteristics, which makes them a good contender for next generation photovoltaic materials. The operating principles of perovskite-based solar cells and their theoretical efficiency limits are discussed. Strategies to surpass these efficiency limits, including tandem solar cell configurations and spectral converters, are also explored. Finally, the bottleneck of the perovskite photovoltaics technology, stability is addressed. Stress factors limit stability at both the material and the device levels are examined. Methods for standardized reporting and assessment of stability datasets are also discussed.

2.1. Perovskite Semiconductors

Perovskites are crystal structure that follow the formula ABX_3 where A-site cation generally comprises organic molecules such as methylammonium ($CH_3NH_3^+$, denoted MA^+), formamidinium ($HC(NH_2)_2^+$, denoted FA^+) or inorganic cations, such as cesium (Cs^+) and rubidium (Rb^+). B is a divalent inorganic cation such as lead (Pb^{2+}) and tin (Sn^{2+}). X is a halide anion mainly iodide (I^-), bromide (Br^-), and chloride (Cl^-). Perovskites have excellent optoelectronic characteristics including bandgap tunability [5],[6], high absorption coefficient [32], long diffusion length [33] and low non-radiative recombination rates [34],[35] which make them suitable for application in the field of thin-film photovoltaics (PV) [36]. The ability to alloy cations and anions of different ionic radii allows tailoring of the optoelectronic characteristics. However, incorporation of ions of different radii also make them more reactive to stress factors such as light, elevated temperature, voltage bias, oxygen and humidity [37],[38]. The feature that is an asset of these high-performing materials can also be a liability.

2.1.1. Structural characteristics

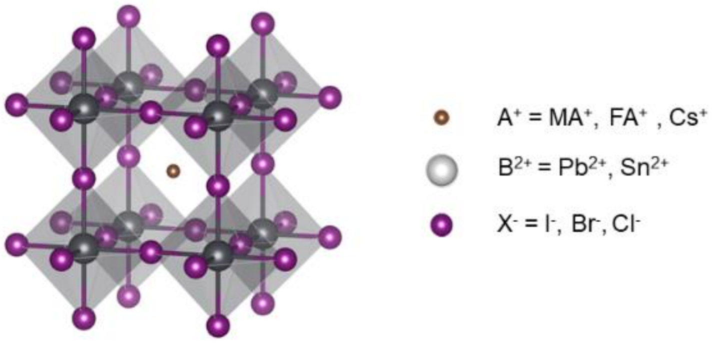

Figure 2.1: Crystal structure of a perovskite semiconductor depicting the position of A^+ cation (MA^+, FA^+ or Cs^+) and B^{2+} cation (Pb^{2+} or Sn^{2+}) alongside X^- anion (I^-, Br^- or Cl^-). Position of A^+ is in the center of the cubohederal with BX_6 octahedra at the corner.

In the crystal structure of ABX_3, A is located in the center of the cubohederal with corner-sharing BX_6 octahedra. The ionic radii and percentage fraction of the A, B and X components determines the formation and phase stability of the crystal structure [39]. The **Equation 2.1** defines the Goldschmidt tolerance factor (t):

$$t = \frac{r_A + r_X}{\sqrt{2}\,(r_B + r_X)} \qquad \text{Equation (2.1)}$$

where, r_A, r_B and r_X are the ionic radii of the cations A, B and anion X, respectively. In case of mixed cation perovskite with a composition of $A_yA'_{(1-y)}BX_3$, an updated version of the above equation, **Equation 2.2** can be used [40].

$$t = \frac{y\,r_A + (1-y)r_{A'} + r_X}{\sqrt{2}\,(r_B + r_X)} \qquad \text{Equation (2.2)}$$

where $r_{A'}$ is the ionic radii of the additional cation used for the mixed cation recipe.

Alongside tolerance factor, octahedral factor is also important for the formation of the perovskite structure. **Equation 2.3** defines the octahedral factor (η):

$$\eta = \frac{r_B}{r_X} \qquad \text{Equation (2.3)}$$

The formation of a stable halide perovskite structure requires that the value of t is between $0.87 < t < 1.1$ and $\eta > 0.44$. If the value of t is beyond these limits, the A cation is too small or too big to form a stable perovskite structure. When $t = 1$, the perovskite structure has the ideal cubic phase. While, the correct range of t and η determines the structural and phase stability of the perovskite crystal[39], a phase-stable perovskite structure might still under go reversible or irreversible degradation under different stress factors [40],[41]. The changes occurring in the performance of perovskites under different stress factors will be covered later in the chapter.

Partial substitution allows gradual replacement of the A cation (MA^+, FA^+ or Cs^+), the B cation (Pb^{2+} or Sn^{2+}) or the X anion (I^-, Br^- or Cl^-). Such substitution of the cations and anions can further modify the existing structural characteristics of these materials. In the archetypical methylammonium lead iodide ($MAPbI_3$), partial substitution of MA^+ with FA^+ and Cs^+, results in the formation of the triple cation recipe $Cs_x(MA_{0.17}FA_{0.83})_{(1-x)}Pb(I_{0.83}Br_{0.17})_3$. When the amount of incorporated Cs is 0%, a non-perovskite phase is existent. However, upon increasing the percentage of Cs to 5% the perovskite phase is formed [42]. Hence, triple cation perovskite is the most commonly used perovskite demonstrating increased phase stability. Alongside the enhanced phase stability, the optoelectronic properties of the perovskite is also important for their application in PV.

2.1.2. Optoelectronic characteristics

Bandgap tunability

The bandgap of the perovskite is determined by the interaction of the B-site cation and the X-site anion. The bandgap of the halide perovskite determines its application in the solar cells. Unlike the conventional Si solar cells, perovskites are a direct bandgap material. The s-orbitals of the B cation and p-orbitals of the X anion determines the valence band maximum while a combination of p-orbitals of the metal and halide determines the conduction band minimum [43].

In $MAPbI_3$, substituting the MA^+ with FA^+ can result in a bandgap variation from 1.64 eV to 1.43 eV. The ionic radii of FA^+ is larger than the ionic radii of MA^+ [44], [45]. In the B site, on substitution of Pb^{2+} with Sn^{2+}, this bandgap can be further lowered to 1.3 eV [5][46][47]. Finally, on substitution of I^- with Br^-, the bandgap can be increased to 2.26 eV[48]–[50]. For the application of perovskite in the tandem solar cells (TSCs) on top of the commercial silicon solar cells, a suitable bandgap of 1.73 eV is required [51]. Partial substitution of I^- with Br^- allows tuning of the bandgap. However, complete substitution of I^- with Br^- might not be ideal for application in the field of PV. In other optoelectronic applications like light emitting diodes (LEDs) and light amplification by stimulated emission of radiation (LASERs), such high bandgap materials are still sought after.

High absorption coefficient

On illumination of perovskite with incident photons, like in other semiconductors, photons having energy greater or equal than the bandgap of the material are absorbed and those with energy less than the bandgap are transmitted. The absorbed energy is used to generate charge carriers i.e. electrons and holes in the semiconductor.

The intensity of the incident light at a distance of x from the incident surface decreases exponentially as per the Beer-Lambert's law.

$$I(x) = I_0 \exp^{-ax} \qquad \text{Equation (2.4)}$$

where I_0 is the incident intensity of light at the incident surface and a is the absorption coefficient. In order to absorb most of the incident photons, the thickness (d) of the absorber needs to be $d > 1/a$.

Perovskites have a high absorption coefficient compared to other semiconductors like silicon or gallium arsenide. Hence, a thinner layer is sufficient to function as an absorber for solar cell application. Thinner absorber also reduces the possibility of the charge carriers undergoing recombination before the charge transport layer collects them. A 220 nm $MAPbI_3$ exhibited an a $>10^4$ cm^{-1} for the wavelength below 700 nm [32]. Such high absorption coefficient makes perovskite an excellent candidate for PV technologies with higher efficiencies.

Long diffusion length

Diffusion length is the distance a photo-generated charge carrier (electron or hole) travels in an absorber before it recombines. Hence, long lifetimes imply low non-radiative recombination rates. The diffusion length of a semiconductor depends on the following equation:

$$L_D = \sqrt{\frac{\mu k_B T}{e} \tau} \qquad \text{Equation (2.5)}$$

where, L_D is the diffusion length, μ is the mobility and τ is the lifetime of the charge carriers and e is the elementary charge. While absorption coefficient determines the minimum thickness required for a semiconductor to absorb most photons incident on it, the diffusion length determines how thick the semiconductor can be before the charge carriers recombine prior to their extraction. Hence, $1/a < d < L_D$ is the ideal thickness of a semiconductor for application in solar cells. This enhances absorption predominantly in the visible spectrum, a key factor in improving solar cell efficiency.

Low non-radiative recombination rates

Upon generation of electrons and holes, the charge carriers can recombine with other charge carriers of opposite polarity. This process is called recombination. As the generated charge carriers are lost before being collected by the charge transport layer, recombination can be detrimental to the performance of a solar cell. Recombination in a semiconductor can be categorized as:

Radiative recombination: An electron and hole generated due to the absorption of a photon recombine with each other accompanied by emission of another photon. Here, the intrinsic loss in energy is radiative and hence, such process is termed as radiative recombination.

Shockley-Read-Hall recombination: This recombination takes place via defects in the bandgap. An electron or a hole can be trapped by a defect located in the bandgap and can recombine with another hole or electron at the same energy state. The defect is assumed to be in the middle of the bandgap (deep traps). If the defects were located at the bandedge, the trapped electrons or holes are more likely to be go back to the conduction band or the valence band.

Auger recombination: In Auger recombination, the energy of electron and hole recombination is transferred to another electron or hole in the conduction or the valence band instead of being emitted as a photon. This electron or hole then thermalizes back to the conduction or the valence bandedge.

Even though, all three types of recombination takes place in the perovskites, their recombination rate are extremely low compared to the other semiconductors. This confirms their high crystal quality and low defect states [52].

The above-mentioned optoelectronic characteristics makes perovskites an ideal candidate for absorber in solar cells.

2.2. Perovskite-based solar cells

2.2.1. Working principle of a single junction perovskite solar cell

Solar cells convert the energy of photons into electrical energy based on the principle of photovoltaic effect. When illuminated with photons above a threshold energy $E \geq E_G$, from the solar spectrum, solar cells generate both current and voltage at the same time, generating electrical power. Here, E_G is the bandgap of the absorber. An ideal solar cell, should be able to absorb all photons above the threshold energy, generate and collect charge carriers i.e. electrons and holes contributing to the power output. With a high absorption coefficient, perovskite solar cells are capable of absorbing more photons to generate and collect more charge carriers. Perovskite solar cells are a type of thin films heterojunction solar cells. A heterojunction is a junction formed between two different semiconductor materials with different bandgaps or electronic properties. In perovskite solar cells, the perovskite layer is the main light absorber and it is sandwiched between two different transport layers. The working of a solar cell can be explained in the following steps:

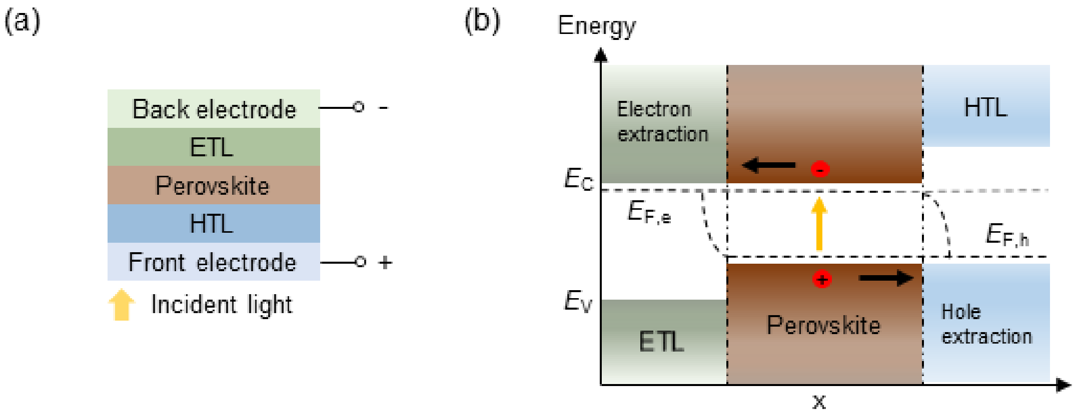

Figure 2.2: (a) A schematic of perovskite solar cell consisting of front electrode, hole transport layer (HTL), perovskite absorber, electron transport layer (ETL) and back electrode. The light enters the solar cell from the front electrode (b) Energy band diagram of a perovskite solar cell under illumination showing electron accumulation in the conduction band (E_C) and hole accumulation in the valence band (E_V). The Fermi level splits into quasi-Fermi levels for electrons ($E_{F,e}$) and holes ($E_{F,h}$), generating a potential difference between the electrodes. Selective charge carriers, the electron transport layer (ETL) and the hole transport layer (HTL) facilitate efficient separation and extraction of charge carriers.

Absorption of incident photons:

Upon transmission through the semi-transparent charge transport layer, the photons reach the absorber. Photons with energy greater than or equal to the threshold energy, E_G are absorbed and remaining photons are transmitted through the absorber as sub-bandgap photons. Photons with energy larger than E_G dissipate the excess energy as thermalization losses.

Generation of electron-hole pairs:

Photon absorption generates electron-hole pairs but it is also associated with intrinsic loss mechanisms in the absorber material.

Separation of the electrons and holes:

The electron-hole pairs quickly dissociate into free positive charge carriers (holes) in the valence band (E_V) and negative charge carriers (electrons) in the conduction band (E_C) of the absorber. The electron and holes are free to move in the conduction and valence band, respectively.

Depending on the force, the charge carriers are exposed to, they can generate drift or diffusion current. If the charge carriers are only exposed to electrical force (force between two charged objects) because of the electric field $\mathbf{E}$, the generated drift current is denoted by [53],[54]:

$$j_{elect,e,h} = en_{e,h}\, \mu_{e,h}\, \mathbf{E} = \sigma_{e,h}\, \mathbf{E} = -\frac{\sigma_{e,h}}{z_{e,h}\, e} \operatorname{grad}\left(z_{e,h}\, e\, \varphi\right) \qquad \text{Equation (2.6)}$$

where e is the elementary charge (with $z_e = -1$ and $z_h = 1$). $n_{e,h}$ is the concentration, $\mu_{e,h}$ is the mobility and $\sigma_{e,h}$ is the electrical conductivity of the charge carriers. φ is the electric potential due to which the charge carriers experience the electric force $-\operatorname{grad}\left(z_{e,h}\, e\, \varphi\right)$.

If the charge carriers experience a chemical force due to the gradient in the charge carrier concentration, the diffusion current is denoted by:

$$j_{diff,e,h} = z_{e,h}\, e\, \left(-D_{e,h} \operatorname{grad}\left(n_{e,h}\right)\right) = -\frac{\sigma_{e,h}}{z_{e,h}\, e} \operatorname{grad}\left(\Phi_{chem,e,h}\right) \qquad \text{Equation (2.7)}$$

where $D_{e,h} = \mu_{e,h}\, k_B T/e$ is the diffusion coefficient, k_B is the Boltzmann constant and T is the temperature. $\Phi_{chem,e,h}$ is the chemical potential due to which the charge carriers experience the chemical force $-\operatorname{grad}\left(\Phi_{chem,e,h}\right)$.

Since the charge carriers experience both electrical and chemical forces simultaneously, the resulting total current is the sum of the above two equations:

$$j_{total,e,h} = -\frac{\sigma_{e,h}}{z_{e,h}\, e} \operatorname{grad}\left(z_{e,h}\, e\, \varphi + \Phi_{chem,e,h}\right) = -\frac{\sigma_{e,h}}{z_{e,h}\, e} \operatorname{grad}\left(\eta_{e,h}\right) \qquad \text{Equation (2.8)}$$

where $\eta_{e,h}$ is the electrochemical potential of the charge carriers [54].

In the next step, a relationship between the electrochemical potential and the Fermi level (E_F) is established. The electrochemical potential is the energy that dictates how charged particles move, combining effects from both chemical concentration and electric fields. The Fermi level represents the energy at which the probability of an electron state being occupied is 50% at thermal equilibrium, as described by the Fermi-Dirac distribution. When the temperature is above the absolute zero ($T >$ 0 °C), states below E_F have a higher probability of being occupied, while those above E_F have a lower probability of being occupied. Under illumination, the increase in charge carrier density causes E_F to shift in two different directions. Increased electron concentration shifts E_F closer to the conduction band minimum, while increased hole concentration shifts it toward the valence band maximum. This apparent contradiction is resolved in steady state by introducing two separate Fermi distributions, one for electrons and one for holes. In dark, the Fermi level remains in equilibrium across all three layers. However, under illumination, photo-generated carriers increases because of increased electron and hole densities in the conduction and valence bands, respectively. As a result, E_F splits into the quasi-Fermi level for electrons ($E_{F,e}$) and the quasi-Fermi level for holes ($E_{F,h}$). This separation is referred to as quasi-Fermi level splitting [55], [56]. The gradient of the Fermi level represents a non-equilibrium state with a driving force for motion of the charge carriers which leaves behind uncovered ionized dopants resulting in a space charge region. Space charge generates an electric field as a result of the carrier redistribution demanded by the Fermi level gradient.

The electrochemical potential of electrons in the conduction band and their quasi-Fermi level $n_e = E_{F,e}$ indicate the occupancy of states in the conduction band. Similarly, the electrochemical potential of holes in valence band and their quasi-Fermi level ($n_h = -E_{F,h}$), indicates the occupancy of states in the valence band. Given the charge numbers with $z_e = -1$ and

z_h = 1 for electrons and holes respectively, the resulting charge currents for electrons and holes are expressed as:

$$j_{total,e,h} = \frac{\sigma_e}{e} \text{ grad } \left(E_{F,e}\right) = \frac{\sigma_h}{e} \text{ grad } \left(E_{F,h}\right) \qquad \text{Equation (2.9)}$$

This indicates that the charge carrier currents depends on the gradients of quasi-Fermi levels and electrical conductivities.

Charge extraction by selective charge carriers:

The charge carriers generated in the absorber upon illumination have to be separated and collected at opposite contacts, in order for them to contribute to extracted power output. The charge transport layers (CTLs): namely electron transport layer (ETL) and hole transport layer (HTL) perform this work. The gradients of the quasi-Fermi levels are not sufficient to give directionality to electrons and holes as they are being extracted by ETL and HTL respectively [57]. Hence, the CTLs also exhibit selectivity of charges i.e. ETLs have high conductivity for electrons and HTLs have high conductivity for holes. The selective charge carriers prevent electrons and holes from recombining symmetrically, forcing them to move in different directions and converting local quasi-Fermi level splitting into spatial gradients. The choice for ETLs and HTLs depends on the architecture of the PSC and will be discussed in **Chapter 3**. Irrespective of the materials chosen for ETL/HTL, the free charge carriers are collected at interface of the absorber with either of the CTLs.

The flow of charge carrier current is in the opposite direction to the maximum gradient of the quasi-Fermi levels. Alongside charge selectivity, the ETL must have a large difference in the E_V to the absorber and the HTL must have a large difference in E_C compared to the absorber. As perovskite have the long charge carrier lifetimes and diffusion lengths, almost all electrons and holes are extracted from the absorber through the ETL and HTL, respectively. The extraction of charge carriers at the respective electrodes allows an electric current to flow through the external load [53].

The energy difference between the electron and hole quasi-Fermi levels $E_{F,e} - E_{F,h}$, can be expressed in terms of electrical energy eV. Here V is the voltage drop between the contacts on the ETL and HTL sides.

Under short-circuit conditions, where the negative type (n-type) and positive type (p-type) regions are directly connected, no potential barrier exists. A net current called the short-circuit current (I_{SC}) flows due to carrier concentration gradients and the effect of selective contacts. Under open-circuit conditions, with the n-type and p-type selective contacts are disconnected, no current flows through the junction. An open-circuit voltage (V_{OC}) is established, equal to the difference between the quasi-Fermi levels of electrons and holes at the terminals of the solar cell and reflects a difference in electrochemical potential. During normal operation under illumination and with an external load, the solar cell functions between these two extremes producing both photocurrent and photovoltage, and thereby generating electrical power. At intermediate points, the external load presents a finite resistance, allowing partial current flow while sustaining a measurable voltage.

At steady state, the current generated by a solar cell under illumination is the sum of all the generated and extracted charge carriers within the absorber. The current density is:

$$j = \int_0^d e\left(G(x) - R(x)\right)\, dx \qquad \text{Equation (2.10)}$$

where d is the thickness of the absorber. The contribution for generation rate G comes from two source: the generation rate caused by thermal radiation at room temperature and the non-equilibrium generation rate caused by illumination $G(x) = G_{dark} + G_{illu}(x)$

In non-equilibrium, the recombination rate R is increased compared to equilibrium at room temperature due to the additional charge carriers generated by illumination

$$R(x) = R_{dark}\ \frac{n_e\, n_h}{n_i^2} = \ R_{dark}\ \exp\frac{E_{F,e}(x) - E_{F,h}(x)}{k_B T} \qquad \text{Equation (2.11)}$$

where n_i is the intrinsic charge carrier density and $n_e,\ n_h$ are the charge carrier concentrations during illumination.

In equilibrium, the generation rate and the recombination rate are equal $(G_{dark} + R_{dark})$ and the current density is given by

$$j = -e\int_0^d \left(G_{dark}\left(1 - \exp\left(\frac{E_{F,e}(x) - E_{F,h}(x)}{k_B T}\right)\right) + \ G_{illu}(x)\right)\ dx \qquad \text{Equation (2.12)}$$

Extraction of charge carriers is possible only if the electrons and holes generated are within the diffusion lengths ($L_e +\ L_h$) from the selective contacts. The integral above is solved only within the absorber with the boundaries $[-\,L_e\,, L_h]$. Given, the electrochemical potentials of the charge carriers inside the absorber and the thermal generation rate do not depend on the location, the equation changes to:

$$j = e\ G_{dark}(\ L_e + L_h)\left(\exp\left(\frac{E_{F,e} - E_{F,h}}{k_B T}\right) - 1\right) - e\int_{-\,L_e}^{L_h} G_{illu}(x)\ dx \qquad \text{Equation (2.13)}$$

The remaining two terms of the generation rates can be understood by examining two limiting scenarios. First, under illumination with an external short-circuit (V = 0), the short-circuit current density j_{SC} is given by:

$$j_{SC} = -\,e\int_{-\,L_e}^{L_h} G_{illu}(x)\ dx \qquad \text{Equation (2.14)}$$

In dark, the $G_{illu}(x) = 0$ and under a large reverse bias, the dark saturation current density is:

$$j = -e\ G_{dark}(\ L_e + L_h) \qquad \text{Equation (2.15)}$$

As previously discussed, the energy difference between the quasi-Fermi levels $E_{F,e} - E_{F,h}$ corresponds to an electrical energy eV. Thus, the total current density can be expressed as:

$$j = j_0\left(\exp\left(\frac{eV}{k_B T}\right) - 1\right) - j_{SC} \qquad \text{Equation (2.16)}$$

This equation describes the characteristic current-voltage behavior of a solar cell. By varying the resistance of the external load, the operating point moves along the *I*-*V* curve, resulting in a both photovoltage (lower than V_{OC}) and a photocurrent (lower than I_{SC}), enabling the generation of electrical power.

2.2.2. Equivalent circuit of a solar cell and *J*-*V* characterization

Equivalent circuits are commonly used to represent the electrical behavior of solar cells. By comparing **Equation 2.16** with the Shockley equation, which characterizes the behavior of a diode, it becomes evident that an ideal solar cell can be modeled as a combination of a diode and a current source. In this model, the photocurrent (I_{ph}) increases with the intensity of illumination, while the diode current (I_d) accounts for radiative recombination losses. Alongside radiative recombination losses, a real solar cell also has resistive losses. The model is extended by incorporating a series resistance (R_s) and a shunt resistance (R_{sh}), completing the one-diode model as depicted in **Figure 2.3 (a)**. In this model, the output current (I) of the solar cell is given by the photocurrent minus the sum of the diode current and the current through the shunt resistance.

$$I = I_{ph} - I_d - I_{sh} \qquad \text{Equation (2.17)}$$

Using the diode current, the output current can be expressed as:

$$I(V) = I_{ph} - I_0[\exp\left(\frac{e(V - IR_s)}{n_{id}k_BT}\right) - 1] - \left(\frac{V + IR_s}{R_{sh}}\right) \qquad \text{Equation (2.18)}$$

where I_0 is dark saturation current, n_{id} is the ideality factor, e is the elementary charge, k_B is the Boltzmann constant, T is the absolute temperature and V is the output voltage.

For an ideal solar cell $R_s = 0$ and $R_{sh} = \infty$ can be assumed,

$$I(V) = I_{ph} - I_0[\exp\left(\frac{e(V)}{n_{id}k_BT}\right) - 1] \qquad \text{Equation (2.19)}$$

The fundamental parameters of a solar cell can be calculated from the current-voltage curve. These parameters hold vital information about performance of a solar cell as shown in **Figure 2.3 (b)**.

Open-circuit voltage (V_{OC}): The maximum voltage available from a solar cell, which occurs at zero current. The bandgap of the absorber E_G determines the maximum voltage that a solar cell can generate.

$$V_{OC} = \frac{n_{id}k_BT}{e}\ln\left(\frac{I_{ph}}{I_0} - 1\right) \qquad \text{Equation (2.20)}$$

Short-circuit current (I_{SC}): The current through the solar cell when the voltage across the solar cell is zero.

$$I_{SC} = I \sim I_{ph} \qquad \text{Equation (2.21)}$$

I_{SC} depends on the input illumination and the illuminated area (A). Current density (I_{SC}/A) makes comparing power generated by cells of different areas more convenient. Hence, short-circuit current density (J_{SC}) is a more commonly used term.

Fill factor (FF): At the V_{OC} and J_{SC} point, the power generated by a solar cell is zero. The FF is the ratio of the maximum power from the solar cell to the product of V_{OC} and J_{SC}.

$$\text{FF} = \frac{V_m J_m}{V_{OC} J_{SC}} \qquad \text{Equation (2.22)}$$

where V_m and J_m are the voltage and current density at the maximum power point (P_m).

The FF of a solar cell can be reduced due to parasitic resistive losses. The parasitic resistances can be categorized as series resistance (R_s) and shunt resistance (R_{sh}).

Series resistance (R_s): The R_s represents losses due to restricted charge carrier transport within the solar cell originating due to contact resistance between the metal contact and the charge transport layer, resistance in the charge transport layers and resistance against movement of current in the absorber. A simple way of calculating series resistance of a solar cell is to find the slope of the J-V curve at the V_{OC} point.

Shunt resistance (R_{sh}): The R_{sh} represents leakage currents (I_{sh}) caused by the imperfections in the absorber material. Shunt resistance of a solar cell can be calculated with the slope of the J-V curve at the J_{SC} point.

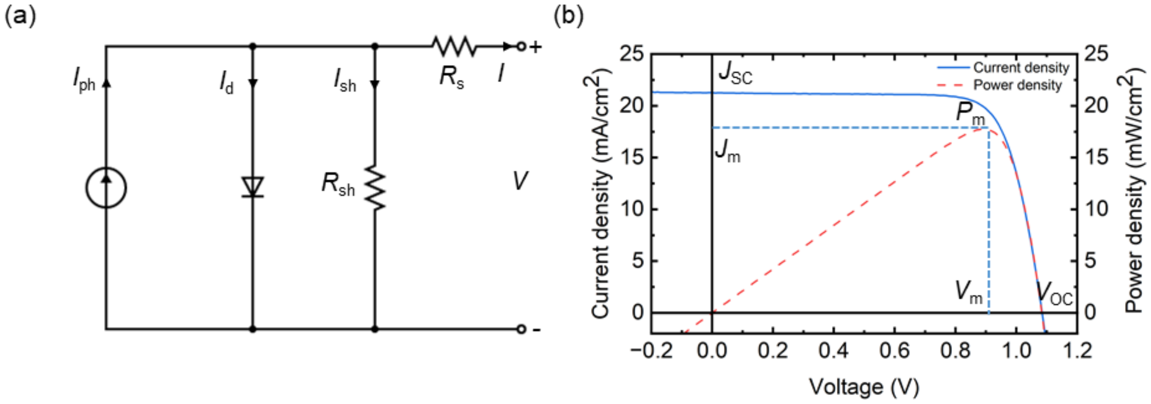

Figure 2.3: (a) One diode model of a solar cell represented by a current source, diode and shunt resistance (R_{sh}) in parallel and series resistances (R_s) in series. (b) Current density-voltage characteristics (J-V characteristics) of a solar cell with performance parameters: open-circuit voltage (V_{OC}), short-circuit current density (J_{SC}), maximum power point (P_m), voltage at maximum power point (V_m) and current at maximum power point (J_m).

Power Conversion Efficiency (PCE):

The power conversion efficiency (PCE) is the key performance metric of a solar cell, defined as the ratio of the power density at the maximum power point (P_m) to the power density of the incident light (P_{in}):

$$PCE = \frac{P_m}{P_{in}} = \frac{V_{OC}\, J_{SC}\, FF}{100\; mW/cm^2} \qquad \text{Equation (2.23)}$$

Under the standard testing condition (STC), 100 mW/cm^2 of AM1.5G spectrum is used as incident illumination. The measurements are performed at a cell temperature of 25 °C [58].

2.2.3. Theoretical efficiency limits of a single junction perovskite solar cell

The maximum efficiency that a solar cell can harvest depends on the bandgap of the absorber. Only photons with energy $E \geq E_G$ can contribute to charge carrier generation. E_G is the bandgap of the absorber. When the energy of the photon $E > E_G$, the excess energy is released and the electron thermalizes to the E_C minimum and hole thermalizes to E_V maximum. Thermalization can be accompanied by release of phonons (lattice vibrations) resulting in generation of heat. When the energy of the photon $E < E_G$ the photons are transmitted through the absorber and are not utilized. These photons are sub-bandgap photons and do not contribute to charge carrier generation. Under the air mass 1.5 global (AM1.5G) solar spectrum, silicon solar cells (with a bandgap of 1.12 eV) lose approximately 32% of the incident solar power due to photon transmission and 19% due to thermalization. The remaining 49% of the irradiance is available usable for electricity generation.

The Shockley-Queisser model quantifies the maximum theoretical efficiency of a single junction solar cell [59]. This can be quantified with the ultimate efficiency (υ), which can be explained as the ratio of the maximum achievable voltage ($V_{\max}$) and maximum generated current density ($J_{\max}$) to the input irradiance of AM1.5G.

$$\upsilon = \frac{V_{max} J_{max}}{P_{in}} \qquad \text{Equation (2.24)}$$

The maximum current density ($J_{\max}$) generated can be represented as

$$J_{max} = e \int_0^{\lambda_G} \phi_{AM1.5G}(\lambda)\ d\lambda \qquad Equation\ (2.25)$$

where λ_G is the wavelength corresponding to the bandgap, $\phi_{AM1.5G}$ is the photon flux density at the standard AM1.5G solar spectrum and e is the elementary charge.

The maximum achievable voltage ($V_{\max}$) is represented as,

$$V_{max} = \frac{E_G}{e} \qquad \text{Equation (2.26)}$$

For a silicon solar cell with a E_G of 1.12 eV, the $J_{\max}$ is 44 mA/cm^2 and the $V_{\max}$ is 1.12 V, resulting in an υ of 49% under an incident power of 100 mW/cm² of AM1.5G.

In reality, the V_{max} cannot be achieved due to the nonzero temperature of the solar cell. At STC, the temperature of the solar cell should be maintained at 25 °C [58]. This limitation is represented by $V_{oc}\ /V_{max}$. The model also considers a FF which takes into account the impedance matching factor for the maximum power output. Hence, the maximum theoretical efficiency of a solar cell which is dependent on E_G and cell temperature can be expressed as:

$$\upsilon_{max} = t_s \frac{FF\ V_{oc} J_{max}}{P_{in}} \qquad \text{Equation (2.25)}$$

where t_s is the probability that a photon with $E \geq E_G$ produces an electron-hole pair. The detailed balance limit of efficiency for silicon solar cells with a bandgap of 1.12 eV is 32.6% [60].

It should be noted that the Shockley-Queisser model is based on several idealized assumptions:

i) 100% absorption of photons with energies $E \geq E_G$

ii) 0% absorption of photons with $E < E_G$

iii) each absorbed photon generates exactly one pair of charge carriers

iv) ideal carrier selectivity of the charge transport layers with negligible ohmic resistance

v) no non-radiative recombination losses

Hence, these limits do not take into account the resistive, optical and non-radiative recombination losses [61]. Hence, the practical limit of a solar cell is much lower than the theoretically estimated values [59],[62].

2.3. Overcoming theoretical efficiency limits

There are numerous possibilities to overcome the efficiency limits among which multi junction solar cells [63],[64], spectral convertors [10],[65] and solar concentrators [66],[67] are a few. Two of these options have been explored in this work, namely multi junction solar cells and spectral convertors. **Figure 2.4** depicts the spectral irradiance of AM1.5G. The photons that can be utilized by a PSC of

E_G =1.57 eV is shown in brown. The low-energy photons, in dark grey, are available for spectral conversion by upconversion or multi junction solar cells. The main objective here is not to boost the theoretical efficiency limits but to study the implications on stability when such technologies are combined with the perovskite PV.

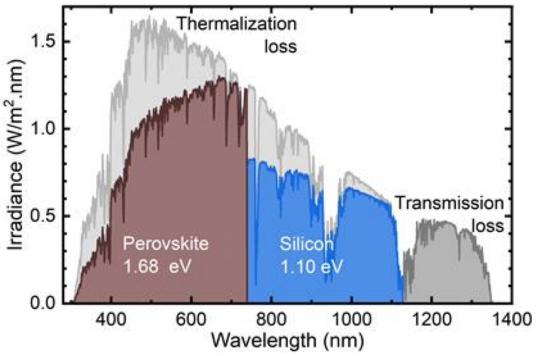

Figure 2.4: Spectral irradiance of the air mass 1.5 global (AM1.5G) utilized by a perovskite solar cell of bandgap, E_G =1.57 eV (brown). The high-energy photons lose their excess energy as thermalization losses (light grey) and the low-energy photons are transmitted through the perovskite solar cell as transmission losses (dark grey). The low-energy photons are available to multi-junction solar cells or upconversion.

2.3.1. Perovskite-based multi junction Solar Cells

A multi junction solar cell implementing absorbers of different bandgaps in order to harvest the solar spectrum more efficiently is called a TSC [63],[68]. Each absorber can harvest photons from different portion of the solar spectrum, which would have been otherwise lost as transmission or thermalization losses. With the ability to tune the bandgap, the attractive feature of perovskite semiconductors then becomes application in tandems with other PV technologies. While high-energy photons ($E \geq E_{G-top}$) are absorbed in the top subcell (wide-bandgap PSC), low-energy photons ($E < E_{G-top}$) are transmitted through the top subcell and absorbed in the bottom subcell (narrow-bandgap PSC, silicon or Copper Indium Gallium Selenide cells. The two subcells can be optically and/or electrically coupled resulting in four-terminal (4T) [69]–[71] or two-terminal (2T) [72]–[74] configurations. Schematic of 2T and 4T configuration is presented in **Figure 2.5 (a)** and **Figure 2.5 (b)** respectively. Both configurations have their own set of advantages and disadvantages.

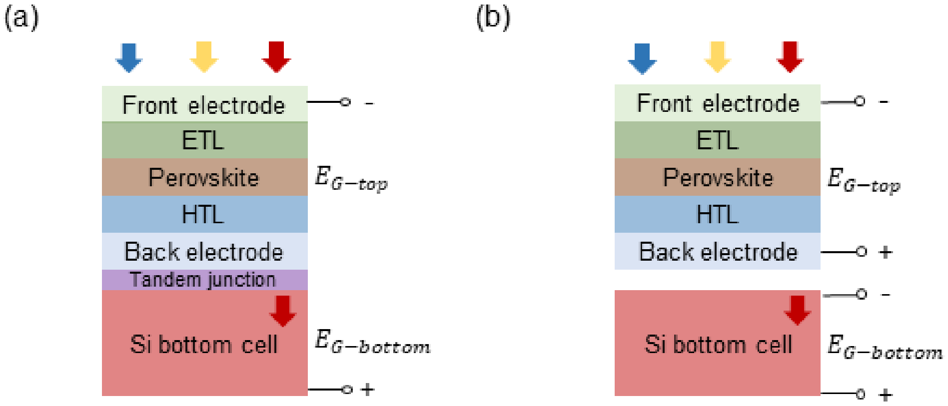

Figure 2.5: (a) Two-terminal (2T) and (b) four-terminal (4T) perovskite- Si tandem solar cells (TSCs). 2T TSCs are optically and electrically interconnected and 4T TSCs are optically interconnected but electrically isolated.

In the 4T configuration, the subcells are coupled optically but are operated separately. As the two subcells are optically coupled, the back electrode of the top subcell and front electrode of the bottom subcell have to be transparent to allow low-energy photons to pass through to the bottom subcell. Since the two subcells have their own current and voltage, the total PCE of the TSC is the sum of the PCEs of the two individual subcells. Hence, the 4T configurations are also more robust against environmental factors such as change in spectrum and temperature variations. This gives 4T TSCs an advantage that the performance of the 4T TSC is not affected by the current of the current limiting subcells. Hence, the performance of the 4T TSC are less affected by spectral variations of the solar spectrum [51]. However, tracking the two subcells individually, can become quite expensive as they require twice as many electronic components [75].

In case of the 2T TSCs, the top subcell is monolithically fabricated on top of the bottom subcell and serially interconnected with the recombination junction comprising of either transparent conductive oxide (TCO) or evaporated metals [72],[74]. The recombination junction allows recombination of the charge carriers from the two subcells. Because of the serial connection of the subcells, the voltage of the 2T TSC is the sum of the voltages of the two individual subcells. The total current of the 2T TSC is the current of the current limiting subcell. Hence, current matching between the two subcells is very important for 2T TSC to have a high current resulting in high PCE [76]. However, current has linear relationship with irradiance and any variations in the daily irradiance including shading; cloudy conditions or soiling can drastically decrease the current of one of the subcells affecting the overall PCE. The record PCE reported with the combination perovskites with various PV technologies as TSCs are presented in **Table 2.1**.

Table 2.1: Record power conversion efficiency (PCE) reported for 2T and 4T perovskite-based tandem solar cells (TSCs)

TSC	2T	Reference	4T	Reference
pero-Si	34.9 %	[4]	29.2%	[77]
all-pero	30.1 %	[4]	-	-
pero-CIS	26.3 %	[4]	29.9%	[78]

2.3.2. Spectral convertors

Spectral converters are materials that modify the energy of incoming photons to better match the absorption capabilities of a solar cell, thereby improving its efficiency. Spectral converters help bridge the mismatch between the solar spectrum and a solar cell with a specific bandgap. The process of spectral conversion can be categorized into:

Upconvertors

Upconverters are materials that absorb two or more low-energy photons in the near infrared (NIR) range and emit one higher-energy photon in the visible (VIS) or ultraviolet (UV) range (shown in **Figure 2.6 (a)**). Upconversion reduces the transmission losses in solar cells and hence, are ususally placed at the backside of the solar cells [79]. Implementation of a mirror-like back surface allows the upconverted photons to be reflected back to the solar cells facilitating reabsorption. Some common upconversion materials are: Lanthanide doped metal fluorides, Lanthanide doped metal oxides and organic dyes. Metal fluorides like Sodium Yttrium Tetrafluoride ($NaYF_4$) [80] or Lithium Yttrium Tetrafluoride ($LiYF_4$) [81] are doped with lanthanides such as Ytterbium (Yb^{3+}) and Erbium (Er^{3+}) for harvesting sub-bandgap photons. Metal oxides including Yttrium(III) oxide (Y_2O_3) [82] and Gadolinium(III) oxide (Gd_2O_3) [83] also require Yb^{3+} and Er^{3+} dopants as sensitizers and activators.

While metal oxide and metal fluoride based upconvertors are chemically stable, they require high excitation intensity for demonstrating high upconversion quantum yield. Organic dyes can also be used as upconversion materials and require low threshold power for excitation, however, they are sensitive to oxygen and less stable [84].

Downconvertors

Downconverters are materials that absorb a high-energy photon in the UV range and emit one or more low-energy photons in the VIS or NIR range (illustrated in **Figure 2.6 (b)**). Ideal placement of downconverters are at the front of the solar cells as they help reduce the thermalization losses in solar cells [85]. Some categories of downconvertors are lanthanide doped metal oxides or fluorides and quantum dots. Yttrium oxyfluoride (YOF) [86], Yttrium orthovanadate (YVO_4) [87] with dopants: Yb^{3+}, Thulium (Tm^{3+}) and Europium (Eu^{3+}) are commonly implemeted as downconvertors. Alongside being stable, Yttrium based downconvertors also demonstrate high photoluminescence quantum yield when doped with Eu^{3+}. Core-shell Cadmium Selenide/ Zinc sulfide (CdSe/ZnS) quantum dots demonstrate down-conversion of the incident photons although the toxicity of Cd is be a concern [88].

Downshifters

Downshifters are materials that absorb high-energy photons in UV range and re-emit photons of lower energy in VIS or NIR range [89]–[91]. Unlike downconversion, which can produce multiple photons, downshifting converts one high-energy photon into one photon of lower energy (depicted in **Figure 2.6 (c)**). Some commonly used downshifting materials are lanthanide doped phosphors, organic dyes and metal organic framework. Cerium-doped yttrium aluminum garnet (YAG:Ce) were introduced into the module of the crystalline silicon solar cells and demonstrated 2.68% increment in the PCE [92].

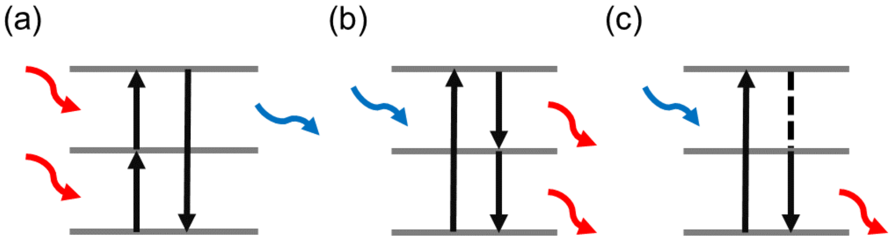

Figure 2.6: Schematic illustration of (a) Upconversion (b) Downconversion and (c) Downshifting. Upconversion is the annihilation of two low-energy photons into a high-energy photon. Downconversion is the splitting up of a high-energy photon into two low-energy photons. Downshifting is conversion of a high-energy photon into a low energy photon.

During upconversion, downconversion and downshifting, the emission might be lost due to reflection losses, escape cones or from the front face [93]. In luminescent solar concentrators, emission are guided for reaching the edges of the converting layer where solar cells are mounted at the edges. They usually consist of spectral convertors dispersed in polymer sheets [94],[95]. **Table 2.2** summarizes the record relative increment reported for implementation of spectral convertors in perovskite solar cells.

Table 2.2: Relative increment in PCE reported for implementation of spectral convertors in perovskite solar cells

Spectral convertors	Material used	Δ PCE_{rel}	Reference
Upconvertors	β-$NaYF_4$:Yb^{3+},Tm^{3+}	20 %	[96]
Downconvertors	Eu−4,7-diphenyl-1,10-phenanthroline	15.3 %	[97]
Downshifters	CdSe/CdS quantum dots	7.4 %	[98]

2.4. Stability of Perovskite-based Solar Cells

The above mentioned excellent optoelectronic characteristics give perovskites the ability to harvest photons efficiently from the solar spectrum. On the one hand, incorporation of different cation and anions allows tailoring of bandgap and hence the optoelectronic characteristics. On the other, incorporation of different size of these cations and anions make perovskites more reactive to stimuli like light, elevated temperature and voltage bias. These stress factors are inherent to the functioning of a solar cell. Hence, degradation of perovskite materials upon exposure to such stress factors is of a major concern. Degradation is the change occurring in the absorber material, one of the employed CTLs or metal contacts, which lowers the PCE of the device (single junction, large area modules or multi junction tandems). A deep understanding of the degradation mechanism under different stress factors is essential to finding the solutions to make this technology one of the promising options in the PV industry.

2.4.1. Intrinsic stability

Intrinsic stability is the stability of solar cells under stress factors that are essential to working of a solar cell namely light, voltage bias and temperature. Ideally, in order to operate as a solar cell, the different components: the absorber, the CTLs, the front and the metal contact should be able to maintain their performance under intrinsic stress factors. However, the real situation is far from ideal. Many of these intrinsic stress factors cause reversible or irreversible changes to one of the components of the PSCs. This section highlights the stress factors and their effect on the PSCs.

Light:

Light induces both positive and negative effects in PSCs. In presence of metastable defects, light soaking has been reported to improve the stability of PSCs. Especially when these defects are in the perovskite absorber, light soaking induces ion migration and subsequent defect passivation reducing the number of defects and improving the long-term stability of PSCs [99]–[101]. On the other hand, light induced performance degradation is also a known phenomenon where the ionic species move and accumulate at the interface of the absorber and the CTLs. Over time, the ionic accumulation prevent further extraction of charge carriers severely reducing the performance of the PSCs [101],[102].

Alongside the absorber itself, light also affects the stability of the CTLs. Fullerene (C_{60}) is one of the ETLs used in PSCs. C_{60} were reported to undergo photo-dimerization under light exposure resulting in formation of defects, which inhibits charge transport [104]. However, recent works report that C_{60} is stable under illumination over extended period of time [105]–[107]. Among the inorganic ETLs used in the early days, TiO_2 exhibited severe degradation under light especially in the UV range [108],[109]. Light-induced desorption of oxygen from the TiO_2 surfaces caused formation of traps and resulted in recombination at the TiO_2 interface[108]. Replacement of TiO_2 with SnO_2 or using a UV filter resolved the issue of degradation under illumination [110]–[113].

Migration of I^- ions from the illuminated area of $MAPbI_3$ has been previously reported [114]. As the perovskite structure implements alloying, both in the cation [115],[116] and halides [50],[117] sites, the process becomes more complicated. Mixed halides were reported to undergo light-induced phase segregation into I^- rich and Br^- rich regions. The charge carriers funnel through the low bandgap I^- region. This phenomenon also known as Hoke's effect was reversible and more pronounced in wider bandgap materials employing >20% Br^- content [118]. Nevertheless, it was still a concern since the attractive feature of perovskite material is band-gap tunability. Application in TSCs requires wide- bandgap perovskites with a bandgap of 1.7-1.8 eV. However, the desired bandgap initially fabricated cannot be retained under light illumination [119]–[121].

Alongside halide migration, A-site cations migration is another concern. In multi cation, mixed halide perovskites, small cation like Cs^+ migrated from the absorber to the HTL. Redistribution of MA^+ and FA^+ in the perovskite layer has also been reported [122]. Occurrence of halide segregation (in range of seconds) and cation segregation (in range of hours) was reported with decrease in performance with extended exposure to light and voltage bias [123]. Degradation at the B-site has also been observed and reported. The I^- ions in the lattice are oxidized by photo-generated holes forming I^- vacancies and interstitials. Neutral interstitials are much smaller than I^- ions and can easily be removed from the lattice into the interstitials resulting in formation of metallic lead Pb^0 [124]. However, lowering defects concentration result in lowering of holes density and slowing down of the interstitial I^- formation.

Grain size plays a vital role in defect passivation in the absorber. Since larger grains have lower number of grain boundaries, this results in less defects at the interface. The activation energy of ionic migration at the grain boundary is lower than at the grain interiors [125]. Hence, perovskite films demonstrating smaller grain size are more prone to ionic migration under illumination. Chloride containing additives are known to contribute to Ostwald's ripening and larger grain growth [125]– [127]. The interface of the absorber layer with both CTLs contain dangling bonds. These bonds can also serve as defects and need to be passivated for enhancing stability. Hence, surface and bulk passivation strategies become essential [128],[129].

Voltage and reverse bias stability:

For extraction of maximum power from a solar cell, maximum power point tracking is the best mode of operation. However, in order to understand degradation mechanism, reports of degradation study under short-circuit condition (charge transport regime) or open-circuit condition (recombination regime) has also been implemented. There are mixed reports of which of the three mode of operation is more detrimental to the solar cells [131],[132]. Photo-degradation is more rapid at higher voltage, since higher voltage induce more carrier concentration and degradation reaction [133]. However, high defect density in the device will result in high ionic concentration resulting in degradation being induced at lower voltages too.

Bias induced degradation becomes a bigger concern in case of modules, which are more prone to partial shading in outdoor conditions. The shaded subcell are put in reverse bias by the adjoining illuminated subcells and can undergo rapid reverse bias degradation followed by breakdown. The large reverse bias current in partially shaded subcell can flow through shunts, creating hotspots [134]. In the silicon PV technology, strings of 18 subcells are bypassed using a bypass diode at the junction box [135]. Such bypassing can also be used in perovskite modules. Silicon modules have a reverse breakdown voltage of -15 V, but for perovskites, modules have a reverse breakdown voltage between

-1 V to -4 V, requiring almost five to ten times more bypass diodes. Hence, the cost of the module increases [133]. By avoiding metal contacts and implementing TCOs as a top contact, one can reduce the sharp decrease in reverse current via tunneling. Though the conductivity of the TCOs decreases at high reverse voltage, they recover partially on dark storage [133].

Elevated temperature:

Throughout the day, the temperature of the atmosphere changes mainly due to the sun. Similarly, the temperature of a solar cell under operation changes due to the heating effect of the sun (or other light sources). Temperature variations can alter the structural characteristics of perovskite material and affect the stability of PSCs as a whole. $MAPbI_3$ is in tetragonal (β) phase between 165 K < T < 337 K [136]. When the temperature falls below 165 K, it transforms to orthorhombic (γ) phase. Only above the temperature of 337 K does $MAPbI_3$ retain the desirable cubic (α) phase. This can be a major setback since these temperature range fall in the operational window of a solar cell. If the phase of a photovoltaic material changes while it is operational, the characteristics and hence the performance of the solar cell will change. Another candidate $FAPbI_3$ also has a severe phase stability problem. It exists in non-perovskite (δ) phase in the range 130 K < T < 300 K. The inorganic counterpart $CsPbI_3$ only forms α phase above 573 K [137]. This temperature is too high for normal operation of a solar cell. The phase retained by a perovskite composition at a particular temperature determines the annealing temperature during fabrication of PSCs. However, after annealing step and removal from heat, the perovskite might not maintain their phase and revert to δ phase. For perovskites compositions, which do not retain α at room temperature, additives can be beneficial [128], [138]–[140].

Another option for maintaining phase stability of these perovskite compositions at room temperature is A-site cation alloying. Cs^+ alloyed FA with minimum amount of MA^+ is the best choice of perovskite composition for higher performance and better stability [42],[141]. Partial substitution of FA^+ with Cs^+ results in a mixed cation perovskite which demonstrates phase stability at room temperature due to contraction of the cubo-octahedral volume [142]. $FA_{0.75}MA_{0.15}Cs_{0.05}Rb_{0.05}Pb(I_{0.83}Br_{0.17})_3$ perovskite composition also demonstrates a high efficiency and an extended stability 85 °C [143]. A-site alloying affects the thermal stability of perovskite due to the weak hydrogen bonding between A-site cation and PbI_2 octahedra [144], [145]. Post fabrication, perovskites that employ multi cations demonstrate cation segregation under elevated temperature during operation. The main reason for cation segregation is cations have different ionic radii and hence different activation energies for ionic migration [146]. B-site cation alloying has allowed lowering of bandgap for all perovskite tandem application but Sn-based perovskite exhibit lower thermal stability than the Pb-based alternatives [147], [148]. Hence, mixed halides are a better alternative for bandgap tuning. $FA_{0.83}Cs_{0.17}Pb(I_{1-x}Br_x)_3$ demonstrates exceptional thermal stability, though halide segregation under light is still prevalent in them[116].

Alongside perovskite absorber, elevated temperature also affect the stability of charge transport layers. The commonly used HTLs, 2,2′,7,7′-Tetrakis(N,N-di-p-methoxyphenylamine)-9,9′-spirobifluorene (Spiro-OMeTAD) and Poly[bis(4-phenyl)(2,4,6-trimethylphenyl)amine] (PTAA) employ 4-tert-butylpyridine (tBP) to homogenize Lithium bis(trifluoromethanesulfonyl) imide (Li- TFSi) doping. However, tBP is volatile at 85 °C [149],[150]. Hence, the stability of is limited at elevated temperature and can be enhanced by using alternatives like Poly(3-hexylthiophene) (P3HT) [151]. Inorganic alternatives like nickel oxide (NiO) for HTL and tin oxide (SnO_2) for ETL exhibit good thermal stability at elevated temperature [152]. Metal contacts evaporated on top of the device architecture for better charge collection introduces additional stability issues. Diffusion of metal ions into the CTLs and perovskite absorber create defect states at the perovskite interface and/or the absorber. The metal ions react with migrated I^- and form metal halide species in presence of light, bias and elevated temperature severely affecting the stability of perovskite solar cells [153],[154]. TCOs like indium tin oxide (ITO) and indium doped zinc oxide (IZO) have higher conductivity and can replace metal electrodes as a less reactive alternatives [154]. Metal electrodes are more of a risk in perovskite modules where the scribed lines are in direct contact with the evaporated metal [20],[154].

2.4.2. Extrinsic stability

During research stage, solar cells are tested in laboratory conditions but eventually these devices have to be operated in an outdoor condition. Taking a PV technology outdoor requires it to be properly encapsulated to protect its different components from degradation due to exposure to environmental factors like humidity and oxygen. Humidity causes the metallic parts like busbars to undergo corrosion while oxygen causes different materials to undergo oxidation [31][30]. Hence, most commercialized PV technologies are encapsulated before the modules are supplied to the market. The most popular choice of encapsulation is polymer sheets like ethyl vinyl acetate (EVA) or thermoplastic polyolefin (TPO) for packaging and glass-glass encapsulation with an edge sealant like polyisobutylene (PIB) [27]–[29]. The robustness of such packaging and encapsulation alongside the performance of the modules usually last over 25 years [155]. This timeframe also affects the levelized cost of electricity of the PV technology [156]. Hence, the warranty provided by the manufacturers is only covered up to this timeframe. However, with time the performance of the modules decreases and the quality of encapsulation is also compromised with weathering [157]. Small amount of oxygen and humidity permeating through the encapsulation can severely affect the performance of perovskite modules. Understanding the mechanism of degradation triggered by such stress factors helps us to develop methods to prevent such degradation.

Oxygen:

In the presence of oxygen, perovskite materials undergo oxidation. The oxidized perovskite further undergo photo-oxidation, in presence of light, making the situation more detrimental. In $MAPbI_3$, iodide vacancies provide a pathway for the oxygen atoms to incorporate into the perovskite lattice structure [124]. Upon incorporation, the oxygen will trap electrons and form superoxide O_2^-.O_2^- are highly reactive and trigger deprotonation of A-site gas, formation of water and PbI_2 [158]. Such reaction can be initiated and can take up to some hours to decompose to yellow PbI_2 [159]. Since, O_2^- triggers an acid-base reaction, incorporation of smaller A-site cations like FA^+ or Cs^+ can make the decomposition byproducts less acidic and more stable to photo-oxidation [160].

Another alternative of Pb-based perovskites are Sn-based perovskites. However, Sn-based perovskites are more susceptible to oxidation. Sn^{2+} in the perovskite lattice rapidly oxidizes to Sn^{4+} upon exposure to oxygen [161],[162]. Such reactions occur in matter of seconds before the rapid degradation takes place. Though Sn-based perovskites are more vulnerable than Pb-based perovskites, they are more attractive as an alternative to replace the more toxic Pb in perovskite-based PV. Moreover, the difference in electronic characteristics of the two materials and hence the bandgap makes all-perovskite tandems realizable [163].

Small molecules and polymers used for charge transport layers are also vulnerable to degradation on exposure to oxygen. Spiro-OMeTAD and PTAA need oxygen to improve their p-type conductivity [164],[165]. Alternatives to oxygen doping of such HTLs is using pre-oxidized HTLs like Spiro-OMeTAD$^+$ TFSI$^-$ [166] or other forms of doping like Cobalt complexes, where the oxidation step can be omitted [167]. Inorganic charge transport layers NiO_X can also be a possible alternative [24], [168] to these oxygen sensitive organic CTLs.

Humidity:

The molecule of water penetrates the perovskite lattice structure and forms monohydrate or dihydrate perovskite. This is a reversible process and when these hydrated perovskites are placed in dry air, they recover to their original form [169]. However, the effect of humidity on perovskite is not always reversible. Certain perovskite compositions containing organic cations are especially vulnerable to humidity [170]. The organic cations form hydrogen bond with the water molecule, which weakens the bond between organic cation and the PbI_6 octahedra. Additional stress factors like heat and voltage bias can further degrade the already degraded perovskites [171],[172]. Humidity reacts with I^- in the perovskite material and forms hydroiodic acid [173]. The result of such decomposition is the formation of byproduct PbI_2. HTLs such as Spiro-OMeTAD and PTAA are notorious for their hygroscopic nature [171].

Plenty of methods to mitigate the detrimental effects of humidity on perovskite has been explored. A higher bromide content in the perovskite composition is known to be more resistant to moisture ingress [174]. Since, Br^- has a smaller ionic radius than I^-, it forms a more compact perovskite lattice structure and hence are more stable. Replacing I^- with thiocyanate (SCN^-) also creates stronger bonding between Pb^{2+} and SCN^-, making the crystal lattice more difficult to moisture ingress and degradation of the perovskite lattice structure [175],[176]. In addition, partial substitution of organic cations like MA^+ and FA^+ with inorganic cation like Cs^+ drastically improves the resilience of the perovskite layer [142],[177]. Incorporation of large cations such as phenylethylammonium [178], aminovaleric acid [179], etc. into the perovskite precursor improves the robustness of the perovskite absorber against humidity. Large cations possess excellent hydrophobic characteristics however due to their large size; these cations are too big for incorporation into the lattice structure of the perovskite. Hence, they rather form 2D layers every n-layers of 3D perovskite. The superior hydrophobic nature of large cations prevent the formation of hydrates of perovskites, minimizing the damage caused by humidity.

Using less hydrophobic alternatives for HTLs like P3HT [180],[181], or inorganic NiO_X can help resolve the issues of hygroscopic HTLs [152]. Passivation on the ETL interface with a thin layer of hygroscopic AlO_X can also improve retention of the device against moisture ingress [182],[183].

2.4.3. Standardized accelerated testing and assessment of stability

The sensitive nature of perovskite semiconductors makes them susceptible to a variety of intrinsic and extrinsic stressors, which governs the failure mechanism of the PSCs under the applied stress factors. Mutual stress factors can result in existence of simultaneous failure mechanism. For e.g. presence of light can result in elevated temperature due to heating effect of light. Light and elevated temperature can affect different components of a PSC, as discussed previously, complicating the situation [184], [185]. Hence, deep understanding of the failure mechanism induced in the PSC due to presence of an individual stress factor is imperative for working towards finding a solution to mitigating the problem.

Accelerated stress tests provide timely indication of problematic areas and potential failure mechanism allowing early prediction of performance and lifetime under different stress factors. Hence, standardized reporting and systematic assessment of stability is crucial for elucidation of the cause of the failure and their mitigation. Commercialized PV technologies like silicon, Copper

Indium Gallium Selenide, Cadmium Telluride, etc. have their standardized accelerated stress testing for quality control of their PV module [186]–[188]. The International Electrotechnical Commission (IEC) is the global benchmark for quality, safety, and bankability of solar cells and modules. While IEC tests do not define performance limits or efficiency, they are essential for ensuring that PV products are reliable, safe, and commercially deployable. The standards and certifications ensure that the PV modules at the consumer end have a lifespan of greater than 25 years [23]. As these standardized protocols are tested at an industrial level and equipment of industrial scales are also easily available.

Due to the susceptible nature of PSCs, systematic analysis of the accelerated stress testing and their comparison is important. However, the technology is still in early-stage of development and different research groups use their affordable, custom-made setups raising concerns over the conditions in which the accelerated stress tests are executed. To overcome these issues, the perovskite community has established protocols for standardizing the measurement and reporting of stability data. These protocols are called International Summit on Organic and Hybrid Perovskite Solar Cell (ISOS) protocols [189]. The protocols are broadly categorized based on the stress factors as summarized in **Table 2.3**. An easy guide is provided on top to understand if light and/or bias is on or off. For each category of light and/or bias, the temperature of the experiment can be varied between room temperature (RT), 85 °C or temperature cycling (Cy). The temperature is cycled between −40 °C to +85 °C. The atmosphere of the accelerated test can also be predetermined as inert, ambient (amb) or with relative humidity (RH) of 50% or 85%. The standard is 85% but if the absorber and/or CTLs are susceptible to humidity, test can also be conducted at 50%.

ISOS protocols are developed on the framework of IEC standards but they are made more flexible to take into account the ambiguous behavior demonstrated by PSCs such as hysteresis, light soaking effect, burn-in decay, partial recovery under diurnal cycling, etc. Hence, the proposed figure of merit T_{80} caters to the ambiguity in degradation trend. T_{80} is the time taken by the device to decrease below 80% of their initial power output [190]. The protocol also provides approaches to calculate T_{80} based on the different degradation behavior exhibited by the solar cells. If a device has a T_{80} of >1000 h in accelerated stress testing, it signifies that the devices can maintain 80% of their initial performance for over 25 years with diurnal cycling in ambient conditions. If the T_{80} <1000 h, the device has failed the quality control testing. Similar standards apply to the commercialized PV technologies too.

Table 2.3: Summary of International Summit on Organic and Hybrid Perovskite Solar Cell (ISOS) protocols for standardized accelerated stress testing of PSCs.

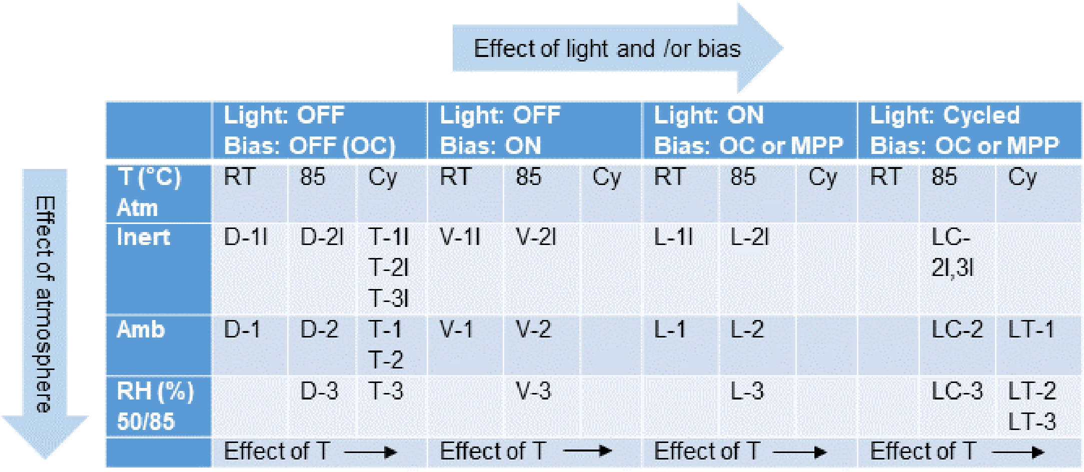

	Light: OFF Bias: OFF (OC)			Light: OFF Bias: ON			Light: ON Bias: OC or MPP			Light: Cycled Bias: OC or MPP		
T (°C) Atm	RT	85	Cy	RT	85	Cy	RT	85	Cy	RT	85	Cy
Inert	D-1I	D-2I	T-1I T-2I T-3I	V-1I	V-2I		L-1I	L-2I			LC-2I,3I	
Amb	D-1	D-2	T-1 T-2	V-1	V-2		L-1	L-2			LC-2	LT-1
RH (%) 50/85		D-3	T-3		V-3			L-3			LC-3	LT-2 LT-3
	Effect of T →			Effect of T →			Effect of T →			Effect of T →		

3. Methods

This chapter describes the experimental details followed in this dissertation. First, the device architecture of the perovskite solar cell is discussed. Material and deposition technique section covers the materials used and the techniques used to deposit them. Then, the basics of structural and morphological characterization techniques used to characterize perovskite thin films is explained followed by the characterization techniques used to analyze the performance and quality of perovskite-based solar cells.

3.1. Architecture of perovskite solar cells

A perovskite solar cell (PSC) comprises of a substrate, usually made up of glass with a layer of transparent conductive oxide (TCO) deposited on one side. The solar cell is fabricated on the side with the TCO deposition, which also functions as one of the electrodes. Other components of the PSC are: the absorber, the positive (p) and the negative (n) charge transport layer and the top electrode. Absorber of a particular bandgap (E_G) absorbs the photons from the solar spectrum. The hole transport layer (HTL) and the electron transport layer (ETL) extracts positive (hole) and negative (electron) charge carriers respectively from the absorber. The top electrode can be a metal contact or a TCO layer.

Based on the sequence of processing of the charge transport layers on the TCO, the architecture of the PSC is determined. PSC can have two architectures: positive-intrinsic-negative (p-i-n) or negative-intrinsic-positive (n-i-p), where i is the intrinsic absorber layer. For a single junction PSC, the light enters from the glass substrate also known as the front electrode.

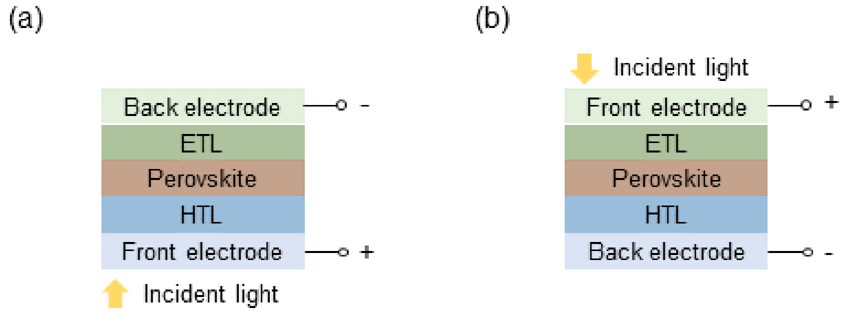

Figure 3.1: (a) positive-intrinsic-negative (p-i-n) and (b) negative-intrinsic-positive (n-i-p) architectures of perovskite solar cells (PSCs). The architecture depends on which charge transport layer is processed on the substrate first as the light is enters the solar cell through this front electrode. In semi-transparent devices, light can enter through both top and back electrode.

3.1.1. p-i-n architecture:

In p-i-n architecture, the hole transport layer (HTL) is processed on the TCO-coated glass substrate as depicted in **Figure 3.1 (a)**. Common choices for HTL are: nickle oxide (NiO_X), poly-[bis-(4-phenyl)-(2,4,6-trimethylphenyl)-amin] (PTAA), poly(3,4-ethylenedioxythiophene): polystyrene sulfonate (PEDOT:PSS) and copper(I) thiocyanate (CuSCN) [191], [192]. In recent years, carbazole-based self-assembled monolayers (SAMs) are quite popular. The lossless interface formed upon processing perovskite layer on top of these monolayers reduce the non-radiative recombination at the interface [193]. Fullerene (C_{60}) with a buffer layer of 2,9-dimethyl-4,7-diphenyl-1,10-phenanthroline (BCP) is used as the electron transport layer (ETL) on top of the perovskite layer in p-i-n architecture [194]. This bilayer ETL is a good option since they can be evaporated on top of the perovskite layer. Apart from NiO_X, most HTLs used are organic compounds and their durability on longer time scale is a concern [195].

3.1.2. n-i-p architecture:

In n-i-p architecture, the ETL is processed first on the TCO coated glass substrate as shown in **Figure 3.1 (b)**. Titanium dioxide (TiO_2) and tin(IV) oxide (SnO_2) are commonly used as ETLs [111],[196]. The inorganic nature of these ETLs make them very durable. However, these ETLs have to be annealed at high temperature, limiting their use with flexible substrates like Polyethylene terephthalate (PET) [197]. 2,2′,7,7′-Tetrakis(N,N-di-p-methoxyphenylamine)-9,9′-spirobifluorene (Spiro-OMeTAD) and Poly[bis(4-phenyl)(2,4,6-trimethylphenyl)amine] (PTAA) are used as HTLs in n-i-p architecture. To increase the conductivity of these HTLs, doping with lithium bis(trifluoromethanesulfonyl)imide (LiTFSi) and tributyl phosphate (tBP) is common [198]. However, the stability under light and elevated temperature of the doped HTLs are a major concern [199], [200].

3.2. Materials and deposition techniques

In **Chapter 4** and **Chapter 5**, double cation middle bandgap perovskite (E_G =1.57 eV) $Cs_{0.18}FA_{0.82}PbI_3$ perovskite is used. There are two reasons for choosing this perovskite: (a) double cation recipe (without MA^+) is more stable at high temperature (b) single halide (pure iodide) recipes do not undergo halide segregation under illumination. Hence, their intrinsic stability is good and suitable for accelerated stress testing under light and elevated temperature. The devices used are single junction employing only one absorber.

All-perovskite tandem solar cells (TSCs) reported in **Chapter 4** comprised of a wide-bandgap perovskite (E_G = 1.78 eV) and a narrow-bandgap perovskite (E_G = 1.26 eV). This bandgap combination is standard for all-perovskite TSCs [20]. All-perovskite TSCs were chosen because of the ease of varying the molarity for controlling the thickness of each subcell. For the purpose of understanding current mismatch and its effect on the stability of TSC, the thickness of the wide-bandgap perovskite topcell was varied. This controlled the amount of light absorbed in the top cell and the amount of light reaching the bottom cell.

In **Chapter 6**, triple cation mixed halide recipe $Cs_{0.05}FA_{0.73}MA_{0.22}Pb(I_{0.77}Br_{0.23})_3$ is used for application in perovskite-silicon TSCs. An absorber with E_G =1.68 eV is ideal for use in tandems with silicon solar cell [51]. The purpose of using perovskite-silicon tandem solar cell in outdoor is because of the robustness of the silicon solar cells. Silicon solar cells are durable and have passed most quality control testing in the IEC standards, making them the most commercially successful PV technology.

Substrates: For single junction devices and all-perovskite TSCs, patterned indium tin oxide (ITO) substrates with sheet resistance 15 Ω/ sq^{-1} (Luminescence Technology) is used. The single junction solar cells were fabricated on 16 × 16 mm^2-patterned ITO substrates. The substrates were cleaned in an ultrasonic bath with acetone and isopropyl alcohol (IPA) followed by oxygen plasma treatment. For TSC, the silicon bottom cells (25 mm × 25 mm) was used. The silicon substrates were washed with acetone and IPA in a spin coater. **Table 3.1** summarizes the details of the precursors and materials used for fabrication of single junction and tandems solar cells.

Table 3.1: Precursors and materials used for single junction and tandems solar cells

	precursors for perovskite		
1.	Lead iodide (PbI$_2$)	10101-63-0	TCI
2.	Lead bromide PbBr$_2$	10031-22-8	TCI
3.	Formamidinium iodide (FAI)	879643-71-7	Greatcell
4.	Methylammonium bromide (MABr)	6876-37-5	Greatcell
5.	Cesium chloride (CsCl)	7647-17-8	abcr
6.	Cesium iodide (CsI)	7789-17-5	TCI
	hole transport layer (HTL) and dopants		
7.	[2-(9H-Carbazol-9-yl)ethyl]phosphonic acid (2PACz)	20999-38-6	TCI
8.	(4-(3,6-Diphenyl-9H-carbazol-9-yl)butyl)phosphonic acid (Ph-4PACz)	2814500-04-2	Lumtec
9.	2,2′,7,7′-Tetrakis(N,N-di-p-methoxyphenylamine)-9,9′-spirobifluorene (Spiro-OMeTAD)	207739-72-8	Lumtec
10.	Lithium bis(trifluoromethanesulfonyl) imide (LiTFSi)	90076-65-6	Sigma Aldrich
11.	4-tert-butylpyridine (tBP)	3978-81-2	Sigma Aldrich
12.	Molybdenum oxide (MoO$_X$)	1313-27-5	Sigma Aldrich
	electron transport layer (ETL) and buffer layer		
13.	Fullerene (C$_{60}$)	99685-96-8	Sigma Aldrich
14.	2,9-dimethyl-4,7-diphenyl-1,10-phenanthroline (BCP)	4733-39-5	Lumtec
15.	Trimethylaluminum (TMA) >98%	75-24-1	Strem
16.	Tetrakis(dimethylamino)tin(IV) (TDMASn) >99.99% Sn	1066-77-9	Strem
17.	Tin (IV) oxide 15% in H$_2$O colloidal dispersion (SnO$_2$)	18282-10-5	Alfa Aesar
18.	C$_{60}$-self-assembled monolayer (SAM- C$_{60}$)	631918-72-4	Lumtec
	solvents		
19.	N,N-dimethylformamide (DMF anhydrous) ≥99.9%	68-12-2	Sigma Aldrich
20.	Dimethyl sulfoxide (DMSO anhydrous) ≥99.9%	67-68-5	Sigma Aldrich
21.	ethyl acetate (EA anhydrous) 99.8%	141-78-6	Sigma Aldrich
22.	2-propanol (IPA anhydrous) ≥99.5%	67-63-0	Sigma Aldrich
23.	1, 2-dichlorobenzene (DCB)	95-50-1	Sigma Aldrich
24.	Chlorobenzene (CB)	108-90-7	Sigma Aldrich
25.	Acetonitrile (ACN)	75-05-8	Sigma Aldrich
26.	Ethanol absolute (EtOH) ≥99.8%	64-17-5	VWR
27.	Methanol (MeOH) ≥99.8%	67-56-1	VWR
	anti-reflection coating		
28.	Magnesium fluoride (MgF$_2$)	7783-40-6	Sigma Aldrich
	solvents for substrate cleaning		
29.	2-propanol (IPA)	67-63-0	VWR
30.	Acetone (ACN)	67-64-1	VWR

3.2.1. Fabrication of p-i-n single junction perovskite solar cells:

In **Chapter 4**, p-i-n architecture with device stack glass/ITO/2PACz/perovskite/C_{60}/SnO_x/IZO/Au is used.

2PACz solution was prepared by dissolving 1.8 mg in 4mL of absolute Ethanol. The 2PACz layer was spin coated on cleaned patterned ITO substrates at 3000 rpm and subsequently annealed at 100°C for 10 min. A 1.1 M of $Cs_{0.18}FA_{0.82}PbI_3$ perovskite solution was prepared by dissolving 1.1 mmol PbI_2 and 0.18 mmol of CsCl in 1 mL solvent mixture of DMF: DMSO in 4:1 volume ratio at 130 °C. In a separate glass vial, 1 mmol of FAI was weighed. The cooled solution with PbI_2 and CsCl was added to this vial. The different stoichiometry solutions were prepared by varying molarity of FAI by 0.05 M, while molarity of both PbI_2 and CsCl was kept the same. For antisolvent quenching (ASQ), the perovskite solution was spin-coated using a two-step procedure. The speed used was 1000 rpm for 10 s and 5000 rpm for 30 s. At the 18 s of the second step, 150 µL of EA was dropped onto the center of the substrate. Vacuum quenching (VQ) was conducted in a square vacuum chamber with inlet and outlet positioned at 90 °. A vacuum duration of approximately 30 s was optimized for all vacuum-quenched devices. The samples were then annealed in an inert atmosphere at 150 °C for 30 minutes. A 20 nm layer of C_{60} was evaporated onto the perovskite film in Angstrom (EvoVac) thermal evaporator. 30 nm of SnO_X was deposited using TDMASn precursor source in atomic layer deposition system by Picosun (r200-advanced). 135 nm indium-doped tin oxide (IZO) was sputtered onto the SnO_X layer to serve as the top contact, using a Kurt J. Lesker (PVD 75) sputtering system. Lastly, gold bands were evaporated in thermal evaporator (VacTec, COAT 320) on the edges of the sample for easy probing during measurements.

3.2.2. Fabrication of n-i-p single junction perovskite solar cells:

In **Chapter 5**, n-i-p architecture with the device stack glass/ITO/SnO_2/ C_{60}-SAM/perovskite/Spiro-OMeTAD/MoO_x/ITO/Au fingers is used.

The colloidal SnO_2 solution was diluted with de-ionized water in a ratio of 1:6.5. The SnO_2 layer was deposited by spin-coating diluted SnO_2 onto patterned ITO substrates at 4000 rpm, followed by annealing at 250°C for 30 min. After annealing, the substrates were treated with oxygen plasma for 1 min before further processing. 7.5 mg of C_{60}-SAM was mixed in 1 mL of DCB and was left on a magnetic stirrer at 65 °C for over-night dissolving. The solution was filtered with a 0.2 µm polytetrafluoroethylene (PTFE) filter before using. C_{60}-SAM was applied as a passivation layer on top of the SnO_2 by spin-coating at 4000 rpm and annealing at 120°C for 5 minutes. The perovskite layer was deposited following the p-i-n architecture recipe and quenched using ASQ. In this work, only reference devices were fabricated using 1.1 M precursor. 80 mg of spiro-OMeTAD was dissolved in 1 mL CB and doped with 17.5 µL lithium bis(trifluoromethanesulfonyl) imide along with 28.5 µL 4-tert-butylpyridine. The Li solution was made beforehand by dissolving 520 mg of lithium bis (trifluoromethanesulfonyl) imide in 1mL ACN. A previously prepared spiro-OMeTAD solution was spin-coated onto the perovskite layer at 4000 rpm for 30 seconds. The films were allowed to age for approximately 12 h in a dry box. A 5 nm layer of MoO_X was thermally evaporated on top of the aged spiro-OMeTAD in a Lesker thermal evaporator, followed by the sputtering of 160 nm of ITO as the top contact. Finally, gold bands were evaporated on the edges for easy probing.

3.2.3. Fabrication of multi junction perovskite-silicon tandem solar cell

Prior to deposition, the silicon bottom cells were further cleaned by a 5-minute UV-ozone treatment. A 15 nm NiO_x layer was then deposited via sputtering from a NiO_x target in a Kurt J. Lesker (PVD 75) sputtering system. Ph-4PACz solution with concentration 0.5 mg mL^{-1} in methanol was spin-coated onto silicon substrate at 3000 rpm for 30 s, followed by annealing at 100 °C for 10 minutes. The 1.5 M perovskite precursor solution consisted of 1.1 mmol FAI, 0.34 mmol of MABr, 1.2 mmol PbI_2, and 0.37 mmol of $PbBr_2$ in DMF: DMSO in 4:1 ratio. CsI was dissolved in DMSO separately and added to the precursor solution. The final solution had 1.2 mmol CsI and the final composition of the solution was $Cs_{0.05}FA_{0.73}MA_{0.22}Pb(I_{0.77}Br_{0.23})_3$ with an excess of 3 mol% PbI_2.

150 µL of the perovskite precursor solution was spin-coated onto the Ph-4PACz-modified silicon substrate using a two-step process: 1000 rpm for 10 s and 5000 rpm for 30 s. At 13 s mark of the second step, 450 µL of EA was dropped as an antisolvent. The films were then annealed at 100 °C for 20 minutes. 1 nm AlOx layer was deposited using atomic layer deposition system by Picosun (r200-advanced) at 90 °C. TMA and H_2O were used as precursors. Both were at room-temperature. 15 nm of C_{60} was thermally evaporated onto the perovskite film using Angstrom (EvoVac) thermal evaporator. A 20 nm SnOx layer was then deposited in the above-mentioned ALD system at 90 °C using TDMASn and H_2O as precursors. TDMASn was heated at 70 °C and H_2O was at room-temperature. Then, 45 nm of indium zinc oxide (IZO) layer was sputtered through a shadow mask using Kurt J. Lesker (PVD 75). A 600 nm Ag finger electrode was thermally evaporated in VacTec thermal evaporator (COAT 320) using a precision shadow mask, with a finger width of ~75 µm. Finally, a 100 nm MgF_2 anti-reflection coating was thermally evaporated on top the Ag layer Angstrom (EvoVac) thermal evaporator.

3.3. Characterization techniques

3.3.1. Characterization of perovskite thin films

The perovskite thin film consists of half stack: glass/ ITO/ 2PACz/ perovskite for p-i-n architecture, unless otherwise specified.

Ultraviolet-visible-near infrared (UV-VIS-NIR) spectroscopy

Ultraviolet-visible-near infrared (UV-VIS-NIR) spectroscopy provides insights into the amount of light absorbed by a thin film across the ultraviolet (UV), visible (VIS), and near infrared (NIR) spectrum. UV-VIS-NIR spectra is used to determine the film's optical property and estimate its bandgap. A xenon lamp (300-800 nm) and halogen lamp (800-1300 nm) served as a light source. A monochromator modulated the light source with a chopper frequency of 580 Hz and an integration time of 400 ms. A beam splitter directed the light into an integrating sphere. For transmittance (T) and reflectance (R) measurements, the perovskite thin film was positioned at the front or back of the sphere, respectively. The transmitted or reflected light was collected within the sphere and detected using a silicon (Si)/ indium gallium arsenide (InGaAs) photodiode. The ratio of the light intensity between the sample and the reference beam was used to determine the optical properties of the film. Absorptance was calculated using the formula

$$A(\lambda) = 1 - T(\lambda) - R(\lambda) \qquad \text{Equation (3.1)}$$

where $T(\lambda)$ is the transmittance and $R(\lambda)$ is the reflectance at a specific wavelength λ.

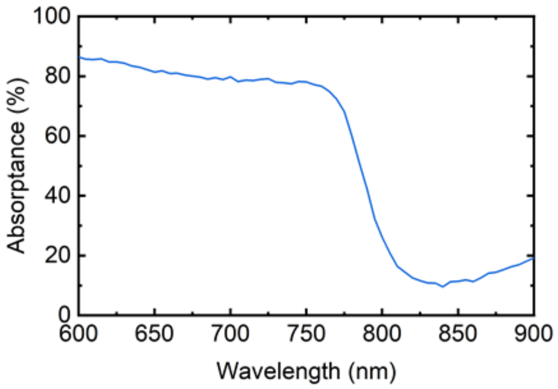

Figure 3.2: Absorptance spectra of a perovskite thin film of bandgap 1.57 eV. The transmittance and reflectance of the thin film was measured with ultraviolet-visible-near infrared (UV-VIS-NIR) spectroscopy. Absorptance was calculated as $A(\lambda) = 1 - T(\lambda) - R(\lambda)$.

Transmittance and reflectance characterization of the perovskite thin films were measured in Photovoltaic Device Characterization System (Bentham, PVE300). An absorptance spectra of a perovskite thin film is depicted in **Figure 3.2**. The perovskite thin film exhibits a high absorptance of ~80% above the sharp band edge at ~790 nm. The perovskite thin film still absorbs ~10% below the bandgap which could be parasitic absorptance of the ITO substrate [201].

X-ray diffraction (XRD)

X-ray diffraction (XRD) provides crucial information about a material's crystal structure, crystal orientation, crystallite size and lattice strain. When a crystalline material is irradiated with X-rays of a specific wavelength (λ), constructive interference of the elastically scattered rays occurs at particular angles (2θ) if Bragg's law is satisfied:

$$n\lambda = 2d\, sin\theta \qquad Equation\ (3.2)$$

where n is an integer, d is the inter-planar spacing, and θ is the angle of incidence between the X-ray beam and the crystal planes.

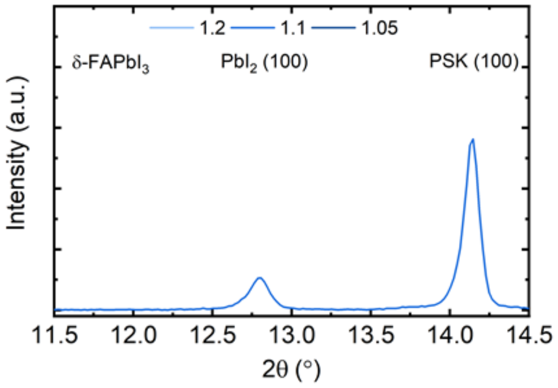

Figure 3.3: X-ray diffraction (XRD) of a perovskite thin film exhibiting high degree of crystallinity with sharp perovskite PSK (100) peak at 2θ = 14.2° alongside some unreacted lead iodide (PbI_2) at 2θ = 12.7°. PbI_2 is one of the precursors used for the fabrication of perovskite thin films.

In this work, XRD characterizations were performed on the perovskite films using a Bruker D2 Phaser system with Cu Kα radiation (λ = 1.54 Å). The X-rays were directed onto the samples through a slit and diffracted beams were collected by a movable LynxEye detector in the Bragg–Brentano geometry. Diffraction data were recorded over a 2θ range of 8° to 32°, with a scan rate of 2° per minute.

A X-ray diffractogram of the perovskite thin film is shown in **Figure 3.3.** The thin film shows a high degree of crystallinity based on the high intensity of the perovskite PSK (100) peak at 2θ = 14.2°. Alongside PSK (100) peak, the diffractogram also shows a peak at 2θ = 12.7° representing the PbI_2 (100) peak. Some unreacted PbI_2 in the precursor could be a source of this peak [103].

Optical microscopy (OM)

Optical microscopy captures magnified images of a sample using a system of lenses. The objective lens, with a short focal length, creates an image of the object in the intermediate plane. This image can be viewed in the eyepiece. The eyepiece can also provide further magnification. While optical microscopy is effective for general imaging, its resolution is limited to approximately 1000× magnification, making it unsuitable for analyzing nanoscale structures.

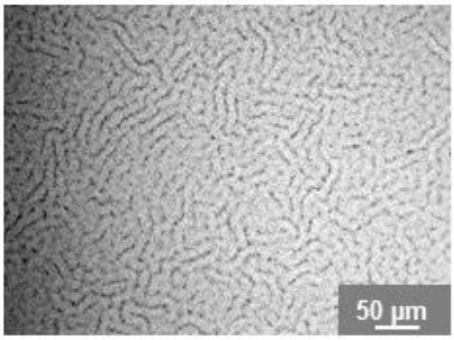

Figure 3.4: Optical microscopy images of a perovskite thin film. Features on a macroscale such as crests (brighter areas) and troughs (darker areas) of the wrinkle formation are visible, giving a clear picture of the quality of the perovskite thin film.

In this work, optical microscopy images of the perovskite films were obtained using a Zeiss Axioplan 2 microscope. An optical microscopy image depicted in **Figure 3.4** shows a spin-coated perovskite thin film quenched using an anti-solvent. The presence of crests (brighter areas) and troughs (darker areas) on the surface verifies that the film is not very planar [202].

Atomic force microscopy (AFM)

Atomic Force Microscopy (AFM) is used to analyze the morphology and roughness with nanometer-scale resolution. Unlike optical microscopy techniques, AFM employs a physical probe to scan the sample surface in both lateral and vertical directions. A sharp tip mounted on a flexible cantilever interacts with the surface. The variations in surface features cause the cantilever to bend. This deflection is detected via laser reflection onto a photodetector.

In contact mode, a feedback loop maintains constant force by adjusting the tip height during raster scanning. In tapping mode, to minimize tip and sample damage, the cantilever oscillates near its resonance frequency without continuous contact. A piezoelectric actuator regulates the cantilever’s height to maintain a consistent oscillation amplitude, with a feedback loop ensuring accurate topographical mapping.

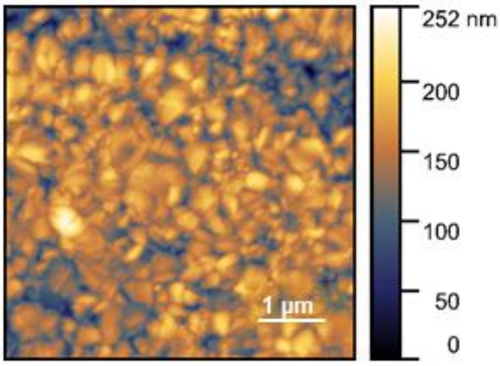

Figure 3.5: Atomic Force Microscopy (AFM) images of a perovskite thin film depicting the inhomogeneity in the surface morphology. The heights appear brighter and the depths appear darker. Maximum root mean square surface roughness of the thin films measured is ~250 nm.

AFM imaging of the perovskite films was performed using a Nano Wizard II system (JPK Instruments) over a scan area of 10 µm × 10 µm. AFM microscopy in **Figure 3.5** shows the perovskite grains and their grain boundaries. The surface of the film is not uniform and shows dark (depth) and bright (height) features [203]. The root mean square roughness of the surface measured is around ~250 nm.

Scanning electron microscopy (SEM)

Scanning Electron Microscopy (SEM) is widely used to examine the morphology of the samples and to obtain additional information such as the elemental composition. In SEM, an electron beam is raster-scanned across the sample surface, and its interaction with the material atoms results in production of various signals containing vital information about the morphology and the elemental composition. Backscattered electrons, produced through elastic interactions with the sample, originate from deeper regions and are sensitive to the atomic number. Region of higher atomic number appear brighter in the images. The secondary electrons provide information about the surface of the sample. Finally, detection of the X-rays coming out of the sample can identify all the different elements contained in the sample.

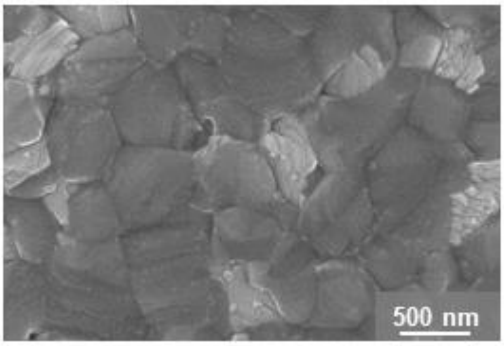

Figure 3.6: Scanning Electron Microscopy (SEM) images of a perovskite thin film. The morphology shows compact films with grain size of ~500 nm. Two types of grains are visible. The darker grains which are the perovskite grains and the brighter grains are the unreacted lead iodide (PbI_2), one of the precursors used for the fabrication of perovskite thin films.

SEM imaging of the perovskite films was conducted using a Zeiss LEO1530 VP microscope equipped with an in-lens detector. Images were acquired at an accelerating voltage of 5 kV and an aperture size of 20 µm. **Figure 3.6** shows an SEM image of the perovskite thin films with large grain size of 500 nm with tight grain boundaries. Alongside the large dark grains of the perovskite, bright grains of PbI_2 are also visible. The source of PbI_2 grains could be the unreacted PbI_2 in the precursor [129].

Cathodoluminescence (CL)

Cathodoluminescence (CL) is a technique for probing material composition, crystal structure, and bandgap energy. When a sample is excited by an electron beam, it emits photons as it relaxes back to its ground state. These emitted photons, typically in the UV, VIS, and NIR regions, are analyzed to characterize the material's optical properties at the nanoscale.

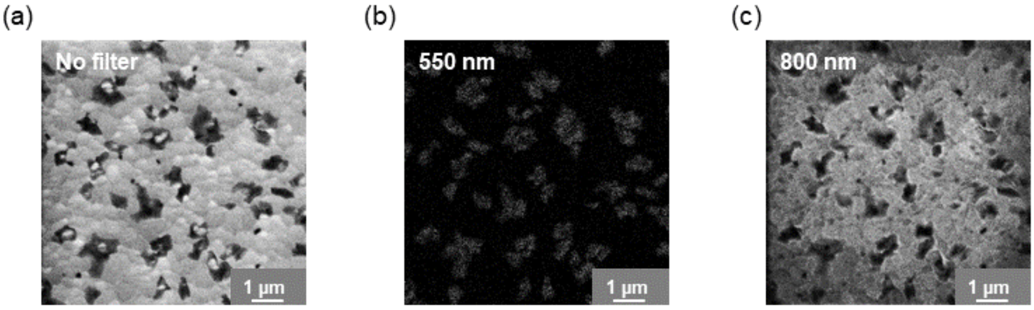

Figure 3.7: Cathodoluminescence (CL) images of a perovskite thin film taken with (a) no filter (b) 550 nm filter (c) 800 nm filter. The filters eliminates the wavelengths that are longer than the wavelength of the filter. When using filter of 550 nm, only materials with wider bandgap are visible. Hence, only the bright spots of PbI_2 (E_G = 2.3 eV) are visible in (b). When a filter of 800 nm is used, low bandgap materials such as perovskite (E_G = 1.57 eV) are also visible in (c).

CL imaging of the perovskite thin films was carried out using an FEI Verios SEM equipped with a Gatan MonoCL4 Elite system. Characterizations were conducted at an accelerating voltage of 3 kV and a beam current of 25 pA. Images were acquired in panchromatic mode using appropriate dichroic filters. In **Figure 3.7 (a)** no filter is used and the image shows two types of grains. On using a filter of 550 nm**,** only bright grains of PbI_2 is visible as seen in **Figure 3.7 (b)** and other region appears dark. PbI_2 has a high bandgap (E_G = 2.3 eV). On using a filter of 800 nm, perovskite grains are also visible as shown in **Figure 3.7 (c)**. Perovskite has a lower bandgap of E_G = 1.57 eV and hence is visible through the high-pass filter [129].

Profilometry

Profilometry is used to gain information about the sample thickness.

Surface profile and thickness of a sample was measured by using a physical probe. The probe moves along the surface of the sample placed on a sample holder to acquire the surface height information. This information is attained by using a feedback loop that monitors the force the sample exerts on the probe. A probe with a specified torque is maintained with the feedback loop. The change in Z direction of the probe is used to reconstruct the surface information of the sample as shown in **Figure 3.8**.

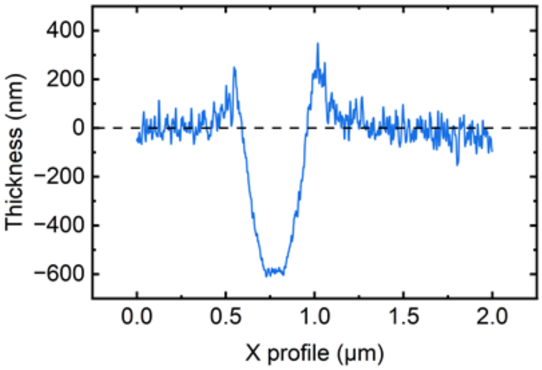

Figure 3.8: Surface profile and thickness measurement of a perovskite thin film. The measured depth of ~ 600nm is the thickness of the film.

Bruker Dektakt XT profilometer was used to measure the thickness of perovskite thin films. A scratch was made on the surface of the perovskite film such that the soft perovskite is scratched out but the hard ITO substrate is not damaged. When the probe scans through the surface it moves horizontally across the scratch and the depth of the scratch is estimated. This is the actual height of the perovskite film ~ 600nm.

3.3.2. Characterization of Perovskite-based Solar Cells

Current density-voltage (J-V) characteristics

The current density-voltage (*J–V*) characteristic of a solar cell is measured by recording the current response of the device as a function of the applied voltage under illumination. Under standard testing condition (STC), 100 mW/cm^2 of AM1.5G spectrum is used and the cell temperature is maintained at 25 °C. This measurement reveals the key performance parameters of the solar cell including open-circuit voltage (V_{OC}), short-circuit current (J_{SC}), fill factor (FF) and power conversion efficiency (PCE). The significance of these performance parameters have been discussed in depth in **Chapter 2**.

While these performance parameters primarily focus on the efficiency of a solar cell, one specific characteristic of PSCs that provides insight into the stability on a device level is the hysteresis index.

Hysteresis index (HI): Due to the presence of ionic species in a PSC, alongside electronic species, the *J-V* curve can be significantly different based on the direction of scan. **Figure 3.9 (a)** shows the difference between forward scan (scan direction: J_{SC} to V_{OC}) and reverse scan (scan direction: V_{OC} to J_{SC}) for a PSC. This difference can be represented by the hysteresis index (HI).

$$HI = \frac{PCE_{\mathrm{RS}} - PCE_{\mathrm{FS}}}{PCE_{\mathrm{RS}}} \qquad \text{Equation (3.3)}$$

This discrepancy exists because ions of different radii migrate at varying speeds under an applied voltage bias. Poling refers to the application of a voltage with a specific polarity to pre-condition the device by redistributing the mobile ions, thereby altering its initial state prior to *J–V* characterization.

J-V characterization of the single junction were measured using a solar simulator (Newport, Oriel Sol3A) equipped with a source meter (Keithley, 2400) and a Xenon lamp. The calibration was performed using a certified Si reference solar cell (Fraunhofer) with KG5 filter (Schott). Sample holders (fabricated in-house) with gold pins were used to contact the cells for electrical characterizations. The active area of the cell was 0.105 cm^2 and an aperture mask of 0.0784 cm^2 was used during characterization. *J–V* characterizations were made at an intensity of 100 mW/cm^2. The temperature of all cells was controlled at 25 °C employing a Peltier element connected to a microcontroller while conducting *J–V* characterization. A scan speed of 600 mV/s was used and no poling was applied.

J-V characterization of the multi junction TSC was measured in a similar set up equipped with a light emitting diode (LED) solar simulator (Wavelabs, Sinus 70). The calibration was performed using a certified silicon reference solar cell (Fraunhofer) with KG0 filter (Schott). The active area of the cell was 1.04 cm^2 and a mask of area 1 cm^2 was used as an aperture mask during characterization.

A scan speed of 600 mV/s was used and no poling was applied for *J-V* characterization of both single junction PSCs and multi junction TSCs.

Maximum power-point (MPP) tracking

The maximum power point (MPP) on the *J–V* curve corresponds to the point where the solar cell delivers its maximum power output (P_m). Tracking the MPP ensures optimal power extraction from the device. This is typically achieved using a MPP tracking algorithm. In this work, the perturb and observe method was employed for MPP tracking.

First, *J–V* characterization is performed to identify the voltage at the maximum power point (V_m). Current is measured at this voltage. After a predetermined time interval, a small perturbation of $\pm V_{perturb}$ is applied around V_m and the current is measured again. Power outputs at V_m, $V_m+V_{perturb}$ and $V_m-V_{perturb}$ are compared. In the subsequent step, the tracking voltage is updated to the point among the three voltages where maximum power is observed. This process is repeated continuously, allowing the system to dynamically follow and maintain operation at the maximum power point.

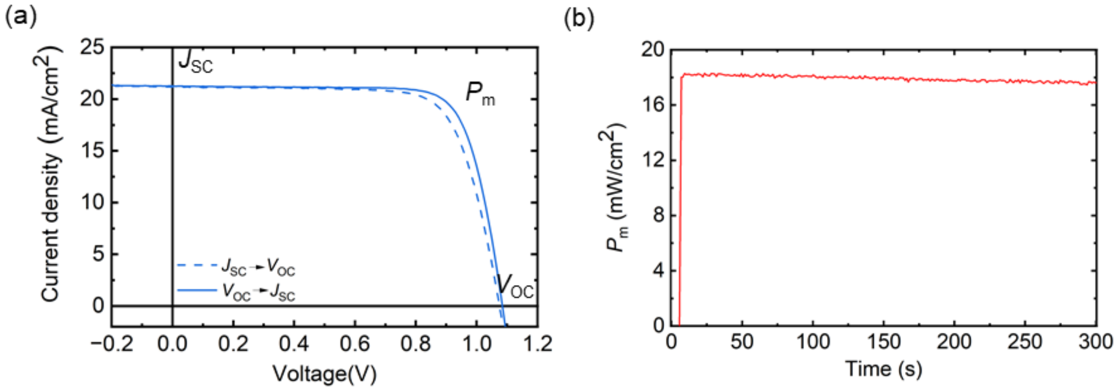

Figure 3.9 (a) Hysteretic behavior between forward scan (scan direction: J_{SC} to V_{OC}) and reverse scan (scan direction: V_{OC} to J_{SC}) of a perovskite-based solar cell. (b) Maximum power output (P_m) extracted from a solar cell by tracking at maximum power point (MPP).

MPP tracking were performed under a class A^{++} LED-based solar simulator (Wavelabs, LS-2). The spectrum was a close match to the AM 1.5G over the relevant spectral range. The MPP measurements were performed in an in-house fabricated holders with temperature control. A $\pm V_{perturb}$ of 10 mV was applied and the tracking interval was every 5 minutes. Stabilized PCE from MPP tracking for a PSC is as depicted in **Figure 3.9 (b).** Given the presence of hysteresis in PSCs and the possibility for differing PCEs between forward and reverse scans, the MPP provides a more reliable measure of the stabilized PCE. During certification, PSCs are typically tracked at the MPP for 5 minutes, and the resulting stabilized efficiency is reported as the certified PCE of the device.

Ideality factor calculation

In an ideal solar cell, every photon with energy $E \geq E_G$ should contribute to an electron-hole pair generation that gets collected by the respective selective charge carrier, as per the Shockley Queisser limit. However, as explained in **Chapter 2** different recombination mechanisms take place simultaneously which reduce the collection of charge carriers. The ideality factor (n_{id}) provides insight about the dominant loss mechanisms responsible for the recombination of charge carriers. The open-circuit voltage measured at different illumination conditions results in a J_{SC} /V_{OC} curve following **Equation 3.4.** Since the J_{SC} /V_{OC} curve is independent of the external series resistance, calculation of ideality factor from this curve is much simpler.

$$n_{id} = \frac{e}{k_B\,T}\frac{d(V_{OC})}{d(ln(J_{SC}))} = \frac{e}{k_B\,T}\frac{d(V_{OC})}{d(J_{SC})}\,J_{SC} \qquad Equation\ (3.4)$$

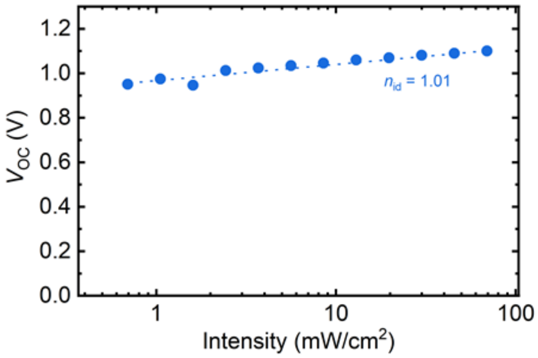

Figure 3.10: Suns-V_{OC} characterization of perovskite solar cell measured from 0.7 to 69.2 mW/cm^2 intensity. The fitting has a slope of 1.01. The ideality factor (n_{id}) = 1.01 represents radiative recombination is the dominant recombination mechanism.

Ideality factor for PSCs was measured on PAIOS system by Fluxim AG. The light intensity from an LED was varied up to 69.2 mW/cm^2 and open circuit voltage decay was measured. **Figure 3.10** represents a Suns-V_{OC} characterization of a PSC. A linear fit yields a slope of 1.01 representing an ideal diode behavior dominated by radiative recombination [204]. No significant contribution from trap-assisted or surface/interface recombination is present in the pristine device.

External quantum efficiency (EQE)

The external quantum efficiency (EQE) can quantify if every photon with energy $E \geq E_G$ in the solar spectrum contributes to J_{SC}. EQE is the ratio of the number of collected electrons (N_e) to the number of incident photons (N_{ph}). This can be achieved by spectrally resolved measurement of J_{SC}.

Spectral response of a solar cell can be defined as the current produced per unit optical power incident on the solar cell.

$$EQE = \frac{N_e}{N_{ph}} \qquad \text{Equation } (3.5)$$

In the ideal case, the EQE of a solar cell is 100%, meaning every incident photon generates a collected charge carrier. However, in practice, the measured EQE is typically lower due to optical and recombination losses. While the ideality factor provides insight into the nature and extent of recombination losses, EQE measurements can help distinguish between optical losses, such as reflection at the front surface and losses due to carrier recombination within the device.

The integration of the EQE spectrum represents J_{SC} that a solar cell can generate under standard illumination conditions. It gives the spectrally resolved photocurrent contribution by summing up the number of charge carriers generated at each wavelength, weighted by the solar spectrum.

$$J_{SC} = e \int EQE\,(\lambda)\; \Phi_{AM1.5}(\lambda)\; d\lambda \qquad \text{Equation (3.6)}$$

where e is the elementary charge, $\Phi_{AM1.5}$ is the photon flux density at the standard AM 1.5G solar spectrum and λ is the wavelength.

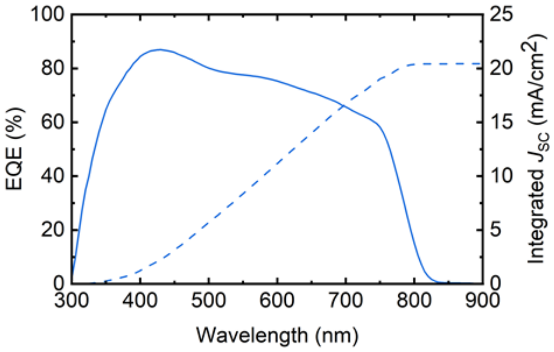

Figure 3.11: External quantum efficiency (EQE) characterization and integrated J_{SC} calculated from EQE for a semi-transparent perovskite solar cell. An integrated J_{SC} of 20.3 mA/cm^2 was measured from the perovskite solar cell.

EQE spectra for PSC were measured in a Photovoltaic Device Characterization System (Bentham, PVE300). A monochromator was used to modulate the xenon and halogen lamp. The chopper frequency of 580 Hz with an integration time of 400 ms was used. Overall intensity of light used was 70 mW/cm^2.

The EQE spectra of a PSC in **Figure 3.11** shows lower intensity at longer wavelengths. This is mainly because of the TCO contact implemented as a top contact. TCO top contact does not provide back reflection like metal contact resulting in generation of slightly lower J_{SC}.

For EQE characterization of TSC, EQE of individual subcell was measured using bias light. For characterization of top cell, a bias light of 940 nm at 100mW/cm^2 was used to saturate the bottom cell. Similarly, for characterization of bottom subcell, a bias light of 465 nm at 100mW/cm^2 was used to saturate the top cell.

Electroluminescence (EL)

In electroluminescence (EL), a solar cell emits light when a forward voltage bias is applied, effectively operating in reverse of the photovoltaic effect, where light generates a photovoltage. As a result, all the loss mechanisms that impact solar cell performance, such as optical, resistive, and recombination losses, can be revealed through EL characterization.

The upper limit for the forward voltage bias is given by the radiative open-circuit voltage,

$$V_{OC,rad} = \frac{n_{id} k_B T}{e} \ln\left(\frac{J_{SC}}{J_{0,rad}} + 1\right) \qquad Equation\ (3.7)$$

The difference (ΔV_{OC}) between the radiative open-circuit voltage ($V_{OC,rad}$) and the actual open-circuit voltage (V_{OC}) measured from J–V characterization, quantifies the voltage loss due to non-radiative recombination.

$$\Delta V_{OC} = V_{OC,rad} - V_{OC} \qquad Equation\ (3.8)$$

This loss provides a useful metric to compare the quality of solar cells based on their recombination dynamics.

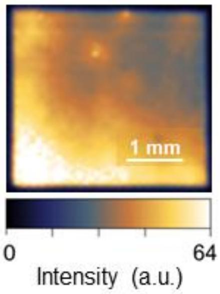

Figure 3.12: Electroluminescence (EL) characterization of a perovskite solar cell showing inhomogenieties like pinholes and edge effects.

EL characterization of the PSCs were performed in an in-house built setup with a CMOS camera synchronized with a filter wheel rotating at 180 rpm, combined with a 470 nm LED bar for excitation. 775 nm short pass and 760 nm long pass filters were also implemented. An image was captured at each filter position as the wheel rotates past the camera . **Figure 3.12** represents the EL image of a degraded PSCs. The film has many inhomogeneity on the surface. The luminescence shows a gradient from the bottom left edge to the top right which arise from a difference in thickness of the film. Some spots are also prominent. This could come from shunts developed in the degraded device [205].

Charge extraction by linearly increasing voltage (CELIV)

Photo CELIV gives information about charge carrier mobility and charge carrier density. A light pulse generates charge carriers in the device before the negative voltage ramp is applied to extract them. This extraction causes a current overshoot that appears on top of a constant displacement current. The mobility of the faster charge carrier can be determined analytically from the peak time of this overshoot. By integrating the overshoot, the charge carrier density can also be estimated.

The extracted charge density is determined by integrating the current overshoot, defined as the difference between the total current and the RC displacement current:

$$N_{CELIV} = \frac{1}{e\,d\,A} \int \big(I(t) - I_{RC}(t)\big)\ dt \qquad \text{Equation (3.9)}$$

where N_{CELIV} is the charge carrier density (electrons or holes) extracted, e is the elementary charge, d is the thickness of absorber and A is the active area of the device. $I(t)$ is the total current as a function of time during the negative voltage ramp and $I_{RC}(t)$ is the displacement current due to the RC response of the device.

Delay time charge extraction by linearly increasing voltage (CELIV)

Delay time CELIV gives information about recombination dynamics. While in photo CELIV, a light pulse is applied before the voltage ramp. In delay time CELIV, the delay time between the end of the pulse and the start of the ramp is varied, allowing the photo generated charge carriers to recombine during the delay time. By plotting the extracted charge against the delay time, the recombination dynamics can be analyzed.

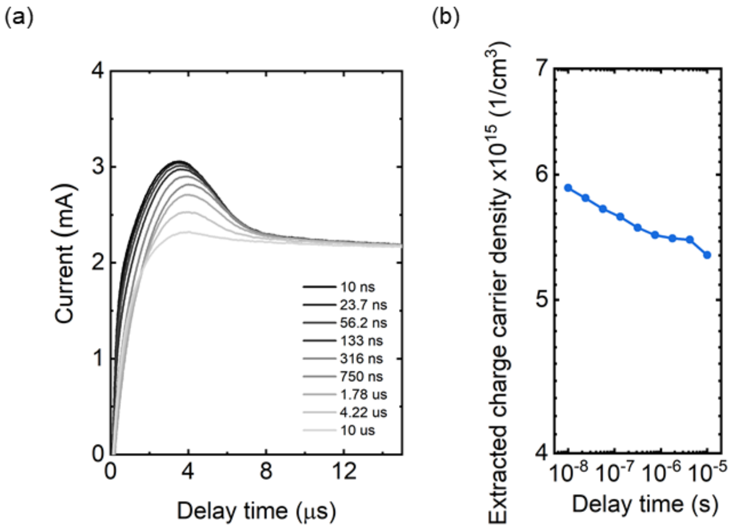

Figure 3.13: (a) Delay time charge extraction by linearly increasing voltage (Delay-time CELIV) measurement of a perovskite solar cells. (b) Extracted charge carrier density vs. delay time plot.

Photo CELIV and delay time CELIV were performed for PSCs on PAIOS system by Fluxim AG. Intensity of 69.2 mW/cm^2 with a light-pulse length of 100 µs and a ramp rate of 40 V/ms was used. Delay-time CELIV measurement of a PSC is represented in **Figure 3.13 (a)**. Delay from 10 ns to 10 µs was implemented between light pulse and charge extraction. The extracted charge carrier density is calculated by integrating the current overshoot. **Figure 3.13 (b)** shows that the extracted charge carries does not decrease drastically with delay time confirming less charge carrier recombination in the PSC [128].

4. Precursor stoichiometry and morphology on dark recovery of perovskite solar cells

Processing parameters during perovskite fabrication influence the thin films properties. While the relationship of a good quality film on the performance of perovskite solar cells have been studied extensively, their impact on the stability of perovskite solar cells are not well understood. In this chapter, the influence of processing parameters like precursor stoichiometry and quenching technique on the crystallization, grain size and morphology of perovskite thin films were studied. The mechanism of degradation of perovskite solar cells under the operational stress factors namely, light, voltage bias and elevated temperature is dependent on the above-mentioned properties of the thin films. Highly accelerated stress testing conducted separately under light exposure (in presence of voltage bias) and elevated temperature conditions help identify the root cause of failure by isolating the effects of each individual stress factor, addressing Objective 1. Characterizations performed on the degraded devices assists in developing an understanding of the changes occurring in the devices as they age under the stress factors. Furthermore, the ability of degraded devices to recover after storage in the dark reveals their behavior under day-night cycling in outdoor conditions. Reporting the device performance post accelerated stress testing encourages statistical and consistent data analysis, which can be crucial to mitigation of the root cause of failure in response to Objective 2. The wide-bandgap and the narrow-bandgap perovskite absorbers were monolithically integrated of into series-connected tandem solar cells. The impact of current matching between subcells on overall device performance and operational stability over extended time periods were investigated in response to Objective 3.

This chapter is based on our publication with the title of "Danger in the dark: Stability of perovskite solar cells with varied stoichiometry and morphology stressed at various conditions"[103] published in *ACS Appl. Mater. Interfaces* 2024, 16, 27450−27462 and authored by *Roja Singh (R.S.)*, Hang Hu, Thomas Feeney, Alexander Diercks, Felix Laufer, Yang Li, The Duong, Fabian Schackmar (F.S.), Bahram A. Nejand (B.A.) and Ulrich W. Paetzold (U.W.P.).*

R.S. contributed to this work by conceptualizing the project alongside *F.S., B.A., and U.W.P. R.S.* performed device fabrication, investigation and data analysis. The final version of the manuscript was written with the contribution of all authors. The detailed contribution list can be found in the Appendix. Most of the figures in this chapter have been adapted or reproduced with the permission of American Chemical Society.

4.1. Introduction

During perovskite fabrication, many processing parameters change intentionally or unintentionally. Precursor stoichiometry and quenching technique are the two main processing parameters that influence the crystallization, grain size and morphology of the final perovskite film. These structural and morphological features influence the device performance and affect the stability of the perovskite solar cells (PSCs) under the different intrinsic stress factors such as light, voltage bias and elevated temperature.

The stoichiometry of the precursor solution plays a crucial role in the crystallization kinetics, significantly influencing both phase stability and long-term stability of the PSCs. Precursor stoichiometry is determined by the molar ratio of the precursor ionic compounds in perovskites: AX and BX_2. Extensive theoretical calculations and experimental studies on the thermodynamics of these materials have advanced the development of phase-stable hybrid and inorganic lead halide perovskites [200],[201]. However, a deeper understanding of unintentional stoichiometric variations during perovskite processing and its effect on the long-term stability remains inconsistent. Perovskites with Pb-rich surfaces showed high power conversion efficiency (PCE), but their performance declined during maximum power point (MPP) tracking [208]. Excess lead iodide (PbI_2) leads to increased hysteresis and instability when exposed to light [209] and the photolysis of the unreacted PbI_2 crystals into metallic lead can quench solar cell performance in both methylammonium (MA) and formamidinium (FA)-based PSCs [210]. Efforts to convert the residual PbI_2 at the buried interface with introducing formamidinium iodide (FAI) and cesium bromide into the electron transport layer (ETL) tin oxide (SnO_2) stabilized the lattice strain, reduced interfacial defects and improved the photostability of the device [211]. In contrast, an excess of the A-cation ionic compound in the precursor solution produced excess organic species around the grain boundaries, obstructing charge carrier transport [209]. However, a small excess of AX (<5% of FAI) can improve long-term stability while preserving the high performance. Though, AX-rich perovskites initially had a lower PCE, their MPP tracking improved and stabilized over time [208].

In addition to the precursor stoichiometry, the quenching process of the wet perovskite film plays a key role in controlling nucleation and crystallization, which ultimately determines the film morphology. The quality of the final film influences both the performance and stability of PSCs. Antisolvent quenching (ASQ) is a well-established and widely used technique for perovskite fabrication [212]. The usage of antisolvent for quenching reduces the solubility of the perovskite solution, creating local super saturation points. These super saturation points initiate the crystallization process in the wet film [213]. However, this method has limitations when it comes to upscaling. Additionally, the rapid quenching in antisolvent-quenched films can cause wrinkles, which increase the film roughness [202]. As an alternative, vacuum quenching (VQ) is commonly used for quenching large-area devices and modules. Perovskite tandems and mini-modules using VQ for fabrication exhibited planar and smooth large-area perovskite films and demonstrated high performance and stability [20]. However, the impact of different morphologies, resulting from the choice of the quenching technique, on the long-term stability has not been explored yet. Given the influence of unreacted precursors, defect sites, crystallization and lattice strain on the quality of the final film, it is crucial to quantify how these factors impact the device stability.

The failure of perovskite devices is primarily driven by stress-related factors. Among the various stress factors that contribute to the instability of PSCs, their degradation under intrinsic stress factors is a major concern. Intrinsic stress factors are stress factors that are present during the operation of a solar cell namely, light, elevated temperature, and voltage bias. In methylammonium lead iodide solar cells the rapid light induced degradation was caused by recombination centers formed due to elevated temperatures and an excess of charge carriers [184]. In cesium formamidinium lead iodide ($Cs_{0.1}FA_{0.9}PbI_3$) the effect of light and stabilized power output was more detrimental than the effect of elevated temperature [214]. For certain perovskite compositions, elevated temperature may have a more detrimental effect, while for others, light-induced degradation or electrical bias could cause a greater damage. To prevent inconsistencies, it is strongly recommended to implement accelerated stress testing protocols under various stress conditions. Domanski et al. investigated the stability of PSCs under various stress factors, including light, elevated temperature, relative humidity and voltage bias. They recommended a set of testing protocols to establish a consensus on the aging process of the PSCs and emphasized statistical reporting would enable reliable comparisons of the PSC stability [215]. The International Summit on Organic and Hybrid Photovoltaics Stability (ISOS) protocols have been adapted by the perovskite and organic solar cell community for accelerated stress testing of the next-generation PV technologies [189]. While majority of accelerated stress testing recommend aging devices under continuous presence of stress factors in order to hasten the degradation process, real-world outdoor operation of solar cells also involve periods of night time with no light (dark) and lower temperature range. In PSC, degradation that occurs during the day cycle, due to light exposure and elevated temperatures, is reversible during the night cycle. Khenkin *et al*. first reported the dynamics of PSC recovery in the dark [216]. The sources of instability in PSCs, such as trap formation and ion migration, can influence their performance and their ability to recover in the dark, ultimately affecting their overall long-term stability in outdoor conditions [211],[212].

To develop an understanding about the trap formation and ionic migration, Azpiroz *et al*. demonstrated that the activation energy for defect formation of iodide interstitial (I_i) and vacancy of iodide or bromide ($V_{I/Br}$) is 0.08 eV, while the formation of methylammonium (V_{MA}) and lead (V_{Pb}) vacancies requires 0.46 eV and 0.8 eV respectively [218]. Hence, activation energy for migration of iodine complexes are much lower as compared to the other ionic complexes [219]. Iodine vacancies are known to migrate even at room temperature, in presence of light and electrical bias [218].

Recent literatures provide a wide array of remedies to mitigate iodide migration. π conjugated aromatic additives can result in strong Pb/X surface interactions including Pb-O bond formation. This can minimize the defect density at the surface, passivating the perovskite surface [220]. Perfluorodecyl iodide has the directional affinity to I_X^- through hydrogen bonding and can confine I_X^- by capturing it, extending the T_{80} to over 2100 h for MPP tracking at 25 °C and 750 h for MPP tracking at 85 °C [221]. Substitution of lead with tin (Sn) has also been reported to reduce iodide migration. Sn vacancies capture the migration of iodide ions slowing down ion diffusion in mixed Sn-Pb perovskite [222]. Implementing a barrier against migration of iodine at the cathode lithium flouride (LiF)/ fullerene (C_{60})/ tin-oxide (SnO_X) /indium tin oxide (ITO) can prevent the oxidation of perovskite/ETL interface increasing the T_{90} lifetime of PSCs to ~1,000 h [223]. T_{80} and T_{90} is the time taken by the device to decrease below 80% and 90% of their initial power output.

This chapter systematically investigates the effect of variations in processing parameters: precursor stoichiometry and quenching technique on the stability of PSCs under the intrinsic stress factors (elevated temperature, light and voltage bias). While the effect of such variations on the device performance has been previously studied, their effect on the long-term stability is not completely understood. **Section 4.2** covers the impact of accidental variations in precursor stoichiometry on device performance of PSCs. The changes in morphology expected with the variations in precursor stoichiometry is explored in **Section 4.3**. **Section 4.4** studies the effect of quenching technique on the morphology of perovskite thin films. **Section 4.5** correlates the variations in precursor stoichiometry to the crystallization of perovskite thin films along with the changes induced to the crystal structure when perovskite thin films when exposed to different stress factors (elevated temperature and light). In **Section 4.6**, the impact of elevated temperature and the combined effect of light with voltage bias on device stability is tested. Post degradation and dark recovery analysis in **Section 4.7** analyses the losses undergone and recovery made in PSCs during the accelerated stress tests and elucidates the root-cause of performance loss in the dark. Understanding the correlation of these processing parameters with performance helps in regulating the repeatability and reproducibility issues of the PSCs. Insight about the dynamics of degradation under the different stress factors assists in mitigation of the root-cause of failure and improving the stability of PSCs.

4.2. Precursor stoichiometry on the performance of perovskite solar cells

With the objective of understanding the contribution of precursor stoichiometry on the device performance, the molar ratio (MR) of cesium formamidinium lead iodide ($Cs_{0.18}FA_{0.82}PbI_3$) precursor solution was changed by varying the molarity of FAI in the reference recipe. The reference recipe already implemented 10% excess PbI_2. MR from 1.2 to 1.0 was tested with a step-size of 0.05 as elaborated in **Table 4.1**. The precursor solution was spin-coated on glass/ indium tin oxide (ITO)/ [2-(9H-Carbazol-9-yl)ethyl]phosphonic acid (2PACz) substrates followed by ASQ. The films were annealed and the subsequent layers Fullerene (C_{60})/ tin oxide (SnO_X)/ indium zinc oxide (IZO) were deposited. Finally, gold busbars were evaporated to enhance charge extraction.

Table 4.1: Stoichiometric variation implemented by changing molar ratio of formamidinium iodide (FAI) in the precursor solution. All units are in mmol/L.

	FAI	CsCl	PbI_2	PbI_2/FAI	FA^+	Cs^+	Pb^+	I^-	Cl^-
1	0.90	0.18	1.10	1.2	0.90	0.18	1.10	3.10	0.18
2	0.95	0.18	1.10	1.15	0.95	0.18	1.10	3.15	0.18
3	1.00	0.18	1.10	1.1	1.00	0.18	1.10	3.20	0.18
4	1.05	0.18	1.10	1.05	1.05	0.18	1.10	3.25	0.18
5	1.10	0.18	1.10	1	1.10	0.18	1.10	3.30	0.18

The performance of the semi-transparent devices did not change drastically with varying the MR; however, they showed an interesting trend in PCE as depicted in **Figure 4.1 (a)**. The contribution of excess PbI_2 in the formation of pinhole free film is of prior knowledge [210],[224]. Hence, in MR 1.0, which has no excess PbI_2, all three performance parameters open-circuit voltage (V_{OC}), fill factor (FF) and short-circuit current density (J_{SC}) are lower than that for the other MRs. With the intention of understanding if, the influence of precursor stoichiometry on the device performance is also retained upon changing the method of quenching, similar procedure for device fabrication was followed. However, instead of using orthogonal solvent, a solvent-free VQ technique was used. Similar variations in performance was observed for devices fabricated with VQ (see **Figure 4.1 (c)**). A comparison of the current density-voltage (*J*-*V*) characterization of the champion devices of different MRs and quenching techniques are presented in **Figure 4.1 (b)** for ASQ and **Figure 4.1 (d)** for VQ. All photovoltaic parameters of champion cells are presented in **Table A4.1** in the **Appendix**.

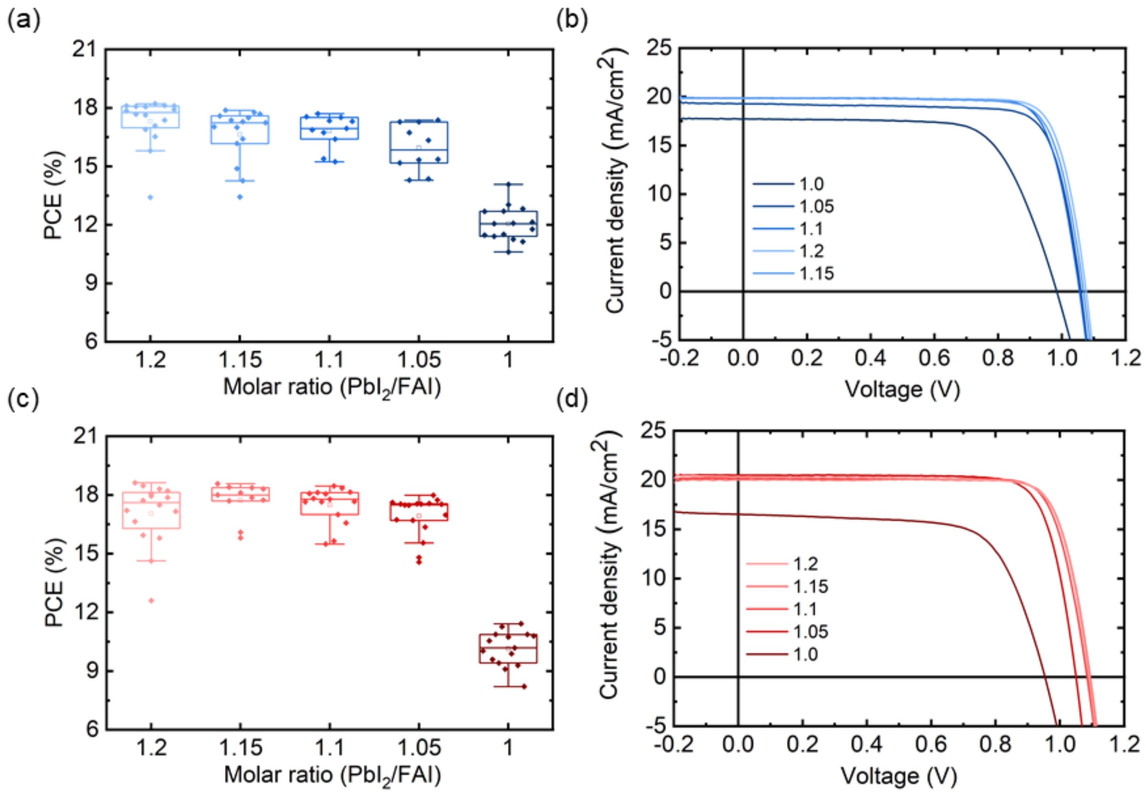

Figure 4.1: (a) Statistical distribution of the power conversion efficiency (PCE) and (b) $J-V$ characteristics of the PSCs using an antisolvent quenching process. (c) Statistical distribution of PCE and (d) $J-V$ characteristics of the PSCs using a vacuum quenching process. Reproduced with permission from American Chemical Society.

Figure 4.2 (a) shows that in comparison to the reference MR 1.1, the V_{OC} of the PSCs increased with the increase in MR (with less FAI in precursor solution). FF and J_{SC} remained unchanged as shown in **Figure 4.2 (b)** and **Figure 4.2 (c)**. The reason for the increase in V_{OC} is that less FAI results in excess PbI_2 in the precursor solution. The excess PbI_2 goes into the grain boundaries and provides a passivating effect, enhancing V_{OC} [209],[224]. The vacuum-quenched PSCs also exhibited a similar trend in PCE and V_{OC} as shown in **Figure 4.2 (d)**. However, one can observe from **Figure 4.2 (f)** that in these devices, J_{SC} increased with the decrease in MR. For MR $\geq$ 1.1, antisolvent-quenched devices grow up to 50 nm thicker compared to the vacuum-quenched films. While in ASQ the excess precursor is washed off, in VQ the excess precursor remains on the surface. Having more FAI in the precursor solution contributes to growing a thicker film upon annealing for vacuum-quenched (MR < 1.1) devices, resulting in higher J_{SC} in the devices [225]. Further details on profilometry measurement are presented in **Table A4.2** in the **Appendix**.

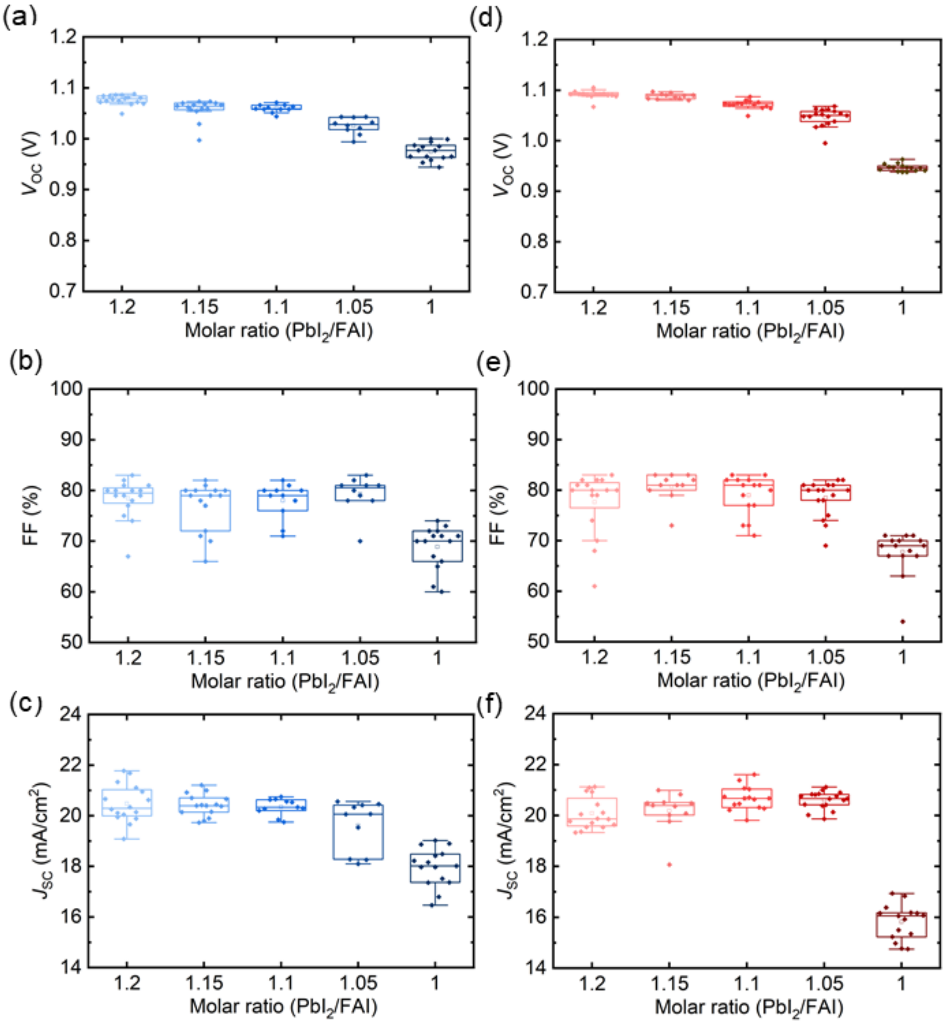

Figure 4.2: Statistical distribution of (a) open-circuit voltage (V_{OC}) (b) fill factor (FF) and (c) short-circuit current density (J_{SC}) of antisolvent-quenched devices with different molar ratios. Statistical distribution of (d) V_{OC} (e) FF and (f) J_{SC} of vacuum-quenched devices with different molar ratios. Adapted with permission from American Chemical Society.

This increase in J_{SC} was further confirmed by the external quantum efficiency (EQE) characterizations as shown in **Figure 4.3 (a)** for antisolvent-quenched and **Figure 4.3 (c)** for vacuum-quenched devices. The intensity of the EQE decreases at longer wavelengths. This is common for semi-transparent devices. Top contact made of IZO does not provide back reflection as compared to metallic contacts and the intensity drops at band edge. The integrated J_{SC} from EQE showed minimal variation as compared to the J_{SC} measured during $J-V$ characterization. The reason behind this discrepancy is EQE is measured at 70 mW/cm^2. If EQE was measured at higher intensity of 100 mW/cm^2 as in $J-V$ characterization, the effects of ionic migration and decrease in J_{SC} would also be visible [226]. Absorptance spectra in **Figure 4.3 (b)** for antisolvent-quenched and **Figure 4.3 (d)** for vacuum-quenched perovskite thin films also depicts that as more FAI is present in the precursor solution, the absorptance of the vacuum-quenched film is increased slightly, confirming the reason for higher J_{SC}.

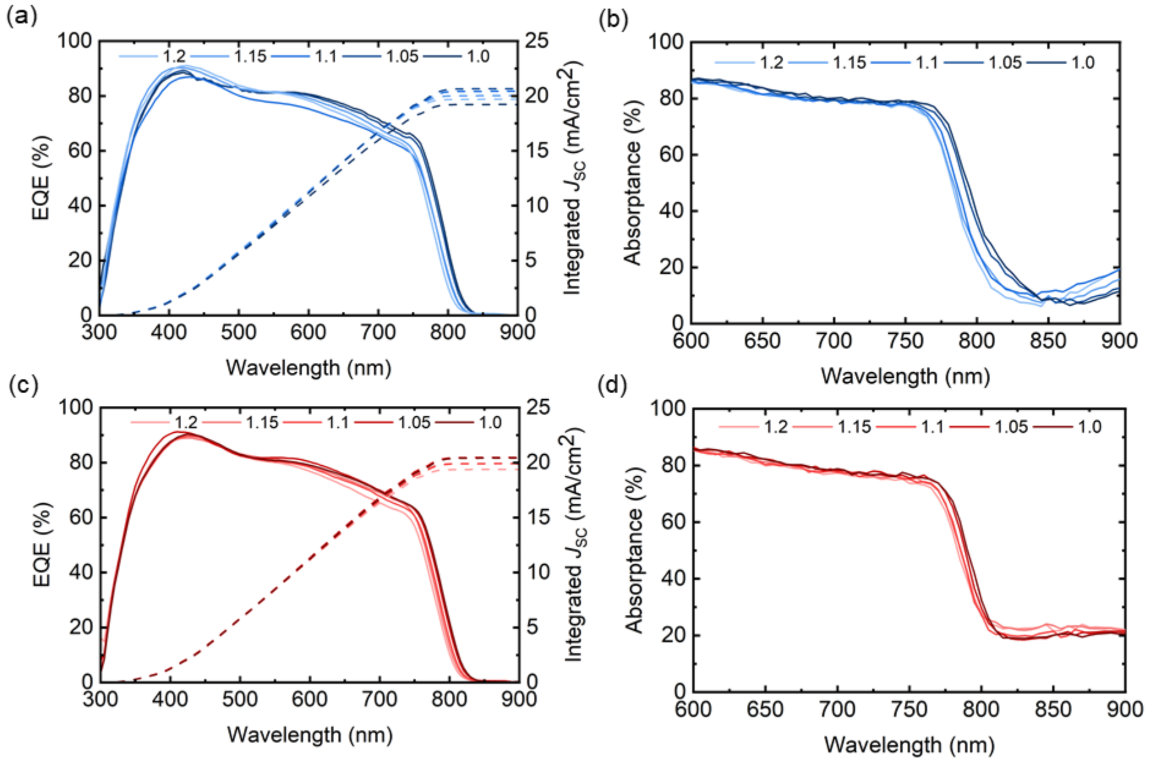

Figure 4.3: (a) External quantum efficiency (EQE) of devices with different molar ratios and (b) absorptance of films with different molar ratios quenched using antisolvent-quenching (ASQ) (c) EQE of devices with different molar ratios and (d) absorptance of films with different molar ratios quenched using vacuum-quenching (VQ). Adapted with permission from American Chemical Society.

Another feature, which changes with changing the MR, is the band edge of the absorptance spectra. The first derivative at the inflection point of EQE confirms that the bandgap of the PSCs changes from 1.58, 1.58, and 1.59 eV for MRs of 1.0, 1.1, and 1.2, as shown in **Figure 4.4 (a)**. The trend in change of bandgap with varying MR is observed in vacuum-quenched devices as well (see **Figure 4.4 (c)**). When the amount of FAI in the precursor solution is increased, more FA$^+$ gets incorporated in the film for the same amount of Cs$^+$ resulting in red-shift in bandgap [227]. This red shift was further verified by Tauc's plot of the absorptance spectra of perovskite films as depicted in **Figure 4.4 (b)** for antisolvent-quenched and **Figure 4.4 (d)** for vacuum-quenched perovskite thin films.

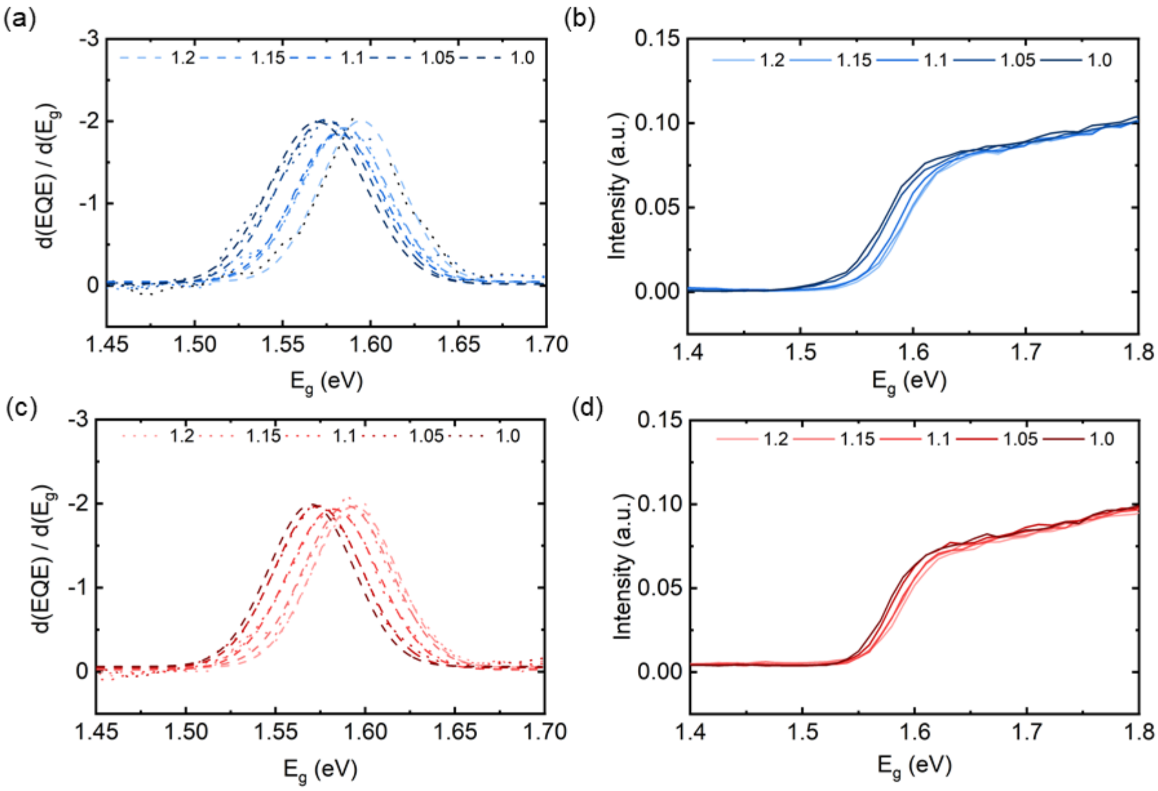

Figure 4.4: (a) Derivative at inflection point of EQE of devices with different molar ratios and (b) Tauc plot from absorptance of films with different molar ratios quenched using ASQ (c) Derivative at inflection point of EQE of devices with different molar ratios and (d) Tauc plot from absorptance of films with different molar ratios quenched using VQ. Adapted with permission from American Chemical Society.

4.3. Precursor stoichiometry on the morphology of perovskite thin films

With a minimal performance variation observed from MR changes and comparable results across quenching methods, the differences between antisolvent-quenched and vacuum-quenched films are further explored. The morphology of annealed perovskite films using scanning electron microscopy (SEM) is analyzed. The SEM images depicted in **Figure 4.5 (a-c)** for antisolvent-quenched perovskite thin films reveals that in comparison with the reference films of MR 1.1, films of MR 1.2 (less FAI) have smaller grain size. Presence of tiny bright particles of excess PbI_2 was also observed at the grain boundary of the dark perovskite grains [129]. On the other hand, the films of MR 1.05 (more FAI) had larger grain size compared to the reference films, with fewer tiny bright particles. Similar change in grain size was also observed in vacuum-quenched films of different MRs as depicted in **Figure 4.5 (d-f)**.

The tiny bright particles appearing on the surface of the MR 1.2 (less FAI) films were further verified using cathodoluminiscence (CL) characterization. When observed through a bandpass filter of 500 nm, the tiny particles exhibit higher CL intensities which correlates with PbI_2 crystallites of bandgap 2.48 eV as shown in **Figure A4.1 (g-i)** [228],[229]. The larger grains appear darker through this filter. Figure **A4.1 (j-l)** shows that when a filter of 800nm is used, the larger grains exhibit higher CL intensity confirming a 3D perovskite phase with a bandgap of ~1.57 eV [129].

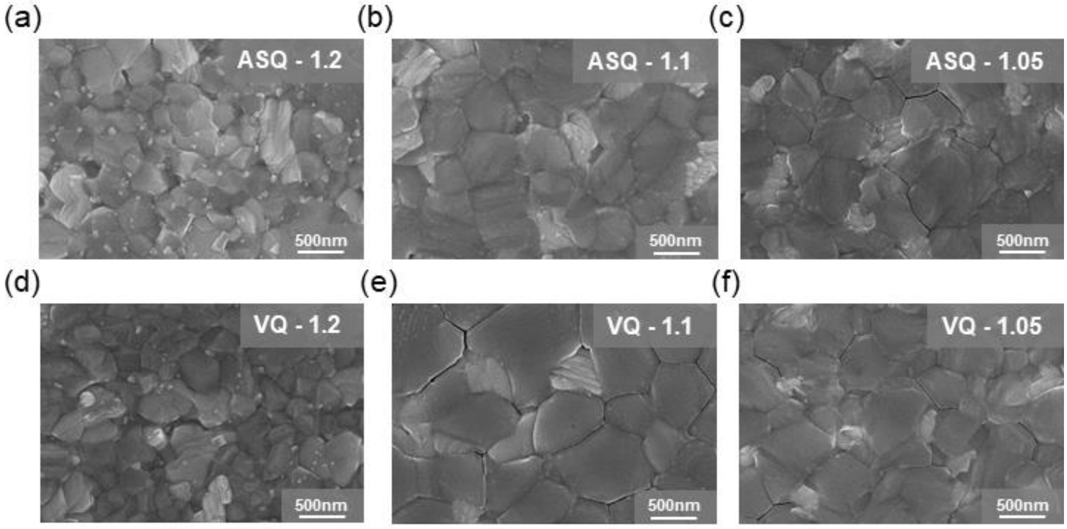

Figure 4.5: Scanning electron microscopy (SEM) images of perovskite thin films with molar ratios of (a) 1.2, (b) 1.1, and (c) 1.05 quenched using ASQ and molar ratios of (d) 1.2, (e) 1.1, and (f) 1.05 quenched using VQ. Adapted with permission from American Chemical Society.

4.4. Quenching technique on the morphology of perovskite thin films

Films subjected to different quenching techniques exhibited no distinct differences at the nanoscale. To investigate potential morphological variations arising from the quenching process, optical microscopy was employed. Though on a magnified scale, films quenched using different quenching techniques exhibited similar morphology, under optical microscopy (OM) prominent difference between the two quenching techniques were observed. OM images in **Figure 4.6 (a-c)** shows the presence of wrinkles in antisolvent-quenched films while vacuum-quenched films were more planar as depicted in **Figure 4.6 (d-f)**. ASQ is a fast quenching process where the strain developed during quenching cannot distribute laterally because of the rigid glass/ITO substrates [230] and is released vertically creating crests and troughs [231]. **Table A4.2** also shows the roughness of the films quenched using different quenching techniques measured using atomic force microscopy (AFM). AFM images in **Figure A4.2 (f-j)** reveals a slight reduction in the root-mean-square surface roughness of VQ films.

The contribution of wrinkles or planar features towards the long-term stability of PSC under different stress conditions like light, elevated temperature and voltage bias has not been studied previously. Before exposing devices comprising these variations in precursor stoichiometry and quenching techniques to different standardized accelerated stress testing protocols for extensive amount of time, one can check the stability of these materials by studying degradation on the perovskite layer only.

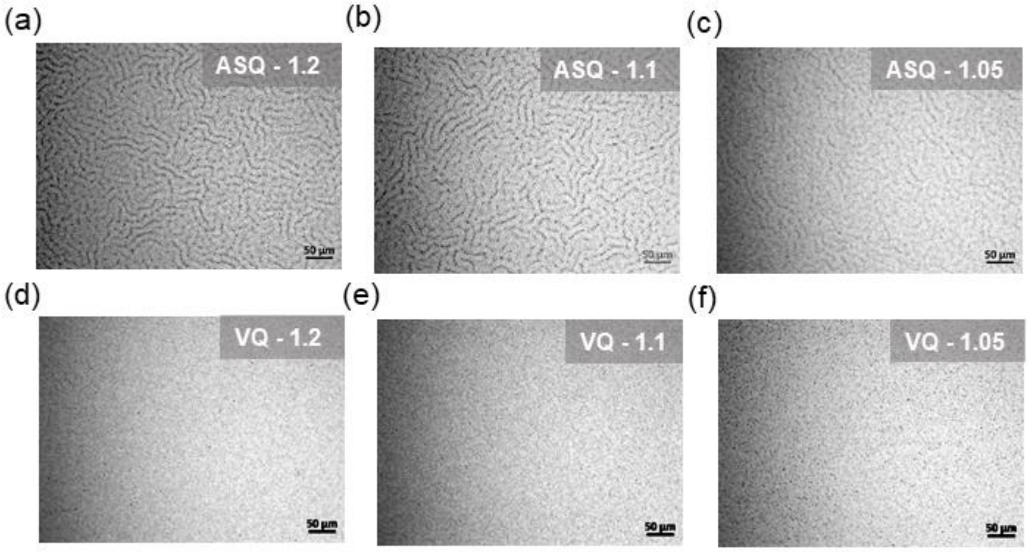

Figure 4.6: Optical microscopy (OM) images of films (a) MR 1.2 (b) MR 1.1 (c) MR 1.05 quenched using ASQ. OM of films (d) MR 1.2 (e) MR 1.1 (f) MR 1.05 quenched using VQ. Adapted with permission from American Chemical Society.

4.5. Precursor stoichiometry on the crystallization of perovskite thin films

In order to monitor the conversion of precursors to the perovskite phase and to gain insight into the byproducts formed during degradation, X-ray diffraction (XRD) was employed. XRD is an effective technique for monitoring structural changes in perovskite crystallites. XRD performed on pristine samples for antisolvent-quenched films shows that as compared to the reference sample of MR 1.1, films with MR > 1.1 showed the presence of a higher PbI_2 (100) peak at $2\theta = 12.7°$ confirming that even after conversion into perovskite, there was still excess PbI_2 in the annealed samples (see **Figure 4.7 (a)**). However, this trend was reversed for films with MR < 1.1. Due to presence of more FAI in the precursor solution, almost all PbI_2 was converted into perovskite and the intensity of PbI_2 (100) peak at a $2\theta = 12.7°$ decreased and the intensity of perovskite PSK (100) = 14.2° increased. The trade-off in intensity of PbI_2 (100) and PSK (100) with decreasing MR was also observed for vacuum-quenched films as seen in **Figure 4.7 (c)**. With the incorporation of larger FA^+ cation into the crystal structure, the full width at half maxima of the PSK (100) peak also broadened resulting in larger crystallite size with decreasing MR [232].

The stability of these films were tested by exposing to different intrinsic stress factors: light (100 mW/cm^2 at 25 °C) and elevated temperature (dark at 85 °C). XRD was performed on the same films after a period of 500 h. PbI_2 (100) / perovskite PSK (100) peak ratio suggests degradation of the perovskite film with PbI_2 being one of the byproducts [233]. As shown in **Figure 4.7 (c)**, the degradation of perovskite into PbI_2 is very prominent on films exposed to elevated temperature. However, the degradation is also visible in films exposed to light. This degradation is more drastic for films with MR > 1.1 (less FAI). The above experiment confirms that both light and elevated temperature induce degradation in the perovskite thin films especially in those implementing less FAI. The degradation was dependent on precursor stoichiometry and independent of the quenching technique implemented (see **Figure 4.7 (d)**).

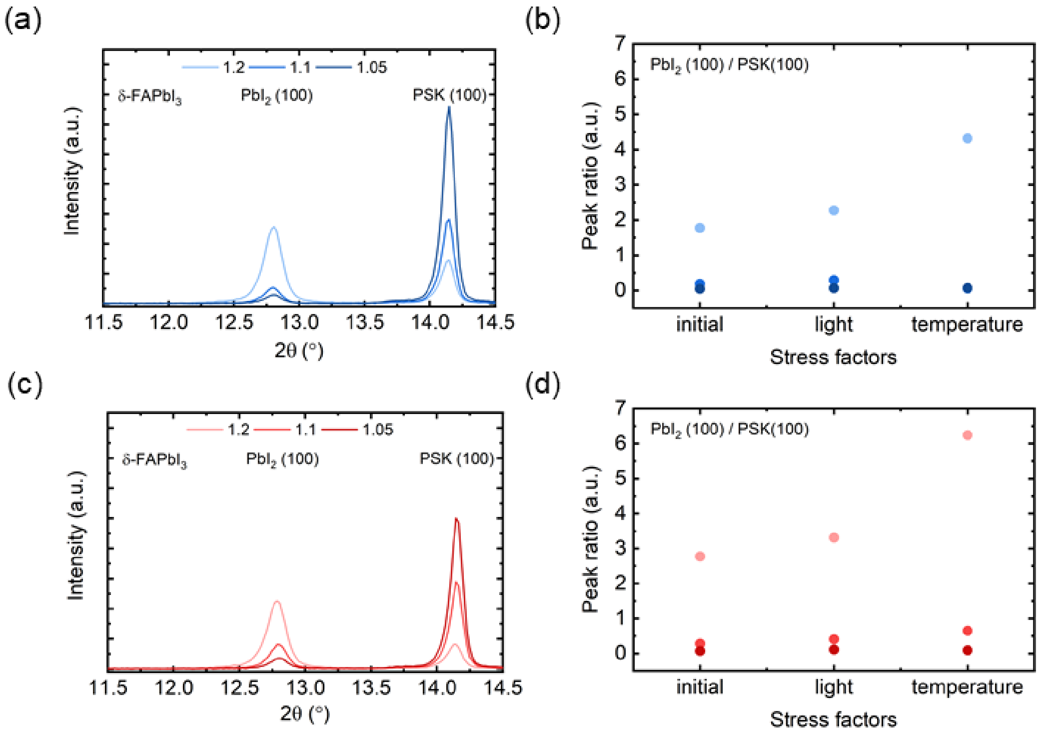

Figure 4.7: X-ray diffraction (XRD) patterns with (a) molar ratios of 1.2, 1.1, and 1.05 quenched using ASQ. (b) Peak ratio of lead iodide PbI_2 (100) / perovskite PSK (100) with molar ratios of 1.2, 1.1, and 1.05 quenched using ASQ and aged for 500h under the mentioned stress factor. XRD patterns with (c) molar ratios of 1.2, 1.1, and 1.05 quenched using VQ. (d) Peak ratio of PbI_2 (100) / PSK (100) with molar ratios of 1.2, 1.1, and 1.05 quenched using VQ and aged for 500h under the mentioned stress factor. Adapted with permission from American Chemical Society.

4.6. Precursor stoichiometry on the stability of perovskite solar cells

To understand if the stability of PSCs is also affected by incorporation of less FAI, completed semi-transparent devices were tested under two important ISOS testing protocols: ISOS-D2I and ISOS-L1I. In real-life scenario, presence of mutual stress factors like elevated temperature and light induce degradation in PSCs simultaneously. For understanding, the root cause of failure induced by each of the stress factors; one can expose the PSCs to these stress factors separately.

4.6.1. Elevated temperature (ISOS-D2I)

Antisolvent-quenched PSCs was introduced to ISOS-D2I protocol (dark and 85 °C) and $J\!-\!V$ characterization was performed intermittently. By the end of 500 h of accelerated stress testing, devices implementing MR > 1.1 (less FAI) and MR < 1.1 (more FAI) both show a drastic degradation mainly due to loss in V_{OC} and FF as shown in **Figure 4.8 (b and d)**. Either degradation of the perovskite layer or the interface of the perovskite layer with one/both of the charge transport layer could cause such decrease in V_{OC} and FF [234],[235]. Also, the thermal expansion coefficient of the rigid substrate (glass/ITO) is different than the thermal expansion coefficient of brittle layers deposited on the substrates and the interfaces formed [230]. This could result in different degree of expansion on application of elevated temperature. However, for the reference devices with MR = 1.1 the performance was stable over a testing period of 500 h.

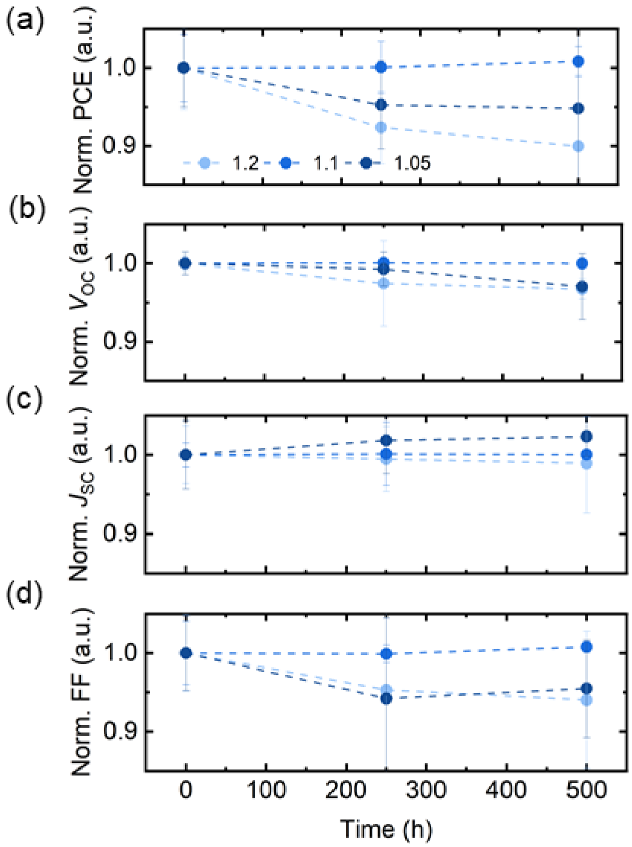

Figure 4.8: Normalized (a) PCE, (b) V_{OC}, (c) J_{SC}, and (d) FF from $J-V$ characterization of ASQ devices of different stoichiometry under ISOS-D2I testing conditions (dark, 85 °C, intermittent $J-V$ characterization) for 500 h. Adapted with permission from American Chemical Society.

The initial and final J-V characterizations before and after the ISOS-D2I protocol was performed. A comparison of $J-V$ characterizations for champion devices before and after the accelerated testing and upon removal of the stress factor is shown in **Figure 4.9 (a-c)**. Though the performance parameters of the champion PSCs in do not change drastically, for a batch of 12 devices, V_{OC} and FF are affected, lowering the overall performance statistically**. Figure 4.9 (d-f)** also verifies the current density for champion devices reported in intermittent $J-V$ characterization with EQE characterizations. No change in the EQE is observed confirming that extracted charge in the overall spectrum is not affected with the accelerated stress test.

Figure A4.3 depicts the stability of vacuum-quenched PSCs of different stoichiometry under ISOS-D2I testing conditions. The stability of vacuum-quenched PSCs are in close agreement with the results of antisolvent-quenched PSCs, further strengthening the fact that quenching technique variation does not affect stability on the long run.

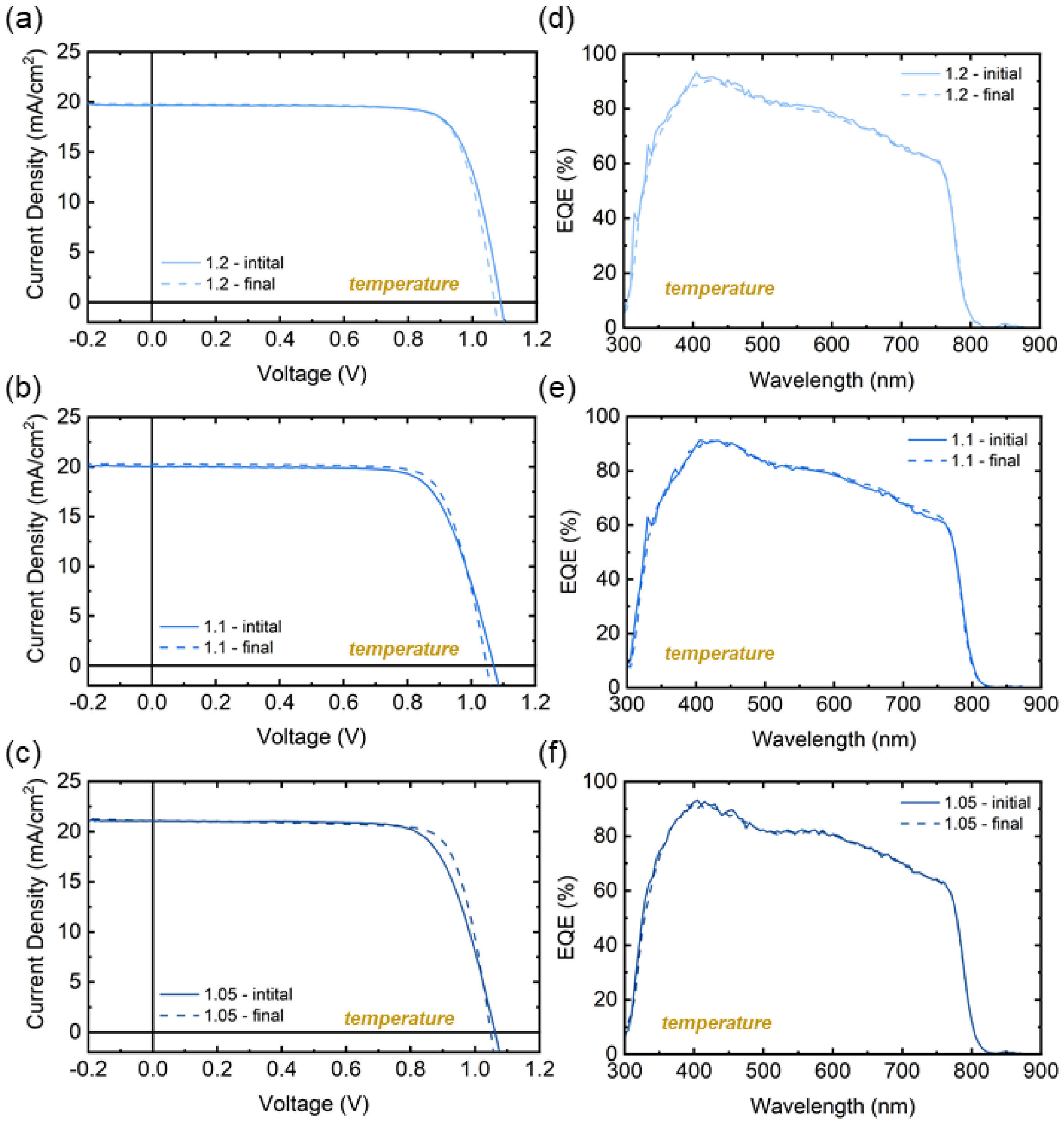

Figure 4.9: Comparison of *J-V* characterization of antisolvent-quenched devices of (a) MR 1.2 (b) MR 1.1 and (c) MR 1.05 measured before (initial) and after (final) ISOS-L1I test. Comparison of EQE of antisolvent-quenched devices of (d) MR 1.2 (e) MR 1.1 and (f) MR 1.05 measured before (initial) and after (final) ISOS-D2I test. Adapted with permission from American Chemical Society.

4.6.2. Light and voltage bias (ISOS-L1I)

As a means to understand the effect of light and voltage bias on the performance of PSCs, a separate batch of semi-transparent PSCs was aged under ISOS-L1I (MPP tracking under light intensity of 100 mW/cm^2 at 25 °C). **Figure 4.10 (a)** shows the maximum power (P_m) during MPP tracking for devices with different MRs. While MR $\leq$ 1.1, are stable under the accelerated stress testing, devices with MR 1.2 (with excess PbI_2) are not stable over a period of 500 h. **Figure 4.10 (b)** confirms that the current density (J_m) decreases during MPP tracking. Ionic accumulation is a phenomenon which blocks charge extraction at the interfaces during MPP tracking [210],[236],[237]. From SEM images in **Figure 4.5 (a-c)**, the grain size of perovskite films with MR 1.2 (less FAI) is smaller compared to the grain size of MR $\leq$ 1.1 (reference and more FAI). The activation energy for ionic migration at the grain boundaries is lower than at the grain interiors [125]. The small grain size in MR 1.2 ensures, more grain boundaries and hence, a lower activation energy for ionic migration resulting in ionic accumulation at the interfaces.

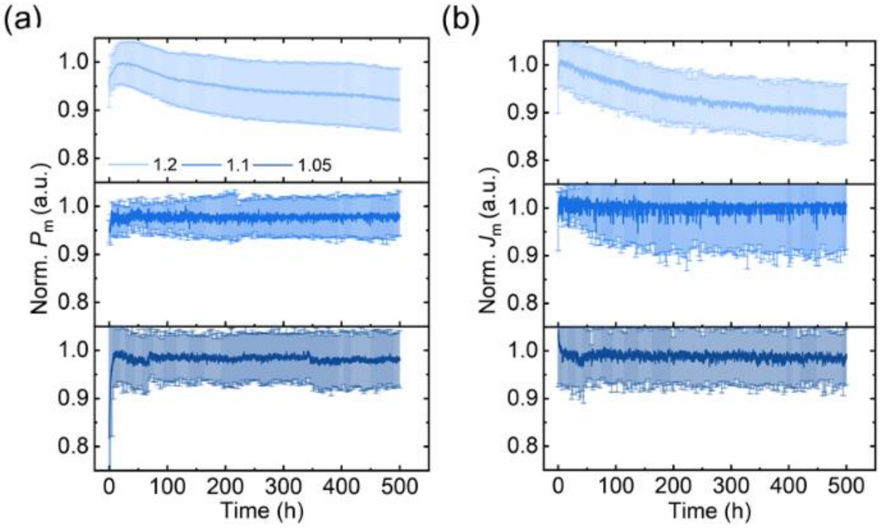

Figure 4.10: Normalized (a) power and (b) current density at the maximum power point (MPP) tracking of antisolvent-quenched devices of different stoichiometry under ISOS-L1I test conditions (100 mW/cm^2, 25 °C, MPP tracking) for 500 h. The power of MR 1.2, M.R. 1.1 and MR 1.0 were normalized with 18.33 %, 18.71 % and 17.95% respectively. Adapted with permission from American Chemical Society.

The initial and final *J*-*V* characterizations measured before and after the ISOS-L1I protocol was performed. Comparison of *J*-*V* characterizations of champion devices performed before and after the accelerated stress test gives a clear picture of what happens in the device once the stress is removed as shown in **Figure 4.11 (a-c)**. Post accelerated stress testing the V_{OC} decreases further for devices with more FAI. The decrease in J_m observed during MPP tracking is not exhibited in *J*-*V* characterizations made after the accelerated stress test. This is verified by EQE characterizations where no change in the EQE is observed in the overall spectrum confirming that extracted charges during EQE characterization is not affected with the accelerated stress test. The redistribution of ionic accumulation during MPP tracking on removal of accelerated stress factor could have caused such an effect [238]. It has also been reported previously that J_{SC} depends sub-linearly on light intensity [239]. Hence, on increasing the light intensity of EQE, the expected decrease in integrated J_{SC} from EQE should match J_m from MPP tracking.

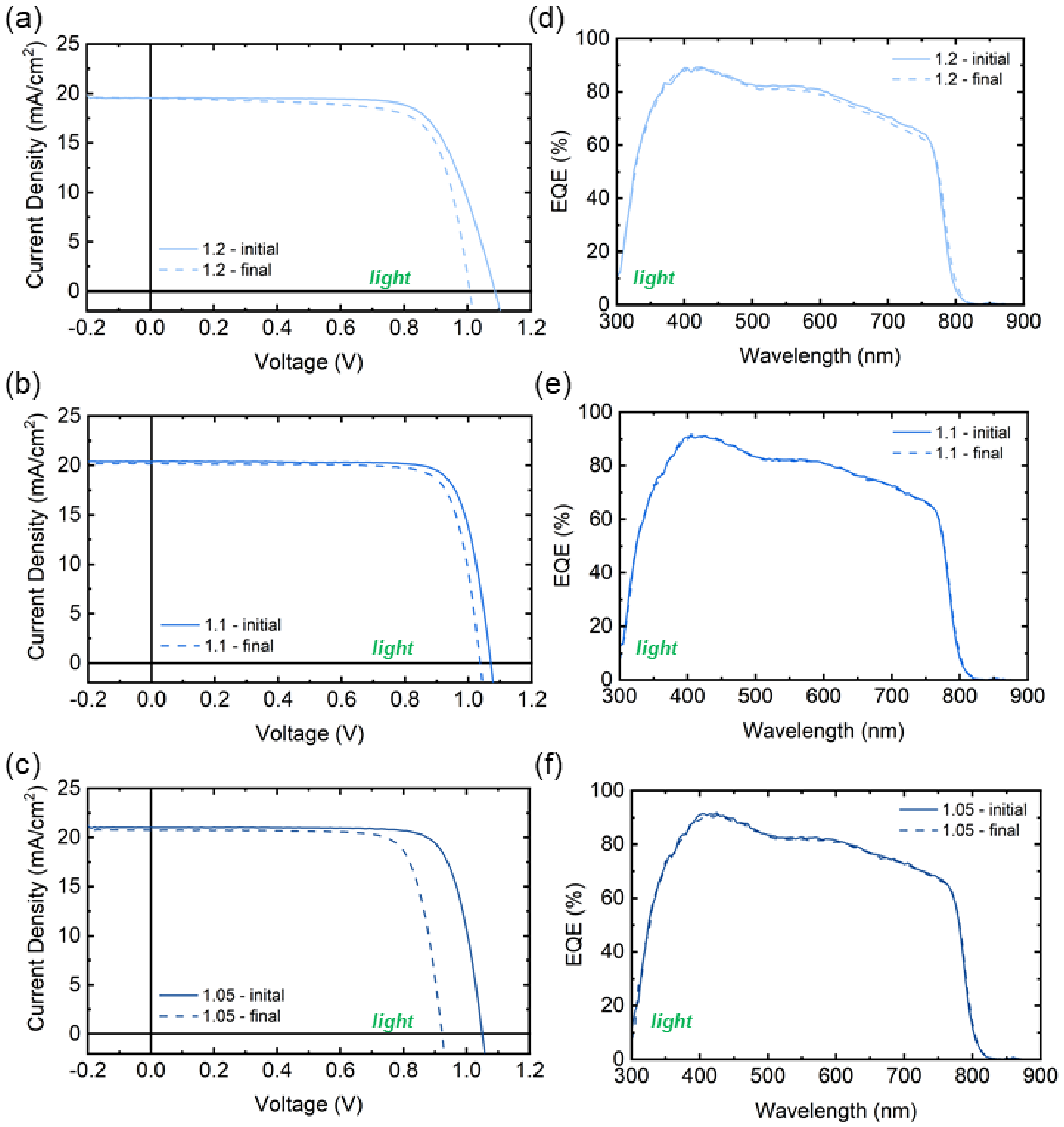

Figure 4.11: Comparison of *J*-*V* characterization of antisolvent-quenched devices of (a) MR 1.2 (b) MR 1.1 and (c) MR 1.05 measured before (initial) and after (final) ISOS-L1I test. Comparison of EQE of antisolvent-quenched devices of (d) MR 1.2 (e) MR 1.1 and (f) MR 1.05 measured before (initial) and after (final) ISOS-L1I test. Adapted with permission from American Chemical Society.

Figure A4.4 depicts the stability of vacuum-quenched PSCs of different stoichiometry under ISOS-L1I testing conditions. The stability of vacuum-quenched PSCs are in close agreement with the results of antisolvent-quenched PSCs.

4.7. Post degradation and dark recovery analysis

Stability is the key obstacle of PSCs and understanding the root cause of degradation is important so that it can be circumvented. Post degradation analysis can give us an insight into what happens in the device during accelerated stress test and how it affects the initial condition of the device. Several papers report the ability of PSCs to recover the performance lost during accelerated stress test by keeping them under dark storage [217],[240],[241]. With an intention of understanding the state of the devices after the accelerated stress testing, the ideality factor on pristine and aged devices was also measured. As shown in **Figure A4.5**, light and voltage bias is more detrimental on PSCs as compared to temperature. For MR = 1.1 i.e. the reference devices, there is no change in the ideality factor before and after ISOS-D2I testing. However, reference devices aged under ISOS-L1I, show higher non-radiative recombination.

To further test if our aged devices also recover their performance under dark storage, they were stored in dark and *J*-*V* characterizations were measured intermittently. Radar plot in **Figure 4.12** compares the initial and final (24 h of dark storage) PCE alongside with the PCE after 250 h of dark storage for devices with different MRs, tested under ISOS-D2I and ISOS-L1I. None of the MRs made a recovery in their performance after dark storage. For devices aged under ISOS-D2I, the overall trend of decrease in performance was comparable to their performance after the accelerated stress test, though lower. However, in case of devices aged under ISOS-L1I, the overall decrease in performance under dark storage was quite unexpected. The performance of MR ≤ 1.1 (more FAI) was stable as shown in **Figure 4.10**. However, once the devices were removed from the stress condition, these stable devices began to lose their V_{OC} as shown in **Figure 4.13**. This loss in V_{OC} is further increased for lower MRs (more FAI).

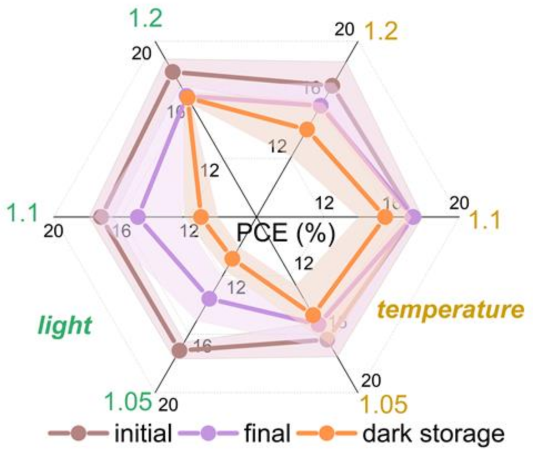

Figure 4.12: Radar plot of the average PCE of devices with different stoichiometry aged under ISOS-D2I (yellow) and ISOS-L1I (green). Devices are measured by $J-V$ characterizations before the accelerated stress testing (brown) and 24 h after the end of 500h of accelerated stress testing (purple) and 250 h (orange) of dark storage. Adapted with permission from American Chemical Society.

Figure A4.6 (a) also shows the radar plot of J_{SC} for devices after dark storage, the overall decrease in J_{SC} is quite similar to devices aged under ISOS-D2I and ISOS-L1I for different MRs. The FF for MR 1.2 (less FAI) aged under ISOS-L1I protocol demonstrates an improvement under dark storage (see **Figure A4.6 (b)**). Redistribution of ionic accumulation could cause such an improvement in FF which is an observed and well-reported phenomenon in bias-induced degradation [242].

The ability of PSCs to recover post accelerated stress testing also depends on the reason behind the decrease in their performance during accelerated stress testing. The decrease in J_m observed in ISOS-L1I is due to ionic accumulation at the interfaces, which can be considered as a transient degradation. Such phenomenon are known to be recoverable upon dark storage as the ions accumulated under light redistribute in the dark. At the same time, deep traps are formed in the perovskite absorber under illumination whose effects are be masked with light induced trap passivation [216]. In dark, the effects of these traps become more prominent. Increase in such deep traps in the devices with MR ≤ 1.1 (more FAI) can cause a drastic decrease in the V_{OC} along with a decrease in the J_{SC} and FF. Shallow traps formed at the interfaces are known to cause a decrease in the latter two parameters. For MR ≤ 1.1, no recovery in FF is observed [242]. The damaged induced by such deep traps in the perovskite absorber, especially at a later stage of degradation is known to be non-recoverable [216].

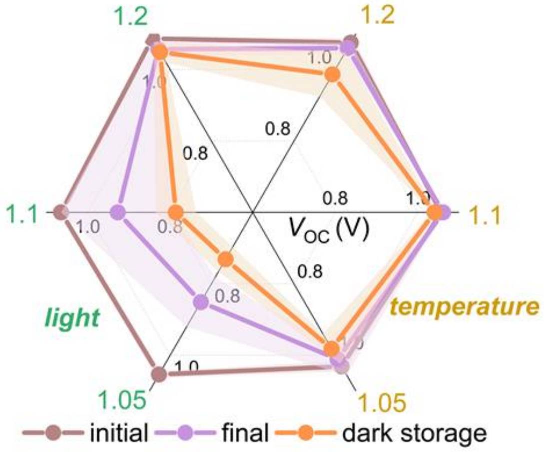

Figure 4.13: Radar plot of the average V_{OC} of devices with different stoichiometry aged under ISOS-D2I (yellow) and ISOS-L1I (green). Devices are measured by $J-V$ characterizations before the accelerated stress testing (brown) and 24 h after the end of 500h of accelerated stress testing (purple) and 250 h (orange) of dark storage. Adapted with permission from American Chemical Society.

To develop an understanding about the location of traps formed in the PSC, electroluminescence (EL) was performed on the devices aged under ISOS-L1I. **Figure 4.14 (a)** shows that in MR 1.05 (more FAI) defect distribution in the perovskite layer, decreasing the luminescence and causing them to appear darker as compared to devices of MR 1.2 (less FAI) as depicted in **Figure 4.14 (b)**. Even though MR 1.2 (less FAI) undergo transient degradation under ISOS-L1I testing, they still show some luminescence related to the local voltage after dark storage [243]. Alongside the luminescence, there are several other features visible in the EL images. The bright lines on the top and bottom of the EL images are due to the gold busbars provided to facilitate charge extraction from the semi-transparent contact. The light incident from the glass side is reflected from the gold busbars hence they appear brighter. A gradient of luminescence is also observed from the edges to the center of the PSCs. This could arise from thickness variation of the perovskite layer caused by the force created during antisolvent drop.

The intrinsic difference that leads to an enhanced defect formation in MR 1.05, can be understood from **Table 4.1**. Adding more FAI in the precursor solution also increases the iodide content. Iodide ions (I^-) have the minimum activation energy for migration of 0.1 eV as compared to organic cations MA^+ (0.5 eV) or Pb^{2+} (0.8 eV) inducing I^- migration under light with presence of bias and at room temperature [218]. The I^- ions migrate towards the ETL and the iodide vacancies ($V_{I^-}^{+}$) migrate towards hole transport layer (HTL). When the migration of I^- ions and $V_{I^-}^{+}$ vacancies to the corresponding charge transport layers are excessive as in the case of MR 1.05 (more FAI), localized shunts are created degrading the quality of the perovskite layer [244]. **Figure A4.7** in **Appendix** shows OM images of perovskite films aged under identical conditions (100 mW/cm^2 light at 25 °C). Dark region with pinholes surrounded by light FA$^+$-rich region in the films shows the extent of the damage occurring inside a complete device, especially at the HTL side. Formation of localized shunting leads to non-radiative recombination in the perovskite layer and resulting in overall loss in V_{OC} and FF.

Delayed-time charge extraction by linearly increasing voltage (CELIV) characterizations also support this claim (see **Figure A4.8**). The charges extracted from the devices with different MRs aged under ISOS-L1I decay drastically over time (see **Figure 4.14 (c)**). Such decay in the charge carrier extraction is not observed for devices aged under ISOS-D2I as shown in **Figure 4.14 (d)**. In addition, fewer charge carriers are extracted for MR ≤ 1.1 (more FAI) as compared to MR = 1.2 (less FAI).

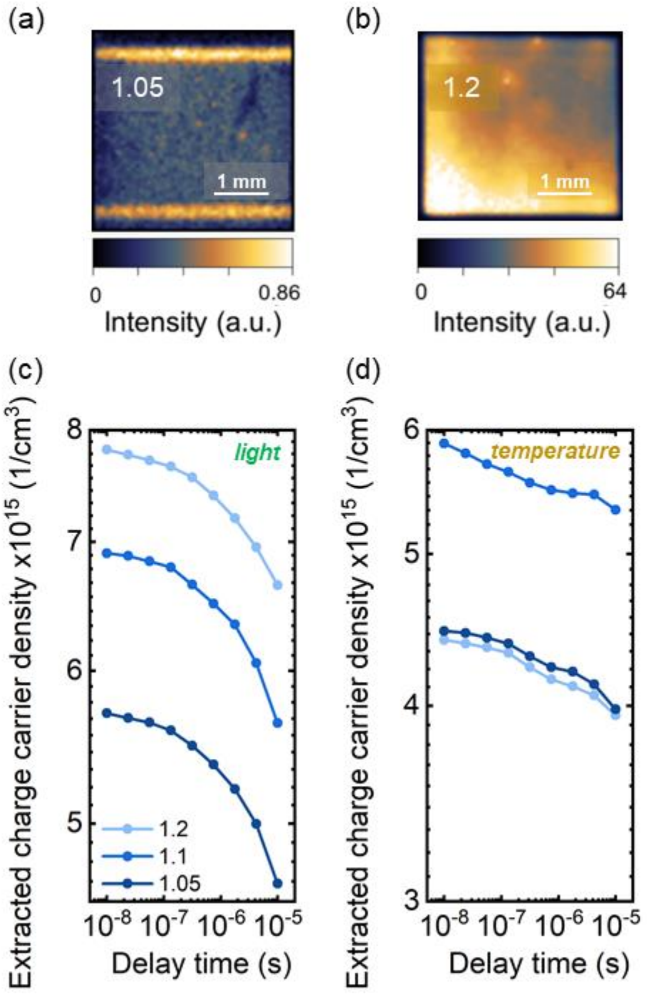

Figure 4.14: Electroluminescence (EL) images of devices with (a) MR 1.05 and (b) MR 1.2 after dark storage of 250 h after ISOS-L1I testing. Extracted charge carrier density of devices with different stoichiometry aged under (c) ISOS-L1I and dark storage of 250 h along with (d) ISOS-D2I and dark storage of 250 h, measured by charge extraction by linearly increasing voltage (CELIV).

Gaining insight into the variations in processing parameters (precursor stoichiometry and quenching technique) and their influence on the degradation of PSCs under various stress factors (elevated temperature and light with voltage bias) can help develop PSCs that not only deliver high performance but can also endure prolonged exposure under standardized accelerated stress tests. Hence, reporting of the stability under different intrinsic stress factors (elevated temperature and light with voltage bias) is imperative for understanding the root cause of failure. Only then, we can mitigate the issues and improve the stability of PSCs. Proper attention should be given to post degradation and dark recovery analyses in order to recognize the effects of such perplexing phenomenon of precursor stoichiometry on dark recovery of PSCs. Such phenomenon which is enhanced in the dark affects the performance of PSCs in real-life conditions such as day-night cycling [240],[245].

As an extension of this work, both wide-bandgap (WBG) and narrow-bandgap (NBG) perovskite absorbers were developed and integrated into all-perovskite TSCs. To investigate the impact of current mismatch between subcells on the performance and stability of the tandem architecture, the thickness of the WBG top cell was systematically varied by adjusting the molarity of the precursor solution. This variation modulates the absorption of high-energy photons by the top cell and consequently alters the photon flux incident on the bottom cell. Device performance and stability were evaluated under continuous illumination with MPP tracking. Post degradation characterization of stressed devices was conducted to assess the degree of degradation in each subcell.

Variations in the thickness of the WBG top cell led to corresponding changes in the performance of the TSCs. In configurations where either the top or bottom subcell limited the current, a reduction in J_{SC} was observed, resulting in decreased PCE. In contrast, TSCs with more balanced current matching between subcells exhibited higher J_{SC} and improved PCE. Under ISOS-L1I accelerated aging conditions, devices with well-matched subcell currents demonstrated excellent operational stability over 350 h of continuous illumination. On the other hand, current mismatch, either top or bottom limitation, led to accelerated degradation and poor stability, highlighting the critical role of current matching both at the onset and throughout the stress testing. Post degradation analysis revealed that the EQE intensity of the WBG top cell declined significantly under bottom-limited conditions, potentially due to the top cell being driven toward reverse bias under severe bottom cell limitation. Further details can be found in **Appendix**: Current mismatch between subcells and stability of all-perovskite tandem solar cells.

4.8. Summary

This chapter examines the impact of processing parameters (precursor stoichiometry and quenching technique) on the morphological and structural properties of perovskite thin films and PSCs. These features influence the failure mechanism when films and devices are exposed to operational stress factors (light with voltage bias and elevated temperature). Understanding the role of these structural and morphological features can be important in resolving the root cause of degradation under different stress factors addressing **Objective 1.**

Section 4.2 demonstrates that on varying molar ratio of PbI_2 and FAI, the performance of the PSCs do not change drastically. MR 1.2 (less FAI) shows improved V_{OC} as a result of excess PbI_2 in the precursor, passivating the grain boundaries. With more FAI in the precursor solution, more FA^+ gets incorporated into the film for the same amount of Cs^+ lowering bandgap. The impact of more FAI in the solution also reflects on the morphology of the perovskite films. **Section 4.3** explains that compared to the reference films of MR 1.1, films employing more FAI showed larger perovskite grain size based on SEM. On the other hand, MR 1.2 (less FAI) had smaller grain size and a distribution of tiny bright particles. CL confirmed these tiny, bright particles to be PbI_2 crystallites.

On a nanoscale, ASQ and VQ showed similar morphology, but on a microscale, as shown in **Section 4.4,** antisolvent-quenched films showed presence of wrinkles (based on OM images). Vacuum-quenched films showed more planar surface and a slight reduction in the root-mean-square surface roughness (measured using AFM).

On examining different precursor stoichiometry, the highest initial power conversion efficiency (MR 1.2) does not correlate to long-term stability under light and voltage bias or elevated temperature, challenging previous reports [246]. **Section 4.5** demonstrates that perovskite films with MR > 1.1 (less FAI) degrades faster under both elevated temperature and light with voltage bias. A byproduct of degradation PbI_2 was detected in the films with XRD. This suggests that additional effects might be responsible for previously reported correlations between performance and stability. Under ISOS-D2I, as discussed in **Section 4.6.1**, reference PSCs (MR = 1.1) did not show any sign of degradation. However, PSCs with MR < 1.1 (more FAI) and with MR > 1.1 (less FAI) both demonstrated decrease in FF and V_{OC}. Either perovskite absorber, interface of perovskite with one of the charge transport layer or the charge transport layers could have been degraded at an elevated temperature of 85 °C. The stability of MR $\leq$ 1.1 (less FAI) was unaffected under ISOS-L1I as shown in **Section 4.6.2**. However, devices with MR > 1.1 showed decrease in J_m during MPP tracking. The smaller grain size and more grain boundaries in these films contributed to lower activation energy for ionic migration at the grain boundaries. Ionic accumulation contribute to reduced charged extraction lowering J_m. **Section 4.6** also demonstrates that the long-term stability of perovskites with same MR is not influenced by the different quenching techniques.

Section 4.7 demonstrates that devices initially stable under light exposure can show reduced performance under dark storage. Localized shunts develop during dark storage in MR $\leq$ 1.1 (reference devices and devices with more FAI). While MR $\leq$ 1.1 maintain their stability under light, I^- ions migration and $V_{I^-}^+$ creation can degrade their performance in the dark. The degradation mechanism is identified as: I^- ions migrating towards the ETL under light, leading to $V_{I^-}^+$ vacancies moving towards the HTL and causing non-radiative recombination in the perovskite absorber. These issues may be masked during operations due to overlapping stress factors (light and voltage bias) and other phenomenon (light induced trap passivation) but can significantly affect the next diurnal cycle and long-term stability. Although I^- ions enhance photon harvesting, making PSCs viable in the photovoltaics industry, they undermine long-term stability, leading to permanent degradation.

Therefore, it is crucial to report stability under different stress factors with emphasis on the post-degradation and the dark recovery analyses, addressing **Objective 2.** These practices encourages statistical and consistent reporting strengthening understanding and mitigation of the issues related to perovskite stability. Variations in the thickness of the WBG top cell affected the performance of all-perovskite TSC by altering current matching between subcells, where imbalances led to reduced J_{SC} and PCE. Under ISOS-L1I accelerated stress testing, devices with well-matched currents showed superior stability, emphasizing the importance of current matching under real-world operating conditions for long-term stability of perovskite-based TSCs (addressing **Objective 3**). The mismatched configurations degraded rapidly with significant loss in EQE intensity of the WBG top cell under bottom-limited conditions.

The following articles have benefitted from this work in understanding that the variations in precursor stoichiometry can impact efficiency, stability and recovery of PSCs [247], [248]. The reversible and irreversible changes which PSCs and perovskite-based TSCs undergo can impact their performance both indoor and outdoor [249], [250],[251]. Such irrecoverable changes in device stability can set a limitation to the application of perovskite photovoltaics and delay commercialization.

5. Sub-bandgap photons harvesting via Upconversion for Perovskite Solar Cells

In this work, an alternative approach to cater to the challenge of utilization of the sub-bandgap photons by using spectral convertors has been attempted. An upconversion single crystal made of BaF_2 *and doped with* Yb^{3+}, Er^{3+} *is placed at the rear of a bifacial perovskite solar cell. Irradiation with a high intensity monochromatic light source at 980nm results in an emission from the upconversion crystal in the spectral range of 520 to 700 nm. Reabsorption of the upconverted photons by the perovskite solar cells contributes to an enhancement in the short-circuit current density at lower incident light intensity. Upon increasing the intensity of the incident light, the short-circuit current density of the perovskite solar cell scales up non-linearly. Hence, by using an inorganic upconversion single crystal the response of perovskite solar cell is extended to the near infrared range resulting in an enhancement in the short-circuit current density. Alongside increase in the short-circuit current density, the effect of elevated temperature, as a consequence of using high intensity monochromatic light source, on the overall performance and stability of the perovskite solar cell is also evaluated, addressing Objective 4.*

This chapter is based on our publication titled "Harvesting Sub-bandgap Photons via Upconversion for Perovskite Solar Cells"[201] published in *ACS Applied Materials and Interfaces* 2021, 13, 54874-54883 authored by *Roja Singh (R.S.)*, Eduard Madirov (E.M.)*, Dmitry Busko, Vasilii A. Konyushkin, Andrey N. Nakladov, Sergey V. Kuznetsov, Amjad Farooq, Saba Gharibzadeh, Ihteaz M. Hossain, Ulrich W. Paetzold, Bryce S. Richards and Andrey Turshatov*.

R.S. and *E.M.* contributed equally to this work. *R.S.* fabricated and investigated the bifacial solar cells. *R.S.* and *E.M.* performed investigations on the combined effect of the bifacial solar cells and the upconversion crystals. *R.S.* performed data analysis and wrote the manuscript. The detailed contribution list can be found in the Appendix. Most of the figures in this chapter have been reproduced or adapted with the permission of American Chemical Society.

5.1. Introduction

The efficiency of the perovskite-silicon tandem solar cells (TSCs) supersedes the performance of a single junction silicon solar cell[4]. Elimination of the performance limiting factors can contribute to further boosting the efficiency of the TSCs. The performance of the TSCs could be limited by constrains such as the current mismatch between the subcells [76], yellowing of the encapsulation [252], or seasonal variation of the solar spectrum [24]. While current matching in subcells can be optimized during the fabrication of the TSCs, operation in the fields over time can cause a larger variation in the current mismatch. The yellowing of the encapsulation material with exposure to the ultraviolet light results in loss in the transparency of the encapsulation [252]. At the same time, the spectral variation can cause blue or red shift which further result in mismatch of the subcells [24]. Hence, maintaining the performance of the perovskite subcell and the quality of the encapsulation over years can be a challenge. The main advantage of the TSCs is their ability to utilize a larger fraction of the solar spectrum that would otherwise remain unused when individual single junction solar cells are operated [253]. In this work, an alternative approach to cater to the same objective has been attempted by using spectral convertors.

Spectral converters can harness photons that lie outside the absorption range of a solar cell and convert them into photons that match the cell’s bandgap, enabling additional light harvesting. These converters are generally classified into three categories: upconversion (UC) [85], downconversion [79], and downshifting [90]. The distinctions between them were detailed in **Chapter 2**. In this chapter, we focus on the optimal integration of perovskite solar cells (PSCs) with upconversion materials. The optoelectronic properties of PSCs, including high absorption coefficients [32] and tunable bandgaps [43] make them ideal candidates not only for TSCs, but also for coupling with UC materials. UC involves the absorption of two or more sub-bandgap (low-energy) photons and the emission of one high-energy photon [85]. When an UC crystal is positioned at the back side of a PSC, high-energy photons from the solar spectrum are absorbed by the PSC, while sub-bandgap (SB) photons pass through it. The UC crystal then absorbs these transmitted low-energy photons, where they are upconverted to high-energy photons [254]. These newly generated photons are reflected back toward the PSC, where they can now be absorbed, leading to an increase in the short-circuit current density (J_{SC}).

Initial investigations into the application of UC in the field of PSCs can be categorized into three main groups. Firstly, UC nanocrystals were introduced into different layers of the PSCs, including the hole transport layer (HTL) [255], electron transport layer (ETL) [256], the perovskite absorber layer [257] itself, and at the interfaces [258]. While this doping initially improved performance up to an optimal concentration due to passivation, surpassing this concentration proved detrimental as the nanocrystals started to act as recombination centers [255],[258]. Secondly, triplet-triplet annihilation upconversion (TTA-UC) was explored for PSCs [259],[260]. Embedded organic dyes within polymeric sheets were placed behind the PSC to serve as an UC layer [84]. Despite showing the potential for enhancing J_{SC}, the requirement for high excitation intensity (10 W/cm^2 or higher) to convert the near infrared (NIR) illumination into the visible range remained a significant limitation[261]. Kinoshita *et al.* reported an enhancement of 0.5 mA/cm^2 in current density, upon excitation of a TTA-UC film at the back side of the PSC with a diode laser (938 nm, 10 W/cm^2) [84]. The third approach involved using UC inorganic materials, either in the form of single crystals or microcrystalline powders, stacked on top of a PSC device. These materials demonstrated higher UC quantum yield compared to nanocrystals due to fewer surface defects which cause luminescence quenching [262]. Additionally, unlike nanoparticles integrated into PSC layers, these materials allowed for thicker UC layers, enhancing absorption. For instance, a densely packed layer of UC nanoparticles with a thickness of 200 nm absorbs only a minimal fraction of incident radiation at 980 nm [261], whereas a single crystal with a thickness of 1-2 mm ensures over 90% absorption. The UC single crystal implemented in this chapter shows nearly eight times stronger enhancement (4 mA/cm^2) at the same intensity used in the report by Kinoshita *et al.* This enhanced performance can be attributed to the higher absorption of the Barium Fluoride (BaF_2) doped with Ytterbium (Yb^{3+}) and Erbium (Er^{3+}) - BaF_2: Yb^{3+}, Er^{3+} single crystal at 980 nm compared to the TTA-UC film. While studies have demonstrated the potential of inorganic crystals, such as Lithium Yttrium Tetrafluoride ($LiYF_4$):Yb^{3+}, Er^{3+} single crystals, to improve PSC performance under specific conditions [81], there is still room for further exploration. Materials like Beta-phase Sodium Yttrium Tetrafluoride (β-$NaYF_4$) [80] and MF_2 hosts (M = Calcium [263], Strontium [261],[263], Ba [264],[263]) have shown promising UC quantum yields (ϕ_{UC}) under specific excitation wavelengths.

Alongside the benefits of incorporating UC materials into PSCs, it is equally important to address the topic of stability, as it remains a critical factor influencing the long-term performance of these devices. The effect of different stress factors like elevated temperature and continuous irradiation on the triplet generation process at the perovskite/Rubrene (Rub) interface was studied [265]. Combination of both stress factors resulted in increased rates of singlet fission and reduced triplet generation and TTA, resulting in diminished ϕ_{UC}. Transient absorption spectra demonstrated successful triplet sensitization even at elevated temperatures. A decrease in UC photoluminescence as a result of a decrease in the of the organic semiconductor was observed under direct excitation [265]. Irannejad *et al.* reported that along with the enhancement in the PSC performance due to light-harvesting, the hydrophobic property of the UC graphene quantum dots introduced in the perovskite/ETL interface leads to an increase in the long-term stability under high humidity condition [266]. Defect passivation and surface modification due to surface passivation with the UC graphene quantum dots resulted in reduction of non-radiative charge carrier recombination, leading to improved performance and stability [266]. Sheng *et al.* also reported that introducing the Rub: Dibenzotetraphenylperiflanthene (DBP) in a $MAPbI_3$ absorber resulted in a champion power conversion efficiency (PCE) of 20.18% as compared to 17.33% in reference devices. The vertical crystal growth of perovskite layer using Rub agglomerates as growing sites and TTA UC process resulted in the improved performance [267]. These unencapsulated devices also exhibited enhanced humidity stability for 14 days at a high humidity condition (50-70 % relative humidity) and 25 °C [267]. These promising trends offer encouraging prospects for the further development of this concept in the photovoltaics sector.

5.2. BaF_2 as a host for upconversion single crystal

Among the materials mentioned above, BaF_2 stands out due to its high ϕ_{UC} and brightness [264]. In this chapter, the inorganic material BaF_2 is utilized as a host for UC in PV the first time. The BaF_2: Yb^{3+}, Er^{3+} UC crystal absorbs the SB photons in the NIR range, upconverts them and reflects it to the PSC (as depicted in **Figure 5.1 (a)**). BaF_2 can be grown as a single crystal and exhibits low phonon energy, which contributes to high ϕ_{UC} by minimizing non-radiative losses [264]. The host is doped with two lanthanide ions, Yb^{3+} and Er^{3+}. Yb^{3+} acts as the sensitizer as it possesses a high absorption cross section in the excited state ($^2F_{5/2}$) and transfers the photons to Er^{3+}, which performs as an activator for the UC process [268]. Since Er^{3+} possesses a state with a similar energy level ($^4I_{11/2}$), the near-resonant nature of these two levels facilitates an efficient energy transfer (ET) process as shown in **Figure 5.1 (b)** [269].

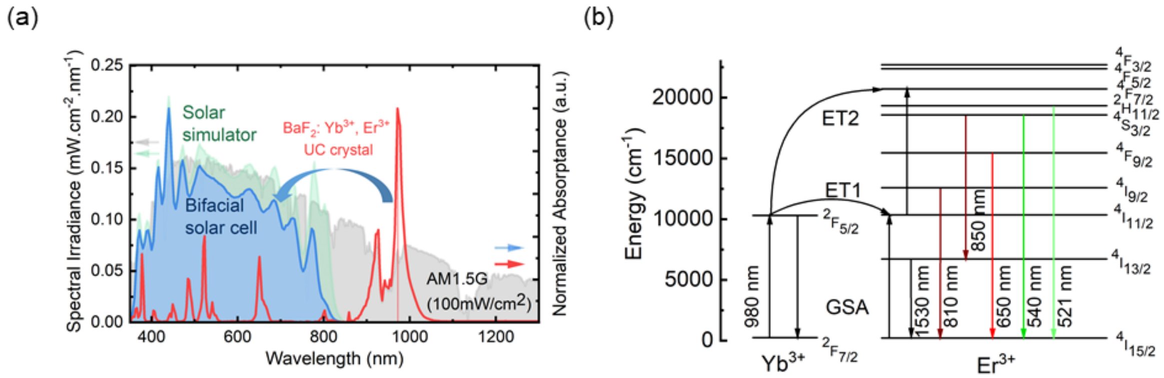

Figure 5.1: (a) Spectral irradiance of air mass 1.5 global (AM1.5G) and solar simulator alongside absorptance of the bifacial perovskite solar cells and BaF_2: Yb^{3+}, Er^{3+} upconversion (UC) crystal. The two or more low-energy photons are upconverted by the UC crystal and transferred to the bifacial solar cell which can absorb the high-energy photons. (b) Energy level diagrams of the Er^{3+} and Yb^{3+} ions along with the energy transfer (ET) UC mechanism. Adapted with permission from American Chemical Society.

The BaF_2: Yb^{3+}, Er^{3+} UC single crystal was synthesized using the Bridgman method [270]. The nominal concentrations of Yb^{3+} and Er^{3+} in the initial charge were 15% and 2%, respectively. These values represent the intended dopant levels prior to the crystal growth. The actual dopant concentrations in the resulting single crystal were determined to be 11.98 mol% for Yb^{3+} and 1.86 mol% for Er^{3+} [264]. The synthesis yielded in a cylindrical single crystal approximately 5 cm in length. For experimental purposes, a 1.7 mm-thick disk was cut from the bulk material. This thickness was selected based on a model predicting optimal UC photon generation variation with thickness, which will be covered in the following section. **Figure 5.2 (a)** depicts the change in ϕ_{UC} and the number of emitted photons post UC as the thickness of UC crystal is varied. Based on this estimation, an UC crystal of 1-1.7mm thickness gives >10^{17} photons after UC. The upconverted emission from multiple emission bands of Er^{3+} because of the transition from excited states to the ground state $^4I_{15/2}$ is shown in **Figure 5.2 (b)**. While the contribution of emissions from wavelengths ≥ 810 nm is either transmitted or reflected by the PSC, the energy of the red and green emissions (< 810 nm) contributes to the photocurrent generation since their energy is higher than the bandgap of the implemented perovskite absorber material.

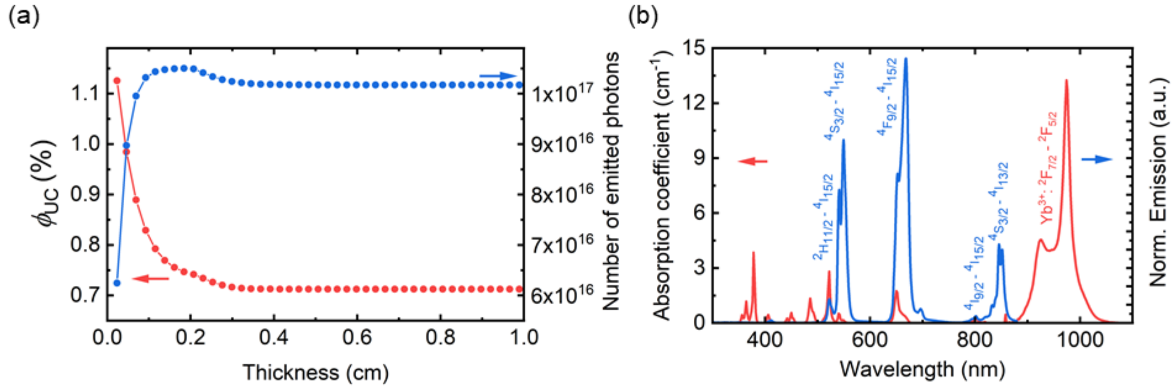

Figure 6.2: (a) Change in upconversion quantum yield (ϕ_{UC}) and number of emitted photons observed as the thickness of upconversion (UC) crystal is varied up to 1cm (b) Absorption coefficient and normalized emission spectra of the UC crystal of thickness 1.7 mm. The emission was measured under 980 nm excitation. Adapted with permission from American Chemical Society.

5.3. Optimal thickness of BaF_2: Yb^{3+}, Er^{3+} upconversion crystal

The thickness of the UC crystal is an important parameter for high ϕ_{UC} and maximum utilization of SB photons. The empirical model is based on the optical properties of a thin UC crystal layer with a thickness of 0.23 mm, which serves as the fundamental unit for calculating the behavior of thicker samples.

(i) The intensity-dependent ϕ_{UC}, along with the absorption and emission spectra of the 0.23 mm sample, are measured (**Figure 5.3 (a)** and **Figure 5.3 (b)**). Thicker samples are then modeled as seamless stacks composed of multiple 0.23 mm layers.

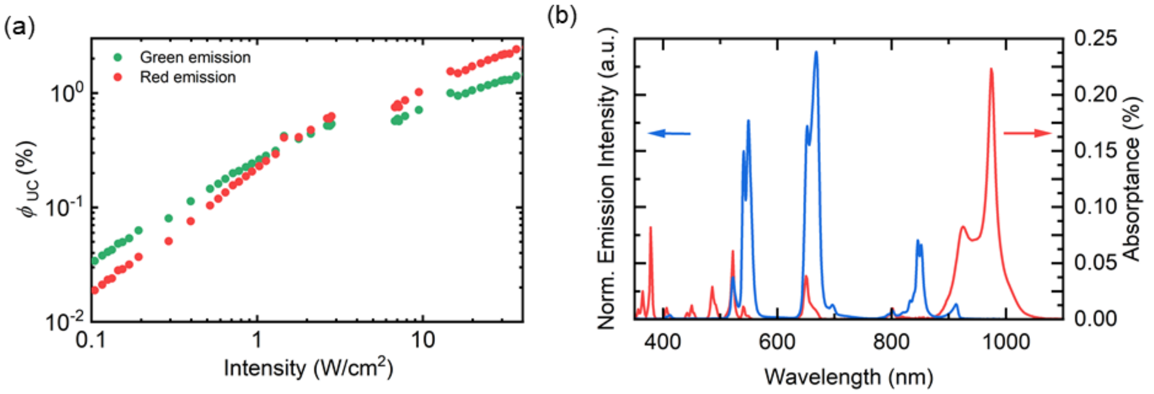

Figure 5.3: Optical properties of a 0.23 mm thick BaF_2:Er^{3+},Yb^{3+} sample (a) Intensity dependence of the upconversion quantum yield (ϕ_{UC}) for green and red emission bands; (b) Absorptance spectrum and normalized emission spectra. Adapted with permission from American Chemical Society.

(ii) The numbers of the absorbed and emitted photons for samples of varying thicknesses are calculated using the following approach. The excitation source is modeled as a narrow laser beam with a wavelength of 976 nm and an intensity of 4.5 W/cm^2. When the excitation beam interacts with the first layer (0.23 mm thick), approximately 22% of the photons are absorbed and subsequently converted into visible-range photons. The quantum yield for this process is determined from the experimentally measured dependence (**Figure 5.3 (a)**). The remaining excitation intensity then reaches the second 0.23 mm layer, and the same calculations are repeated. Since ϕ_{UC} is intensity-dependent, each successive layer exhibits a reduced ϕ_{UC}. Given that the sample has a mirror on its rear surface, the portion of excitation light that reaches the back is assumed to be reflected with 100% reflectance and passes through the sample again in the reverse direction. Calculations are similarly performed for this reflected excitation. The cumulative results are shown in **Figure 5.4 (a)**.

(iii) The reabsorption of emitted light within the sample is evaluated as follows. Using the experimentally measured emission and absorption spectra of a 0.23 mm thick sample, the intensities of the two main emission bands are calculated for varying sample thicknesses. Reabsorption within the 0.23 mm sample is assumed to be negligible. For samples of greater thickness, the emission spectrum is calculated by multiplying the recorded emission spectrum by the absorptance spectrum of the BaF_2:Er^{3+},Yb^{3+} material corresponding to that thickness. The resulting spectra are then integrated over two wavelength ranges: 500- 600 nm, corresponding to the green emission band, and 600-750 nm, corresponding to the red emission band (labeled 'Green' and 'Red' in **Figure 5.4 (b)**, respectively). The ratio of the integrated intensity of a 0.23 mm sample to that of thicker samples is taken as the fraction of emission remaining after reabsorption (**Figure 5.5 (a)**).

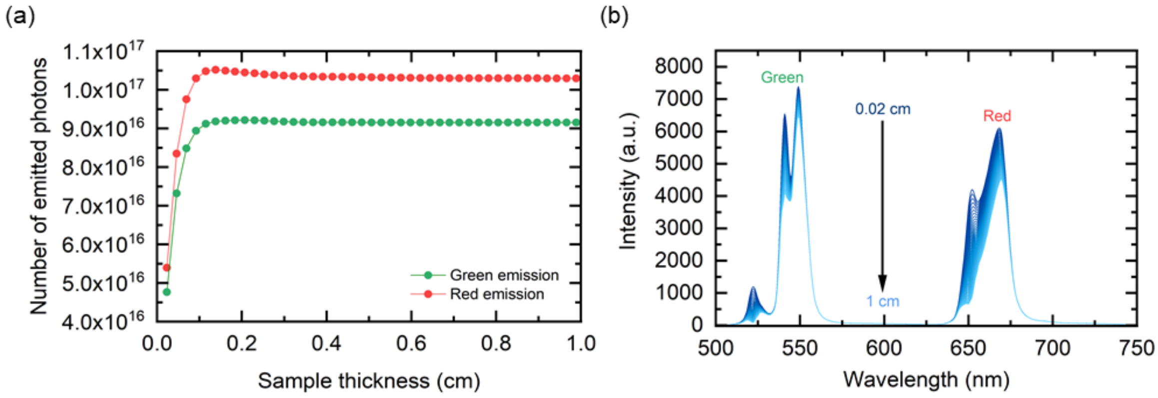

Figure 5.4: (a) Variation of number of emitted photons with the thickness of the crystal (b) The calculated emission spectra of samples with various thickness. Adapted with permission from American Chemical Society.

(iv) To account for the escape cone of the emitted light, basic geometric assumptions are applied as illustrated in **Figure 5.5 (b)**. The sample is modeled as a flat disk with a diameter of 10 mm, and the excitation beam is assumed to strike precisely at its center. Emission is considered to be uniformly distributed over a full solid angle of 4π steradians.

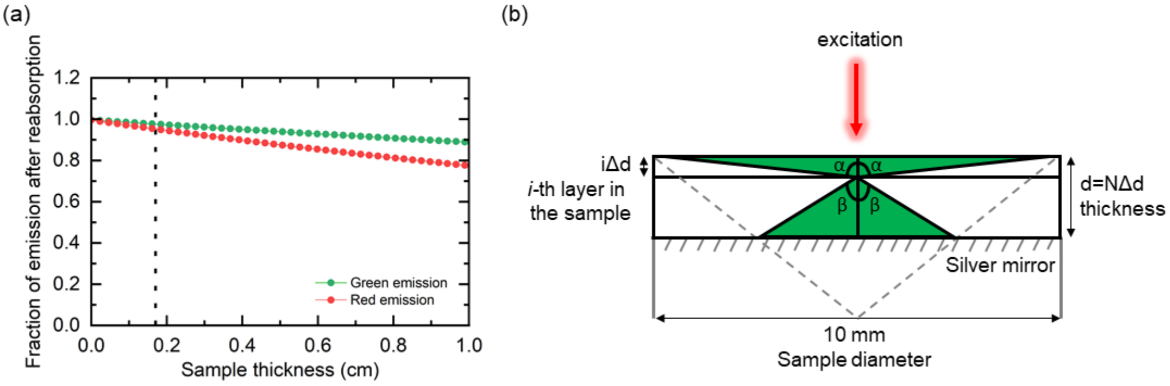

Figure 5.5: (a) Fraction of emitted light after the reabsorption. The dotted line shows the thickness of 1.7 mm used in the experiments. (b) Emission escape cone. The areas highlighted in green represent the emission angles from which photons can be harvested through the top surface of the crystal. Adapted with permission from American Chemical Society.

When excitation reaches the i-th layer within the crystal, the resulting emission can be divided into two components: one directed above the layer and the other below. For the emission above the layer to be harvested from the top surface of the crystal, it must fall within the angle denoted as α. This angle is calculated as follows using **Equation 5.1**:

$$\alpha = \arctan\left(\frac{r_C}{i.\Delta d}\right) \qquad \text{Equation 5.1}$$

Here, r_C = 5 mm is the radius of the UC crystal, i denotes the layer number, and Δd = 0.23 mm represents the unit thickness.

Due to the presence of a reflective mirror on the backside of the sample, a portion of the emission directed below the layer can also be harvested from the top surface after reflection. For this to occur, the emission must lie within the angle denoted as β, which is calculated using **Equation 5.2**:

$$\beta = \arctan\left(\frac{r_C}{2.d - i.\Delta d}\right) \qquad \text{Equation 5.2}$$

In this context, r_C = 5 mm is the radius of the UC crystal, d represents the total thickness, i is the layer number, and Δd = 0.23 mm is the unit thickness.

The total fraction of photons that can be harvested from the top surface of the crystal is then calculated as $\frac{\alpha}{\alpha+\beta}$

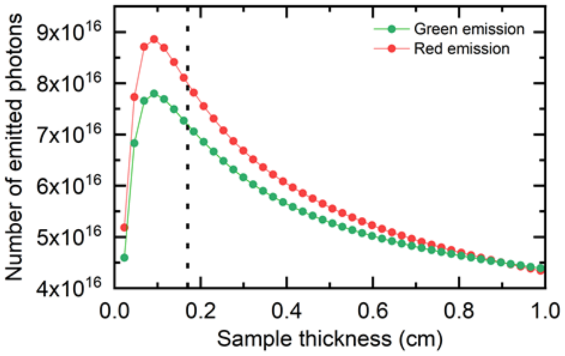

Figure 5.6: Variation in the number of emitted photons as a function of crystal thickness, accounting for reabsorption and escape cone effects. Adapted with permission from American Chemical Society.

The resulting number of photons emitted within the escape cone, accounting for (i) the intensity dependence of ϕ_{UC} (ii) and reabsorption effects (iii) as a function of sample thickness is shown in **Figure 5.6**. The results indicate that an optimal thickness range of 1 to 1.7 mm yields the highest number of emitted photons, exceeding 90% of the maximum. Therefore, a crystal thickness of 1.7 mm was chosen for this study, offering both near-optimal photon emission and improved mechanical stability for easier handling.

5.4. Enhancement in J_{SC} by harvesting sub-bandgap photons

While the selection of the material and thickness of the UC crystal meets all the necessary criteria, the choice of PSC must be equally favorable to ensure optimal utilization of the upconverted photons. In this chapter, the absorber layer selected is a double-cation perovskite, $Cs_{0.18}FA_{0.82}PbI_3$, which has a bandgap of 1.57 eV [271], [272]. Hence, photons with energies below 1.57 eV (wavelengths above 810 nm) are not sufficient to generate electron-hole pairs in the perovskite absorber layer. Other choices of absorber among lead-based perovskites are formamidinium lead iodide ($FAPbI_3$) which offers one of the lowest bandgaps at 1.47 eV [273]. However, $FAPbI_3$ is thermodynamically unstable at room temperature and tends to degrade into the non-photoactive δ-phase [273]. To stabilize the photoactive α-phase at ambient conditions, small amounts of additives such as cesium (Cs) or methylammonium (MA) are typically introduced [139],[268]. Hence, an absorber with approximately 18% Cs to stabilize the perovskite structure was selected. While this additive improves thermal stability, it also leads to a slight increase in the bandgap to 1.57 eV [274]. The influence of elevated temperature on the PSC performance is discussed in more detail in the following section. Although other narrow-bandgap absorbers, such as methylammonium lead iodide ($MAPbI_3$) [275] and tin–lead (Sn-Pb) [276] perovskites, offer narrower bandgaps, they suffer from significantly poor thermal stability, making them less suitable for the stability-focused objectives of this chapter. The PSCs examined in this chapter were fabricated in a bifacial negative (n)-intrinsic (i)-postive (p) architecture, as detailed in a **Chapter 3**.

The device architecture of glass/indium tin oxide (ITO)/ tin oxide (SnO_2)/ Fullerene self-assembled monolayer (C_{60}-SAM)/ perovskite/ 2,2′,7,7′- Tetrakis(N,N-di-p-methoxyphenylamine)-9,9′-spirobifluorene (Spiro-OMeTAD)/ Molybdenum oxide (MoO_X)/ ITO/ gold (Au) fingers is used. The bifacial PSCs exhibited a good baseline performance with a mean PCE of 17.5% and a mean J_{SC} of 21.3 mA/cm^2 as depicted in **Figure A5.1 (a) and Figure A5.1 (b)**. As a bifacial solar cell does not give back reflection from the TCO top contact, the J_{SC} is around 1 mA/cm^2 less as compared to same devices with a metal top contact. A mean open-circuit voltage (V_{OC}) of 1.06 V and a mean fill factor (FF) of 75% (see **Figure A5.1 (c) and Figure A5.1 (d)**) demonstrated robust devices with a stabilized output power (P_m) of 17% during maximum power point (MPP) tracking (see **Figure 5.7 (a)**). Alongside demonstrating good stability, high transmittance in NIR range is essential for a maximum number of SB photons to reach the UC crystal. In NIR range (980 nm), the bifacial PSC transmitted ~50% of the incident light as shown in **Figure 5.7 (b)**. The transmittance from both the top side (ITO) and the back side (glass substrate) was comparable, indicating that incident NIR photons can pass through either side with minimal parasitic absorption losses.

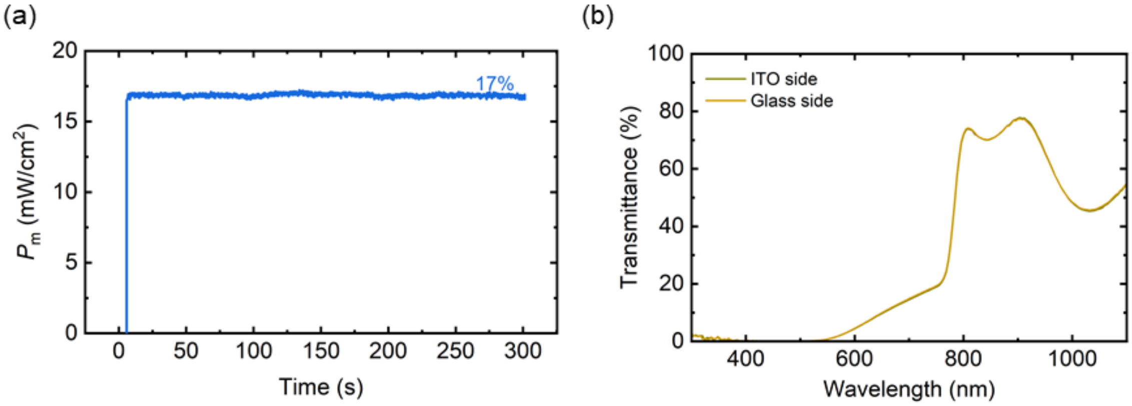

Figure 5.7: (a) Power output (P_m) during maximum power point (MPP) tracking of bifacial perovskite solar cell (PSC). (b) Transmittance of the PSC device stack measured from the top (Indium Tin Oxide side) represented by green line and bottom (glass side) represented by yellow line. Adapted with permission from American Chemical Society.

Alongside the UC crystal and bifacial solar cell, a well-integrated setup can further enhance the efficiency of the upconversion process. A schematic of the experimental setup implemented to understand the contribution of upconverted SB photons to J_{SC} is depicted in **Figure 5.8 (a)**. The UC crystal was placed at the backside of the PSC on a stage to ensure that the parasitic absorption does not affect the operation of the PSC. Silicon immersion oil with refractive index (n) of ~ 1.49 [277] was used as an index matching liquid (IML) for good optical coupling between the PSC and UC crystal (n ~ 1.48) at 980 nm [278]. The backside of the UC crystal was coated with Ag as a back reflector for the purpose of reflecting the upconverted emission back to the PSC. Henceforth, the combination of PSC with UC crystal at the back side is referred to as PSC-UC device. The PSC-UC device combination was irradiated with a light emitting diode (LED) solar simulator limited to a wavelength of 850 nm. The solar simulator provided an intensity of ~70 mW/cm² and is referred to as broadband (BB) illumination.

A tunable continuous-wave Titanium-Sapphire (Ti:Sa) laser pumped by a 532 nm laser was used to generate 980 nm emission to match the peak absorption range (974–980 nm) of the BaF_2:Yb^{3+}, Er^{3+} crystal and is referred to as SB illumination. A fraction of the beam, reflected off a quartz wedge placed in the beam path, was directed to a photodiode power sensor, connected to a power meter to monitor and control the laser intensity. The measured power was calibrated to reflect the actual power incident on the sample. For ease of calibrating intensity of SB illumination, the spectrum of BB illumination was limited to <850 nm. An image of the experimental setup is shown in **Figure 5.8 (b)**. The green and red emissions from the PSC upon illumination by NIR illumination is clearly visible.

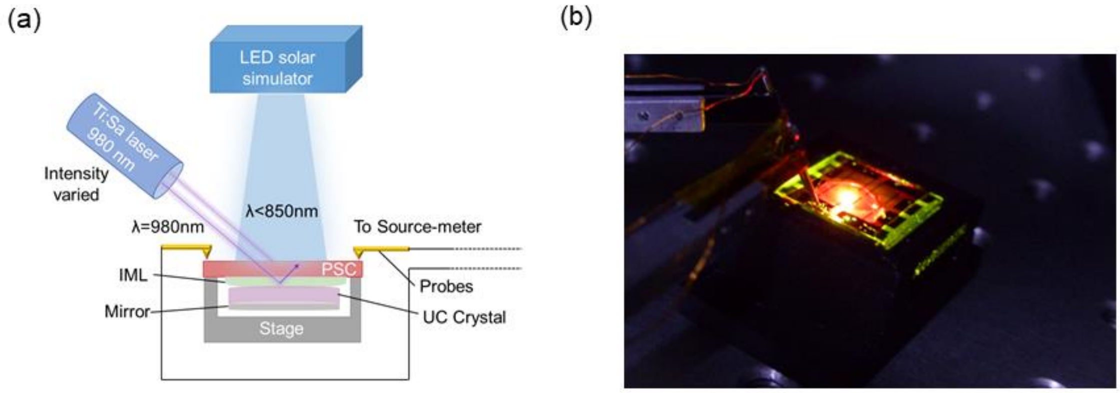

Figure 5.8: (a) Schematic representation of the experimental setup used for the characterization of enhancement in J_{SC} and the overall influence of upconversion (UC) on the perovskite solar cell (PSC)-UC device. The UC crystal (pink) was placed at the backside of the PSC inside a stage (grey). The PSC-UC device was illuminated with a solar simulator (<850 nm) and laser (980nm) and current density-voltage (J-V) characterization was performed with Au probes (yellow). (b) Image of the experimental setup implementing PSC-UC device on the stage. Adapted with permission from American Chemical Society.

Upon irradiating the PSC-only with BB illumination of ~70 W/cm^2, a J_{SC} of 22 mA/cm^2 was measured. On additional 4.5 W/cm^2 of SB illumination along with the BB illumination the PSC-UC device showed an enhancement in J_{SC} of 0.4 mA/cm^2 to 22.4 mA/cm^2 as shown in **Figure 5.9 (a)**. The contribution of upconverted photon to the enhancement in J_{SC} ($\Delta J_{SC,UC}$), is the difference between the short-circuit current measured under BB+SB illumination and the short-circuit current measured only under BB illumination divided by the area of the laser beam spot (A_{spot}) of the SB illumination (see **Equation 6.3**)

$$\Delta J_{\mathrm{SC,UC}} = \frac{I_{\mathrm{SC(BB+\,SB\,illumination)}} - I_{\mathrm{SC(BB\,illumination)}}}{A_{\mathrm{spot}}} \qquad \text{Equation (5.3)}$$

where, $I_{SC(BB+SB\ illumination)}$ is the short-circuit current measured under BB+SB illumination, $I_{SC(BB\ illumination)}$ is the short-circuit current only under BB illumination and A_{spot} is the size of the laser beam spot.

The source of the enhancement in J_{SC} is clarified through spectral dependence characterizations of $\Delta J_{SC,UC}$. **Figure 5.9 (b)** illustrates that in the range of 880-1000 nm, the enhancement in $\Delta J_{SC,UC}$ is prominent. This follows the trend of the absorption coefficient of the UC crystal as shown in **Figure 5.2 (b)**. However, on illuminating PSC-only device with BB+SB illumination, no enhancement is observed. Similarly, no enhancement in $\Delta J_{SC,UC}$ is observed upon illuminating PSC- UC device with BB illumination only. This confirms that the combination of UC crystal and SB illumination results in the observed increase of the J_{SC}. The reflection of the upconverted SB photons from the evaporated Ag on the backside of the UC crystal is reabsorbed by the PSC. However, along with the desired enhancement in J_{SC}, a decrease in V_{OC} and FF of the PSC-UC device is observed (see **Figure 5.9 (a)**). This behavior will be investigated in the next section.

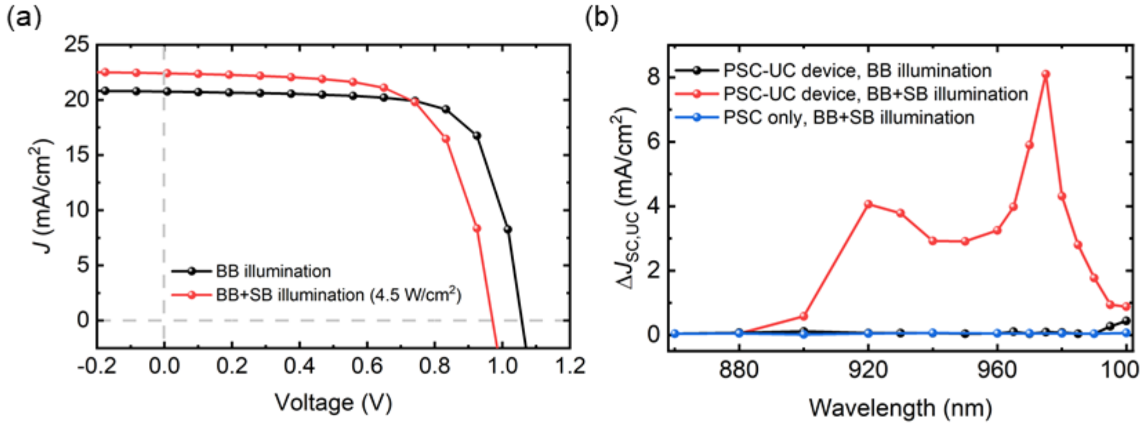

Figure 5.9: (a) Current density-voltage (J-V) characteristic of the perovskite solar cell (PSC)- upconversion (UC) device excited with only BB illumination (black) and BB+SB illumination (red). Intensity at sub-bandgap (SB) illumination was at 4.5 W/cm^2. (b) Spectral dependence of enhancement in short-circuit current density ($\Delta J_{\mathrm{SC,UC}}$) measured from 860−1000 nm, ~ 4.2 W/cm^2 at different conditions: PSC-UC device and with only broadband (BB) illumination (black), PSC-UC device with BB+SB illumination (red), and PSC-only with BB+SB illumination (blue). Adapted with permission from American Chemical Society.

5.5. Elevated temperature due to continuous laser illumination

One possibility for the decrease in V_{OC} and FF could be because of the elevated temperature due to continuous laser illumination. With the aim of understanding the effect of the elevated temperature on the performance of PSCs, the thermal coefficient of the PSC was calculated. The PSC-only devices was heated from 25 to 85 °C on a sample holder with a Peltier element and current density-voltage (J-V) characterizations were performed. The devices were held at a specific temperature for 2 minutes prior to J-V characterization to ensure thermal equilibrium between the device and the sample holder. The temperature range was selected based on standard testing conditions (STC), where devices are typically evaluated at 25 °C and accelerated stability testing protocols, which commonly use 85 °C as the benchmark temperature within the photovoltaic community. **Figure 5.10 (a)** shows that even though J_{SC} remains unaffected due to the increasing temperature, V_{OC} and FF show a linear decrease of 0.17 rel%/°C and 0.18 rel%/°C respectively resulting in a cumulative decrease of 0.33 rel%/°C in PCE. Using a thermal imager, the correct temperature of the PSC-only device under SB illumination of 4.2 W/cm^2 was estimated to be 41.2 °C (see **Figure 5.10 (b)**). At this temperature, the V_{OC} decrease is approximately 0.97 V, which is in agreement with the V_{OC} observed in **Figure 5.9 (a)**. The increased temperature causes reduction in the built-in voltage [279],[280], resulting in an increase in minority charge carrier recombination [281],[282] directly affecting the V_{OC} [283],[284] and FF [102]. Such effect of increasing temperature is more visible when measuring the stabilized power output (P) of the system, where the devices are illuminated continuously under BB and/or SB illumination, during the MPP tracking.

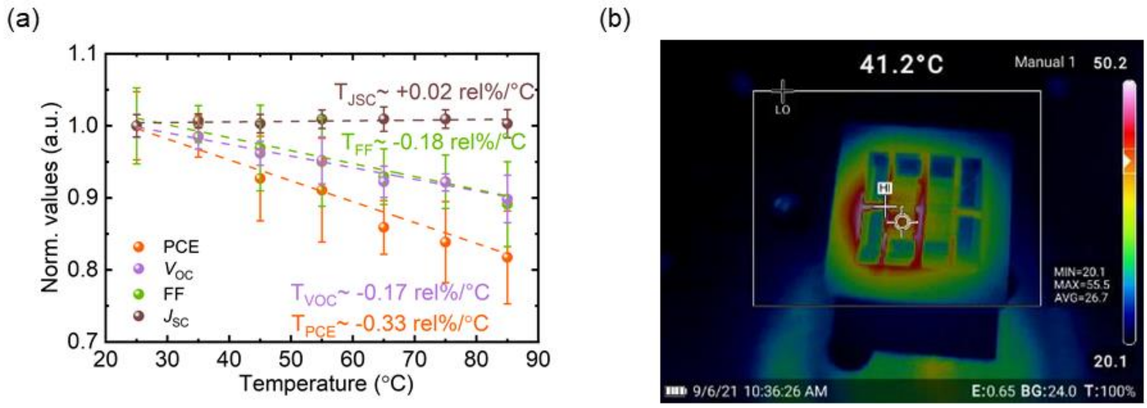

Figure 5.10: Thermal coefficient of perovskite solar cell (PSC) heated between 25 °C to 85 °C. The thermal coefficient of short-circuit current density (J_{SC}) is depicted in brown, fill factor (FF) in green, open circuit voltage (V_{OC}) in purple and power conversion efficiency (PCE) in orange. (b) Image of the PSC- upconversion (UC) device taken through a thermal imager. The PSC exhibits a temperature of 41.2 °C and the UC crystal is around 50.2 °C under sub-bandgap (SB) illumination. Adapted with permission from American Chemical Society.

To understand the distinction between the effect of increased temperature due to laser illumination or BB illumination, the BB illumination was kept on throughout the experiment. However, the SB illumination was cycled at 980 nm (~ 4.2 W/cm^2) with a period of 200 s and 50% duty cycle. For the PSC-only device during MPP tracking, the value of J remains constant during the period when the SB illumination is on (see **Figure 5.11 (a)**). This confirms that in absence of the UC crystal, the value of J is unaltered even with the presence of the SB illumination. However, the voltage (V) of the PSC-only device decreases severely during the ON cycle of the SB illumination due to additional heat that was generated in the device. The P also decreases as a consequence of the increased temperature. In the PSC-UC device, the value of J is enhanced during the ON cycle of SB illumination, as depicted in **Figure 5.11 (b)**. This further confirms the UC of SB photons in the presence of the UC crystal and SB illumination. Though the voltage decreases during the ON cycle of SB illumination, the enhancement in current compensates for this loss and overall P is increased. This shows that the photons of the SB illumination do not only contribute to thermalization as seen in the PSC-only device but also to UC and increase in J due to photocurrent generation.

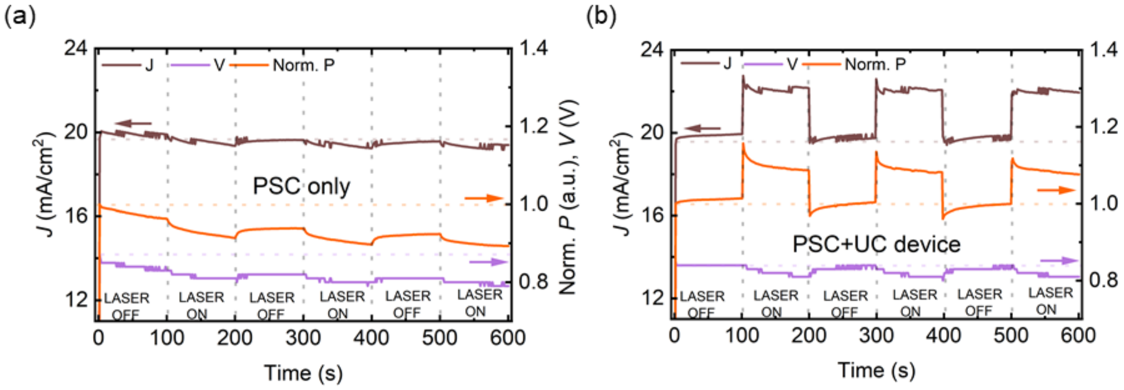

Figure 5.11: Current density (J, brown), normalized stabilized power output (P, orange), and voltage (V, purple) tracked for (a) the PSC-only and (b) the PSC-UC device near the maximum power point (MPP) over 600 s. Continuous air mass 1.5 global (AM1.5G) illumination and additional cycled sub- bandgap excitation at (980 nm, 4.2 W/cm^2) having a period of 200 s and 50% duty cycle was the source of illumination. Adapted with permission from American Chemical Society.

5.6. Higher irradiation intensity of SB illumination on enhancement in J_{SC}

As quantum yield depends highly on the intensity of the incident photons, UC becomes a non-linear process [285]. In order to study the effect of intensity on the $\Delta J_{SC,UC}$, the geometric concentration of the laser on the sample was enhanced by employing a 100 cm focal length lens. This modification made it a possibility to reach to higher intensities. A lens was placed in the beam path such that the laser focuses on the crystal with a smaller beam spot. With such an arrangement, an intensity from 5.54 to 38.8 W/cm^2 was achieved. There are two options of placing the optics, (i) between the PSCs and the single crystal and (ii) between the light source and the solar cell. Though the first option increases the quantum yield of the UC process, it also disrupts the collection of UC emission by the solar cell [254]. Hence, in this chapter the second option of placing the optics was chosen. As shown in **Figure 5.12 (a)**, the UC quantum yield (ϕ_{UC}) varies at varying intensity, at low illumination intensity of about 0.6 W/cm^2, ϕ_{UC} is only around 0.2%. However, with increasing excitation intensity, the ϕ_{UC} increases steadily with values >1% at intensities exceeding 10 W/cm^2.

To verifying if the observed increase in ϕ_{UC} with intensity also results in an increase in $J_{SC,UC}$, the intensity of SB illumination was increased between 0.6 and 4.5 W/cm^2 and the corresponding J_{SC} was measured. **Figure 5.12 (b)** depicts the corresponding enhancement in $\Delta J_{SC,UC}$ for the higher SB illumination intensities. The characterization at lower intensity exhibits higher deviation. This could arise from the accuracy with which $\Delta J_{SC,UC}$ or the area of irradiation spot (A_{spot}) can be measured. The laser beam size was characterized using a camera-based beam profiler positioned at the sample location. An image of the beam profile was captured, and the beam was assumed to have an elliptical shape. The axes of the ellipse were extracted from Gaussian fits, with the 1/e^2 beam widths determined as 1.699 times the full width at half maxima. **Table 5.1** shows the variation in measurement of the X and Y axis of the beam spot for calculation of A_{spot} and **Figure A5.2** depicts the beam spot with and without the focusing lens.

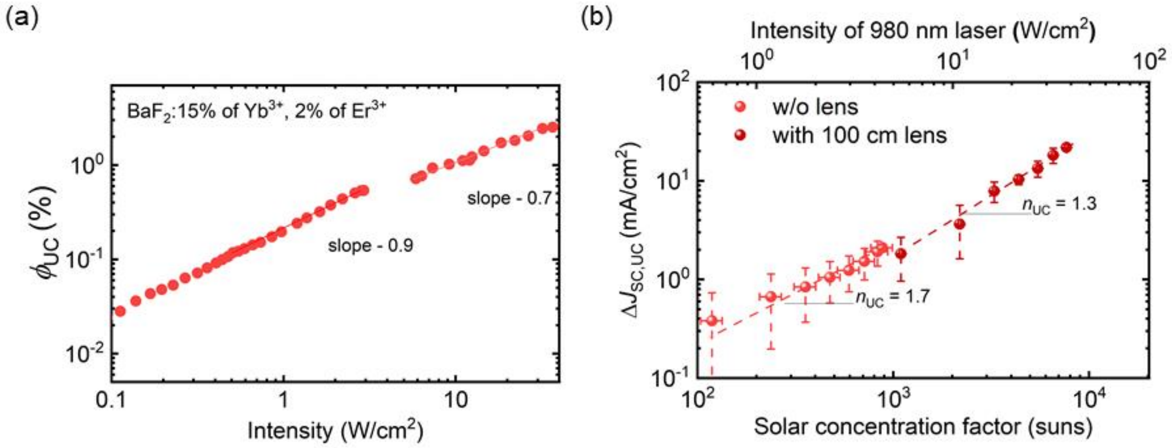

Figure 5.12: (a) Intensity dependence of upconversion quantum yield (ϕ_{UC}) of the UC crystal is the sum of quantum yields for green and red UC peaks (b) Enhancement in upconverted current density ($\Delta J_{SC,UC}$) obtained for various solar concentrations. Red represents data without focusing and dark red represents data with the use of a lens with a focal length of 100 cm. Adapted with permission from American Chemical Society.

Table 5.1: Average beam size estimation with and without focusing lenses.

#	w/o lens		with lens	
	X, µm	Y, µm	X, µm	Y, µm
1	2882	2313	930	783
2	2898	2295	918	777
3	2916	2307	915	778
4	2753	2342	931	775
5	2803	2464	935	773
6	2863	2487	923	768
7	2886	2450	937	777
Mean area, cm^2	0.15		0.02	
Standard deviation, cm^2	0.01		1.77.10^{-4}	

To estimate how concentrated a BB spectrum such as AM1.5G needs to be to get the same photon intensity in the NIR range and achieve the same $\Delta J_{\mathrm{SC,UC}}$, a concentration factor (C) was calculated. C converts the excitation spectra of SB photons (in W/cm^2) used for the experiment to an equivalent solar concentration of AM1.5G, and was calculated based on the **Equation 5.4** [286],[287].

$$\mathrm{C} = \frac{N_{\mathrm{exp}} * T_{\mathrm{cell}}\ (@980\ \mathrm{nm}) * A_{\mathrm{UC}}(@980\ \mathrm{nm})}{\int_{860\ \mathrm{nm}}^{1080\ \mathrm{nm}} N_{\mathrm{AM1.5G}} * T_{\mathrm{cell}} * A_{\mathrm{UC}}\ \mathrm{d}\lambda} \qquad \text{Equation (5.4)}$$

Here $N_{\mathrm{AM1.5G}}$ and N_{exp} are the photon flux densities of the AM1.5G spectrum and the spectrum used for the experiment. T_{cell} and A_{UC} are the transmittance of the cell and absorptance of the UC. As per our calculation, a concentration of 197 times the AM 1.5G sunlight (from 860 nm to 1080 nm at 70 mW/cm^2) would be necessary to achieve the same effect as 1 W/cm^2 of laser illumination at 980 nm.

At lowest intensity of laser i.e. 120 Suns, the $\Delta J_{\mathrm{SC,UC}}$ compared to the reference is about ~0.4 mA/cm^2. This enhancement scales up significantly to ~2.1 mA/cm^2 at a higher intensity of 880 suns. With introduction of focal lens, a maximum enhancement of ~21.8 mA/cm^2 was achieved at 7650 suns. Hence, the possibility to double the J_{SC} using UC would require the incident irradiation to be ~7650 suns, which is an unrealistic value for solar cells. Hence, the limitation of the application of UC in solar cells will be covered in the following section.

Table 5.2: Enhancement in J_{SC} due to UC with constant BB illumination of 70 mW/cm^2 and intensity variation of SB illumination optics

Optics condition	SB illumination power (mW)	SB illumination intensity (W/cm^2)	Solar concentration factor (suns)	$\Delta J_{\mathrm{SC,UC}}$ (mA/cm^2)
w/o lens	5	0.6 ± 0.08	120 ± 15	0.4 ± 0.35
	35	4.5 ± 0.56	880 ± 110	2.1 ± 0.13
with 100 cm lens	10	10.0 ± 0.19	2230 ± 37	4.0 ± 2.01
	35	38.8 ± 0.65	7650 ± 128	21.8 ± 1.59

The power coefficient (n_{UC}) describes how the intensity of UC luminescence (I_{UC}) depends on the excitation intensity (I_{exc}). The **Equation 5.5** describes the relationship between the two quantities and is calculated as $n_{UC} = slope + 1$ from **Figure 5.12 (b)**.

$$I_{UC} = (I_{exc})^{n_{UC}} \qquad \text{Equation (5.5)}$$

At low illumination intensity, the n_{UC} is equal to 1.7. However, at intensities higher than 4.5 W/cm^2, n_{UC} decreases to 1.3. This decrease in n_{UC} can origin from different loss mechanisms that exist in the PSC-UC device. The reflection loss of 4% can be expected for normal incidence from air on a surface with $n > 1$ in the PSC-only device [93]. The transmittance from the front side (ITO side) and the backside (glass side) of the bifacial PSC is ~50% at 980 nm (see **Figure 5.7 (b)**). With the PSC-UC device, additional reflection losses would exist between UC crystal-air and air-PSC interface in case the PSC and UC crystal are not optically coupled [93]. The index matching liquid used should help reduce this loss. In addition to reflection losses from the front side of the UC crystal, losses from the escape cones can also reduce the incident excitation by ~26% [93]. Though a back reflector was implemented, the reflected light is still lost from the front face [93]. Only 20% of the incident light is absorbed at 980 nm by the solar cell (see **Figure 5.13 (a)**).

Alongside the optical losses, the energy of the absorbed photons is also dissipated as heat. As demonstrated previously, increased temperature can result in reduction of V_{OC} and FF, decreasing the performance of the PSC-UC device (see **Figure 5.10 (a)**). This decrease in performance could occur due to an increase in temperature of the PSC as an effect of prolonged exposure to the intense SB illumination [234],[235]. However, for a highly concentrated source of illumination such as the laser, convection cooling might not be as effective [288]. Since an UC crystal is used at the back side of the solar cell, active cooling is also not possible. The UC crystal has properties of glass, a bad thermal conductor. The thickness of the UC crystal implemented in this work is less than 1-1.7 mm. For UC crystal BaF_2:Yb^{3+}, Er^{3+}, this thickness ensures that the number of emitted photons is high (see **Figure 5.2 (a)**). Hence, there are possibilities to implement newer UC materials with higher ϕ_{UC} and enhance the number of SB photons harvested. The PSC-UC device can successfully implement such materials to further boost J_{SC} and make the system better.

Contrary to our work, Chen et al. utilized $LiYF_4$:Yb^{3+}, Er^{3+} UC crystal on top of the PSC and achieved an excellent enhancement at 7−8 solar constants [81]. However, the implication of placing the UC crystal in the path of incident light can lead to additional parasitic absorption losses. UC crystals absorb incident solar spectrum in the range of 350-850 nm, which further reduces the amount of photons reaching the solar cell. Hence, the possibility of achieving high performance enhancement due to UC can definitely be a challenge. Additionally, achieving a light concentration of 8 solar constant using only a solar simulator can be quite difficult. Availability of details such as the type of laser used, filter implemented to achieve the stimulated sunlight (>800 nm), and beam area measurement can makes direct comparison of the $LiYF_4$:Yb^{3+},Er^{3+} and BaF_2:Yb^{3+},Er^{3+} more convenient.

5.7. Limitation of upconversion in photovoltaics

In order to quantify the enhancement in J_{SC} and critically analyze the application of UC in PSCs, External Quantum Efficiency (EQE) characterization of the PSC-only and PSC-UC device was performed. The EQE characterization can give additional verification of the enhancement observed in J_{SC} along with the information about which spectral range this enhancement comes from. **Figure 5.13 (b)** shows that for the NIR region, the EQE is almost four orders of magnitude lower than in the ultraviolet and visible range. The highest observed EQE is 2.75×10^{-2} % at 975 nm at an intensity of 4.2 W/cm^2. As discussed before, an intensity of ~7650 suns would be required to double the J_{SC} by using an UC crystal. Increasing the intensity of SB illumination to such high levels can result in unintentional heating of the PSC. The consequence of increased temperature resulted in decrease in the V_{OC} and FF of the PSC, decreasing the overall performance of the PSCs. Feasibility of effective cooling mechanism has been explored in the previous section.

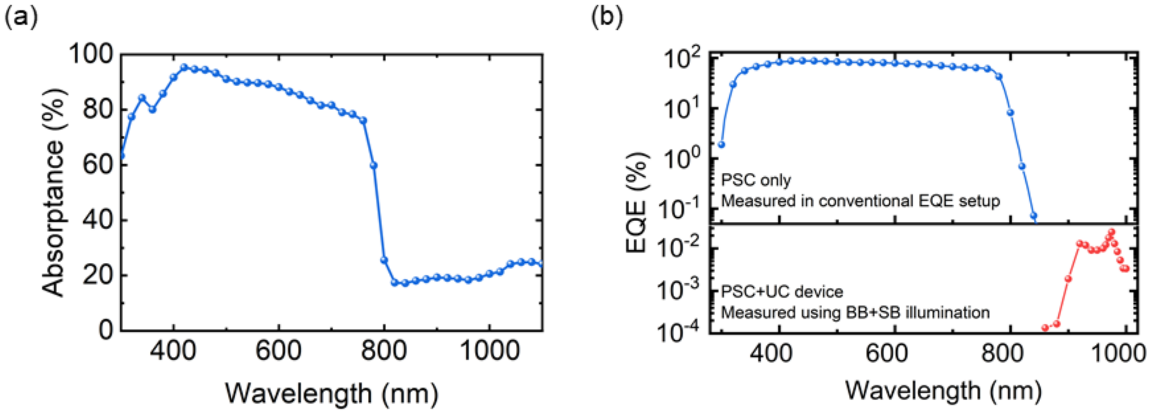

Figure 5.13: (a) Absorptance of perovskite solar cell (PSC) in ultraviolet-visible-near infrared (UV-VIS-NIR) range. The PSC absorbs ~25% (b) External Quantum Efficiency (EQE) of PSC, measured in a conventional EQE setup (blue), along with the EQE of PSC-UC device measured using BB+SB illumination (red). Adapted with permission from American Chemical Society.

This chapter is a proof of concept that harvesting SB photons by using UC single crystal can be implemented in PSCs. However, this system also has its limitations. Synthesis of UC crystals with materials exhibiting higher ϕ_{UC}, as discussed above can be explored. The host material implemented already demonstrates a high ϕ_{UC} of 10.0% for Er^{3+} (2 mol%) and Yb^{3+} (3 mol%) concentration of the dopant under 490 W/cm^2 of excitation at 976 nm. This is already has the highest ϕ_{UC} reported for inorganic UC materials [264]. The difficulty to achieve good UC under non-concentrated solar intensity is definitely a challenge [289]. Requirement of a lowest threshold intensity of 5×10^3 W/m^{-2} for 1400−1650 nm has been reported [290]. This is almost two order of magnitude higher than the intensity of AM1.5G at his wavelength range.

Fabrication of a device architecture that is more robust to the increment in temperature can better utilize the upconverted photons without a decrease in V_{OC} and FF. However, the absorber material implemented, $Cs_{0.18}FA_{0.82}PbI_3$ demonstrates intrinsic stability at room temperature and robustness at elevated temperature. However, the HTL used in this chapter is organic Spiro-OMeTAD, which is more vulnerable at high temperature. Spiro-OMeTAD uses dopants lithium bis(trifluoromethanesulfonyl) imide (Li-TFSi) and tBP (4-tert-butylpyridine). Li-TFSi is used to improved the hole conductivity and tBP is used to increase the homogeneity of Li-TFSi in the solution. Chances of the temperature reaching 85 °C during experiments mentioned in this chapter are high. At 85 °C, tBP is volatile and could result in decreased conductivity of Spiro-OMeTAD due to agglomeration of Li-TFSi [140], [150]. The reduced value of V_{OC} and FF observed in **Figure 5.9 (a)** and **Figure 5.10 (a)** could be a result of degraded Spiro-OMeTAD. Inorganic HTLs like NiO_X could be a suitable alternative to this issue. Such modification might contribute to higher J_{SC} with utilization of the SB photons, while still maintaining the other performance parameters of the solar cells.

5.8. Summary

This work reports on the utilization of SB photons in PSC by implementing an UC single crystal BaF_2:Yb^{3+}, Er^{3+}. It investigates the optical properties of the UC single crystal such as high absorption in NIR range and excellent ϕ_{UC} reported for inorganic MF_2 upconversion crystal. Minimal thickness of 1-1.7 mm is required for maximum utilization of SB photons. This thickness was determined based on the model developed by studying the optical properties of a stack of 0.23mm thick discs made of the same upconversion single crystal. A 1.7 mm thick UC crystal with reflector when placed at the backside of a PSC is capable of absorbing the SB photons, upconverting it and reflecting it back to the PSC. Excitation of the BB illumination (<850 nm) along with the SB illumination on a PSC- UC device exhibits an enhancement of ~0.4 mA/cm^2 in J_{SC} at lower intensity. Spectral dependence of $\Delta J_{SC,UC}$ measured from 860−1000 nm confirms that the observed enhancement in J_{SC} is indeed due to UC of the SB photons. The enhancement is negligible when either the SB illumination or the UC crystal is absent. Usage of high intensity laser as a light source results in higher $\Delta J_{SC,UC}$ alongside elevated temperature due to the heating effect of the high intensity laser used as a source for SB illumination. The effects of the elevated temperature is visible with the decrease in performance of the PSCs, mainly due to loss in V_{OC} and FF. With light soaking under constant BB illumination and cyclic SB illumination at 4.2 W/cm^2, the PSC-UC device showed an increase in J during the ON cycle of SB illumination without any decrease in V. However, in the PSC-only device, a decrease in V was observed as a consequence of thermalization due to intense laser illumination, addressing **Objective 4**.

Additionally, the interrelation of UC and illumination intensity with SB photons is explored. $\Delta J_{SC,UC}$ was not significant at lower intensity of 0.6 W/cm^2 whereas at an enhanced intensity of 4.5 W/cm^2, a prominent enhancement of ~2.09 mA/cm^2 was measured. As the intensity was increased, the $\Delta J_{SC,UC}$ showed a non-linear increment up to almost doubling of the J_{SC} at an incident intensity of 7650 suns. However, the possibility to double the J_{SC} by implementing concentrated light can be interesting, such high intensities are not practical for PV application. Developing absorber materials that can sustain higher temperature or implementing inorganic charge transport layers that are more robust at higher operational temperatures can make the device architecture more suitable for such an application. Growing single crystals with larger diameter and higher ϕ_{UC} can help push this technology further. These limitations leave us with some possibilities for exploration of the most efficient way to utilize UC in PV. From using nanophotonic structures [292], plasmonics [293], concentrated light [94], etc. the options endless. While spectral converters alone may not revolutionize the PCE of the ingle junction solar cells, their integration into a smart tandem and photon management architectures (like light-trapping, back-side UC, or front-side DC coatings) offers a realistic pathway to surpass 30–35% efficiencies in the perovskite-silicon TSCs in the coming years.

6. Outdoor setup for perovskite-based solar cells

In this study, the feasibility of operating perovskite–silicon tandem solar cells (TSCs) under outdoor conditions is investigated. A robust encapsulation strategy is developed to mitigate the influence of extrinsic environmental stressors, such as moisture and oxygen, on device stability. By effectively isolating these extrinsic factors, the impact of diurnal stressors, including varying temperature, varying solar irradiance, and angular distribution of incident irradiance on the performance and long-term stability of the tandem devices is assessed. Given the two-terminal configuration of the TSCs, these time dependent stressors can induce imbalances in current generation between the subcells, thereby affecting overall device performance and possibly accelerating degradation. To evaluate systematically these effects, a custom-designed outdoor measurement setup is constructed, incorporating essential sensors and instrumentation to monitor the encapsulated tandem solar cells under real-world environmental conditions. During first measurement conducted in the mild spring season, the encapsulated perovskite-silicon tandem devices exhibit a significant performance loss, with the performance dropping below 80% of the initial value after approximately 240 hours. This degradation was irreversible, indicating severe fatigue behavior. Post degradation analyses revealed that the performance loss originated from the perovskite top cell. Spectrally resolved characterization indicated spatial inhomogeneity in the perovskite layer attributed to photoinduced phase segregation, revealing insights into the ongoing processes on a device level as a response to the diurnal stress factors.

This chapter is based on an unpublished work by Roja Singh (*R.S.*), Lingyi Fang, Mark Schneider and Ulrich W. Paetzold (*U.W.P.*).

R.S. and *U.W.P.* conceptualized the project. *R.S.* developed the encapsulation recipe for perovskite single junction and perovskite-silicon tandem solar cells. *R.S.* designed the outdoor setup, implemented and tested it. The investigation, data analysis and data interpretation were done by *R.S.*

6.1. Introduction

Outdoor measurements are critical for accurately assessing the real-world performance and long-term stability of perovskite-silicon tandem solar cells (TSCs). Perovskite-silicon TSCs are emerging as a leading candidate for the next-generation photovoltaics due to their high power conversion efficiencies (PCEs) exceeding 30% under the standard test conditions (STCs) [4]. Laboratory measurements, while essential for benchmarking, often fail to replicate the diurnal environmental factors such as temperature variations, input irradiance variation and angular distribution of incident irradiance , all of which can significantly affect the performance of the TSCs [24],[294]. Such stress factors will be referred to as the diurnal stress factors. Alongside the extrinsic stress factors, such as oxygen and humidity, (which have been discussed in **Chapter 2**) and the diurnal stress factors, the outdoor conditions also have additional issues like soiling [295],[296]. Hence, outdoor testing allows for a more comprehensive understanding of the device behavior under the actual operating conditions with different stress factors playing a role, complicating the identification of the degradation pathways [297]. Hence, developing robust energy yield models can beneficial for understanding degradation dynamics of photovoltaic (PV) systems in outdoor conditions. However, such data are indispensable for optimization of stable devices for the outdoors [298], design improvements for encapsulation [299] and thermal management strategies [300]. Without outdoor testing, the scalability and bankability of perovskite-silicon tandem technology remain uncertain, especially given the known instability challenges of hybrid perovskite materials. In the following section, we look into the variations in the outdoor conditions and their effect on the perovskite-based solar cells.

Humidity

Humidity is one of the most detrimental environmental stressors for perovskite solar cells (PSCs) due to the hygroscopic nature of many perovskite precursors and the presence of organic cations. Water molecules can infiltrate the perovskite layer through micro-defects in encapsulation, initiating a hydrolysis reaction that leads to the formation of lead iodide (PbI_2) and the release of volatile species like hydroiodic acid (HI) and methylamine (CH_3NH_2) [173]. This degradation is especially pronounced in perovskites containing methyl ammonium (MA^+), though even more stable mixed-cation systems implementing formamidinium (FA^+) and cesium (Cs^+) based systems remain susceptible at high relative humidity (RH > 65%) or under cycling between dry and humid states [170]. In TSCs, moisture ingress can also degrade the charge transport layers (CTLs), compromising interfacial quality and charge extraction efficiency. Furthermore, synergistic effects of humidity and light (photoinduced degradation) exacerbate this process by enhancing ion mobility and defect formation [171], [172]. Long-term outdoor exposure studies consistently show that insufficient encapsulation or barrier layer design leads to rapid performance loss in humid environments [301].

Oxygen

Oxygen ingress is a critical degradation pathway in perovskite-silicon tandem solar cells, particularly when encapsulation is imperfect or insufficient. Oxygen typically diffuses very slowly, but even low levels can initiate degradation if humidity and light are also present. Once oxygen comes in contact with the perovskite layer, it initiates oxidative degradation, particularly under illumination. Light in presence of oxygen generates reactive oxygen species called superoxide (O_2^-) [158]. O_2^- attack organic cations like methyl ammonium (MA^+) or formamidinium (FA^+) in the perovskite leading to breakdown into PbI_2 and volatile compounds such as CH_3NH_2 and HI [302]. In TSCs, the top perovskite subcell degrades first, acting as the oxygen-sensitive layer. Eventually, failure of the entire tandem architecture occurs, even if the silicon subcell is intact.

Temperature variations

Perovskite materials are thermally sensitive and temperature variations in outdoor environments can induce mechanical and chemical degradation pathways in the TSCs [300], [303]. Thermal expansion mismatch between the perovskite, transport layers, and silicon subcell can result in interfacial delamination, cracking, and morphological changes in the perovskite layer [230]. Additionally, elevated temperatures (> 60 °C) accelerate ion migration in $MAPbI_3$ and mixed-cation variants[304]. This ion migration can lead to phase segregation, hysteresis in current density-voltage (*J*-*V*) characteristics and degradation of the interfaces with the CTLs[226]. Repeated diurnal heating and cooling cycles can also cause irreversible changes in device performance[26]. The thermal stress accumulates in the material and affects the nighttime recovery, resulting in fatigue behavior[305]. The temperature during the night is reported to have a significant role in recovery dynamics of the perovskite material[26]. Unlike silicon, whose temperature coefficients are well understood and managed [306], the thermal behavior of perovskites remains a major reliability bottleneck in tandem architectures.

Input irradiance variation

The spectral distribution of sunlight shifts throughout the day and across seasons, affecting the current-matching condition essential for optimal performance in monolithic two-terminal (2T) perovskite-silicon tandem solar cells [298]. Perovskite top cells typically have a bandgap between 1.65- 1.75 eV and absorb primarily in the ultraviolet-visible range (UV-VIS), while the silicon bottom cell harvests infrared (IR) photons [307]. Under standard AM1.5G illumination, this spectral division is ideal; however, real-world spectral variations, especially due to cloud cover, atmospheric scattering, or latitude, alter the photon flux in the active range of each subcell [308]. If the current generated by the top and bottom cells becomes mismatched, the tandem system operates sub-optimally, with the overall photocurrent limited by the lower of the two subcells [309]. Moreover, spectral imbalance can cause underutilization of either subcell, inducing long-term stress that accelerates degradation, particularly at interconnecting recombination junctions [310]. Understanding and mitigating the impact of spectral variation is thus essential for accurately predicting energy yield in diverse climates and over the seasons.

Angular distribution of incident irradiance

The changing position of the sun and panel orientation alters the optical path and absorption profile within the TSC, changing the angular variation in solar irradiance and influencing photon management and device performance [311]. Perovskite layers, which often have a high refractive index, are particularly sensitive to incident angle due to increased reflectance losses at oblique angles [312]. These optical losses are compounded by parasitic absorption in the transport layers and non-ideal anti-reflection coatings [313]. In monolithic tandems, the angular sensitivity of the top perovskite cell affects not only its own absorption but also the spectral profile reaching the silicon bottom cell [314]. As a result, angular distribution of incident irradiance induces a dynamic current mismatch, which can reduce the overall energy yield [315]. Moreover, repeated exposure to UV-rich, off-angle irradiation may promote localized heating and photochemical degradation, especially in the encapsulation [157].

Soiling

Soiling is particularly detrimental to perovskite-silicon TSCs due to their spectral sensitivity and dependence to current matching. Unlike traditional silicon cells, the spectral imbalance caused by selective absorption due to soiling makes TSCs more vulnerable [316]. Soiling reduces the incident light intensity reaching the active layers by scattering or absorbing part of the solar spectrum. In TSCs, this is particularly critical due to the layered bandgap architecture [316]. Perovskite top cell absorbs the high-energy photons (400-750 nm range) and the silicon bottom cell absorbs the lower-energy photons (>750 nm) [298]. Soiling reduces the total available light and alters the spectral distribution; often reducing UV and VIS light more significantly than IR due to wavelength-dependent scattering and absorption. This disproportionately affects the perovskite layer, which is more reliant on high-energy photons, leading to imbalance in current generation between the two subcells [317]. Thus, mitigation strategies such as anti-soiling coatings, frequent cleaning and optimized optical designs are critical to maintaining performance and long-term reliability of perovskite-silicon TSCs.

Initial work reveal that the degradation of PSCs in outdoor conditions emerges from the temperature cycles. The temperature coefficient of -0.17 % /K signifies loss in performance emphasizing sensitivity to outdoor heating [318]. Performance loss due to elevated temperature mainly attributed to loss in V_{OC} (-0.12 % /K) [318]. Temperature is the dominant stressor in outdoor condition, more so than irradiance, but temperature coefficient of perovskite PV more robust as compared to the other PV technologies. Crystalline silicon solar cells have a temperature coefficient of -0.08%/K [306].

Investigations into the outdoor operating temperatures and their effect on current matching of subcells of 2T perovskite/silicon TSCs reveal that contrasting temperature dependencies of the subcell bandgaps influence real-world efficiency and guide optimal perovskite bandgap selection for field deployment. Unlike silicon, whose bandgap narrows with rising temperature, perovskite bandgaps widen (blue-shift) as temperature increases [298]. This mismatch shifts the cell away from the current-matching optimum crucial for 2T TSCs operation. Current mismatch reduces tandem current density (J_{SC}) when operating temperatures significantly exceed STC temperature of 25 °C baseline [298]. Using temperature-dependent modeling, the total tandem current and efficiency as functions of perovskite bandgap and temperature were mapped. For realistic outdoor operation above ~55 °C, the ideal perovskite bandgap at 25 °C should be < 1.68 eV, lower than previously assumed optimal values of ~1.73 eV [298]. Narrower bandgaps with bromide-lean compositions are thus preferable as they offer both better phase stability and optimized field performance [298]. Design and test of 2T tandems must integrate temperature adjusted bandgap optimization, not rely solely on STC values [298]. Temperature sensitivity introduces a significant variable beyond voltage drops, current matching must be evaluated under realistic thermal stress. Findings support industry trends toward bromide-lean perovskites (1.65–1.68 eV) for stable, high-efficiency field performance.

Another study linking outdoor cycling measurement and empirical modeling to assess metastability driven energy losses in PSCs revealed that light soaking recovery, driven by temperature and irradiance, leads to ~5 % annual yield losses in PSCs and ~3 % in TSCs, critical for real-world deployment [25]. Their validated model offers a basis for more accurate reliability and assessments of perovskite PV technologies. PSCs suffer a performance dip overnight that recovers when illuminated post sunrise via a light soaking process lasting from a few hours up to a full solar day. The warmer the cell and the more sunlight, the faster and stronger the recovery. This behavior highlights the hysteresis-like, history-dependent response driven by ion migration and charge trapping and release in the perovskite structure [25].

While most lab stability tests use constant illumination, which fails to reproduce the metastable behaviors observed with natural day-night cycles outdoors, Khenkin *et al*. addressed a crucial gap and compared outdoor stability with indoor stability [24]. Devices exhibited dramatically different degradation behaviors under light cycling versus constant illumination. Some PSCs degraded faster when cycled, even though dark recovery was expected to mitigate the loss. Ion migration and trap dynamics in perovskites induce slow processes (lasting up to hours) aligned with day-night cycles [24]. These processes cause performance shifts, sometimes reversible after dark storage, complicating outdoor degradation tracking. Indoor light cycling responses correlated with outdoor behavior, supporting indoor cycling tests as better alternatives than constant light protocols [24]. Outdoor data over seasons showed patterns of degradation and recovery corresponding to indoor cycling phases. PSCs displayed strong seasonal variation, summer enhancements vs. winter decrement, even when environmental stressors were milder [24]. Minimum night temperatures affected the effects of the metastable states, affecting measured lifetimes [24]. Seasonality and environmental variations make PSC outdoor stability non-trivial to assess.

To date, most outdoor PSC studies span between weeks to months. Remec *et al*. report four years (~2,000 days) of continuous outdoor maximum power point (MPP) tracking under natural diurnal and seasonal cycles, making it one of the longest PSC outdoor datasets to date [295]. PSCs show pronounced day-night performance variation. Efficiency drops overnight, and then recovers during daylight via light soaking [295]. Recovery kinetics range from hours to full days. Metastable performance variations saturate differently across devices, depending on architecture and degradation state, creating complex diurnal trends [295]. In summer, many PSCs exhibited higher normalized performance compared to winter, even with higher temperatures, due to longer daylight and spectral shifts enhancing perovskite absorption [295]. Seasonal amplitude varied significantly across architectures. Some showed strong swings, others were more stable, highlighting material/interface dependencies. Ion migration and defect-trap interactions drive metastable and seasonal behaviors with effects accumulation over weeks/months [295]. Recovery and degradation patterns depend on both thermal stress (daytime heat driving irreversible changes) and dark relaxation, leading to net seasonal performance shifts. Seasonality and metastability are inseparable from the long-term performance of these perovskite-based PV systems [295].

Seasonal peaks and troughs are driven by light and thermal cycles with a strong dependence of cycle timing on device chemistry. Daytime peak temperatures significantly accelerate irreversible, long-term degradation [26]. Elevated daytime temperatures damage interfaces and promote ion migration, leading to long-term PCE loss [26]. Nighttime cooling triggers metastable relaxation, causing reversible declines in performance the next morning [26]. Light cycling tests confirm these dark recovery processes seen in the field [26]. Seasonal variation drastically alters outdoor stability metrics, highlighting that lab tests without seasonal context are misleading. PSCs degrade faster during hot summers due to higher daytime temperatures [26]. Cooler seasons see slower degradation, but nighttime cold affects transient recovery.

Standard outdoor degradation is driven by ion migration under forward bias during the day and dark relaxation at night. Reproducing this indoors without light would enable cost-effective, large-scale module testing. Forward bias aging induced ion migration leading to charge transport blockage, development of macroscopic defects, and a deteriorated response to brief light soaking [248]. Higher bias caused faster degradation, with clear structural and electronic changes [248]. During post-bias rest period, partial recovery in charge transport was observed [248]. However, increased non-radiative recombination persisted, implying that ionic redistribution left a lasting impact [248]. Observed dynamics closely mimic PSC behavior during 20-month outdoor testing in Berlin. Spring-summer periods with higher light and temperature correspond to the forward-bias aging mode. Fall-winter periods map to the post-bias rest/recovery phase. This alignment suggests outdoor ion migration can be replicated in the dark through electrical bias cycling [248]. Ion migration under forward bias leads to defect clustering, charge extraction hindrance, and residual impacts even after dark recovery. Dark storage mitigates some ion-induced stress but leaves behind enhanced recombination zones due to redistributed ions [248].

Hence, studying PSCs and perovskite-based TSCs under the diurnal stress factors can broaden our knowledge about the performance of these PV technologies under real world condition. Access to an outdoor setup can narrow the gap between laboratory expertise and commercial deployment. Unfortunately, developing such multi-channel measurement setup and making them weatherproof does not come at a low cost. The setup also needs ample space without obstructions. Because of these underlying reasons, not many groups have access to an outdoor setup. In this chapter, we develop some primary aspects, which are essential towards making outdoor measurements for perovskite-based solar cells a success. From procedure for development of a robust encapsulation, to requirements of the setup and finally first set of measurements and speculations of the prospective reason behind the trend observed in dataset is presented.

6.2. Robust encapsulation for perovskite-based solar cells

The first step in this direction is development of a robust encapsulation technique to protect the PSCs and TSCs from degradation induced due to the extrinsic stress factors.

6.2.1. Encapsulation of single junction perovskite solar cells

The PSCs are fabricated on the standard substrate layout of 30×30 mm^2 as shown in **Figure 6.1 (a)**. The green strips are ITO and yellow strips are the metal contacts. The layout for encapsulation is depicted in **Figure 6.1 (b)**. The red lines are laser-scribed lines. This layout provides ITO even below the metal contact preventing peeling of metal contact during stress test and increasing reliability.

The single junction PSCs were fabricated with similar techniques as reported in **Chapter 3**. The swiping of perovskite (pink) has to be done on all four sides before evaporating the metal contacts. The contacting of the individual pixel is done using wires and silver paste as shown in **Figure 6.1 (c)**. Thin wires (0.25 mm^2) are used to contact the individual pixels. The wires are fixed onto the contacts using silver paste depicted with green dots in the schematic. Upon application of the silver paste and wire, the PSC has to be annealed at 85 ºC for 15 min on a hotplate to evaporate the solvent in the silver paste. Once the substrates have cooled down, further encapsulation steps are executed. Only six pixels in the center of the substrates can be used since Polyisobutylene (PIB), as shown in **Figure 6.1 (d)**, will cover the pixels at the edge. The metal contact below the PIB has to be peeled off using a scotch tape before encapsulation to ensure good adhesion of the PIB with the substrate and the cover glass. The cover glass used for encapsulation is of the same dimension as the PSC. The lamination is performed in two steps in a laminator preheated to 85 °C. In the first "vacuum step“, the pressure in both chambers of the laminator is reduced to 0.01 bar. A silicone membrane separates the chambers of the laminator. In the second "pressure step", the silicone membrane of the laminator is filled with nitrogen. The top glass is pressed onto the bottom substrate and the encapsulants adheres the substrate to the top glass.

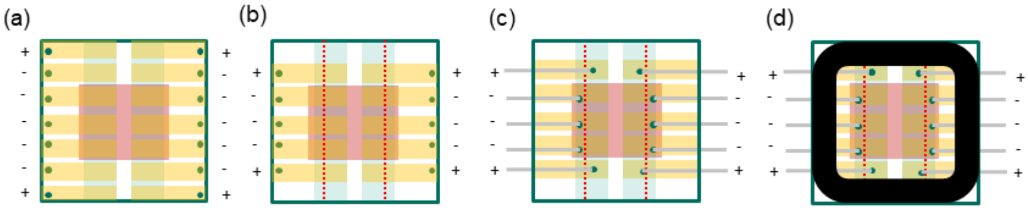

Figure 6.1: Schematic of (a) standard layout of substrates (b) layout for encapsulation (c) wired contacting scheme for encapsulation (d) edge encapsulation using Polyisobutylene (PIB) of single junction perovskite solar cells.

Depending on the edge encapsulant (used on the edges) and area encapsulant (used over the active area), encapsulation of single junction PSCs can be categorized as:

Edge encapsulation: 5 mm thick PIB strips are placed on all four edges of the PSC. It is preferable to have PIB both above and below the wire. This prevents moisture and oxygen from seeping into the encapsulation between the wires and the top glass or substrates. Schematic of edge encapsulation is depicted in **Figure 6.2 (a)**. While this type of encapsulation might be the most easy to implement, the active area of the PSCs, being uncovered with any encapsulant, can be exposed to humidity and oxygen when the edge sealant if compromised.

Edge encapsulation with area encapsulant: Due to the sensitivity of the perovskite layer to humidity and oxygen, a Thermoplastic Polyolefin (TPO) sheet of dimension of 20 × 20 mm^2 is placed above the active area of the device. The TPO melts during lamination and hence a smaller dimension is used so that the TPO does not ooze out of the encapsulation. Schematic of edge encapsulation with TPO is depicted in **Figure 6.2 (b)**. This type of encapsulation provides decent protection against humidity and oxygen.

Blanket encapsulation: For blanket encapsulation, instead of TPO, PIB is used above the active area too. Schematic of blanket encapsulation is depicted in **Figure 6.2 (c)**. Since opaque single junction PSCs are bottom illuminated, having PIB above active area does not disrupt the working of the PSCs. However, visible changes that the device undergoes might only be noticeable from the bottom glass side.

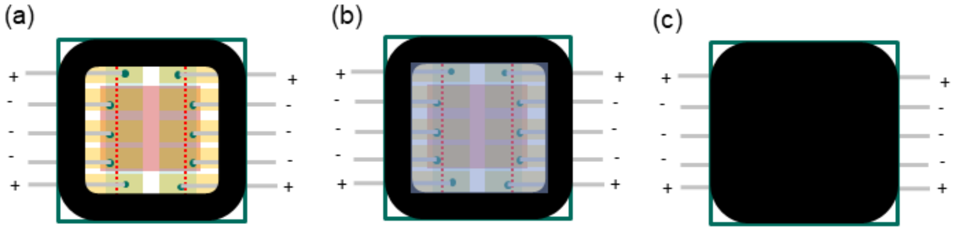

Figure 6.2: Schematic of encapsulation of perovskite solar cell using (a) edge encapsulation using PIB (b) edge encapsulation with area encapsulation using PIB and TPO as area sealant (c) blanket encapsulation using PIB.

In order to understand which encapsulation technique provides more superior protection against humidity and oxygen, a batch of single junction PSCs were exposed to high humidity testing at 85 %RH in a climatic chamber. The devices were aged for a period of 1000 h, the samples were removed from the climatic chamber and *J-V* characterization was performed intermittently. **Figure 6.3 (a)** shows that PIB only devices fail the test by dropping below T_{90} in only 50 h and the combination of PIB and TPO lasted for 300 h. PIB used as a blanket encapsulation provided a far superior protection which maintained over 100% of the performance even after 1000 h of testing.

The water vapor transmission rate (WVTR) of PIB is ~ 1 × 10^{-3} g/(m^2.d) [319] and that of TPO is ~3 g/(m^2.d) [320]. Hence, it gives a far superior protection against humidity as depicted in **Figure 6.3 (a**). **Figure 6.3 (b)** shows that there is very less decrease in voltage when the devices fail the high humidity test. Mostly current density of the devices decrease. **Chapter 2** discusses the degradation mechanism under humidity resulting in formation of lead iodide (PbI_2) [173], a byproduct of degradation, which prevents the perovskite absorber from generating as much photocurrent as before the degradation. Though humidity induced degradation is reported to be reversible upon reheating[169], we did not observe complete recovery of the performance loss even after heating the samples post the high humidity testing. A possible reason for this might be the devices were degraded far beyond repairs and back conversion of PbI_2 to perovskite was not successful. For devices implementing PIB as blanket encapsulation, slight improvement in performance is observed during the period of high humidity testing. During the test, the devices are aged in high humidity but in dark condition. Spontaneous enhancement has been previously reported for PSCs during which, the devices exhibit enhancement in PCE post fabrication, while being stored in the dark for a few days [321]. The reason for such enhancement in performance has been attributed to trap-states passivation. Given the robustness of blanket encapsulation, the devices are well protected against high humidity and the benefits of spontaneous enhancement become noticeable.

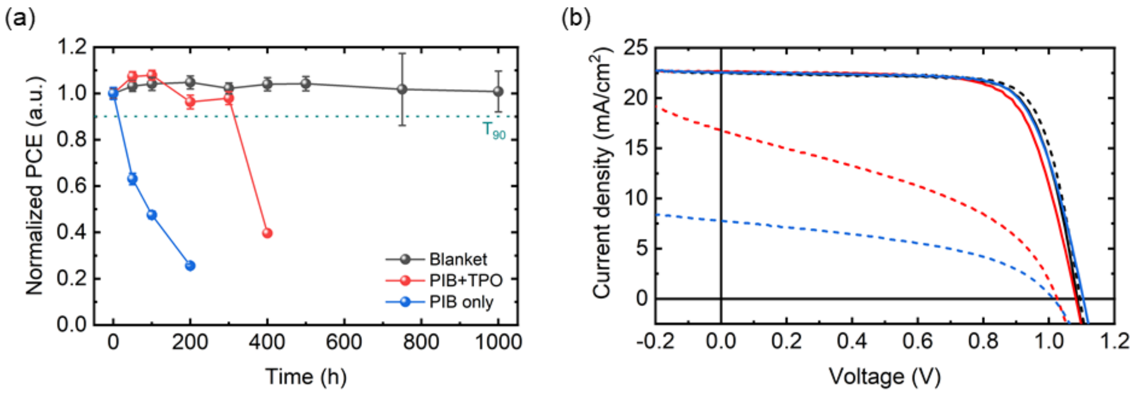

Figure 6.3: (a) Comparison of different encapsulation schemes aged at 85%RH. (b) *J-V* characterization made before (solid line) and after (dotted line) the test at 85%RH.

After having determined the best encapsulation technique for single junction PSC, we look into the distinctions between single junction PSCs and perovskite-silicon TSCs. The single junction PSCs are bottom illuminated. Hence, blanket encapsulation is applicable to this device architecture. However, perovskite-silicon TSCs are top illuminated due to the opaque nature of the silicon bottom cell. Hence, the next best option of edge encapsulation with area encapsulant is optimized for perovskite-silicon TSCs.

6.2.2. Encapsulation of perovskite-silicon tandem solar cells

Optimization of the encapsulation for perovskite-silicon TSCs is more complicated than for the single junction PSCs because of the following reasons. Silicon has a different temperature coefficient than the perovskite layer implemented in the top cell. The silicon substrate is also more brittle than the glass substrate and prone to breaking especially in high vacuum conditions inside the laminator. A schematic of the encapsulation technique used for perovskite-silicon TSC is depicted in **Figure 6.4**. Instead of using thin wires as in the case of single junction PSCs, a solar ribbon with conductive adhesive is used. This prevents the complications that arise with the solvents of the silver paste and the additional annealing step before encapsulation.

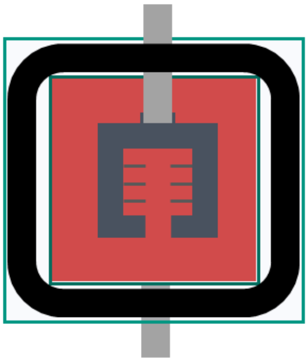

Figure 6.4: Schematic of encapsulation for perovskite-silicon tandem solar cell.

With different layers and interfaces existing in each subcell, the effect of high temperature and pressure during encapsulation on the performance of the perovskite-silicon TSCs needs to be quantified. The details of the device architecture and fabrication technique has already been covered in **Chapter 3**. The performance parameters before (pre) and after (post) encapsulation is compared in **Figure 6.5**. The average open-circuit voltage (V_{OC}) and the short-circuit current density (J_{SC}) of the devices do not change drastically post lamination. However, after encapsulation the variance of the fill factor (FF) increases. The effect of annealing under high temperature and pressure during encapsulation could impact the series (R_s) and shunt resistance (R_{sh}) of the TSCs resulting in such variation in FF and PCE.

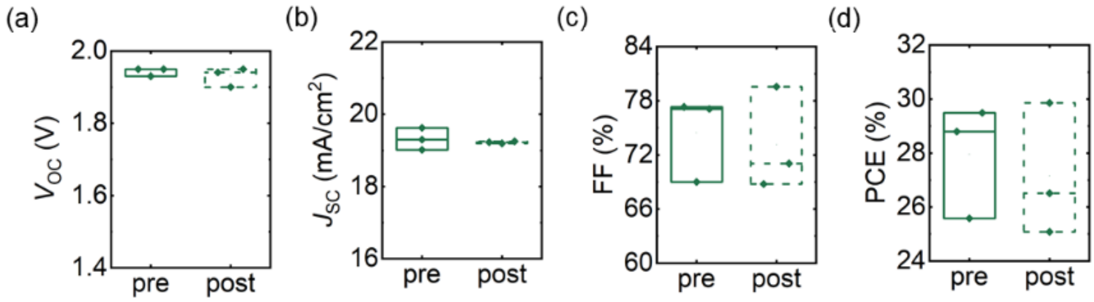

Figure 6.5: Performance parameters (a) V_{OC} (b) J_{SC} (c) FF (d) PCE of perovskite-silicon tandem solar cells before (pre) and after (post) encapsulation.

With the intention of testing if the modifications made for the encapsulation of the TSCs also retains the robustness under the high humidity condition, humidity tests were performed at 65%RH for encapsulated perovskite-silicon TSCs. As per the International Summit on Organic and hybrid perovskite Solar cell (ISOS) protocols, the testing protocols for perovskite implementing methyl ammonium cation (MA^+) has been relaxed to a lower humidity levels of 65 %RH [189]. For a testing period of 1000 h, the TSCs exhibited no decrease in performance (see **Figure 6.6**), confirming that modifications made for TSCs work well even in high humidity conditions. Slight fluctuations observed can be attributed to experimental errors during measurement.

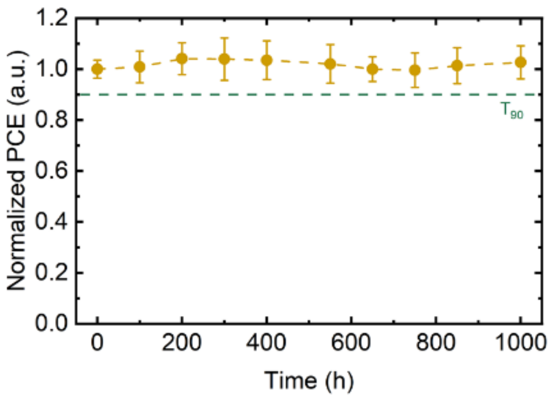

Figure 6.6: Encapsulated perovskite-silicon tandem solar cells (TSC) aged at 65%RH.

The results above confirms the applicability of the encapsulation technique tested for TSCs for outdoor applications. One possibility why similar encapsulation technique failed for PSCs as observed in **Figure 6.3 (a)** might be the nature and number of wires used for PSCs. The wires used in single junction PSCs encapsulation were round and one substrate implemented ten wires. The point where each of these wires come out of the encapsulation could possibly be a place for moisture ingress and potential compromise to the encapsulation. The wires implemented in TSC encapsulation were flat and each substrate required only two wires. This severely decreased the points of humidity ingress in the packaging and made the encapsulation tighter and more robust.

6.3. Requirements of an outdoor setup

With the development of the encapsulated perovskite-silicon TSCs, in order to have stable measurements in the outdoor condition, the features and specifications of the outdoor setup are also important. Bias induced damages can accelerate degradation in the PSCs [322]. Hence, the hardware and algorithm implemented should work in the range suitable for the PSCs and perovskite-based TSCs as not to cause additional bias-induced degradation. As discussed previously, other intrinsic stress factors such as light and temperature vary depending on the day and night time (referred to as diurnal stress factor), and hence cannot be controlled. In the following section, we look into the requirements of an outdoor setup, the hardware and software implemented alongside the working of the entire setup.

The outdoor setup continuously measures solar cell performance by either tracking the solar cell at MPP or measuring *J-V* characteristics in intervals. Among the two methods, MPP tracking is the best option as it allows measurement of the stabilized power of a solar cell [189]. Environmental parameters such as temperature and irradiance are important input parameters for understanding the response of the solar cell to the environmental factors. Hence, these parameters have to be monitored continuously. Obstructions such as shadow, leaves and droppings might disrupt the maximum power extraction/continuous measurement of the solar cells, hence monitoring the solar cells over time is can also make interpretation of the measurement data simpler. The main objective of such measurement setup is to generate maximum power from the solar cell during the interval of the day and store the power in an inverter. This objective is fulfilled by an integration between the hardware components and software to achieve optimized system performance. A picture of the outdoor setup installed at Karlsruhe Institute of Technology as shown in **Figure 6.7**. First, we look into the hardware components, their roles and integration. Additional images is available in **Appendix**.

Figure 6.7: Outdoor setup installed in Solar Park, Campus North, Karlsruhe Institute of Technology for measuring perovskite-based solar cells.

6.3.1. Components and Specifications

Irradiation sensor

The irradiance sensor is designed for the real-time measurement of solar irradiance. Irradiance sensor is made of high quality crystalline silicon cell of a known illumination area. The current that the irradiance sensor generates is a known quantity, which can be used to calibrate the input irradiance. Hence, it works as the reference cell and converts incident sunlight into a small direct current (DC) current that is proportional to the irradiance in mW/cm². This signal is then conditioned and output in a specific sensitivity range compatible with the data acquisition system. When connected to a data acquisition system, its analog output is read, digitized and logged by a data logger.

Temperature sensor

The PT100 is a type of resistance temperature detector widely used for precise temperature measurement. It operates on the principle that the electrical resistance of pure platinum increases linearly with temperature. The "100" in PT100 denotes a resistance of 100 Ω at 0 °C [323]. As the temperature rises, the resistance of the platinum element increases in a predictable and repeatable manner, typically at a rate of approximately 0.385 ohms/°C for standard Class B sensors [323]. The PT100 sensor is connected behind the solar cell in a 2-wire configuration using a thermal adhesive. The resistance is measured by passing a small current through the element and measuring the resulting voltage drop, from which the temperature is calculated using standardized resistance-temperature conversion tables (such as IEC 60751). The PT100 has a wide temperature range suitable for operation in the field of PV. The converted value is used to correlate PV performance with ambient temperature changes. Additional signal conditioning on the analog signal is necessary before the data is converted to a digital format.

Analog to digital convertor

Advantech ADAM-6017L is an 8-channel analog input module designed for data acquisition and process control applications. It interfaces with supervisory control systems and processors via serial or Ethernet communications and provides high-resolution, isolated analog input measurement. Each of the 8 analog input channels accepts either voltage or current signals, converting the analog signals into precise digital representations through a sigma-delta 16-bit Analog to Digital Convertor (ADC) [324]. The input range can also be configured. The ADC continuously scans input channels in sequence and applies onboard signal conditioning circuitry including filtering and isolation to minimize noise and interference. The isolated architecture prevents ground loops and allows the module to interface with sensors operating at different reference potentials. Data collected by the

ADAM-6017L can be accessed in real time through Modbus protocol commands via serial interfaces, allowing logging to data logger on request or control functions based on sensor inputs.

Switching power supply

A switching power supply is an electronic power converter that efficiently converts electrical power from one voltage level to another using high frequency switching components. The basic working principle involves rapidly switching the input voltage on and off and controlling the duty cycle to regulate the output voltage. This switching action creates a pulsating voltage, which is smoothed by inductors, capacitors and transformers to produce a stable DC output in suitable range [325]. Switching power supplies offer smaller size, lighter weight and better thermal performance compared to their counterparts. However, they require careful design to minimize electromagnetic interference due to their high-frequency operation [325]. The HDR-100-15 delivers a reliable and efficient output in a compact Deutsches Institut für Normung (DIN) -rail format. With full universal input, solid protections and safety compliance certifications, HDR-100-15 is a versatile choice for automated systems. The HDR-100-15 has an input range of 85-264 V_{AC} (AC is Alternating Current) and output range of 15 V_{DC} at 6.7 A. It provides DC power to other components in the setup. However, a DC-DC converter might be needed if the components require other voltage input (Raspberry Pi- 5V, ADAM-6017L module- 10 V_{DC}, signal conditioning circuit and other devices 12- 24V_{DC})

Processor

Raspberry Pi 4B is a powerful and low-cost single-board computer built on a single circuit board, integrating processor, storage and input/output interfaces. It collects, processes, and stores data (voltage or current signal). It runs on Raspberry Pi operating systems and has micro SD card slot for data storage. A set of 40 physical pins for the purpose of input/output allows digital communication with external devices. Connectivity via USB ports, Ethernet, Wi-Fi and Bluetooth are a possibility. The Pi 4B also supports accessories like camera modules, hardware attached on top and cases with active cooling. Its performance and connectivity makes it suitable for a wide range of applications. A 5 V/3 A power adapter with a USB-C connector provides power supply to this powerful processor. It runs Python scripts for data acquisition, data logging and remote data access. The Raspberry Pi 4B acts as the central data logger and communicates with ADAM-6017L via Modbus Transmission Control Protocol (TCP)/ Internet Protocol (IP) over Ethernet. TCP/IP is the foundational communication protocol suite for the internet and most modern networks [326]. It defines how data is packaged, addressed, transmitted, routed, and received across networks [326]. The Modbus TCP interface communicates over Ethernet using the Modbus TCP protocol, allowing easy integration with the Raspberry Pi. The Modbus TCP module also includes two channels of digital output for switching external devices or signaling.

6.3.1. Perturb and observe algorithm

Perturb and observe algorithm continuously checks if the tracking is taking place at MPP [327]. If not, it adjusts the tracking voltage such that the tracking is taking place at MPP. The basics of the perturb and observe algorithm is covered in **Chapter 3**. Modifications were introduced to make this algorithm more suited for MPP tracking under dynamic conditions like varying irradiance [328]. The new algorithm is called adaptive perturb and observe. The details of its working are available in **Appendix**. First dataset measured using adaptive perturb and observe is also presented.

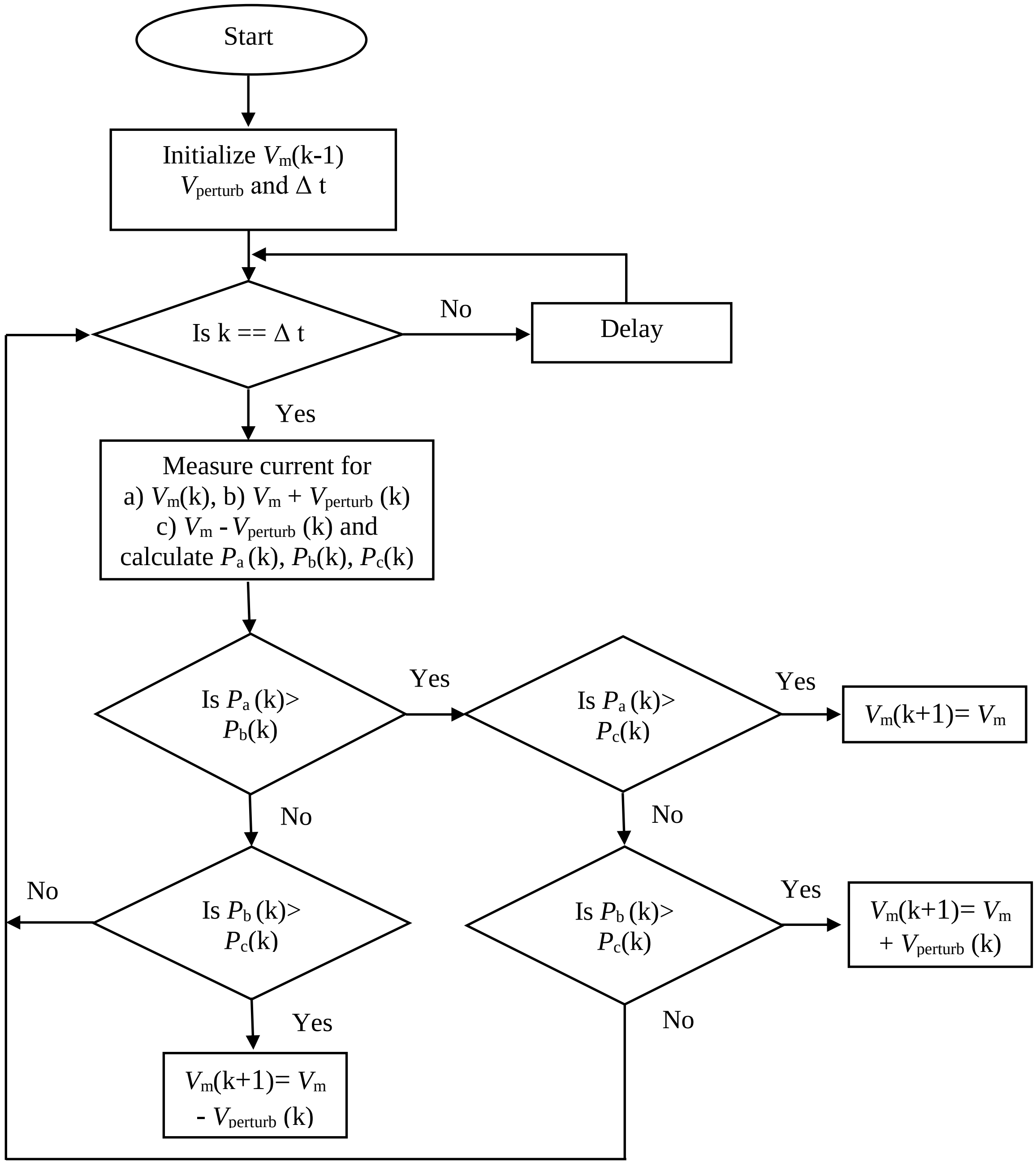

Figure 6.8: Flow chart depicting the working of perturb and observe algorithm

6.3.2. Working of the outdoor setup

This section explains the working flow of the outdoor setup. A block diagram depicting the working of an outdoor setup is shown in **Figure 6.9**.

Step 1: Power Up

The switching power supply converts AC mains ($220V_{AC}$ to $15\ V_{DC}$) and after additional DC-DC conversion powers the ADC, processor, temperature sensors and irradiance sensors. It also provides input for the solar cell.

Step 2: Signal Acquisition

The temperature sensors measures the ambient or module temperature and irradiance sensor measures the input irradiance. Solar cell output is measured using electronic load. All voltage and current analog signals are routed to the ADC.

Step 3: Data Communication

The ADC converts analog signals to digital and communicates values over Ethernet to the processor.

Step 4: Data Logging and Processing

The processor periodically queries the ADC using Modbus TCP/IP via Python scripts. The data is timestamped and stored in the SD card.

Step 5: Accessing data

Site-to-site connections using encryption is used to access and monitor the system remotely.

Step 6: Changing configurations

The parameters for the tracking of the solar cells and the system in general can be controlled via remote access over secure connections.

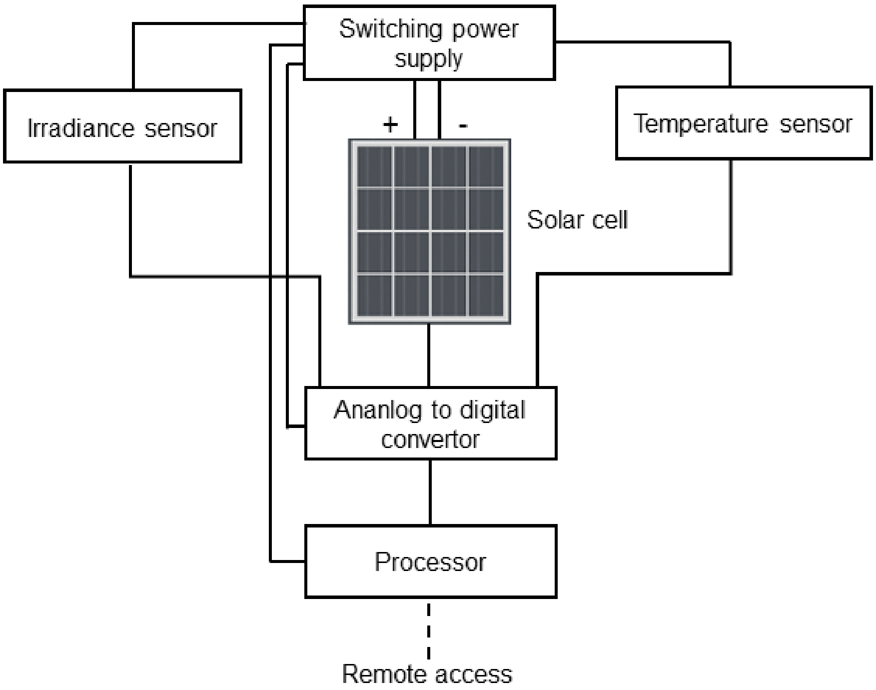

Figure 6.9: Block diagram depicting the working of an outdoor setup.

6.4. Assessing perovskite-silicon tandem solar cells under real-world condition

In order to study the performance and stability of the perovskite-silicon TSCs in outdoor conditions, the encapsulated TSCs were installed in the solar field and connected to the electrical setup described in the above section. This section assesses the relationship between diurnal stress factors like input irradiance variation spectra and temperature variations on the performance and stability of perovskite-silicon TSCs. The variations of the ambient temperature and its effect on the voltage at MPP (V_m) is an interesting observation considering most literatures report ambient temperature variations to be a more detrimental stress factor than input irradiance variation [26], [298]. Clear diurnal cycles of temperature, with nighttime as low as ~2 °C and daytime with highs of ~24 °C was observed as depicted in **Figure 6.10 (a)**. Variability in V_m observed on April 2 and April 9 show cooler profiles in temperature compared to other days. On these days, the TSC fails to reach the peak performance and generates < 1.5 V. However, the reason for lower voltage generation seems to be an effect of irradiance rather than temperature. The voltage generated on April 6, when the temperature ~12 °C, among one of the lowest recorded temperature for midday however, supports this observation, the voltage generated on this day was ~1.7 V since it was a clear and sunny day. On days when sunny condition is observed, especially around midday, a peak voltage of 1.7 V is generated. Sharp rise in V_m up to midday and fall thereafter is observed on most days (apart from April 2 and April 9). Our interpretation of this rise and fall is the average cell temperature. Post midday, the cell temperature increases and the voltage sees a sharp decrease. This behavior is due to the dependence of the V_{OC} on the temperature [283], [284]. However, on April 2 and April 9 the cloudy conditions begin before midday and the voltage lags below 1.5 V. However, the temperature in the range between 5 °C to 25 °C does not affect voltage drastically, suggesting that the device is reasonably tolerant to moderate variations in temperature. Effect of temperature variations are present but not dominant within this moderate temperature range. Voltage shows a clear diurnal profile, tightly coupled with daytime exposure and temperature variations exhibit typical spring-like weather.

Figure 6.10 (b) evaluates the influence of the incident solar irradiance on the photocurrent generation. Depending on the weather, the solar irradiance peaks up to 100 mW/cm². At STC condition, the input irradiance is fixed at 100 mW/cm^2 [58]. The irradiance follows a periodic daily cycle with clear diurnal patterns. This shows direct dependence of the photocurrent on solar irradiance and the J_m ranges up to 17 mA/cm². The device maintains this performance consistently under irradiance values near 100 mW/cm^2. The TSCs shows stable operation under consistent solar exposure, with performance variations closely tied to drops in irradiance. The power output shows a strong diurnal cycle, peaking during midday and dropping to zero at night. Clear periodicity is observed on sunny days with P_m reaching near the maximum of ~ 26 mW/cm². Performance disruptions are evident on cloudy days, aligning with previously noted dips in irradiance and photocurrent generated. Dark blue shaded regions represent cloudy days.

Sudden drops or irregularities are evident on cloudy days (April 5 and April 9) likely due to overcast conditions reducing irradiance. On these days, the generation of current density at MPP (J_m) is lower than on average sunny days. April 7 – April 9 shows three consecutive cloudy days, J_m fails to reach the peak value again on April 11, despite the day being clear. The shape of the peak on April 10 already shows a much sharper rise to peak intensity as compared to the rest of the days. From April 2 - April 9, the J_m follows the profile of the input irradiance. However, on the last two days J_m peaks with a delay, affecting the generation of overall power density at MPP (P_m) as seen in **Figure 6.11 (a)**. The reason for such peculiar shape can be attributed to fatigue behavior.

Fatigue behavior in perovskite solar cells is the gradual performance degradation that occurs when the device is subjected to repeated or prolonged cycles with electrical, thermal, or light stress [236], [241]. Unlike immediate device failure, fatigue is a time-dependent and reversible (in shorter intervals) or irreversible (on longer periods) process that affects long-term stability and durability. Fatigue behavior reflects in this work as the interplay between photoinduced degradation leading to trap formation on sunny days followed by reduced solar irradiance with the inability to passivate the traps on cloudy days [245]. Even on the next diurnal cycle of sunny day, the device cannot recover in performance.

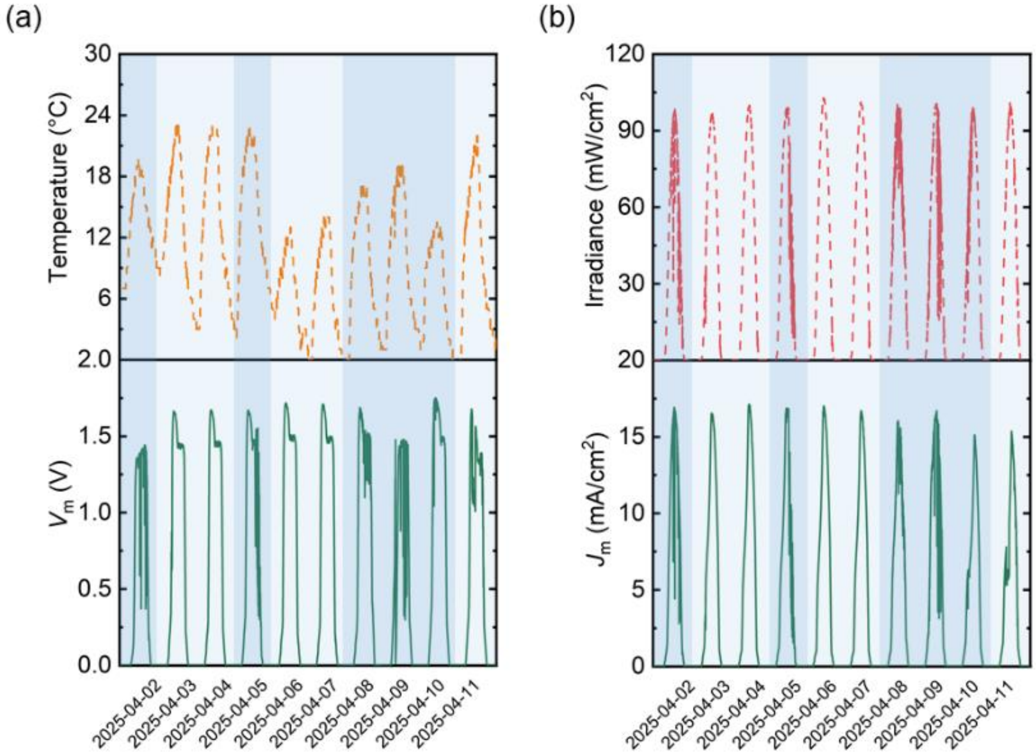

Figure 6.10: (a) Daily irradiance and current generated alongside (b) temperature variations and voltage generated at maximum power point of best performing perovskite-silicon tandem solar cells. Sunny days (light blue) and cloudy days (dark blue) are segregated with different backgrounds.

To understand the combined effect of the outdoor conditions on the operational stability and performance degradation of the TSCs, a parameter called performance ratio (PR) is used. PR is the ratio of the real-world efficiency of a solar cell relative to the theoretical performance under STC [24].

$$performance\ ratio = \frac{\int_{t_1}^{t_2} Pm\,dt}{PCE_{STC} \cdot \int_{t_1}^{t_2} irradiance\,dt} \qquad Equation\ 7.1$$

Figure 6.11 (b) represents the performance decrease as a function of cumulative time in hours, showing long-term device stability with extraction of the T_{80} metric [189]. This is a common benchmark in photovoltaic research to estimate useful device lifetime. The error bars indicates the variability. For the first 150 h, the PR remains quite stable ~1, suggesting initial stability and absence of significant degradation in the TSCs. A noticeable decline begins around 180 h with a drop below 0.8 by ~240 h. PR decreases after three consecutive cloudy days (April 8- April 10) and the TSCs are unable to recover the device performance even during next sunny day. T_{80} > 200 hours under real-world conditions can be considered moderately stable for emerging technologies like perovskites.

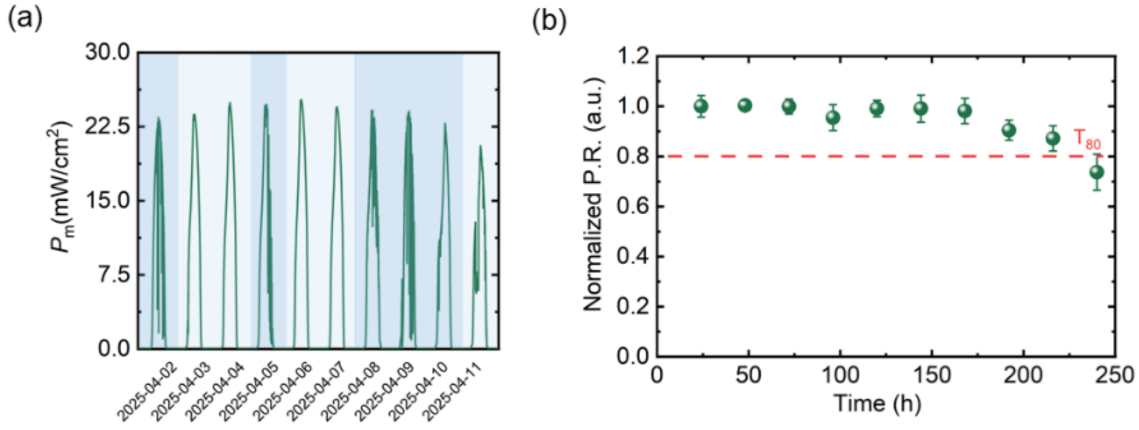

Figure 6.11: (a) Daily power generated by the best performing perovskite-silicon tandem solar cells at maximum power point and (b) normalized performance ratio variations over a period of 250 h. Sunny days (light blue) and cloudy days (dark blue) are segregated with different backgrounds.

6.5. Degradation of encapsulated perovskite-silicon tandem solar cells

Post degradation analysis gives us insights into the state of the device after the stress tests are over. *J-V* characterization of the champion TSC after measurement in the outdoor setup displays a decrease in all three performance parameters V_{OC}, J_{SC} and FF (see **Figure 6.12 (a) and Table 6.1**). The degradation mechanism could be a combined effect of many ongoing phenomenon. From the effects of elevated temperature, phase segregation and non-radiative recombination affecting V_{OC} [283], [284], to light induced defect formation in perovskite layer and irreversible ionic accumulation leading to decrease in J_{SC} and FF [242]. The encapsulation being compromised and ingress of moisture could be another reason for loss in performance [301]. While the data of a champion device is reported here, the trend is consistent over three tandems measured simultaneously.

Table 6.1: Photovoltaic parameters of the champion perovskite-silicon TSCs before (pre) and after (post) the outdoor testing

Condition	PCE (%)	FF (%)	V_{OC} (V)	J_{SC} (mA/cm^2)
Pristine	25.1	69.8	1.82	19.7
Degraded	12.7	41.7	1.65	18.6

With an intention of understanding the reason behind the degradation and isolate the subcell, which undergoes most damage, EQE characterization was performed. Spectral characterization like EQE can help isolate if the damage occurs in UV-VIS range (top cell) or IR range (bottom cell). **Figure 6.12 (b)** shows the comparison of the EQE characterization performed on the champion cell before and after the outdoor testing. It is clear that the top cell i.e. the perovskite subcell undergoes a more drastic degradation with the intensity of EQE falling below 50% post stress testing. In wide-bandgap (WBG) perovskite, employed in the top cell, the bandgap are exceeding 1.68 eV [298]. Such WBG recipe employing higher Bromide (Br^-) content is prone to phase segregation. Phase segregation is a critical challenge that undermines long-term operational stability and performance in TSCs. Under input irradiance variation or thermal variations, the iodide (I^-) ions and Br^- ions become mobile and tend to segregate spatially, forming I^--rich and Br^--rich domains [118]. This photoinduced phase segregation leads to bandgap inhomogeneity, charge funneling through the low bandgap regions and the emergence of localized low-bandgap trap states, which act as non-radiative recombination centers [214]. As a result, charge carrier extraction becomes less efficient and both V_{OC} and J_{SC} are reduced. In perovskite-silicon TSCs, this degradation in the WBG top cell compromises the current matching with the silicon bottom cell, a critical requirement for maintaining performance of serially connected TSCs. The current of the TSC is limited by the subcell with lower J_{SC}. The instability of the WBG absorber limits the operational power output of the TSCs and causes a gradual decline in the overall device performance and PR.

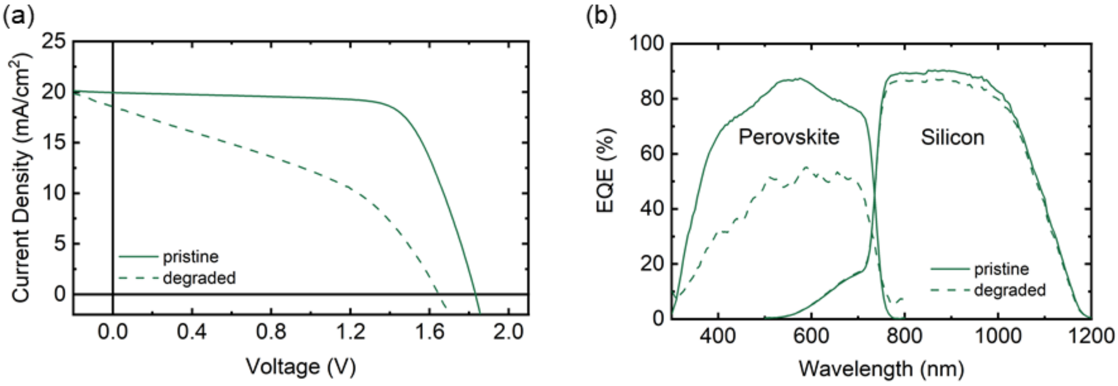

Figure 6.12: Comparison of before (pre) - after (post) (a) *J-V* characterization and (b) EQE of best performing perovskite-silicon tandem solar cells tracked at maximum power point under real-world condition.

To quantify the damage induced in the perovskite subcell during outdoor measurements, photoluminescence (PL) imaging was performed on the degraded TSCs and compared with pristine devices (see **Figure 6.13 (a)**). **Figure 6.13 (b)** depicts the inhomogenieties observed in the perovskite top cell exhibited with the different PL intensities over the surface. These inhomogenieties could arise from the uneven distribution of optoelectronic properties like bandgap or due to different recombination rates. The pristine device exhibits more homogeneity with uniform bandgap over the surface.

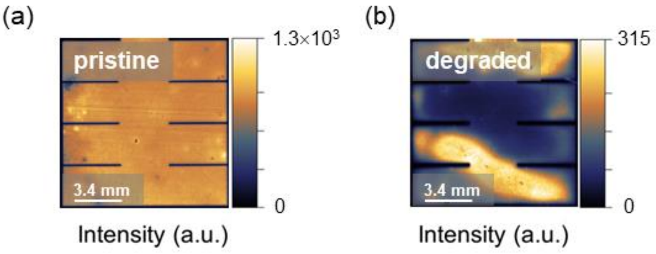

Figure 6.13: Photoluminescence of (a) pristine and (b) degraded perovskite-silicon tandem solar cell measured at maximum power point tracking in outdoor condition.

Alongside the damage in the WBG of the top cell, which is easily detectable with spectrally resolved techniques like EQE and PL imaging, there could be additional damage to different CTLs and recombination layer implemented. While the damage on these layers are more difficult to trace, their effect on the decrease in performance and stability of the TSCs cannot be overlooked. These effects collectively hinder the commercial viability of TSCs, emphasizing the need for more stable perovskite materials and strain-recoverable crystal structures to mitigate the effects of phase segregation and fatigue behavior under operational stress.

Further device optimization with absorber of lower bandgap (lower Br^- content) can help select the suitable absorber for outdoor measurement both for performance and stability. Additives in the absorber can also improve the ability of the perovskite layer to fight against and delay irreversible fatigue behavior. Carefully designed experiments would be required to isolate the root cause of degradation. Additional characterizations might help in quantifying the damage each subcell undergoes. While implementing all suggested changes might take a long time, the results will work in favor of the longevity of the PSCs and TSCs operated in outdoor conditions.

6.6. Summary

This study presents the development of an optimized encapsulation strategy designed to protect perovskite-silicon TSCs from extrinsic environmental stressors such as oxygen and humidity. The encapsulated TSCs demonstrated exceptional stability, maintaining 100% of their initial PCE for over 1000 h under high humidity conditions of 65 % RH (addressing **Objective 5**).

An outdoor measurement setup was developed to investigate the performance of encapsulated perovskite-silicon TSCs under diurnal stress conditions. The system was equipped with temperature and irradiance sensors to monitor environmental variations throughout the day and night. Signals from both the sensors and the solar cells were conditioned and digitized via an ADC, which interfaced with a central processor using standard TCP/IP protocols. A power supply, including switching power modules and DC-DC converters, ensured appropriate voltage and current supply to all components. A perturb and observe algorithm was implemented to enable efficient MPP tracking, allowing rapid convergence under dynamically changing outdoor conditions. Using this setup, initial outdoor measurements of the encapsulated TSCs were conducted. The devices exhibited stable performance for up to 180 h. However, the photocurrent progressively decreased, and the maximum power output (P_m) dropped below the T_{80} threshold after approximately 240 h. Achieving a T_{80} lifetime of ~240 h under real-world conditions demonstrates a promising level of operational stability for TSCs, effectively addressing **Objective 6**.

J-*V* and EQE characterizations confirmed that degradation was localized in the perovskite top subcell. Repeated light and thermal cycling induced strain within the perovskite absorber, leading to irreversible structural damage known as fatigue behavior. This degradation in the top cell restricted the J_{SC} of the TSC, as the total current was limited by the current-mismatched perovskite subcell. A measurable decline in both V_{OC} and J_{SC} of the TSC was observed. Further analysis using PL imaging revealed significant spatial inhomogeneity in the perovskite layer, attributed to elevated temperature and light induced halide phase segregation between I^- and Br^- -rich regions in the WBG perovskite absorber (>1.68 eV). The lower-bandgap (I^--rich) domains promoting charge carrier funneling acted as non-radiative recombination centers and localized defect accumulation over time. These regions evolved into trap states, escalating recombination losses and accelerating performance decline. Further device optimization using absorbers with lower bandgaps achieved by reducing Br^- may enable the selection of more suitable perovskite compositions for outdoor operation, balancing both performance and environmental stability. Additionally, the incorporation of specific additives into the perovskite absorber can enhance its resistance to stress-induced degradation, thereby delaying the onset of irreversible fatigue behavior.

7. Summary and outlook

This work explores how processing parameters, specifically precursor stoichiometry and quenching technique, affect the morphological and structural characteristics of perovskite thin films. These morphological and structural properties play a crucial role in determining the failure mechanisms when the perovskite films and perovskite solar cells (PSCs) are subjected to operational stressors such as light, voltage bias and elevated temperatures. Developing insight about the influence of structural and morphological properties is essential for identifying the underlying causes of degradation under various stress factor. The most damaging intrinsic stress factor was the operation of the solar cell under continuous illumination and maximum power point (MPP) tracking. Iodide (I^-) ions have the lowest activation energy for migration among other cations and anions. Under illumination in presence of voltage bias, I^- migration is triggered even at room temperature. During this process, I^- ions migrate toward the electron transport layer (ETL), while iodide vacancies (V_I^+) move toward the hole transport layer (HTL). When I^- migration become excessive, as observed in the case of devices with more formamidinium iodide (FAI), localized shunts formation cause degradation in the perovskite layer’s quality. Poor film quality of perovskite influences recovery in the dark, which could have adverse effects in the stability of PSCs in outdoor conditions.

With bandgap engineering, both wide-bandgap (WBG) and narrow-bandgap (NBG) perovskite absorbers were developed and integrated into all-perovskite tandem solar cells (TSCs). Degradation in one of the subcells results in current mismatch between the subcells affecting the TSCs performance and stability. The influence of such mismatch was studied by systematically varying the precursor solution molarity and thickness of the WBG top cell. This adjustment influenced the absorption of high-energy photons in the top cell, thereby changing the photon flux reaching the bottom cell. TSCs with better current matching between subcells maintained excellent operational stability for over 350 h of continuous illumination and MPP tracking. In contrast, current mismatch, whether limited by the top or bottom cell, resulted in faster degradation and reduced stability, highlighting the importance of current matching both initially and throughout the stress testing. Post-degradation analysis revealed a significant drop in the external quantum efficiency (EQE) intensity of the WBG top cell under bottom-limited condition, likely caused by the top cell being driven toward reverse bias when the bottom cell is severely limited. This highlights the need to investigate alternative strategies for more effective utilization of sub-bandgap photons.

Upconversion (UC) materials are specifically engineered to address this challenge. When positioned on the backside of the PSC, an upconversion crystal with a reflector can absorb the sub-bandgap (SB) photons, upconvert them, and reflect the upconverted photons back into the PSC. Under combined broadband (BB) illumination (<850 nm) and SB laser illumination (~980 nm), the PSC-UC device shows an increase of approximately 0.4 mA/cm^2 in short-circuit current density (J_{SC}) at lower SB intensities. The spectral dependence of the enhancement in J_{SC}, measured between 860 and 1000 nm, confirms that this enhancement arises from the upconversion of the SB photons. Using a higher SB leads to a greater enhancement in J_{SC} but also raises the temperature due to the laser-induced heating.

This temperature rise negatively affects PSC performance, primarily through reductions in open-circuit voltage (V_{OC}) and fill factor (FF). As the light intensity increases, enhancement in J_{SC} exhibits a nonlinear rise, nearly doubling of the J_{SC} at an incident intensity of 7650 suns. While doubling J_{SC} through concentrated light is interesting, such extreme intensities are impractical for photovoltaic applications. This raises concerns about the applicability of the novel approach of upconversion in the field of PSCs.

Finally, an attempt to measure the perovskite-silicon TSCs in outdoor conditions was made. A robust encapsulation fitting the perovskite-silicon TSCs architecture was developed. An outdoor setup with suitable hardware and software for tracking of the PSCs and TSCs was established. The encapsulated TSCs maintained stable performance for up to 180 h in moderate spring-like weather condition. However, the photocurrent gradually declined, and the maximum power output (P_m) decreased below the T_{80} threshold after about 240 h. Achieving a T_{80} lifetime of ~ 240 h under real-world conditions represents a good starting point for TSCs. EQE characterization confirmed that degradation was concentrated in the perovskite top subcell. Repeated light and thermal cycling induced strain in the perovskite absorber, causing irreversible structural damage characteristic of fatigue behavior. Degradation in the top cell limited the J_{SC} of the TSCs, as the overall current was constrained by the current mismatch in the perovskite subcell. A noticeable decline in both V_{OC} and J_{SC} was observed. Photoluminescence (PL) imaging further revealed significant spatial inhomogeneity in the perovskite layer hinting towards halide phase segregation. Elevated temperature and light induce halide phase segregation in the WBG perovskite top cell (bandgap >1.68 eV). The lower-bandgap (I^- -rich region) facilitate as charge carrier funneling sites. Over time, formation of localized defect accumulation in I^- - rich region act as non-radiative recombination centers.

The changes that can be implemented in the perovskite solar cell (PSC) and the perovskite-silicon tandem solar cells (TSC) which can enhance the long-term stability of these photovoltaic technologies are mentioned below. Alongside, suggestions to better understand the degradation mechanism in indoor condition in presence of mutual stress factors or outdoor condition in presence of diurnal stress factor is also included.

Improvement in the perovskite solar cells

Interfacial and bulk engineering play a vital role in improving the stability of PSCs. Employing surface passivation layer with low defect density between the perovskite layer and the electron transport layer can act as a barrier to ion migration. Furthermore, reducing defect density in the perovskite bulk through grain boundary passivation significantly hinders ion migration pathways. Passivation of the perovskite bulk with large cations can reduce the effects of I^- migration and instability. In NBG perovskites, the substitution of lead (Pb^{2+}) with tin (Sn^{2+}) can also reduce I^- migration. Sn vacancies capture the migrating I^- ions and slow down the ion diffusion in Sn-Pb perovskite. Replacing a portion of the I^- with more stable halides like bromide (Br^-) or chloride (Cl^-) has shown an improvement in I^- ion confinement. Hence, both NBG and WBG perovskites are more resilient to I^- ions migration.

Limitations in the tandem solar cells

The major limiting factor in the outdoor measurement of the perovskite-silicon TSCs was the degradation in the WBG perovskite top cell and overall fatigue behavior. Halide segregation in mixed halides employing higher bromide content (>20%) is more severe. WBG used for perovskite-silicon TSCs in this work employs 23% Br^-. Hence, incorporation of small amount of Cl^- to reduce the Br^- content to <20% can potentially address the problem of halide segregation. The improvements suggested above for bulk and surface passivation of PSCs can cater to the issue of fatigue behavior observed in outdoor condition. Cycles of thermal and light stress develop accumulated strain in the perovskite crystal structure, preventing structural recovery, which is witnessed as fatigue behavior over time.

Indoor measurement with simultaneous application of intrinsic stress factor

The investigation of PSCs under simultaneous exposure to intrinsic stress factors, namely light, voltage bias, and elevated temperature, revealed a compounded degradation effect. When subjected to light and MPP tracking simultaneously, the PSCs exhibited a decline in current at MPP (J_m), primarily due to ion accumulation between the perovskite layer and the interfaces. Under elevated temperature alone, a reduction in open-circuit voltage (V_{OC}) and fill factor (FF) was observed, indicating thermally induced degradation mechanisms. Stability testing under ISOS-L2I conditions, which involve continuous illumination and MPP tracking at 80 °C, further demonstrated a significant drop in output power at the MPP (P_m), highlighting the synergistic and detrimental impact of combined stress factors on device performance. Loss in P_m is linear (see **Figure 8.1 (a)** with an extrapolated T_{80} lifetime of approximately 280 h. The International Summit on Organic and Hybrid Perovskite Solar Cells (ISOS) provides standardized testing protocols widely adopted for evaluating the stability of emerging photovoltaic technologies such as perovskite and organic solar cells. T_{80} refers to the time at which a device retains 80% of its initial performance under specified stress conditions. The results indicate that, under the combined influence of continuous illumination, voltage bias, and elevated temperature, a consistent decline in both the J_m and V_m is prevalent as shown in **Figure 8.1 (b)**.

Transition between indoor and outdoor condition

The continuous application of stress factors, as commonly employed in accelerated aging tests, may not accurately represent the real-world degradation behavior of PSCs and TSCs. In outdoor environments, these devices are exposed to diurnal cycles, where stress conditions such as illumination and temperature fluctuate between day and night. Incorporating cyclic stress conditions in testing protocols can be advantageous, particularly because perovskite materials have demonstrated partial recovery during nighttime (dark) periods. For devices that experience reversible degradation or fatigue-like behavior, stress cycling provides a more realistic degradation profile. Therefore, indoor testing that includes periodic cycling of intrinsic stressors, such as light and temperature, may offer a more accurate assessment of long-term stability and device lifetime under practical operating conditions. This approach better mimics outdoor performance and helps bridge the gap between laboratory testing and testing under the real-world condition.

Outdoor measurement with energy yield modelling

Understanding degradation mechanisms through energy yield modeling offers valuable insights into how environmental variables, such as fluctuating temperature and varying solar irradiance, contribute to the long-term degradation of PSCs and TSCs. This approach enables the correlation of real-world operating conditions with degradation phenomena specific to the PSCs and TSCs such as light-induced degradation, potential-induced degradation and thermal stress. Importantly, energy yield modeling can incorporate dynamic factors like nighttime recovery and material fatigue, providing a more realistic estimation of device lifetime. Serving as a bridge between laboratory-based degradation studies and field performance data, energy yield modeling not only aids in predicting long-term stability but also enhances the interpretation of performance losses observed in outdoor photovoltaic systems.

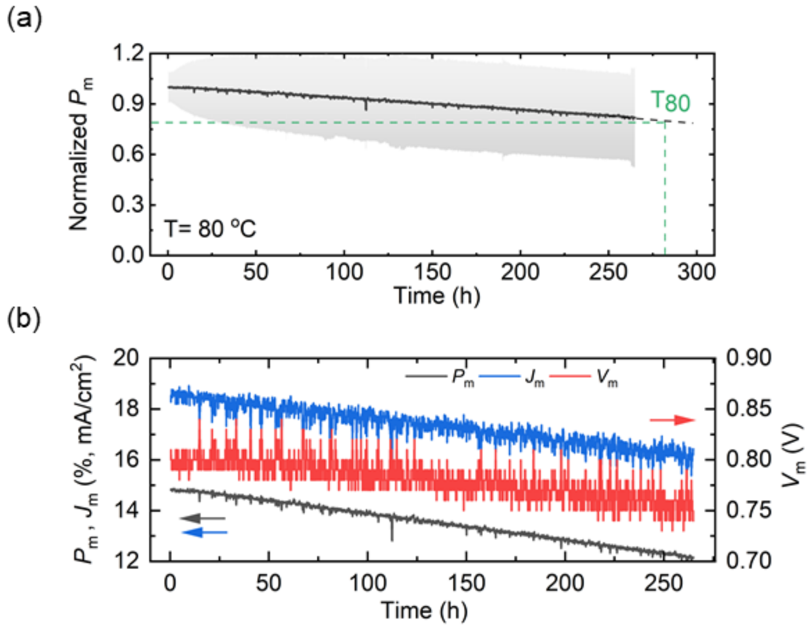

Figure 8.1: (a) Normalized power at maximum power point (P_m) for semi-transparent $Cs_{0.18}FA_{0.82}PbI_3$ devices at 80 °C with an extrapolated T_{80} of 280h. T_{80} is the time up until which the sample maintains 80% of their initial performance. (b) Drop in both current and voltage at maximum power point (J_m and V_m) is the reason behind the loss in performance.

Cleaning soiling over time

While advanced modeling techniques such as energy yield simulations are essential for predicting and understanding complex degradation scenarios, basic maintenance practices, such as routine cleaning of solar cell surfaces, play an equally critical role in ensuring data reliability. Regular cleaning prevents the accumulation of dust and debris, which can otherwise introduce external variability, obscure true performance trends, and lead to misinterpretation of degradation behavior. This simple yet effective step helps maintain system consistency, ensuring that observed trends reflect intrinsic material or device responses rather than extrinsic artifacts.

The insights and methodologies developed in this work is a valuable contribution to advancing the stability of PSCs and perovskite-based TSCs. From elucidating the origins of film properties governed by fabrication process variables to evaluating the stability of PSCs under intrinsic stress factors, this work provides a comprehensive understanding of device behavior. When integrated into TSCs, the (in)stability of the PSC subcell critically influenced the overall tandem performance. Additionally, strategies for protecting TSCs against extrinsic environmental stressors were developed which were important for isolating the effects of extrinsic stress factors while investigating the impact of diurnal stress factors on the long-term stability of these devices. This work bridges the gap between laboratory-scale research and field deployment, marking a significant step toward the practical application of PSC and perovskite-based TSC technologies.

Appendix

A. Appendix of Chapter 4

Table A4.1: Photovoltaic parameter and bandgap information of devices of different precursor stoichiometry quenched using ASQ and VQ along with bandgap of from derivative at inflection point of EQE of devices of different precursor stoichiometry and quenching technique.

Quenching	Molar ratio	PCE (%)	V_{OC} (V)	FF (%)	J_{SC} (mA/cm^2)	Bandgap (eV)
ASQ	1.2	18.2	1.08	0.83	20.33	1.59
	1.15	17.87	1.07	0.82	20.37	1.58
	1.1	17.69	1.06	0.81	20.65	1.58
	1.05	17.37	1.04	0.81	20.56	1.57
	1	12.69	0.99	0.71	18.15	1.56
VQ	1.2	18.47	1.09	0.8	21.13	1.59
	1.15	18.57	1.09	0.83	20.39	1.59
	1.1	18.45	1.08	0.82	20.7	1.58
	1.05	17.98	1.05	0.82	20.82	1.57
	1	11.26	0.96	0.76	16.83	1.57

Table A4.2: Thickness measured by profilometry and surface roughness measured by atomic force microscopy (AFM) of devices of different precursor stoichiometry and quenching technique.

Quenching	Molar ratio	Thickness (nm)	Surface roughness (nm)
ASQ	1.2	492±7.0	30±1.5
	1.15	498±7.1	28±3.9
	1.1	501±3.2	29±1.4
	1.05	495±9.1	30±2.5
	1	496±8.5	28±0.7
VQ	1.2	452±8.3	26±3.6
	1.15	463±6.2	24±2.4
	1.1	459±3.6	24±1.9
	1.05	493±6.6	24±2.8
	1	491±6.5	25±1.8

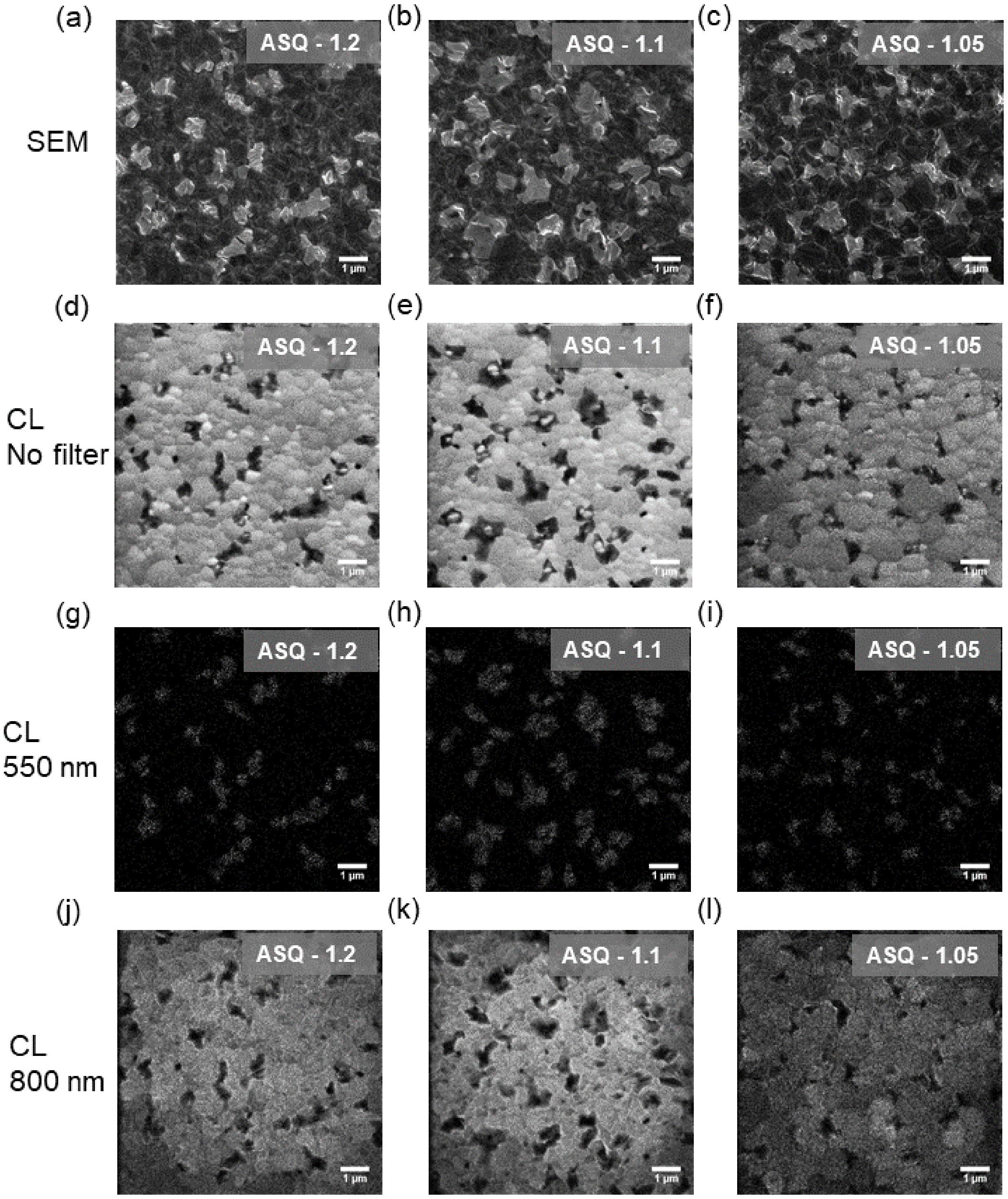

Figure A4.1: Scanning electron microscopy (SEM) of (a) MR 1.2 (b) MR 1.1 (c) MR 1.05. Cathodoluminescence (CL) images of perovskite films without filters (d) MR 1.2 (e) MR 1.1 (f) MR 1.05. CL images of perovskite films with band pass filter of 550 nm (g) MR 1.2 (h) MR 1.1 (i) MR 1.05. CL images of perovskite films with band pass filter of 800 nm (j) MR 1.2 (k) MR 1.1 (l) MR 1.05. All samples were quenched using ASQ.

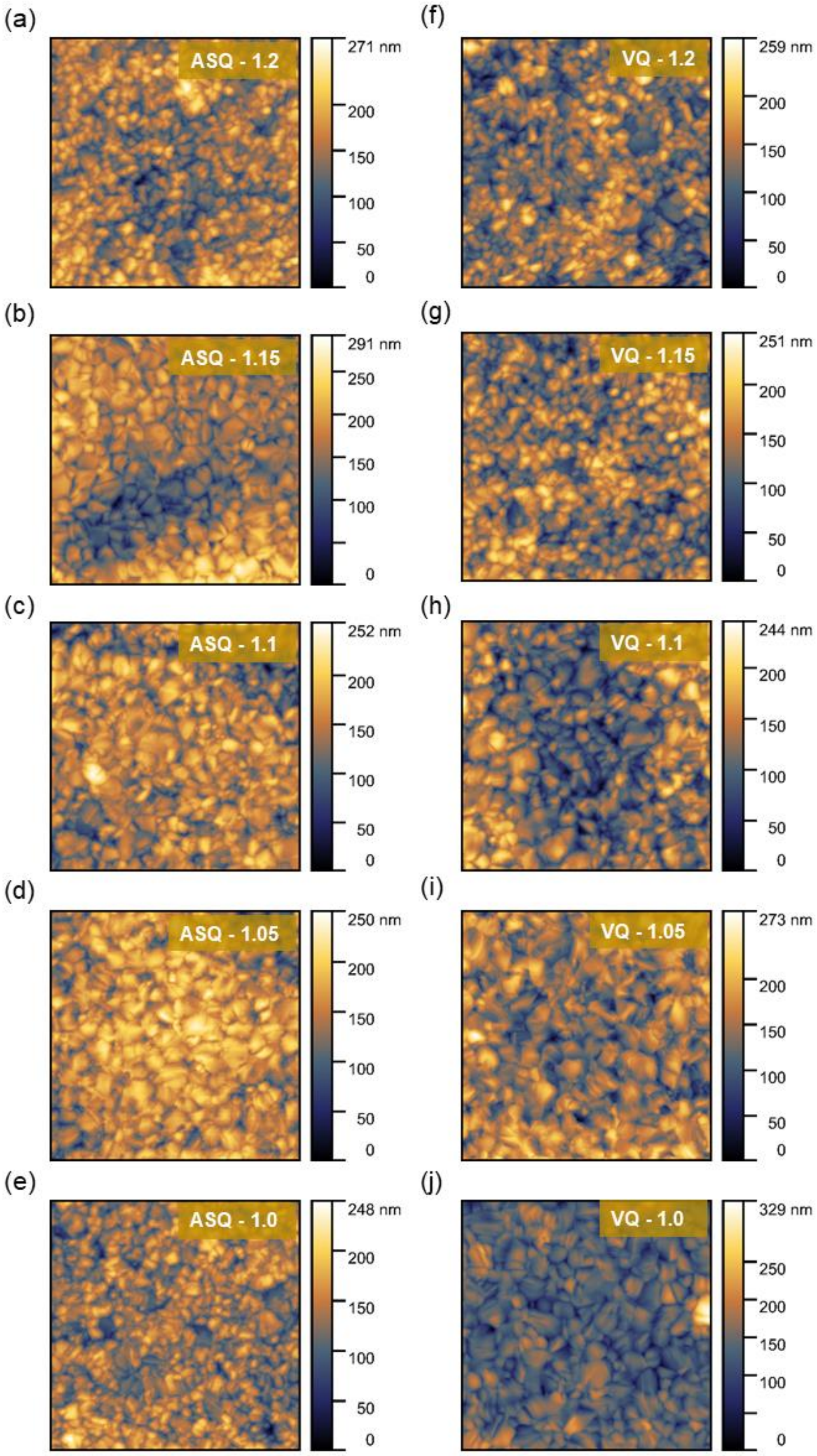

Figure A4.2: Atomic force microscopy (AFM) images of (a-e) antisolvent-quenched films and (f-j) vacuum-quenched films.

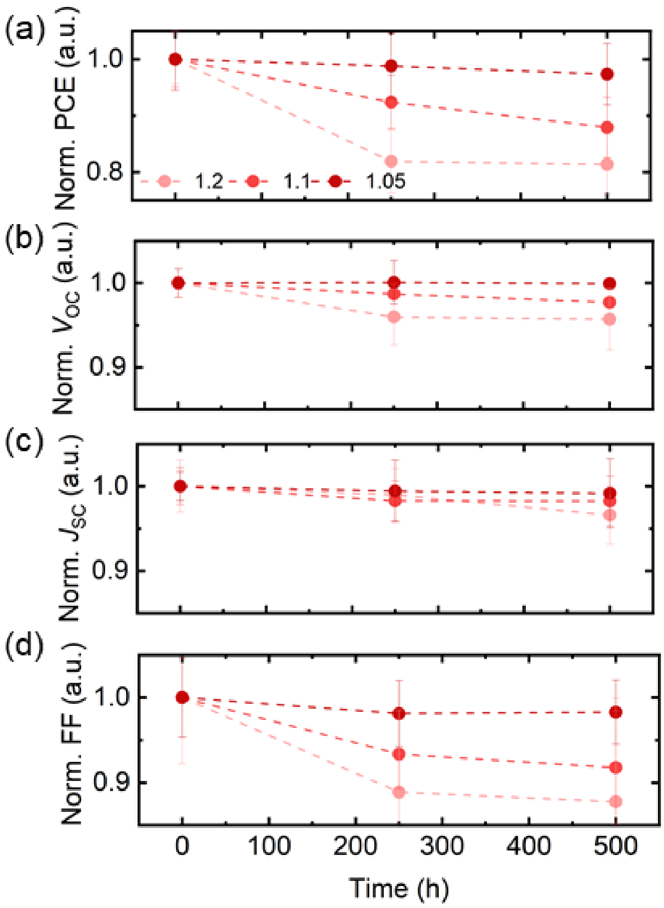

Figure A4.3: Normalized (a) PCE, (b) V_{OC}, (c) J_{SC}, and (d) FF from $J-V$ characterizations of vacuum-quenched devices of different stoichiometries under ISOS-D2I testing conditions (dark, 85 °C, intermittent $J-V$ characterizations) for 500 h.

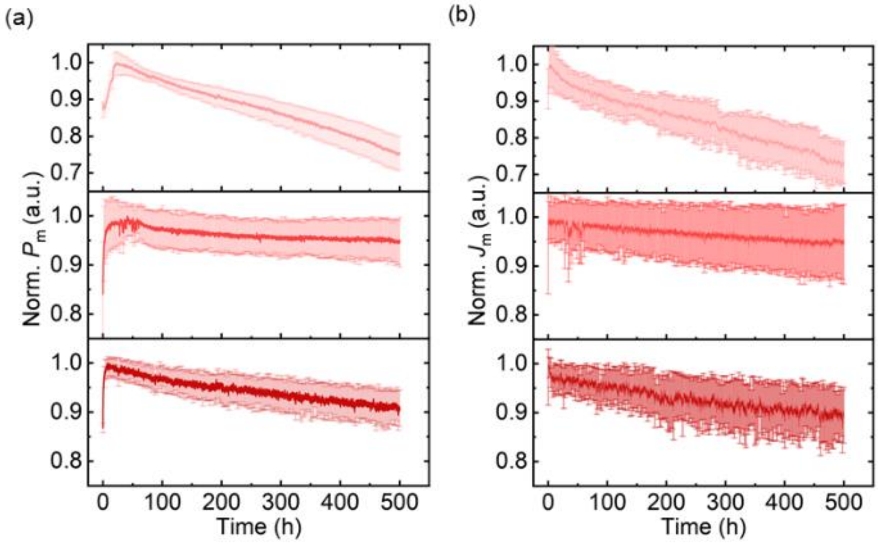

Figure A4.4: Normalized (a) power and (b) current density at the maximum power point (MPP) tracking of vacuum-quenched devices of different stoichiometries under ISOS-L1I test conditions (100 mW/cm^2, 25 °C, MPP tracking) for 500 h.

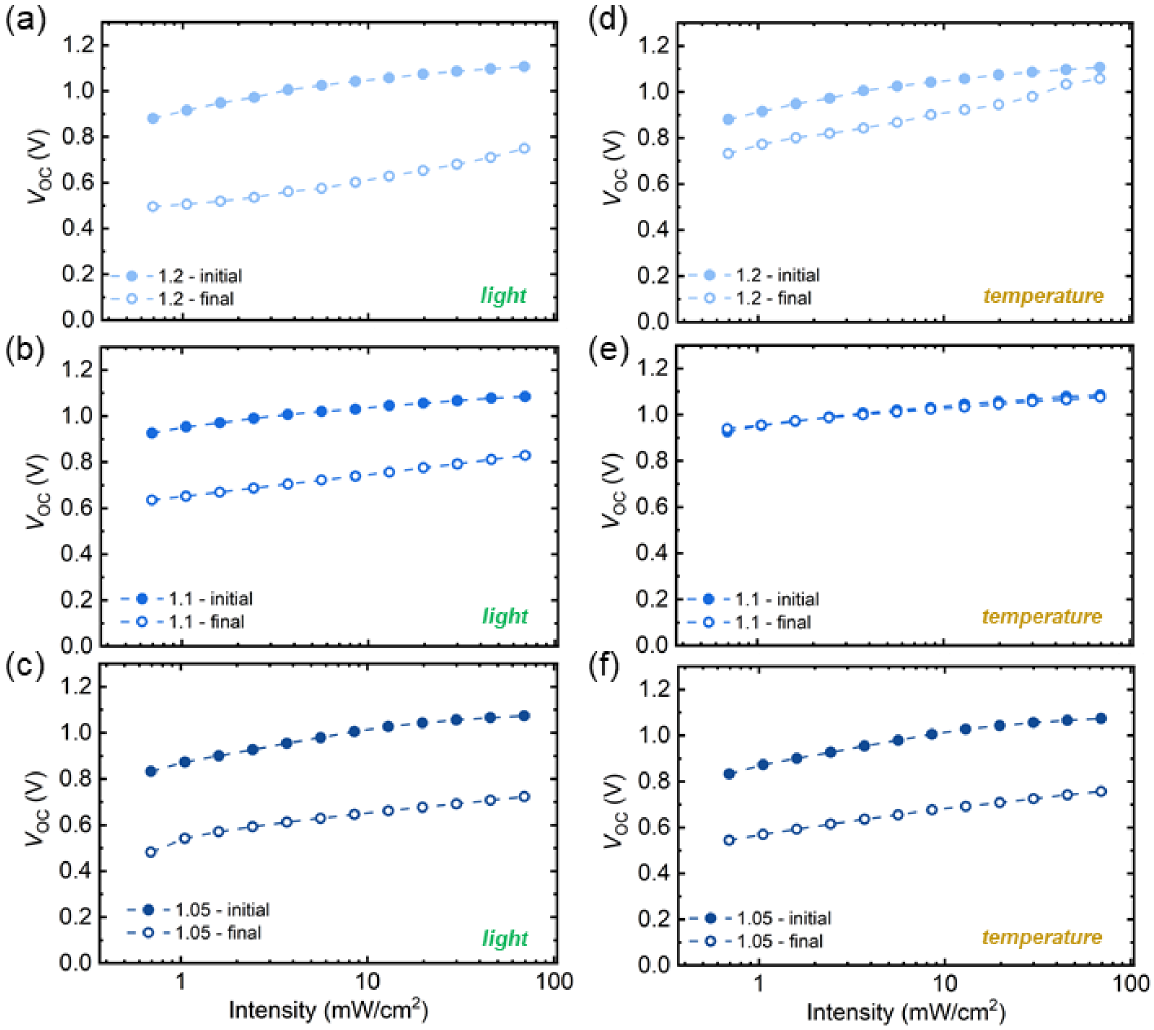

Figure A4.5: Comparison of ideality factor of antisolvent-quenched devices of (a) MR 1.2 (b) MR 1.1 and (c) MR 1.05 measured before (initial) and after (final) ISOS-L1I test. Comparison of ideality factor of antisolvent-quenched devices of (d) MR 1.2 (e) MR 1.1 and (f) MR 1.05 measured before (initial) and after (final) ISOS-D2I test.

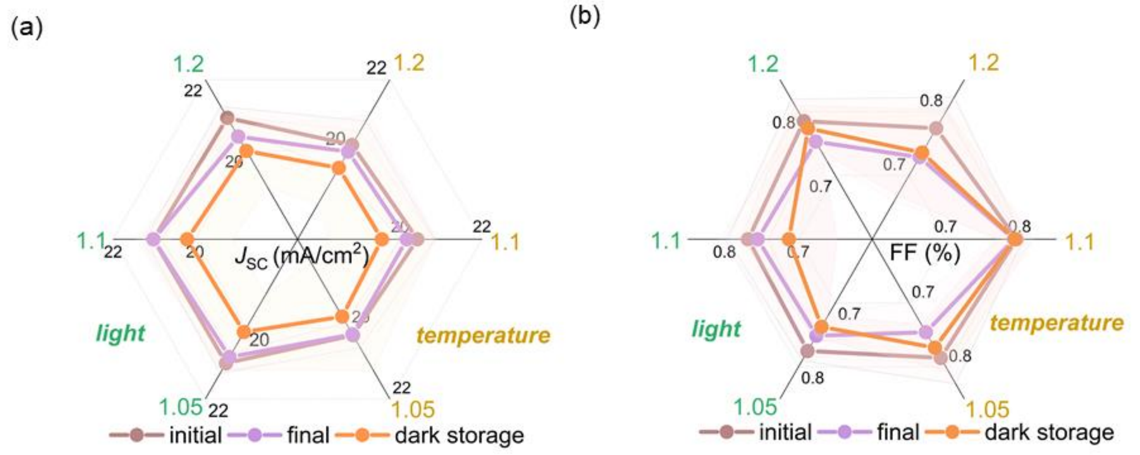

Figure A4.6: Radar plots of (a) average J_{SC} and (b) average FF of devices with different precursor stoichiometry aged under ISOS-D2I (red) and ISOS-L1I (blue). $J-V$ characterizations before the accelerated testing (brown) and after 24 h (purple) and 250 h (orange) of dark storage.

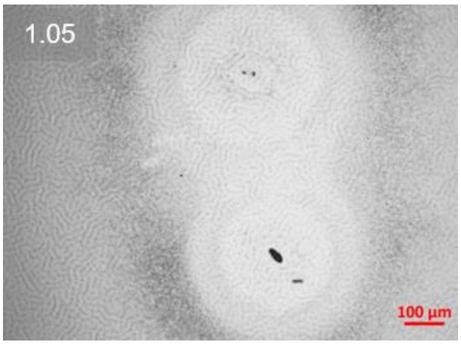

Figure A4.7: Optical microscopy (OM) images of antisolvent-quenched films of MR 1.05 aged under light at 25 °C for 500 h.

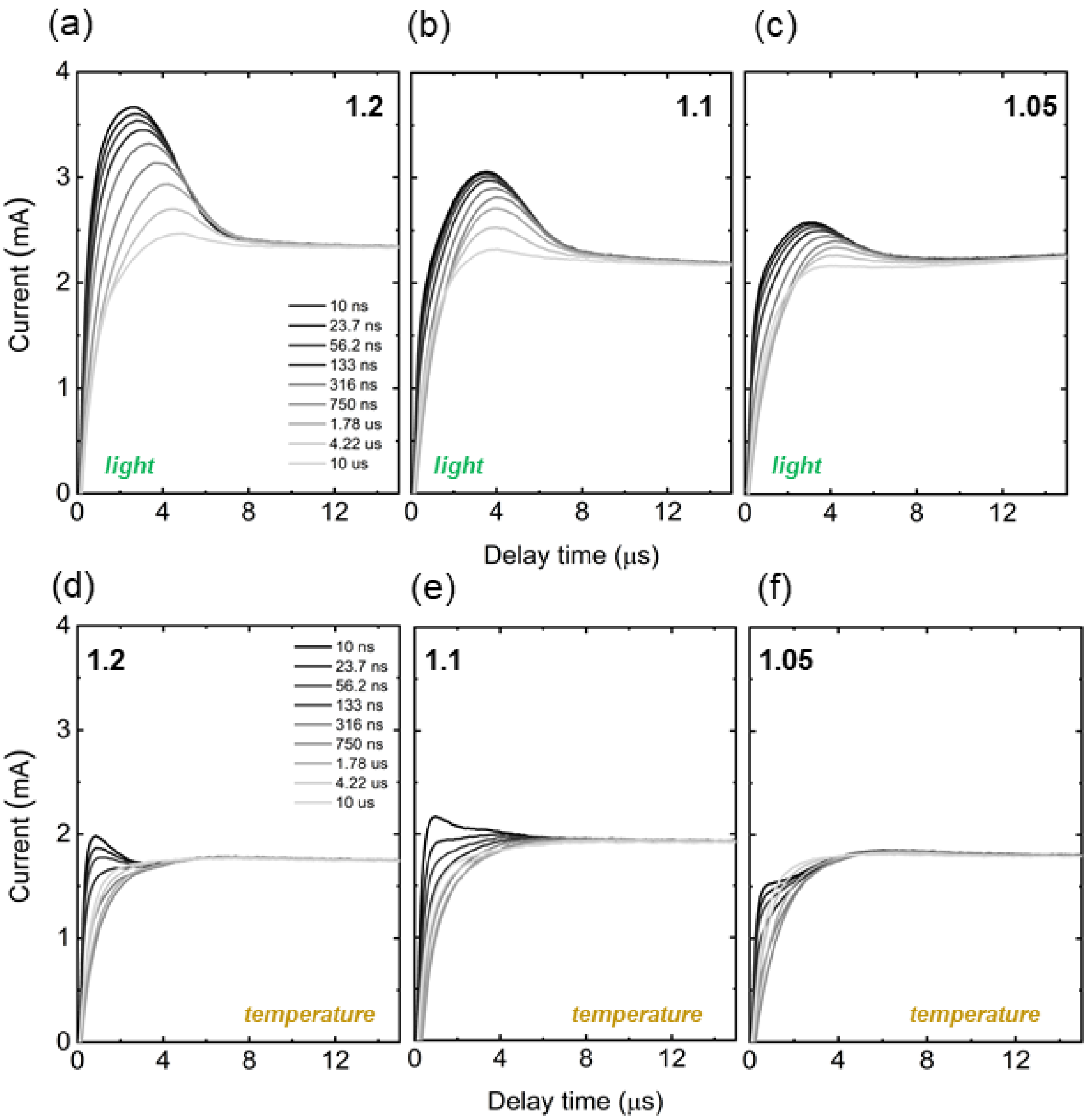

Figure A4.8: Charge extraction by linearly increasing voltage (CELIV) with delay time of antisolvent-quenched devices of (a) MR 1.2 (b) MR 1.1 and (c) MR 1.05 aged under ISOS-L1I. Charge extraction by linearly increasing voltage (CELIV) with delay time of antisolvent-quenched devices of (d) MR 1.2 (e) MR 1.1 and (f) MR 1.05 aged under ISOS-D2I

Current mismatch between subcells and stability of all-perovskite tandem solar cells

Current matching between subcells in two-terminal tandem solar cells

Two-terminal (2T) monolithic tandem solar cells (TSCs) are an advanced photovoltaic architecture designed to enhance the power conversion efficiency (PCE) by stacking multiple absorber layers with complementary bandgaps in a single integrated structure [20]. This configuration allows the TSCs to utilize the solar spectrum more effectively by dividing the photon energy range among subcells. The top cell absorbs the high-energy photons and transmits the lower-energy photons to the bottom cell. The 2T design ensures a compact structure with a single current path, simplifying the module integration and reducing the interconnection losses. Resistive and optical losses are also relatively lower in comparison to the four terminal (4T) configuration [315]. While shared electrodes and minimized wiring reduces the series resistance losses, the absence of an additional optical interface reduces the reflection and absorption losses, in comparison to the 4T configuration, enhancing current output in the 2T configuration [76]. However, this architecture requires a careful current matching between the subcells, as they are connected in series. By optimizing material selection and bandgap engineering, monolithic 2T TSCs can significantly outperform single junction devices in harvesting photons across the ultraviolet (UV), visible (VIS), and near infrared (NIR) regions pushing the theoretical efficiency limits.

Current matching plays a critical role in determining the overall performance and stability of the 2T TSCs configuration. In such an architecture, the total current output is limited by the subcell generating the lowest current, making precise current matching between the top and the bottom cell essential for maximizing the PCE. Any mismatch in current, arising from the spectral imbalance, optical losses, parasitic absorption, shading or suboptimal layer thickness, results in underutilization of the available charge carriers, leading to significant losses in the short-circuit current density (J_{SC}), limiting PCE of the TSC [310]. This challenge requires meticulous design of the device stack, including anti-reflection coatings (ARCs), transparent conductive layers (TCOs), and spectral filtering to ensure balanced photon absorption among the subcells. Moreover, bandgap engineering of the perovskite absorber is often employed to tailor the absorption onset and align the current generation with the bottom cell. Thus, achieving near-ideal current matching is fundamental to unlocking the full potential of the 2T monolithic TSCs and pushing their efficiencies towards and beyond the theoretical efficiency limits of the single junction devices.

Importance of studying stability in all-perovskite tandem solar cells

Studying stability in all-perovskite TSCs offers several scientific and practical advantages over perovskite-silicon TSCs, making them a more suitable platform for fundamental and systematic stability investigations. Some reasons are mentioned below:

Material system homogeneity

In all-perovskite TSCs, both the top and bottom subcells are based on the same class of materials- metal halide perovskites. The structural and chemical similarity between the subcells allow isolation and study of processes inducing intrinsic degradation mechanisms (such as halide migration, ion accumulation and metal migration) without the complications introduced by dissimilar materials such as crystalline silicon. Perovskite-silicon TSCs involve fundamentally different material systems with distinct degradation pathways, making it difficult to decouple the origin of the failure modes.

Bandgap Tunability

All-perovskite TSCs offer greater flexibility in tuning the bandgap and thickness of both subcells, which enables controlled studies on how optical absorption, charge transport, and recombination affect the performance and the long-term stability. Such tunability is far more limited in perovskite-silicon TSCs, where silicon has a fixed bandgap and optical properties, limiting the design space for experimental stability studies.

Interface engineering

In all-perovskite TSCs, the interfaces between the two perovskite layers and the charge transport layers are tailored for perovskites. These interfaces are more controllable during fabrication and better understood as compared to the perovskite-silicon interface. With interfaces between different materials, complexities like thermal expansion mismatch, interlayer diffusion, and parasitic absorption may arise. All-perovskite TSCs allow systematic engineering and passivation of the interface layers without introducing extrinsic complexities, facilitating clearer insights into interfacial stability.

Accelerated Aging and Degradation Analysis

Because perovskites are more chemically reactive and sensitive to external stimuli (light, heat, bias, oxygen and humidity), all-perovskite TSCs tend to degrade faster than silicon-based TSCs. While this is a disadvantage for long-term operation, it becomes a significant advantage for studying degradation mechanisms, as it allows accelerated aging studies and identification of failure modes on shorter timescales. This can lead to quicker iteration and testing of mitigation strategies.

While perovskite-silicon TSCs currently lead in certified efficiency and commercial viability, all-perovskite TSCs provide a more controlled, flexible and accelerated environment for understanding and improving the stability of perovskite materials and devices. For research focused specifically on unraveling the intrinsic and interfacial degradation mechanisms, they offer a larger design space for parameter variations. Insights gained from all-perovskite TSCs studies can be directly transferable to perovskite-silicon TSCs, since the top perovskite cell in both architectures typically shares similar compositions and fabrication processes.

Architecture of all perovskite tandem solar cells

In 2T TSCs, the wide-bandgap (WBG) top cell and the narrow-bandgap (NBG) bottom cell must be spectrally complementary and their current generation must be balanced. Any deviation from ideal current matching, caused by thickness variation, optical interference effects or intrinsic material degradation, can introduce electrical stress across one or both subcells. A current limited bottom cell subjected to excess voltage from a stronger top cell can accumulate excess charge carriers, leading to increased local heating [329], ion migration and recombination [76]. All of these processes are known to trigger degradation in the perovskite materials. Under mismatched current conditions, parts of the tandem stack may operate under local reverse or forward bias, depending on charge carriers injection or extraction under illumination [330]. Reverse bias stress is particularly harmful for perovskite layers, potentially inducing ion accumulation with the charge transport layer [133]. Along with the reverse bias induced degradation, current mismatch escalates thermal instabilities due to localized heating, especially when one subcell is limited and dissipates excess energy as heat [331].

Moreover, under irradiation, mismatch promotes dynamic shifts in charge carrier concentration and built-in electric fields, which can accelerate trap formation and non-radiative recombination.

In all-perovskite TSCs, both the wide-bandgap (WBG) and narrow-bandgap (NBG) subcells are susceptible to different degradation mechanisms. WBG perovskites often suffer from halide segregation and voltage instability [118]. NBG perovskites (typically Sn-Pb based) are prone to Sn^{2+} oxidation and poor ambient stability [332]. However, problems related to ambient stability can be addressed by implementing a robust encapsulation technique. Deliberate current mismatch achieved, by varying the top absorber thickness can be used as a diagnostic tool to stress one subcell preferentially, thereby isolating its degradation behavior [76]. This controlled decoupling is particularly valuable for identifying the dominant instability mechanism in complex TSC stacks. Hence, current mismatch in all-perovskite TSCs act as a sensitive indicator of structural, optical, and electrical robustness. It provides a realistic view as to how internal stresses translate into performance loss and device failure. Investigating current mismatch not only helps optimize tandem efficiency, but also serves as a strategic way to understanding and enhancing the long-term stability of these promising photovoltaic devices.

Inducing current mismatch among subcells in all-perovskite tandem solar cells

Thickness optimization and bandgap engineering of the WBG perovskite absorber are pivotal strategies for achieving effective current matching in the monolithic all-perovskite TSCs. The WBG absorber's thickness is essential, as it directly influences light absorption, carrier extraction, and optical transmission to the bottom cell. A thicker WBG layer can enhance absorption of high-energy photons, increasing its J_{SC}, but may also reduce the photon flux reaching the bottom cell, leading to current mismatch. Conversely, a thinner layer may transmit more light but underutilize the high-energy photons of the spectrum. Therefore, experimental thickness tuning must be conducted in TSCs to strike an optimal balance or induce a scenario of top/bottom cell current limitation.

Simultaneously, bandgap engineering through compositional tuning by adjusting the ratio of the halide (Br/I) or the cation (FA/MA/Cs) content enables control over the spectral absorption edge of the WBG perovskite, ensuring that its absorption complements that of the NBG subcell. A bandgap in the range of 1.65-1.75 eV is generally targeted for the WBG top cell to ensure optimal spectral division and minimal thermalization losses. Furthermore, such tuning must also consider material stability, phase segregation risks and defect density. Halide segregation is a critical challenge in WBG PSCs, especially of those with high bromide (Br^-) content. High Br^- content are employed to achieve bandgaps in the range of 1.65-1.8 eV for TSC applications [118]. Incorporating iodide (I^-) and Br^- anions in mixed halide perovskites, leads to a desirable widening of the bandgap alongside introduction of thermodynamic instability under illumination or thermal stress. Halide segregation is a process in which Br^- and I^- ions migrate and phase-segregate into Br-rich and I-rich domains. The I-rich regions tend to form lower-bandgap domains that act as recombination centers and trap sites, severely impairing charge carrier dynamics and leading to open-circuit voltage losses and long-term performance degradation [333]. However, reports confirmed the dynamic and reversible nature of this segregation, often occurring on timescales of seconds to minutes under illumination [333]. Strategies to suppress halide segregation include compositional engineering with incorporation of Cs^+ to stabilize the crystal lattice, surface passivation and use of additives or 2D/3D perovskite architectures to inhibit ion migration [334]. Despite these efforts, complete mitigation remains elusive, making halide segregation a central focus in the development of stable, high-efficiency WBG perovskite absorbers for TSCs applications.

The benefits of these engineering approaches are critical for achieving near-ideal current matching, thereby unlocking the high-efficiency potential of all-perovskite TSCs. Given that the primary motivation of this work is understanding device stability, any associated stability concerns cannot be overlooked. Bandgap engineering with varying Br^- content influence the long-term device stability. Therefore, thickness optimization is selected as a more controlled and stable method to intentionally induce current mismatch between the subcells, allowing for systematic investigation without compromising the structural or operational integrity of the devices.

The all-perovskite TSCs used in this chapter implements a 1 M of $FA_{0.8}Cs_{0.2}Pb(I_{0.6}Br_{0.4})_3$ WBG with bandgap, E_G = 1.78 eV and a 2 M of $(Cs_X(FA_{0.83}MA_{0.17})_{(1-X)}Sn_{0.5}Pb_{0.5}I_3$ NBG with E_G ~ 1.26 eV. The content of Cs used was 2.5%. The device structure of the top cell is glass/indium tin oxide (ITO)/ (2-(9H-carbazol-9-yl)ethyl)phosphonic acid (2PACz)/ WBG perovskite absorber/ propane-1,3-diammonium iodide ($PDAI_2$)/ fullerene (C_{60})/ tin oxide (SnO_X)/ recombination layer: indium zinc oxide (IZO) ~15nm [20]. The NBG was fabricated on top of the recombination junction for a seamless monolithic device interconnection. The bottom cell comprises of poly(3,4-ethylenedioxythiophene) polystyrene sulfonate (PEDOT:PSS)/ NBG perovskite absorber/ ethylenediammonium iodide ($EDAI_2$)/ phenylC_{61}-butyric acid methyl ester (PCBM)/ C_{60}/ bathocuproine (BCP)/ gold (Au) back electrode [20]. A 100 nm thick ARC of magnesium fluoride (MgF_2) was evaporated on the glass side of the TSCs in order to reduce the reflection losses. To intentionally induce a current mismatch, the precursor molarity of the WBG top cell was systematically varied from 0.6 M to 1.2 M in increments of 0.2 M. The NBG bottom cell was then processed on top of this WBG top cell as shown in **Figure A4.9**. The details of all-perovskite TSC fabrication can be found in **Chapter 3**. This molarity optimization of WBG top cell resulted in a thickness variation of the top cell absorber layer (see **Table 5.1**).

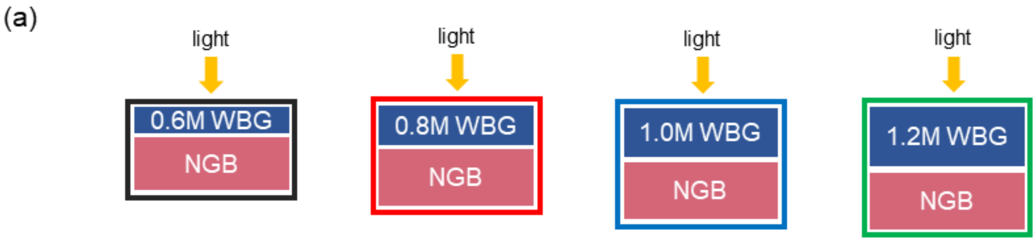

Figure A4.9: Current mismatch induced in the subcells of all-perovskite tandem solar cells (TSCs) by changing the thickness of the top cell. The molarity of the top cell was varied from 0.8 M to 1.2 M to control the amount of light the top cell absorbs and the amount of light that is transmitted to the bottom cell. The current generation in each subcell can be independently tuned.

Table A4.3: Variation in the thickness of the WBG perovskite layer by changing molarity of the precursor solution.

Molarity (M)	Thickness (nm)
0.6	186 ± 5
0.8	273 ± 7
1.0	382 ± 2
1.2	569 ± 3

The variation in the WBG absorber thickness is designed to modulate the absorption of the high-energy photons in the top cell, thereby regulating the photon flux transmitted to the bottom cell. This deliberate tuning is expected to influence not only the overall device performance but also the long-term operational stability of all-perovskite TSCs.

Current mismatch in the subcells and performance

To investigate the influence of top cell thickness variation on the device performance, *J–V* characterizations were conducted on the fabricated tandem solar cells (TSCs). Reference devices prepared with a 1.0 M top-cell precursor concentration exhibited a champion PCE of 22%, with an average efficiency of 20%. As shown in **Figure A4.10 (a)**, statistical analysis of other concentration variants reveals that devices fabricated with 0.6 M and 0.8 M precursors yielded lower average PCEs of 16.1% and 18.6%, respectively. Similarly, the 1.2 M variant also demonstrated a reduced average PCE of 18.7%. Among the photovoltaic parameters, the J_{SC} was the most significantly affected by top cell thickness variation, as expected and illustrated **in Figure A4.10 (b)**. The reference devices (1.0 M) achieved the highest average J_{SC} of 13.9 mA/cm^2, followed closely by the 0.8 M variant at 13.6 mA/cm^2, indicating better current matching between the subcells. The more divergent variants, 0.6 M and 1.2 M, exhibited lower average J_{SC} values of 12.7 mA/cm^2 and 12.9 mA/cm^2, respectively due to current mismatched between the subcells.

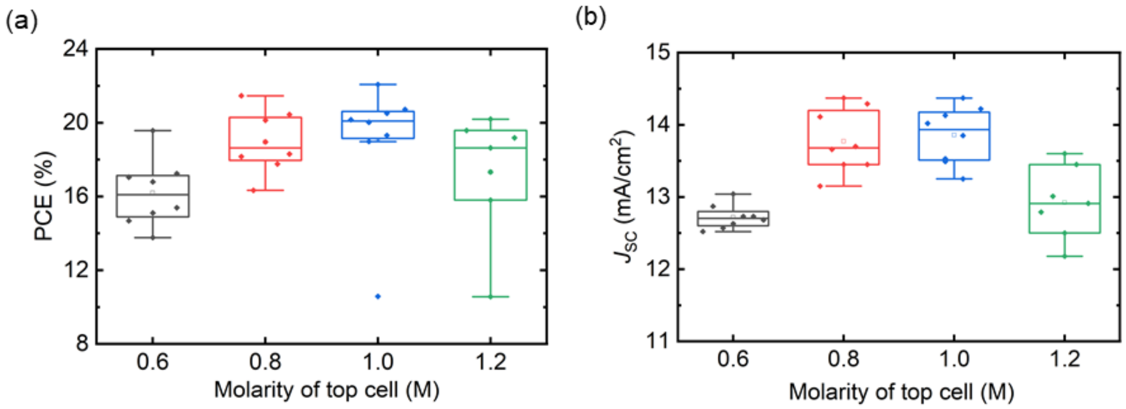

Figure A4.10: Statistical distribution of (a) power conversion efficiency (PCE) and (b) short-circuit current density (J_{SC}) of the all-perovskite tandem solar cells (TSCs) with different thickness of the top cell. The variation in PCE closely follows the J_{SC} generated by the TSCs.

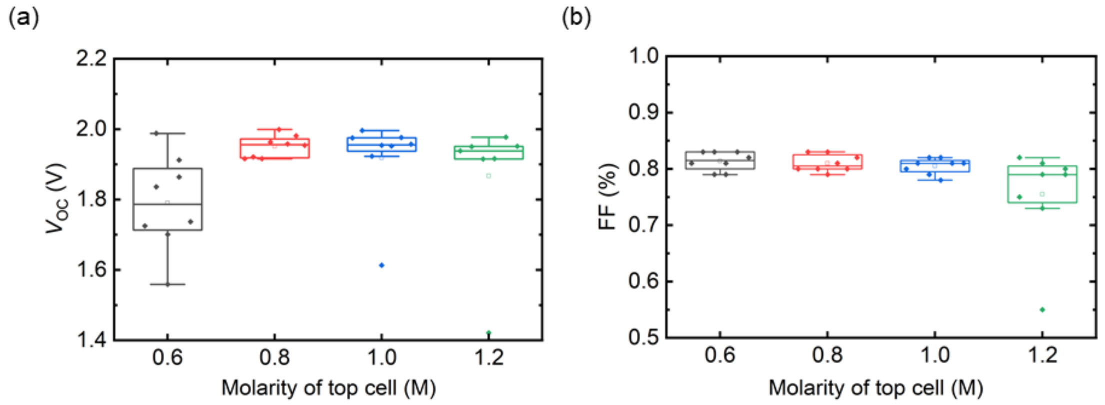

Figure A4.11: Statistical distribution of (a) open-circuit voltage (V_{OC}) and (b) Fill factor (FF) of the all-perovskite tandem solar cells (TSCs) with different thickness of the top cell.

Other photovoltaic parameters exhibited minimal variation with changes in the top-cell thickness. The reference device (1.0 M) demonstrated the highest V_{OC} of 2.00 V reflecting successful integration of the two subcells, with an average of ~ 1.95 V. Interestingly, the 0.8 M variant showed the highest average V_{OC} at 1.96 V. In contrast, the 0.6 M and 1.2 M devices exhibited slightly lower average V_{OC} of 1.79 V and 1.94 V, respectively (see **Figure A4.11 (a)**). The fill factor (FF) also remained relatively consistent across different variants, with both the 1.0 M and 1.2 M TSCs exhibiting an average FF of ~ 74%. These devices also demonstrate slightly more vertical and flat profiles before the knee of the *J-V* characterization. The 0.6 M and 0.8 M variants displayed slightly lower average FF values of ~ 70% as depicted in **Figure A4.11 (b),** possibly because of internal resistive losses. The photovoltaic performance parameters of the champion devices of each variant is shown in **Table A4.4**.

Table A4.4: Photovoltaic parameters and integrated J_{SC} of the champion all-perovskite TSCs with different WBG molarity.

Molarity (M)	PCE (%)	FF (%)	V_{OC} (V)	J_{SC} (mA/cm^2)	Int. $J_{SC(WBG)}$ (mA/cm^2)	Int. $J_{SC(NBG)}$ (mA/cm^2)
0.6	19.6	0.76	1.99	12.9	12.8	14.2
0.8	21.5	0.75	1.98	14.4	14.9	13.3
1.0	22.1	0.78	2.00	14.2	15.8	12.6
1.2	20.2	0.8	1.98	12.8	16.6	12.0

EQE measurements were conducted to further verify the J_{SC} contributions from the top and bottom subcells. A white light with an intensity of 70 mW/cm^2 was used as the primary illumination source. To isolate the response of the bottom subcell, a blue bias light (100 mW/cm^2) was employed to saturate the top subcell, thereby enabling accurate measurement of the bottom cell J_{SC}. Conversely, a red bias light of the same intensity was applied to saturate the bottom subcell, facilitating J_{SC} measurement of the top subcell under top cell limited conditions. Based on the EQE measurements only 0.6 M was top cell limited with 12.8 mA/cm^2 of integrated J_{SC}, a close match with the J_{SC} measured from *J-V* characterization. In other cases with the bottom cell limitations, the integrated J_{SC} from EQE characterization showed lower values of J_{SC} in comparison with the J_{SC} measured from the *J–V* characterization. A voltage bias in the EQE setup, along with light bias, can assist in efficient charge extraction from the bottom cell.

Figure A4.12 (a) shows the *J–V* characterizations of the champion TSCs of each variant. The higher value of J_{SC} exhibited in 0.8 M and 1.0 M directly influences the PCE of these devices, further confirming better current matching in the subcells leads to better performance in the 2T TSCs. In 0.6 M and 1.2 M variants, suboptimal photon absorption or increased optical/electrical losses leads to current mismatch between the top and bottom subcells and the PCE suffers. **Figure A4.12 (b)** displays the EQE spectra of the 2T all-perovskite TSCs. The devices fabricated with varying top-cell precursor molarity corresponds to different absorber layer thicknesses and influences the spectral response across the device stack.

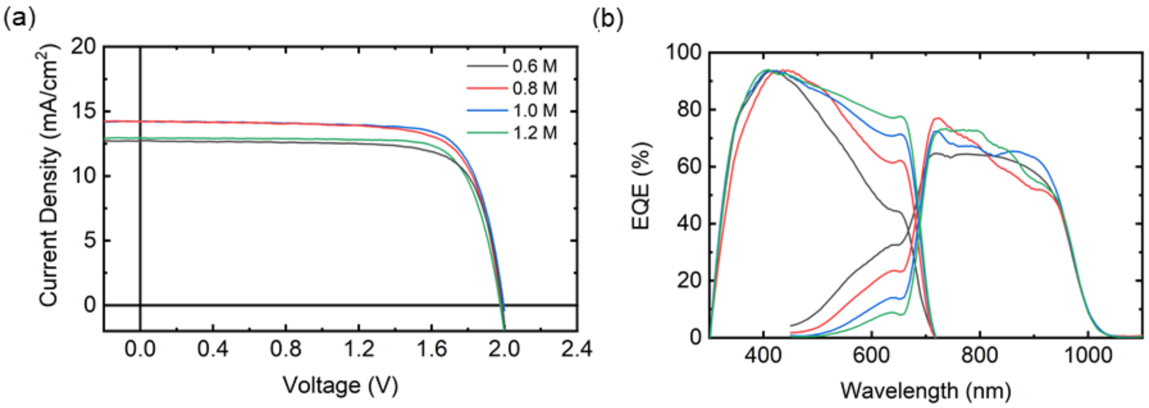

Figure A4.12: (a) Current density-voltage (*J*−*V*) characteristics of the champion all-perovskite tandem solar cells (TSCs) with varying thickness of the top cell and (b) External quantum efficiency (EQE) characterization for the corresponding champion all-perovskite TSCs.

The first half of the EQE spectra appears in the UV-VIS region (~350 - 750 nm), associated with the WBG top cell, which absorbs higher-energy photons. Across all variants, the peak EQE values in this region around 90%, indicating efficient photon harvesting by the top cell at ~ 400 nm. However, variation in curve height and slope reflects differences in absorption onset and spectral utilization due to the top cell thickness variation. Thinner top cells with 0.6 M and 0.8 M correspond to curves with earlier EQE roll-off after 400 nm, showing reduced absorption in this region, allowing more photons to reach the bottom subcell. Thicker top cells with 1.0 M and 1.2 M show stronger absorption up to ~700 nm. Good absorption in the top cell limits the photon flux to the bottom cell and reducing current in the bottom cell.

The second half of the EQE occurs beyond ~750 nm and is attributed to the NBG bottom cell. The absorption is sensitive to how much light is transmitted through the top cell. Devices with thinner top layers demonstrate higher EQE in the NIR region (~750 - 1000 nm), due to higher photon transmission to the bottom subcell. A crossover region (~700 - 750 nm) is observed between the responses of the two subcells, marking the transition in spectral contribution. This region is particularly sensitive to interferential effects, parasitic absorption, thickness of top cell and plays a crucial role in photon flux balancing between subcells. The best current matched variants 0.8 M and 1.0 M show a more balanced EQE area under both the top and bottom subcell curves. Devices with excessively thin or thick top absorbers exhibit asymmetric EQE responses, indicating photon imbalance and reduced TSC performance. The EQE characterization when integrated with the *J-V* characterization helps to elucidate the influence of top cell optical engineering on the device performance.

Current mismatch in the subcells and stability under ISOS-L1I

To investigate the impact of current mismatch between subcells on the long-term stability of all-perovskite TSCs, devices with varying thickness of the top cell were subjected to maximum power point (MPP) tracking measurements. Devices with 0.6 M of top cell, the only top cell limited variation exhibits a linear decay in power at MPP (P_m) throughout the interval of operation of 350 h, indicating poor operational stability (see **Figure A4.13 (a)**). This instability originates from a loss in current density at MPP (J_m) as shown in **Figure A4.13 (b)**. Insufficient absorption in the top cell results in top cell underperformance and higher susceptibility to degradation. Moreover, WBG cells are more susceptible to halide segregation that could further induce ionic migration [118], accumulation at the interfaces restricting charge collection [103]. TSCs with better current matching such as 0.8 M however, demonstrate excellent operational stability, maintaining nearly constant current over the entire testing period. Normalized J_m remains close to unity with minimal variation, indicating robust film quality and efficient current balancing between the subcells. This configuration appears to offer an ideal balance between optical absorption and photostability, suggesting superior top-cell thickness and morphology. Devices with higher current mismatch and bottom cell limitation as seen in 1.0 M also show a significant burn-in J_m within the first few hours. This exponential decrease is followed by a linear slow degradation reaching ~60% of the initial value. Despite its highest initial performance as observed in earlier *J-V* and EQE characterizations, this variant suffers from substantial instability over time. Interfacial instabilities or degradation in the NBG absorber layer could be one of the reasons behind the photoinduced degradation. The last and the worst performing variant with 1.2 M of top cell initially shows a sharp dip possibly due to light soaking effects or interfacial ion migration, followed by a notable recovery and gradual stabilization. Light induced trap passivation in films of poor quality with high trap density could result in such behavior [216]. The devices stabilize around ~90% of the initial J_m, showing delayed but acceptable recovery behavior. The thicker top cell enable better photon absorption but at the cost of initial instability due to potential internal stress or increased defect density.

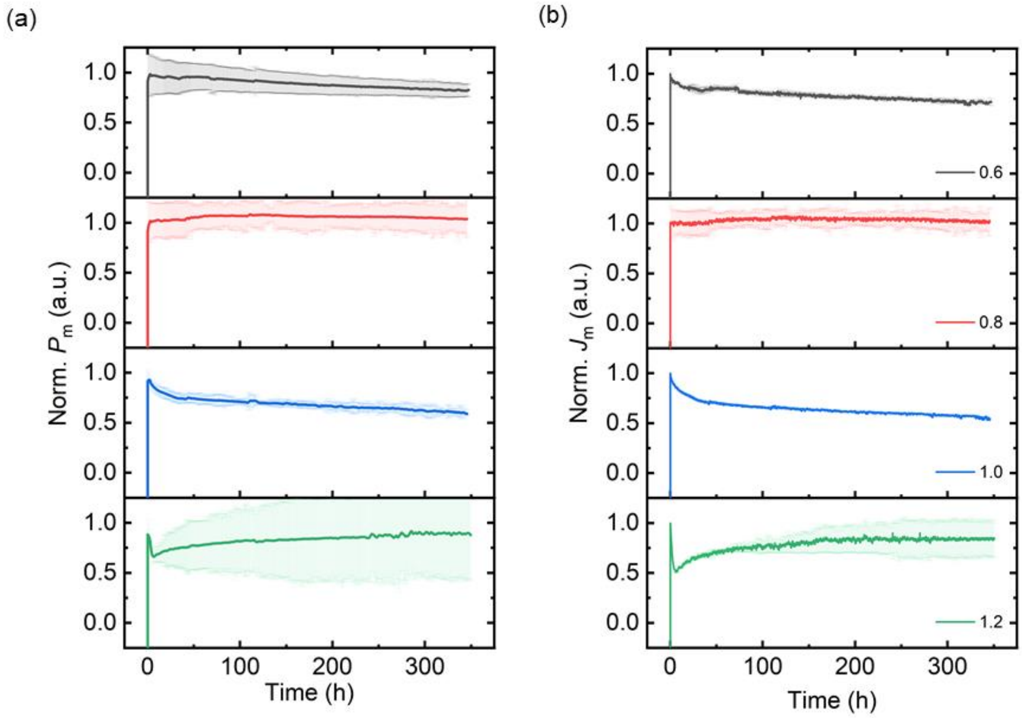

Figure A4.13: Normalized (a) power and (b) current density at the maximum power point (MPP) tracking of all-perovskite tandem solar cells (TSCs) with varying thickness of the top cell.

Surprisingly, 1.2 M are the only variants that exhibit gradual loss in voltage at MPP (V_m), confirming our hypothesis of high trap density and poor film quality (see **Figure A4.14**). Devices with varied molarity of top cell from 0.6 M to 1.0 M show very stable V_m during the entire 300 h.

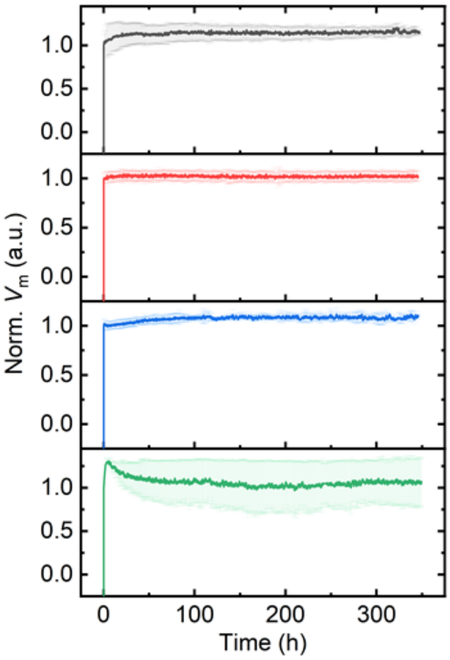

Figure A4.14: Normalized (a) voltage at the maximum power point (MPP) tracking of all-perovskite tandem solar cells (TSCs) with varying thickness of the top cell. The variation in thickness was induced by changing molarity of the precursor solution: 0.6 M (black), 0.8 M (red), 1.0 M (blue) and 1.2 M (green).

This approach facilitates a comprehensive understanding of how limitations in individual subcells affect the operational stability and degradation pathways of all-perovskite TSCs over prolonged periods. By deliberately inducing current limitation in a specific subcell, the resulting accelerated degradation highlights the underlying weaknesses and failure mechanisms within that subcell. Identifying and mitigating these subcell-specific issues allows for targeted optimization, ultimately leading to a more robust tandem architecture that combines high performance with long-term operational stability.

Post degradation analysis of individual subcells

Identifying the origins of subcell-specific instability, as highlighted in the previous section, is essential for uncovering the root causes of degradation and implementing effective mitigation strategies to address them. In this section, post-degradation analysis on the aged tandem devices is conducted to evaluate the extent and the cause of performance loss. Spectrally resolved characterization technique, such as EQE serve as a powerful diagnostic tool for probing subcell-level, wavelength-specific degradation and elucidating the mechanisms responsible for long-term performance decline.

Comparison of the EQE characterization before and after the accelerated stress testing ISOS-L1I for varying thickness of WBG is depicted in **Figure A4.15**. In the case of WBG limitation, both top and bottom subcell undergo minimal degradation post stress testing (see **Figure A4.15 (a)**). One of the major degradation mechanism anticipated for WBG degradation is halide segregation. However, halide segregation are partially recoverable in the dark. Post stress testing, when devices are moved to EQE setup for characterization, light and voltage bias are absent. This could be a reason behind such a recovery. In the case of the bottom cell limitation, the bottom cell undergoes degradation, however, more degradation is observed in the top cell. This phenomenon is observed in all three cases of bottom cell limitation (see **Figure A4.15 (b)-(d)**) where, the intensity of the EQE for WBG decreases below 80%. The most extreme is the case of 1.2 M of WBG, where the top cell degrades below 80% and the NBG degrades below 60% of the EQE intensity. In case of bottom cell limitation, the excess charge carriers in the WBG top cell cannot be extracted efficiently. This leads to charge accumulation with increased probability of non-radiative recombination. WBG perovskites are less stable thermodynamically than their NBG counterparts. If the bottom cell severely limits current or degrades as seen in the case of 1.2 M, the WBG can be put into reverse bias triggering electrochemical instability and field-induced ion migration [335].

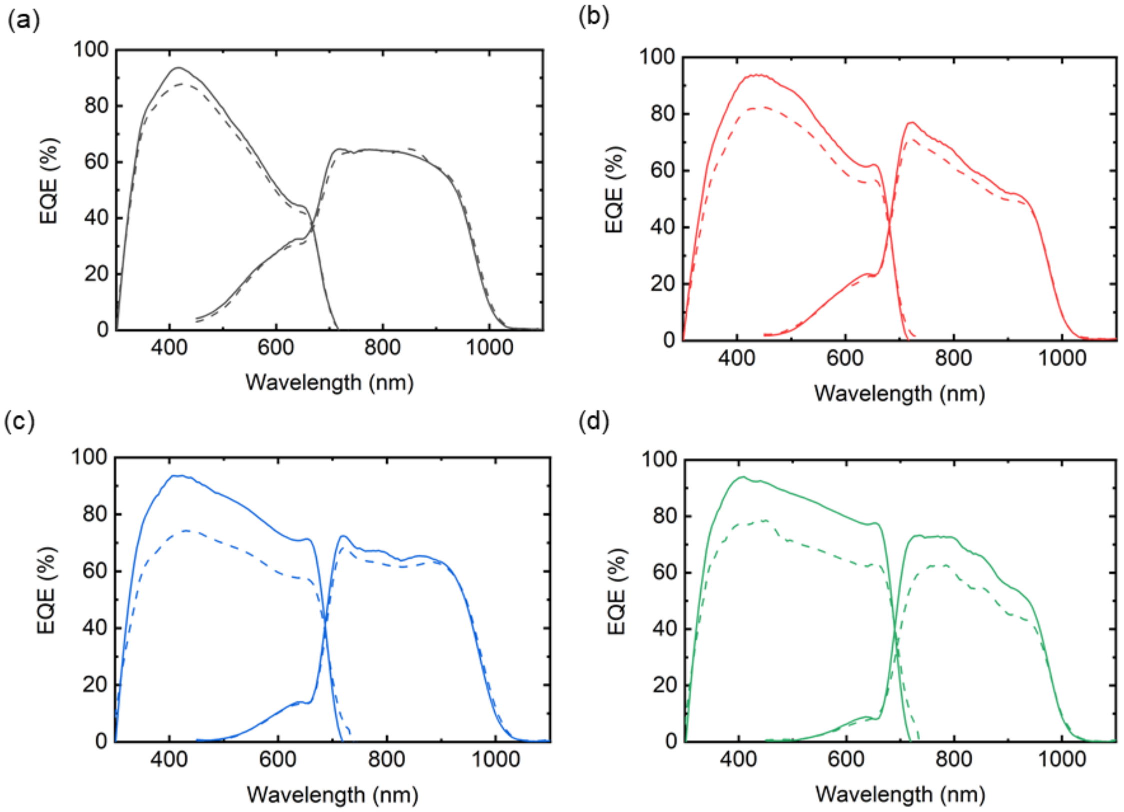

Figure A4.15: External quantum efficiency (EQE) characterization of the all-perovskite tandem solar cells before (solid line) and after (dotted line) aged under ISOS-L1I stress test. The variation in thickness was induced by changing molarity of the precursor solution: 0.6 M (black), 0.8 M (red), 1.0 M (blue) and 1.2 M (green).

The hysteresis of pristine TSCs are more pronounced in case of bottom cell limitation (see **Figure A4.16)**. As a result, a sharp decrease in P_m and J_m is visible for 1.2 M as seen in **Figure A4.16 (a)** and **Figure A4.16 (b)**. The *J-V* characterization performed post degradation shows the hysteresis further increases post stress test pointing towards poor conductivity of charge transport layers or poor interfacial qualities. These results confirm that the current matching in subcells are critical not just for performance, but also for the long-term stability of all-perovskite tandem solar cells.

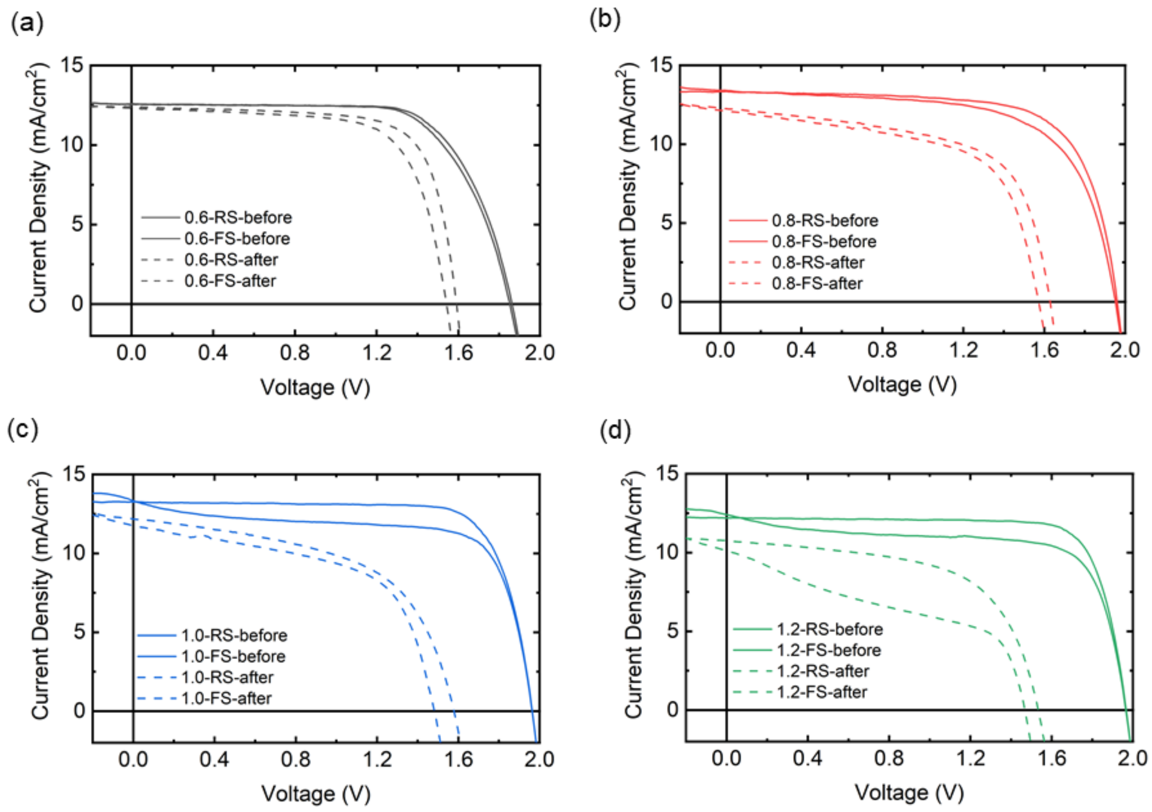

Figure A4.16: Before-after comparison of current density-voltage ($J-V$) characteristics of the all-perovskite tandem solar cells aged under ISOS-L1I stress test.

Summary

Dynamic environmental conditions, such as spectral shifts, changes in irradiance and temperature variations can exacerbate current mismatch in TSCs, decreasing the device performance and compromising with long-term stability. The situation is worsened when one of the subcell is less stable than the other is and undergoes permanent degradation. Hence, it is important to understand the root cause of degradation of each subcell such that strategies can be mitigated to address the subcell specific degradation problem. In order to probe into the instability issue within the subcells, subcell limitation was deliberately induced by engineering the thickness of the WBG top cell via precursor molarity variation. From the performance parameters and monitoring the operational stability suggests that current matching and film quality are correlated to initial device performance as well as long-term stability retention of the all-perovskite TSCs. The 0.8 M device outperforms others in terms of operational stability, highlighting the importance of moderate absorber thickness that ensures sufficient absorption in the top cell while maintaining favorable transmission to the bottom cell. On the other hand, both lower (0.6 M) and higher (1.0 M, 1.2 M) molarity values introduce undesirable effects. Too thin layer of WBG results in poor light harvesting and increased vulnerability to degradation with halide segregation, while too thick WBG layer may suffer from increased strain, high trap density or ion migration, all of which can accelerate degradation. The case of the 1.2 M device, which recovers after initial degradation, could be indicative of reversible ionic migration or trap passivation. This illustrates how device engineering must strike a balance between achieving optimal PCE and ensuring device stability, a core challenge for commercializing perovskite TSCs.

B. Appendix of Chapter 5

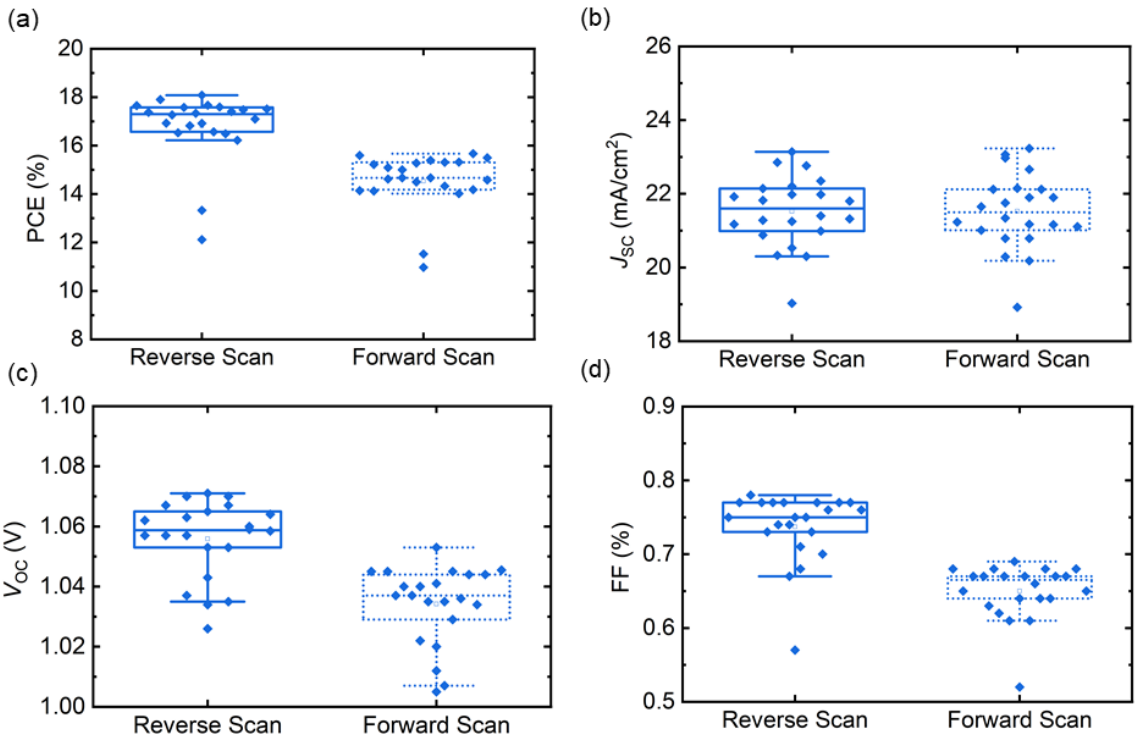

Figure A5.1: Statistics for bifacial $Cs_{0.17}FA_{0.83}PbI_3$ PSCs: (a) power conversion efficiency (PCE) (b) short-circuit current density (J_{SC}) (c) open circuit voltage (V_{OC}) and (d) fill factor (FF) for reverse scan (solid line) and forward scan (dotted line). Current density-voltage (*J-V)* characterization was measured at a scan rate of 600 mV/s.

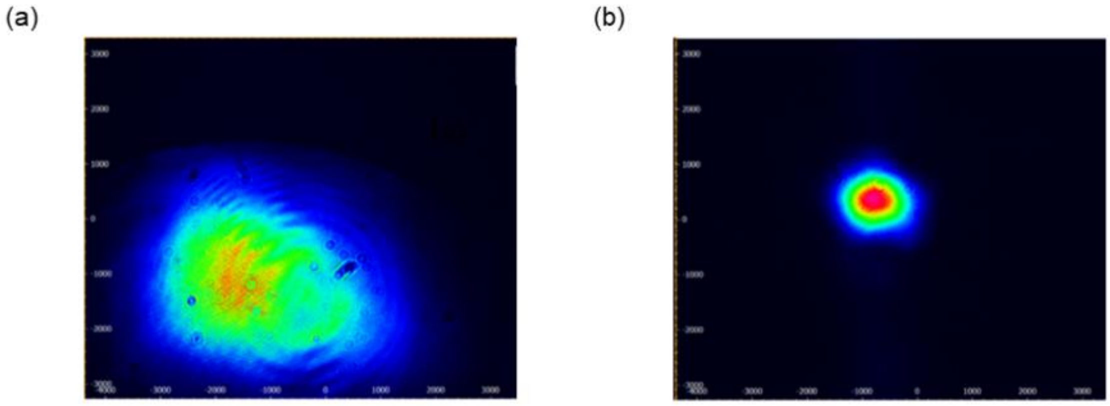

Figure A5.2: Measurement of the X and Y axis of the beam spot for calculation of beam spot (A_{spot}) for laser source (a) w/o lens and (b) with lens (focal length=100cm)

C. Appendix of Chapter 6

Figure A6.1: Cabinet with with electrical components to protect them from environmental factors.

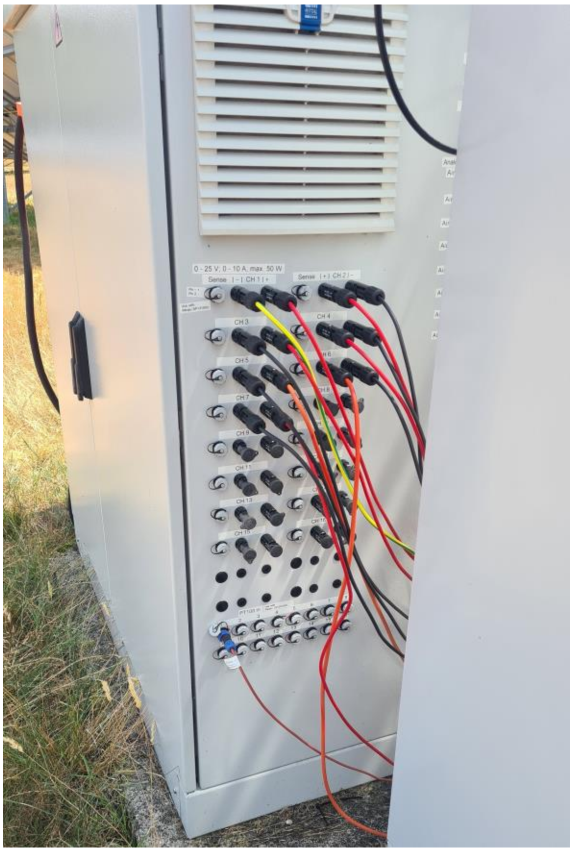

Figure A6.2: The connections for solar cells (red and black wires) and for temperature sensor (brown wire).

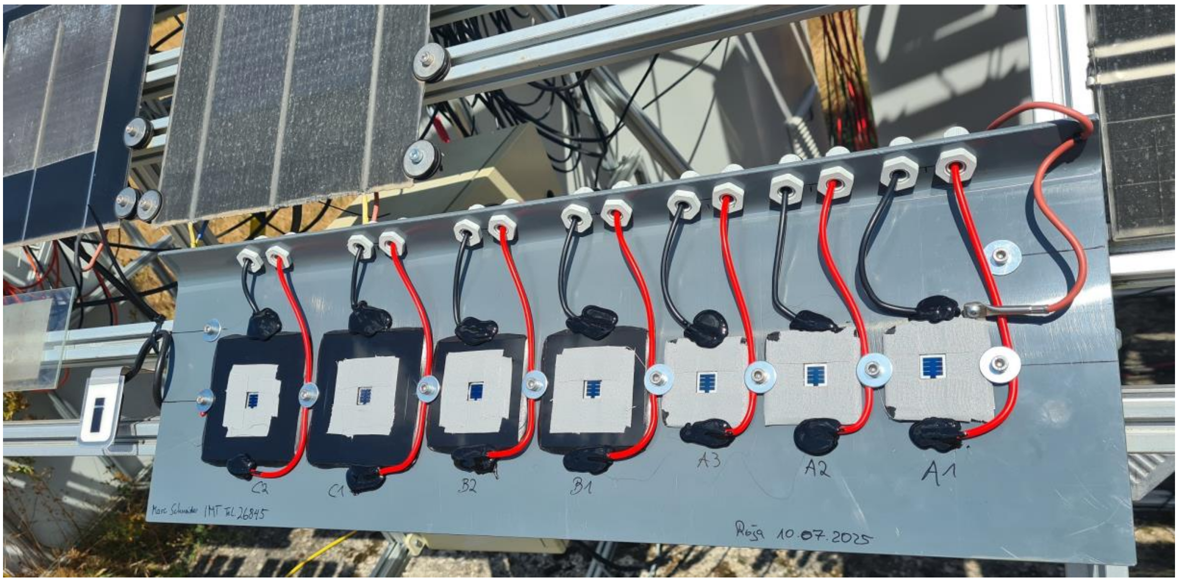

Figure A6.3: Sample board for securing encapsulated solar cells on the Bosch profile. The temperature sensor with brown wire is connected at the back of one of the samples. The reference cell (white) is on the left side of the sample board.

Figure A6.4: Waterproof MC4 connectors for connecting solar cells with the electrical connectors. The connection of irradiance sensor (black) and LAN (blue/red) to the cabinet is also waterproof.

Figure A6.5: Bosch profile structure for fastening solar cells for measurement in the outdoor condition. A camera monitors the samples for obstruction.

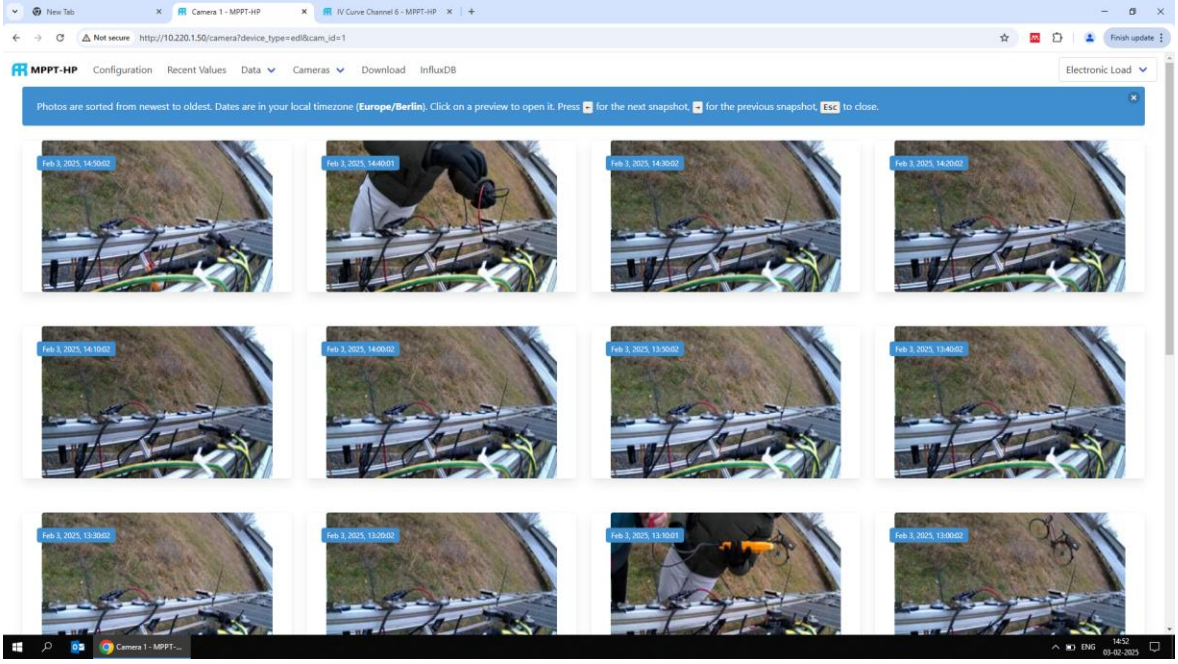

Photos are sorted from newest to oldest. Dates are in your local timezone (**Europe/Berlin**). Click on a preview to open it. Press ← for the next snapshot, → for the previous snapshot, Esc to close.

Figure A6.6: Time stamped images from the camera for monitoring the samples

Adaptive perturb and observe algorithm

Adaptive perturb and observe is an updated version [327] of the perturb and observe algorithm. Modifications introduced in this algorithm offer better tracking efficiency and stability under dynamic conditions [328].

- First voltage V_m(k) and current I_m(k) of the solar cell is measured and power P_m(k) is calculated. Here k is the kth instance and V_m, I_m and P_m are the voltage, current and power at MPP
- The differences in voltage output (ΔV_m(k)) = V_m(k) - V_m(k-1) is calculated and the difference in power output (ΔP_m(k)) = P_m(k) - P_m(k-1) is calculated.
- A step size S(k) dynamically is determined, proportional to $|\Delta P_m(k)|$
- Perturb voltage by S(k) in the current direction
- If ΔP(k)>0, continue perturbing in same direction
- If ΔP(k)<0, reverse the perturb direction
- Update the step size S (k+1) based on new measurement.

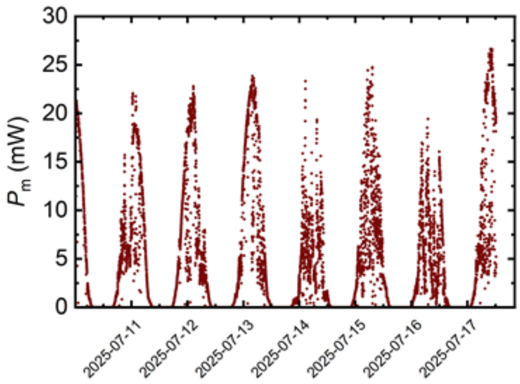

Figure A6.7: First dataset generated using adaptive perturb and observe algorithm.

References

[1] United Nations Climate Change *Paris agreement* https://unfccc.int/process-and-meetings/the-paris-agreement (Accessed: 03-Jun-2025)

[2] IEA *Share of renewable electricity generation by technology, 2000-2030* https://www.iea.org/data-and-statistics/charts/share-of-renewable-electricity-generation-by-technology-2000-2030 (Accessed: 03-Jun-2025)

[3] Fraunhofer *Photovoltaic report* https://www.ise.fraunhofer.de/en/publications/studies/photovoltaics-report.html. (Accessed: 03-May-2025).

[4] NREL *Best Research-Cell Efficiency Chart* https://www.nrel.gov/pv/cell-efficiency.html. (Accessed: 03-Jun-2025).

[5] R. Prasanna *et al.*, "Band Gap Tuning via Lattice Contraction and Octahedral Tilting in Perovskite Materials for Photovoltaics," *J. Am. Chem. Soc.*, vol. 139, no. 32, pp. 11117–11124, 2017.

[6] T. J. Jacobsson *et al.*, "Exploration of the compositional space for mixed lead halogen perovskites for high efficiency solar cells," *Energy Environ. Sci.*, vol. 9, no. 5, pp. 1706–1724, 2016.

[7] J. J. Cordell *et al.*, "Technoeconomic analysis of perovskite/silicon tandem solar modules," *Joule*, vol. 9, no. 2, p. 101781, 2025.

[8] N. N. Lal *et al.*, "Optics and Light Trapping for Tandem Solar Cells on Silicon," *IEEE J. Photovoltaics*, vol. 4, no. 6, pp. 1380–1386, 2014.

[9] K. Alberi *et al.*, "A roadmap for tandem photovoltaics," *Joule*, vol. 8, no. 3, pp. 658–692, Mar. 2024.

[10] B. S. Richards *et al.*, "Enhancing the performance of silicon solar cells via the application of passive luminescence conversion layers," *Sol. Energy Mater. Sol. Cells*, vol. 90, no. 15, pp. 2329–2337, 2006.

[11] B. S. Richards *et al.*, "Luminescent layers for enhanced silicon solar cell performance: Down-conversion," *Sol. Energy Mater. Sol. Cells*, vol. 90, no. 9, pp. 1189–1207, 2006.

[12] H. Zhu *et al.*, "Bridgman Method for Growing Metal Halide Single Crystals: A Review," *Inorganics*, vol. 13, no. 2. 2025.

[13] C. Yang *et al.*, "Achievements, challenges, and future prospects for industrialization of perovskite solar cells," *Light Sci. Appl.*, vol. 13, no. 1, p. 227, 2024.

[14] D. B. Ritzer *et al.*, "Upscaling of perovskite solar modules: The synergy of fully evaporated layer fabrication and all-laser-scribed interconnections," *Prog. Photovoltaics Res. Appl.*, vol. 30, no. 4, pp. 360–373, 2022.

[15] K. Geistert *et al*, "Controlling Thin Film Morphology Formation during Gas Quenching of Slot-Die Coated Perovskite Solar Modules," *ACS Appl. Mater. Interfaces*, vol. 15, no. 45, pp. 52519–52529, 2023.

[16] H. Eggers *et al.*, "Perovskite Solar Cells with Vivid, Angle-Invariant, and Customizable Inkjet-Printed Colorization for Building-Integrated Photovoltaics," *Sol. RRL*, vol. 6, no. 4, p. 2100897, 2022.

[17] H. Hu *et al.*, "Void-free buried interface for scalable processing of p-i-n-based $FAPbI_3$ perovskite solar modules," *Joule*, vol. 7, no. 7, pp. 1574–1592, 2023.

[18] Y. Miao *et al.*, “Green solvent enabled scalable processing of perovskite solar cells with high efficiency,” *Nat. Sustain.*, vol. 6, no. 11, pp. 1465–1473, 2023.

[19] C. Duan *et al.*, “Scalable fabrication of wide-bandgap perovskites using green solvents for tandem solar cells,” *Nat. Energy*, vol. 10, no. 3, pp. 318–328, 2025.

[20] B. Abdollahi Nejand *et al.*, “Scalable two-terminal all-perovskite tandem solar modules with a 19.1% efficiency,” *Nat. Energy*, vol. 7, no. 7, pp. 620–630, 2022.

[21] S. Baumann *et al.*, “Stability and reliability of perovskite containing solar cells and modules: degradation mechanisms and mitigation strategies,” *Energy Environ. Sci.*, vol. 17, no. 20, pp. 7566–7599, 2024.

[22] T. J. Silverman *et al.*, “Durability research is pivotal for perovskite photovoltaics,” *Nat. Energy*, 2025.

[23] J. H. Wohlgemuth *et al.*, “Long Term Reliability of Photovoltaic Modules,” in *2006 IEEE 4th World Conference on Photovoltaic Energy Conference*, vol. 2, pp. 2050–2053, 2006.

[24] M. Khenkin *et al.*, “Light cycling as a key to understanding the outdoor behaviour of perovskite solar cells,” *Energy Environ. Sci.*, vol. 17, no. 2, pp. 602–610, 2024.

[25] M. Remec *et al.*, “From Sunrise to Sunset: Unraveling Metastability in Perovskite Solar Cells by Coupled Outdoor Testing and Energy Yield Modelling,” *Adv. Energy Mater.*, p. 2304452, 2024.

[26] R. K. Gupta *et al.*, “Seasonal Effects on Outdoor Stability of Perovskite Solar Cells,” *Adv. Energy Mater.*, vol. 15, no. 8, p. 2403844, 2025.

[27] F. J. Pern, “Ethylene-vinyl acetate (EVA) encapsulants for photovoltaic modules: Degradation and discoloration mechanisms and formulation modifications for improved photostability,” *Die Angew. Makromol. Chemie*, vol. 252, no. 1, pp. 195–216, 1997.

[28] B. Adothu *et al.*, “Newly developed thermoplastic polyolefin encapsulant–A potential candidate for crystalline silicon photovoltaic modules encapsulation,” *Sol. Energy*, vol. 194, pp. 581–588, 2019.

[29] J. Schmidtke, “Commercial status of thin-film photovoltaic devices and materials,” *Opt. Express*, vol. 18, no. S3, pp. A477–A486, 2010.

[30] G. J. Jorgensen *et al.*, “Moisture transport, adhesion, and corrosion protection of PV module packaging materials,” *Sol. Energy Mater. Sol. Cells*, vol. 90, no. 16, pp. 2739–2775, 2006.

[31] S. S. Hegedus and B. E. McCandless, “CdTe contacts for CdTe/CdS solar cells: effect of Cu thickness, surface preparation and recontacting on device performance and stability,” *Sol. Energy Mater. Sol. Cells*, vol. 88, no. 1, pp. 75–95, 2005.

[32] S. De Wolf *et al.*, “Organometallic Halide Perovskites: Sharp Optical Absorption Edge and Its Relation to Photovoltaic Performance,” *J. Phys. Chem. Lett.*, vol. 5, no. 6, pp. 1035–1039, 2014.

[33] S. D. Stranks *et al.*, “Electron-hole diffusion lengths exceeding 1 micrometer in an organometal trihalide perovskite absorber,” *Science.*, vol. 342, no. 6156, pp. 341–344, 2013.

[34] Y. Chen *et al.*, “Extended carrier lifetimes and diffusion in hybrid perovskites revealed by Hall effect and photoconductivity measurements,” *Nat. Commun.*, vol. 7, p. 12253, Aug. 2016.

[35] C. Wehrenfennig, G. E. Eperon, M. B. Johnston, H. J. Snaith, and L. M. Herz, “High Charge Carrier Mobilities and Lifetimes in Organolead Trihalide Perovskites,” *Adv. Mater.*, vol. 26, no. 10, pp. 1584–1589, 2014.

[36] Z. Xiao and Y. Yan, “Progress in Theoretical Study of Metal Halide Perovskite Solar Cell Materials,” *Adv. Energy Mater.*, vol. 7, no. 22, 2017.

[37] J. P. Correa-Baena *et al.*, “Promises and challenges of perovskite solar cells,” *Science*, vol. 358, no. 6364, pp. 739–744, 2017.

[38] T. A. S. Doherty *et al.*, “Stabilized tilted-octahedra halide perovskites inhibit local formation of performance-limiting phases,” *Science,* vol. 374, no. 6575, pp. 1598–1605, 2021.

[39] S. Arrhenius *et al.*, “Formability of ABX_3 (X = F, Cl, Br, I) halide perovskites,” *Acta Crystallogr. Sect. B Struct. Sci.*, vol. 64, no. 6, pp. 702–707, 2008.

[40] R. J. D. Tilley *et al.*, *Perovskites: Structure–Property Relationships,* vol. 42, no. 4. 2017.

[41] W. Travis *et al.*, “On the application of the tolerance factor to inorganic and hybrid halide perovskites: a revised system,” *Chem. Sci.*, vol. 7, no. 7, pp. 4548–4556, 2016.

[42] M. Saliba *et al.*, “Cesium-containing Triple Cation Perovskite Solar Cells: Improved Stability, Reproducibility and High Efficiency,” *Energy Environ. Sci.*, no. 9, pp. 1989-1997, 2016.

[43] W.J. Yin *et al.*, “Unique Properties of Halide Perovskites as Possible Origins of the Superior Solar Cell Performance,” *Adv. Mater.*, vol. 26, no. 27, pp. 4653–4658, 2014.

[44] G. Kieslich *et al.*, “Solid-state principles applied to organic–inorganic perovskites: new tricks for an old dog,” *Chem. Sci.*, vol. 5, no. 12, pp. 4712–4715, 2014.

[45] M. Becker *et al.*, “Formation of hybrid ABX_3 perovskite compounds for solar cell application: first-principles calculations of effective ionic radii and determination of tolerance factors,” *Dalt. Trans.*, vol. 46, no. 11, pp. 3500–3509, 2017.

[46] F. Hao *et al.*, “Anomalous Band Gap Behavior in Mixed Sn and Pb Perovskites Enables Broadening of Absorption Spectrum in Solar Cells,” *J. Am. Chem. Soc.*, vol. 136, no. 22, pp. 8094–8099, 2014.

[47] J. Im *et al.*, “Antagonism between Spin–Orbit Coupling and Steric Effects Causes Anomalous Band Gap Evolution in the Perovskite Photovoltaic Materials $CH_3NH_3Sn_{1-x}Pb_xI_3$,” *J. Phys. Chem. Lett.*, vol. 6, no. 17, pp. 3503–3509, 2015.

[48] T. J. Jacobsson *et al.*, “Exploration of the compositional space for mixed lead halogen perovskites for high efficiency solar cells,” *Energy Environ. Sci.*, vol. 9, no. 5, pp. 1706–1724, 2016.

[49] S. Gharibzadeh *et al.*, “2D/3D Heterostructure for Semitransparent Perovskite Solar Cells with Engineered Bandgap Enables Efficiencies Exceeding 25% in Four-Terminal Tandems with Silicon and CIGS,” *Adv. Funct. Mater.*, vol. 30, no. 19, p. 1909919, 2020.

[50] J. H *et al.*, “Chemical management for colorful, efficient, and stable inorganic-organic hybrid nanostructured solar cells,” *Nano Lett.*, vol. 13, no. 4, pp. 1764–1769, 2013.

[51] M. H. Futscher *et al.*, “Efficiency Limit of Perovskite/Si Tandem Solar Cells,” *ACS Energy Lett.*, vol. 1, no. 4, pp. 863–868, 2016.

[52] J. Chen *et al.*, “Causes and Solutions of Recombination in Perovskite Solar Cells,” *Adv. Mater.*, vol. 31, no. 47, p. 1803019, 2019.

[53] Peter Würfel, “Physics of Solar cell,” in *Physics of Solar Cells: From Principles to New Concepts*, .

[54] U. Würfel *et al.*, “Charge Carrier Separation in Solar Cells,” *IEEE J. Photovoltaics*, vol. 5, no. 1, pp. 461–469, 2015.

[55] P. Caprioglio *et al.*, “On the Relation between the Open-Circuit Voltage and Quasi-Fermi Level Splitting in Efficient Perovskite Solar Cells,” *Adv. Energy Mater.*, vol. 9, no. 33, p. 1901631, 2019.

[56] T. Hellmann *et al.*, “The Electronic Structure of MAPI-Based Perovskite Solar Cells: Detailed

Band Diagram Determination by Photoemission Spectroscopy Comparing Classical and Inverted Device Stacks," *Adv. Energy Mater.*, vol. 10, no. 42, p. 2002129, 2020.

[57] P. Lopez-Varo *et al.*, "Device Physics of Hybrid Perovskite Solar cells: Theory and Experiment," *Adv. Energy Mater.*, vol. 8, no. 14, pp. 1–36, 2018.

[58] C. R. Osterwald *et al.*, "IV-1 - Standards, Calibration and Testing of PV Modules and Solar Cells," Elsevier Science, pp. 793–816, 2003.

[59] W. Shockley *et al.*, "Detailed balance limit of efficiency of p-n junction solar cells," *J. Appl. Phys.*, vol. 32, no. 3, pp. 510–519, 1961.

[60] S. Rühle, "Tabulated values of the Shockley-Queisser limit for single junction solar cells," *Sol. Energy*, vol. 130, pp. 139–147, 2016.

[61] K. Yoshikawa *et al.*, "Silicon heterojunction solar cell with interdigitated back contacts for a photoconversion efficiency over 26%," *Nat. Energy*, vol. 2, no. 5, p. 17032, 2017.

[62] T. Tiedje2003,, "Limiting efficiency of silicon solar cells," *IEEE Trans. Electron Devices*, vol. 31, no. 5, pp. 711–716, 1984.

[63] M. Yamaguchi, "Multi-junction solar cells and novel structures for solar cell applications," *Phys. E Low-dimensional Syst. Nanostructures*, vol. 14, no. 1, pp. 84–90, 2002.

[64] S. Liu *et al.*, "Triple-junction solar cells with cyanate in ultrawide-bandgap perovskites," *Nature*, vol. 628, no. 8007, pp. 306–312, 2024.

[65] D. M. Kroupa *et al.*, "Quantum-Cutting Ytterbium-Doped $CsPb(Cl_{1-x}Br_x)_3$ Perovskite Thin Films with Photoluminescence Quantum Yields over 190%," *ACS Energy Lett.*, vol. 3, no. 10, pp. 2390–2395, 2018.

[66] V. M. Andreev *et al.*, "Concentrator PV modules and solar cells for TPV systems," *Sol. Energy Mater. Sol. Cells*, vol. 84, no. 1, pp. 3–17, 2004.

[67] Q. Lin *et al.*, "Hybrid Perovskites: Prospects for Concentrator Solar Cells," *Adv. Sci.*, vol. 5, no. 4, p. 1700792, 2018.

[68] M. Yamaguchi, "III–V compound multi-junction solar cells: present and future," *Sol. Energy Mater. Sol. Cells*, vol. 75, no. 1, pp. 261–269, 2003.

[69] P. Löper *et al.*, "Organic–inorganic halide perovskite/crystalline silicon four-terminal tandem solar cells," *Phys. Chem. Chem. Phys.*, vol. 17, no. 3, pp. 1619–1629, 2015.

[70] F. Lang *et al.*, "Perovskite Solar Cells with Large-Area CVD-Graphene for Tandem Solar Cells," *J. Phys. Chem. Lett.*, vol. 6, no. 14, pp. 2745–2750, 2015.

[71] J. Werner *et al.*, "Efficient Near-Infrared-Transparent Perovskite Solar Cells Enabling Direct Comparison of 4-Terminal and Monolithic Perovskite/Silicon Tandem Cells," *ACS Energy Lett.*, vol. 1, no. 2, pp. 474–480, 2016.

[72] J. P. Mailoa *et al.*, "A 2-terminal perovskite/silicon multijunction solar cell enabled by a silicon tunnel junction," *Appl. Phys. Lett.*, vol. 106, no. 12, p. 121105, 2015.

[73] C. D. Bailie *et al.*, "Semi-transparent perovskite solar cells for tandems with silicon and CIGS," *Energy Environ. Sci.*, vol. 8, no. 3, pp. 956–963, 2015.

[74] S. Albrecht *et al.*, "Monolithic perovskite/silicon-heterojunction tandem solar cells processed at low temperature," *Energy Environ. Sci.*, vol. 9, no. 1, pp. 81–88, 2016.

[75] N. N. Lal *et al.*, "Perovskite Tandem Solar Cells," *Adv. Energy Mater.*, vol. 7, no. 18, p. 1602761, Sep. 2017.

[76] E. Köhnen *et al.*, "Highly efficient monolithic perovskite silicon tandem solar cells: analyzing the influence of current mismatch on device performance," *Sustain. Energy Fuels*, vol. 3, no. 8, pp. 1995–2005, 2019.

[77] Solliance *Two world-records for 4T perovskite tandem* https://www.solliance.eu/2021/two-world-records-for-4t-perovskite-tandem/. (Accessed: 26-Jun-2025).

[78] H. Liang *et al.*, “29.9%-efficient, commercially viable perovskite/$CuInSe_2$ thin-film tandem solar cells,” *Joule*, vol. 7, no. 12, pp. 2859–2872, 2023.

[79] T. Trupke *et al.*, “Improving solar cell efficiencies by down-conversion of high-energy photons,” *J. Appl. Phys.*, vol. 92, no. 3, pp. 1668–1674, 2002.

[80] M. Kaiser *et al.*, “Power-dependent upconversion quantum yield of $NaYF_4:Yb^{3+},Er^{3+}$ nano- and micrometer-sized particles – measurements and simulations,” *Nanoscale*, vol. 9, no. 28, pp. 10051–10058, 2017.

[81] X. Chen *et al.*, “Highly Efficient $LiYF_4:Yb^{3+}$, Er^{3+} Upconversion Single Crystal under Solar Cell Spectrum Excitation and Photovoltaic Application,” *ACS Appl. Mater. Interfaces*, vol. 8, no. 14, pp. 9071–9079, 2016.

[82] K. Yamamoto, M. Fujii, S. Sowa, K. Imakita, and K. Aoki, “Upconversion Luminescence of Rare-Earth-Doped Y_2O_3 Nanoparticle with Metal Nano-Cap,” *J. Phys. Chem. C*, vol. 119, no. 2, pp. 1175–1179, 2015.

[83] H. Guo, N. Dong, M. Yin, W. Zhang, L. Lou, and S. Xia, “Visible Upconversion in Rare Earth Ion-Doped Gd_2O_3 Nanocrystals,” *J. Phys. Chem. B*, vol. 108, no. 50, pp. 19205–19209, 2004.

[84] M. Kinoshita *et al.*, “Photon Upconverting Solid Films with Improved Efficiency for Endowing Perovskite Solar Cells with Near-Infrared Sensitivity,” *ChemPhotoChem*, vol. 4, no. 11, pp. 5271–5278, 2020.

[85] T. Trupke *et al.*, “Improving solar cell efficiencies by up-conversion of sub-band-gap light,” *J. Appl. Phys.*, vol. 92, no. 7, pp. 4117–4122, 2002.

[86] N. A. M. Saeed *et al.*, “Down-conversion of YOF: Pr^{3+}, Yb^{3+} phosphor,” *Opt. Mater. (Amst).*, vol. 110, pp. 110516, 2020.

[87] G. Jiang, *et al.*, “Broadband downconversion in $YVO_4:Tm^{3+},Yb^{3+}$ phosphors,” *J. Rare Earths*, vol. 31, no. 1, pp. 27–31, 2013.

[88] B. Sadeghimakki *et al.*, “Proof of down-conversion by CdSe/ZnS quantum dots on silicon solar cells,” in *2014 IEEE 40th Photovoltaic Specialist Conference (PVSC)*, pp. 2262–2266, 2014.

[89] V. Badescu *et al.*, “Improved model for solar cells with down-conversion and down-shifting of high-energy photons,” *J. Phys. D. Appl. Phys.*, vol. 40, no. 2, p. 341, 2007.

[90] V. Badescu *et al.*, “Influence of some design parameters on the efficiency of solar cells with down-conversion and down shifting of high-energy photons,” *J. Appl. Phys.*, vol. 102, no. 7, p. 73102, 2007.

[91] W. G. J. H. M. van Sark *et al.*, “Simulating performance of solar cells with spectral downshifting layers,” *Thin Solid Films*, vol. 516, no. 20, pp. 6808–6812, 2008.

[92] G. Shao *et al.*, “Luminescent down shifting effect of Ce-doped yttrium aluminum garnet thin films on solar cells,” *Appl. Phys. Lett.*, vol. 107, no. 25, pp. 253904, 2015.

[93] J. C. Goldschmidt, “Novel Solar Cell Concepts,” University of Konstanz, 2009.

[94] Q. Liu, H. Liu, D. Li, W. Qiao, G. Chen, and H. Ågren, “Microlens array enhanced upconversion luminescence at low excitation irradiance,” *Nanoscale*, vol. 11, no. 29, pp. 14070–14078, 2019.

[95] C. Tummeltshammer *et al.*, “Losses in luminescent solar concentrators unveiled,” *Sol. Energy Mater. Sol. Cells*, vol. 144, pp. 40–47, 2016.

[96] M. Que *et al.*, “Enhanced conversion efficiency in perovskite solar cells by effectively utilizing near infrared light,” *Nanoscale*, vol. 8, no. 30, pp. 14432–14437, 2016.

[97] L. Jiang *et al.*, “Enhancing the Photovoltaic Performance of Perovskite Solar Cells with a Down-Conversion Eu-Complex,” *ACS Appl. Mater. Interfaces*, vol. 9, no. 32, pp. 26958–26964, 2017.

[98] M. M. Tavakoli *et al.*, “Highly efficient and stable inverted perovskite solar cells using down-shifting quantum dots as a light management layer and moisture-assisted film growth,” *J. Mater. Chem. A*, vol. 7, no. 24, pp. 14753–14760, 2019.

[99] H. Tsai *et al.*, “Light-induced lattice expansion leads to high-efficiency perovskite solar cells,” *Science.*, vol. 360, no. 6384, pp. 67–70, 2018.

[100] X. Fu *et al.*, “Photoluminescence study of time- and spatial-dependent light induced trap de-activation in $CH_3NH_3PbI_3$ perovskite films,” *Phys. Chem. Chem. Phys.*, vol. 18, no. 32, pp. 22557–22564, 2016.

[101] S. G. Motti *et al.*, “Controlling competing photochemical reactions stabilizes perovskite solar cells,” *Nat. Photonics*, vol. 13, no. 8, pp. 532–539, 2019.

[102] D. Bartesaghi *et al.*, “Competition between recombination and extraction of free charges determines the fill factor of organic solar cells,” *Nat. Commun.*, vol. 6, no. 1, pp. 1–10, 2015.

[103] R. Singh *et al.*, “Danger in the Dark: Stability of Perovskite Solar Cells with Varied Stoichiometries and Morphologies Stressed at Various Conditions,” *ACS Appl. Mater. Interfaces*, vol. 16, no. 21, pp. 27450–27462, 2024.

[104] E. T. Hoke *et al.*, “The role of electron affinity in determining whether fullerenes catalyze or inhibit photooxidation of polymers for solar cells,” *Adv. Energy Mater.*, vol. 2, no. 11, pp. 1351–1357, 2012.

[105] K. Wojciechowski *et al.*, “C_{60} as an Efficient N-Type Compact Layer in Perovskite Solar Cells,” *J. Phys. Chem. Lett.*, vol. 6, no. 12, pp. 2399–2405 2015.

[106] H. Tsai *et al.*, “High-efficiency two-dimensional Ruddlesden–Popper perovskite solar cells,” *Nature*, vol. 536, pp. 312–316, 2016.

[107] Y. Wu *et al.*, “Thermally Stable $MAPbI_3$ Perovskite Solar Cells with Efficiency of 19.19% and Area over 1 cm2 achieved by Additive Engineering,” *Adv. Mater.*, vol. 29, no. 28, pp. 1–8, 2017.

[108] T. Leijtens *et al.*, “Overcoming ultraviolet light instability of sensitized TiO_2 with meso-superstructured organometal tri-halide perovskite solar cells,” *Nat. Commun.*, vol. 4, 2013.

[109] A. Farooq *et al.*, “Spectral Dependence of Degradation under Ultraviolet Light in Perovskite Solar Cells,” *ACS Appl. Mater. Interfaces*, vol. 10, no. 26, pp. 21985–21990, 2018.

[110] F. Bella *et al.*, “Improving efficiency and stability of perovskite solar cells with photocurable fluoropolymers,” *Science*, vol. 354, no. 6309, pp. 203–206, 2016.

[111] H.-S. Rao *et al.*, “Improving the Extraction of Photogenerated Electrons with SnO2 Nanocolloids for Efficient Planar Perovskite Solar Cells,” *Adv. Funct. Mater.*, vol. 25, no. 46, pp. 7200–7207, 2015.

[112] Q. Jiang *et al.*, “Enhanced electron extraction using SnO_2 for high-efficiency planar-structure $HC(NH_2)_2PbI_3$-based perovskite solar cells,” *Nat. Energy*, vol. 2, no. 1, p. 16177, 2016.

[113] W. Ke *et al.*, “Low-Temperature Solution Processed Tin Oxide as an Alternative Electron Transporting Layer for Efficient Perovskite Solar Cells.,” *J. Am. Chem. Soc.*, vol. 137, no. 21, pp. 6730–6733, 2015.

[114] D. W. DeQuilettes *et al.*, “Photo-induced halide redistribution in organic-inorganic perovskite films,” *Nat. Commun.*, vol. 7, 2016.

[115] K. A. Bush *et al.*, "23.6%-Efficient Monolithic Perovskite/Silicon Tandem Solar Cells With Improved Stability," *Nat. Energy*, vol. 2, no. 4, pp. 1–7, 2017.

[116] D. P. McMeekin *et al.*, "A mixed-cation lead mixed-halide perovskite absorber for tandem solar cells," *Science*, vol. 351, no. 6269, pp. 151–155, 2016.

[117] G. E. Eperon *et al.*, "Formamidinium lead trihalide: a broadly tunable perovskite for efficient planar heterojunction solar cells," *Energy Environ. Sci.*, vol. 7, no. 3, pp. 982–988, 2014.

[118] E. T. Hoke *et al.* "Reversible photo-induced trap formation in mixed-halide hybrid perovskites for photovoltaics," *Chem. Sci.*, vol. 6, no. 1, pp. 613–617, 2015.

[119] M. T. Hörantner *et al.*, "The Potential of Multijunction Perovskite Solar Cells," *ACS Energy Lett.*, vol. 2, no. 10, pp. 2506–2513, 2017.

[120] A. You *et al.*, "Modeling of two - junction, series - connected tandem solar cells using top - cell thickness as an adjustable parameter," *J. Appl. Phys.*, vol. 68, no. 1990, pp. 1890–1895, 1996.

[121] B. Zhao *et al.*, "High Open-Circuit Voltages in Tin-Rich Low-Bandgap Perovskite-Based Planar Heterojunction Photovoltaics," *Adv. Mater.*, vol. 29, p. 1604744, 2017.

[122] J. A. Christians *et al.*, "Tailored interfaces of unencapsulated perovskite solar cells for >1,000 hour operational stability," *Nat. Energy*, vol. 3, no. 1, pp. 68–74, Jan. 2018.

[123] K. Domanski *et al.*, "Migration of cations induces reversible performance losses over day/night cycling in perovskite solar cells," *Energy Environ. Sci.*, vol. 10, no. 2, pp. 604–613, 2017.

[124] G. Y. Kim *et al.*, "Large tunable photoeffect on ion conduction in halide perovskites and implications for photodecomposition," *Nat. Mater.*, vol. 17, no. 5, pp. 445–449, 2018.

[125] L. McGovern *et al.*, "Grain Size Influences Activation Energy and Migration Pathways in MAPbBr3Perovskite Solar Cells," *J. Phys. Chem. Lett.*, vol. 12, no. 9, pp. 2423–2428, 2021.

[126] C. Mu *et al.*, "Quantitative Doping of Chlorine in Formamidinium Lead Trihalide ($FAPbI_{3-x}Cl_x$) for Planar Heterojunction Perovskite Solar Cells," *Adv. Energy Mater.*, vol. 7, no. 6, 2017.

[127] J. Dagar *et al.*, "Compositional and Interfacial Engineering Yield High-Performance and Stable p-i-n Perovskite Solar Cells and Mini-Modules," *ACS Appl. Mater. Interfaces*, vol. 13, no. 11, pp. 13022–13033, 2021.

[128] H. Hu *et al.*, "Void-free buried interface for scalable processing of p-i-n-based $FAPbI_3$ perovskite solar modules," *Joule*, vol. 7, no. 7, pp. 1574–1592, 2023.

[129] S. Gharibzadeh *et al.*, "Two birds with one stone: dual grain-boundary and interface passivation enables >22% efficient inverted methylammonium-free perovskite solar cells," *Energy Environ. Sci.*, vol. 14, no. 11, pp. 5875–5893, 2021.

[130] Y. Pan *et al.*, "Surface chemical polishing and passivation minimize non-radiative recombination for all-perovskite tandem solar cells," *Nat. Commun.*, vol. 15, no. 1, pp. 7335, 2024.

[131] Z. Wang *et al.*, "Efficient ambient-air-stable solar cells with 2D–3D heterostructured butylammonium-caesium-formamidinium lead halide perovskites," *Nat. Energy*, vol. 2, no. 9, pp. 17135, 2017.

[132] K. Domanski *et al.*, "Systematic investigation of the impact of operation conditions on the degradation behaviour of perovskite solar cells," *Nat. Energy*, vol. 3, no. 1, pp. 61–67, 2018.

[133] A. R. Bowring *et al.*, "Reverse Bias Behavior of Halide Perovskite Solar Cells," *Adv. Energy Mater.*, vol. 8, no. 8, 2018.

[134] W. Li *et al.*, “Sparkling hot spots in perovskite solar cells under reverse bias,” *ChemPhysMater*, vol. 1, no. 1, pp. 71–76, 2022.

[135] W. Herrmann *et al.*, “Hot spot investigations on PV modules-new concepts for a test standard and consequences for module design with respect to bypass diodes,” in *Conference Record of the Twenty Sixth IEEE Photovoltaic Specialists Conference - 1997*, pp. 1129–1132, 1997.

[136] M. T. Weller *et al.*, “Complete structure and cation orientation in the perovskite photovoltaic methylammonium lead iodide between 100 and 352 K,” *Chem. Commun.*, vol. 51, no. 20, pp. 4180–4183, 2015.

[137] G. E. Eperon *et al.*, “Inorganic caesium lead iodide perovskite solar cells,” *J. Mater. Chem. A*, vol. 3, no. 39, pp. 19688–19695, 2015.

[138] Q. Wang *et al.*, “Stabilizing the α-Phase of $CsPbI_3$ Perovskite by Sulfobetaine Zwitterions in One-Step Spin-Coating Films,” *Joule*, vol. 1, no. 2, pp. 371–382, 2017.

[139] A. Swarnkar *et al.*, “Quantum dot-induced phase stabilization of α-$CsPbI_3$perovskite for high-efficiency photovoltaics,” *Science*, vol. 354, no. 6308, pp. 92–95, 2016.

[140] A. Binek *et al.*, “Stabilization of the Trigonal High Temperature Phase of Formamidinium Lead Iodide,” *J. Phys. Chem. Lett.*, vol. 6, no. 7, p. 150316103833007, 2015.

[141] N. Li *et al.*, “Microscopic Degradation in Formamidinium-Cesium Lead Iodide Perovskite Solar Cells under Operational Stressors,” *Joule*, vol. 4, pp. 1743–1758, 2020.

[142] J. W. Lee *et al.*, “Formamidinium and Cesium Hybridization for Photo-and Moisture-Stable Perovskite Solar Cell,” *Adv. Energy Mater.*, vol. 5, p. 1501310, 2015.

[143] M. Saliba *et al.*, “Incorporation of rubidium cations into perovskite solar cells improves photovoltaic performance,” *Science* , vol. 354, no. 6309, pp. 206–209, 2016.

[144] K. L. Svane *et al.*, “How Strong Is the Hydrogen Bond in Hybrid Perovskites?,” *J. Phys. Chem. Lett.*, vol. 8, no. 24, pp. 6154–6159, 2017.

[145] J. W. Lee, S. Tan, S. Il Seok, Y. Yang, and N.-G. Park, “Rethinking the A cation in halide perovskites,” *Science*, vol. 375, no. 6583, p. eabj1186, 2025.

[146] M. Bag *et al.*, “Kinetics of Ion Transport in Perovskite Active Layers and Its Implications for Active Layer Stability,” *J. Am. Chem. Soc.*, vol. 137, no. 40, pp. 13130–13137, 2015.

[147] A. F. Akbulatov *et al.*, “Comparative Intrinsic Thermal and Photochemical Stability of Sn(II) Complex Halides as Next-Generation Materials for Lead-Free Perovskite Solar Cells,” *J. Phys. Chem. C*, vol. 123, no. 44, pp. 26862–26869, 2019.

[148] P. Wu *et al.*, “Efficient and Thermally Stable All-Perovskite Tandem Solar Cells Using All-FA Narrow-Bandgap Perovskite and Metal-oxide-based Tunnel Junction,” *Adv. Energy Mater.*, vol. 12, no. 48, p. 2202948, 2022.

[149] C. D. Bailie *et al.*, “Melt-infiltration of spiro-OMeTAD and thermal instability of solid-state dye-sensitized solar cells,” *Phys. Chem. Chem. Phys.*, vol. 16, no. 10, pp. 4864–4870, 2014.

[150] A. K. Jena *et al.*, “Severe morphological deformation of Spiro-OMeTAD in (CH_3NH_3) PbI_3 solar cells at high temperature,” *ACS Energy Lett.*, vol. 2, no. 8, pp. 1760–1761, 2017.

[151] Q. Lou *et al.*, “A two-in-one additive strategy for poly(3-hexylthiophene)-based perovskite solar cells with improved efficiency and stability,” *Cell Reports Phys. Sci.*, vol. 6, no. 4, p. 102515, 2025.

[152] M. Kim *et al.*, “Recent research trends in inorganic charge transport materials for next-generation perovskite solar cells,” *Renew. Sustain. Energy Rev.*, vol. 219, p. 115835, 2025.

[153] K. Domanski *et al.*, “Not All That Glitters Is Gold: Metal-Migration-Induced Degradation in Perovskite Solar Cells,” *ACS Nano*, vol. 10, no. 6, pp. 6306–6314, Jun. 2016.

[154] C. C. Boyd *et al.*, “Barrier Design to Prevent Metal-Induced Degradation and Improve Thermal Stability in Perovskite Solar Cells,” *ACS Energy Lett*, vol. 3, no. 7, pp. 1772–1778, 2018.

[155] M. D. Kempe *et al.*, “Moisture ingress prediction in polyisobutylene-based edge seal with molecular sieve desiccant,” *Prog. Photovoltaics Res. Appl.*, vol. 26, no. 2, pp. 93–101, 2018.

[156] I. M. Peters *et al.*, “The value of stability in photovoltaics,” *Joule*, vol. 5, no. 12, pp. 3137–3153, 2021.

[157] M. C. C. de Oliveira *et al.*, “The causes and effects of degradation of encapsulant ethylene vinyl acetate copolymer (EVA) in crystalline silicon photovoltaic modules: A review,” *Renew. Sustain. Energy Rev.*, vol. 81, pp. 2299–2317, 2018.

[158] N. Aristidou *et al.*, “Fast oxygen diffusion and iodide defects mediate oxygen-induced degradation of perovskite solar cells,” *Nat. Commun.*, vol. 8, 2017.

[159] H. Tsai *et al.*, “Oxygen Degradation in Mesoporous $Al_2O_3/CH_3NH_3PbI_{3-x}Cl_x$ Perovskite Solar Cells: Kinetics and Mechanisms,” *Nature*, vol. 6, no. 13, pp. 312–317, 2016.

[160] A. Yadegarifard *et al.*, “FA/Cs-based mixed Pb–Sn perovskite solar cells: A review of recent advances in stability and efficiency,” *Nano Energy*, vol. 112, p. 108481, 2023.

[161] Z. Shi *et al.*, “Lead-Free Organic–Inorganic Hybrid Perovskites for Photovoltaic Applications: Recent Advances and Perspectives,” *Adv. Mater.*, vol. 29, no. 16, 2017.

[162] F. Hao *et al.*, “Lead-free solid-state organic–inorganic halide perovskite solar cells,” *Nat. Photonics*, vol. 8, no. 6, p. 489, 2014.

[163] G. E. Eperon *et al.*, “Perovskite-perovskite tandem photovoltaics with optimized band gaps,” *Science*, vol. 354, no. 6314, pp. 861–865, 2016.

[164] U. B. Cappel *et al.*, “Oxygen-Induced Doping of Spiro-MeOTAD in Solid-State Dye-Sensitized Solar Cells and Its Impact on Device Performance,” *Nano Lett.*, vol. 12, no. 9, pp. 4925–4931, 2012.

[165] J. H. Heo *et al.*, “Efficient inorganic-organic hybrid heterojunction solar cells containing perovskite compound and polymeric hole conductors,” *Nat. Photonics*, vol. 7, no. 6, pp. 486–491, 2013.

[166] W. H. Nguyen, C. D. Bailie, E. L. Unger, and M. D. McGehee, “Enhancing the Hole-Conductivity of Spiro-OMeTAD without Oxygen or Lithium Salts by Using $Spiro(TFSI)_2$ in Perovskite and Dye-Sensitized Solar Cells,” *J. Am. Chem. Soc.*, vol. 136, no. 31, pp. 10996–11001, Aug. 2014, doi: 10.1021/ja504539w.

[167] J. Burschka *et al.*, “Tris(2-(1H-pyrazol-1-yl)pyridine)cobalt(III) as p-Type Dopant for Organic Semiconductors and Its Application in Highly Efficient Solid-State Dye-Sensitized Solar Cells,” *J. Am. Chem. Soc.*, vol. 133, no. 45, pp. 18042–18045, 2011.

[168] Y. Guo *et al.*, “Efficient inverted perovskite solar cells with a low-temperature processed NiOx/SAM hole transport layer,” *J. Mater. Chem. C*, vol. 12, no. 4, pp. 1507–1515, 2024.

[169] A. M. A. Leguy *et al.*, “Reversible hydration of $CH_3NH_3PbI_3$ in films, single crystals, and solar cells,” *Chem. Mater.*, vol. 27, no. 9, pp. 3397–3407, 2015.

[170] J. A. Christians *et al.*, “Transformation of the Excited State and Photovoltaic Efficiency of $CH_3NH_3PbI_3$ Perovskite upon Controlled Exposure to Humidified Air,” *J. Am. Chem. Soc.*, vol. 137, no. 4, pp. 1530–1538, 2015.

[171] S. N. Habisreutinger *et al.*, “Carbon Nanotube/Polymer Composites as a Highly Stable Hole Collection Layer in Perovskite Solar Cells,” *Nano Lett.*, vol. 14, no. 10, pp. 5561–5568, 2014.

[172] T. Leijtens *et al.*, “Mapping Electric Field-Induced Switchable Poling and Structural Degradation in Hybrid Lead Halide Perovskite Thin Films,” *Adv. Energy Mater.*, vol. 5, no.

20, 2015.

[173] J. M. Frost *et al.*, “Atomistic origins of high-performance in hybrid halide perovskite solar cells,” *Nano Lett.*, vol. 14, no. 5, pp. 2584–2590, 2014.

[174] C. L. C. Ellis *et al.*, “Hybrid Perovskites with Larger Organic Cations Reveal Autocatalytic Degradation Kinetics and Increased Stability under Light,” *Inorg. Chem.*, vol. 59, no. 17, pp. 12176–12186, 2022..

[175] Q. Jiang *et al.*, “Pseudohalide-Induced Moisture Tolerance in Perovskite $CH_3NH_3Pb(SCN)_2I$ Thin Films,” *Angew. Chemie Int. Ed.*, vol. 54, no. 26, pp. 7617–7620, 2015.

[176] Q. Tai *et al.*, “Efficient and stable perovskite solar cells prepared in ambient air irrespective of the humidity,” *Nat. Commun.*, vol. 7, pp. 1–8, 2016.

[177] C. Yi *et al.*, “Entropic stabilization of mixed A-cation ABX3 metal halide perovskites for high performance perovskite solar cells,” *Energy Environ. Sci.*, vol. 9, no. 2, pp. 656–662, 2016.

[178] L. N. Quan *et al.*, “Ligand-Stabilized Reduced-Dimensionality Perovskites,” *J. Am. Chem. Soc.*, vol. 138, no. 8, pp. 2649–2655, 2016.

[179] G. Grancini *et al.*, “One-Year stable perovskite solar cells by 2D/3D interface engineering,” *Nat. Commun.*, vol. 8, p. 15684, 2017.

[180] E. H. Jung *et al.*, “Efficient, stable and scalable perovskite solar cells using poly(3-hexylthiophene),” *Nature*, vol. 567, no. 7749, pp. 511–515, 2019.

[181] M. Spalla, L. Perrin, E. Planes, M. Matheron, S. Berson, and L. Flandin, “Effect of the Hole Transporting/Active Layer Interface on the Perovskite Solar Cell Stability,” *ACS Appl. Energy Mater.*, vol. 3, no. 4, pp. 3282–3292, 2020.

[182] F. J. Ramos *et al.*, “Versatile perovskite solar cell encapsulation by low-temperature ALD-Al_2O_3 with long-term stability improvement,” *Sustain. Energy Fuels*, vol. 2, no. 11, pp. 2468–2479, 2018, doi: 10.1039/c8se00282g.

[183] J. Zhang *et al.*, “Al_2O_3 Underlayer Prepared by Atomic Layer Deposition for Efficient Perovskite Solar Cells,” *ChemSusChem*, vol. 10, no. 19, pp. 3810–3817, 2017.

[184] B. Chen *et al.*, “Synergistic Effect of Elevated Device Temperature and Excess Charge Carriers on the Rapid Light-Induced Degradation of Perovskite Solar Cells,” *Adv. Mater.*, vol. 31, no. 35, p. 1902413, 2019.

[185] T. Duong *et al.*, “Light and elevated temperature induced degradation (LeTID) in perovskite solar cells and development of stable semi-transparent cells,” *Sol. Energy Mater. Sol. Cells*, vol. 188, pp. 27–36, 2018.

[186] E. D. Dunlop *et al.*, “20 years of life and more: where is the end of life of a PV module?,” *Thirty-first IEEE Photovoltaic Specialists Conference, 2005.*, pp. 1593–1596, 2005.

[187] L. C. Olsen *et al.*, “Approaches to Encapsulation of Flexible CIGS Cells,” *SPIE Proceedings*, vol. 7048. SPIE, pp. 176–183, 2008.

[188] M. Ross *et al.*, “Improvement in Reliability and Energy Yield Prediction of Thin-Film CdS/CdTe PV Modules,” in *2006 IEEE 4th World Conference on Photovoltaic Energy Conference*, vol. 2, pp. 2148–2151, 2006.

[189] M. V. Khenkin *et al.*, “Consensus statement for stability assessment and reporting for perovskite photovoltaics based on ISOS procedures,” *Nat. Energy*, vol. 5, no. 1, pp. 35–49, 2020.

[190] M. Saliba *et al.*, “Measuring Aging Stability of Perovskite Solar Cells,” *Joule*, vol. 2, no. 6, pp. 1019-1024, 2018.

[191] J. Y. Jeng *et al.*, “Nickel oxide electrode interlayer in $CH_3NH_3PbI_3$ perovskite/PCBM planar-heterojunction hybrid solar cells,” *Adv. Mater.*, vol. 26, no. 24, pp. 4107–4113, 2014.

[192] Y. Yao *et al.*, “Organic Hole-Transport Layers for Efficient, Stable, and Scalable Inverted Perovskite Solar Cells,” *Adv. Mater.*, vol. 34, no. 44, p. 2203794, 2022.

[193] A. Farag *et al.*, “Evaporated Self-Assembled Monolayer Hole Transport Layers: Lossless Interfaces in p-i-n Perovskite Solar Cells,” *Adv. Energy Mater.*, vol. 13, no. 8, p. 2203982, 2023.

[194] A. N. Bartynski *et al.*, “A Fullerene-Based Organic Exciton Blocking Layer with High Electron Conductivity,” *Nano Lett.*, vol. 13, no. 7, pp. 3315–3320, 2013.

[195] T. H. Schloemer *et al.*, “Doping strategies for small molecule organic hole-transport materials: impacts on perovskite solar cell performance and stability,” *Chem. Sci.*, vol. 10, no. 7, pp. 1904–1935, 2019.

[196] A. Kojima *et al.*, “Organometal halide perovskites as visible-light sensitizers for photovoltaic cells,” *J. Am. Chem. Soc.*, vol. 131, no. 17, pp. 6050–6051, 2009.

[197] D. Yang *et al.*, “High efficiency flexible perovskite solar cells using superior low temperature TiO2,” *Energy Environ. Sci.*, vol. 8, no. 11, pp. 3208–3214, 2015.

[198] Z. Hawash *et al.*, “Moisture and Oxygen Enhance Conductivity of LiTFSI-Doped Spiro-MeOTAD Hole Transport Layer in Perovskite Solar Cells,” *Adv. Mater. Interfaces*, vol. 3, no. 13, p. 1600117, 2016.

[199] A. K. Jena *et al.*, “Role of spiro-OMeTAD in performance deterioration of perovskite solar cells at high temperature and reuse of the perovskite films to avoid Pb-waste,” *J. Mater. Chem. A*, vol. 6, no. 5, pp. 2219–2230, 2018.

[200] R. S. Sanchez *et al.*, “Light-induced effects on Spiro-OMeTAD films and hybrid lead halide perovskite solar cells,” *Sol. Energy Mater. Sol. Cells*, vol. 158, pp. 189–194, 2016.

[201] R. Singh *et al.*, “Harvesting Sub-bandgap Photons via Upconversion for Perovskite Solar Cells,” *ACS Appl. Mater. Interfaces*, vol. 13, no. 46, pp. 54874–54883, 2021.

[202] S. G. Kim *et al.*, “How antisolvent miscibility affects perovskite film wrinkling and photovoltaic properties,” *Nat. Commun. 2021 121*, vol. 12, no. 1, pp. 1–10, 2021.

[203] R. Schmager *et al.*, “Laminated Perovskite Photovoltaics: Enabling Novel Layer Combinations and Device Architectures,” *Adv. Funct. Mater.*, vol. 30, no. 9, p. 1907481, 2020.

[204] K. J. Rietwyk *et al.*, “Ideality Factor Mapping of Back-Contact Perovskite Solar Cells,” *Adv. Energy Mater.*, vol. 13, no. 9, p. 2200796, 2023.

[205] S. Ternes *et al.*, “Correlative In Situ Multichannel Imaging for Large-Area Monitoring of Morphology Formation in Solution-Processed Perovskite Layers,” *Sol. RRL*, vol. 6, no. 3, p. 2100353, 2022.

[206] B. W Park *et al.*, “Intrinsic Instability of Inorganic–Organic Hybrid Halide Perovskite Materials,” *Adv. Mater.*, vol. 31, no. 20, p. 1805337, 2019.

[207] A. Ciccioli *et al.*, “Thermodynamics and the Intrinsic Stability of Lead Halide Perovskites CH3NH3PbX3,” *J. Phys. Chem. Lett.*, vol. 9, no. 13, pp. 3756–3765, 2018.

[208] W. Song *et al.*, “Critical Role of Perovskite Film Stoichiometry in Determining Solar Cell Operational Stability: a Study on the Effects of Volatile A-Cation Additives,” *ACS Appl. Mater. Interfaces*, vol. 14, p. 27922−27931, 2022.

[209] T. J. Jacobsson *et al.*, “Unreacted PbI_2 as a Double-Edged Sword for Enhancing the Performance of Perovskite Solar Cells,” *J. Am. Chem. Soc.*, vol. 138, no. 32, pp. 10331–10343, 2016.

[210] G. Tumen-Ulzii *et al.*, “Detrimental Effect of Unreacted PbI_2 on the Long-Term Stability of Perovskite Solar Cells,” *Adv. Mater.*, vol. 32, no. 16, 2020.

[211] Y. Gao *et al.*, “Elimination of unstable residual lead iodide near the buried interface for the stability improvement of perovskite solar cells,” *Energy Environ. Sci.*, vol. 16, no. 5, pp. 2295–2303, 2023.

[212] Z. Liang *et al.*, “Homogenizing out-of-plane cation composition in perovskite solar cells,” *Nature*, vol. 624, pp. 557–563, 2023.

[213] S. Ghosh *et al.*, “Antisolvents in Perovskite Solar Cells: Importance, Issues, and Alternatives,” *Adv. Mater. Interfaces*, vol. 7, no. 18, p. 2000950, 2020.

[214] N. Li *et al.*, “Microscopic Degradation in Formamidinium-Cesium Lead Iodide Perovskite Solar Cells under Operational Stressors,” *Joule*, vol. 4, no. 8, pp. 1743–1758, 2020.

[215] K. Domanski *et al.*, “Systematic investigation of the impact of operation conditions on the degradation behaviour of perovskite solar cells,” *Nat. Energy*, vol. 3, no. 1, pp. 61–67, 2018.

[216] M. V. Khenkin *et al.*, “Dynamics of Photoinduced Degradation of Perovskite Photovoltaics: From Reversible to Irreversible Processes,” *ACS Appl. Energy Mater.*, vol. 1, no. 2, pp. 799–806, 2018.

[217] P. Yadav *et al.*, “Intrinsic and interfacial kinetics of perovskite solar cells under photo and bias-induced degradation and recovery,” *J. Mater. Chem. C*, vol. 5, no. 31, pp. 7799–7805, 2017.

[218] J. M. Azpiroz *et al.*, “Defect migration in methylammonium lead iodide and its role in perovskite solar cell operation,” *Energy Environ. Sci.*, vol. 8, no. 7, pp. 2118–2127, 2015.

[219] T. S. Sherkar *et al.*, “Recombination in Perovskite Solar Cells: Significance of Grain Boundaries, Interface Traps, and Defect Ions,” *ACS Energy Lett.*, vol. 2, no. 5, pp. 1214–1222, 2017.

[220] R. Wang *et al.*, “Improving the efficiency and stability of perovskite solar cells using π-conjugated aromatic additives with differing hydrophobicities,” *Energy Environ. Sci.*, vol. 16, no. 6, pp. 2646–2657, 2023.

[221] X. Ren *et al.*, “Mobile iodides capture for highly photolysis- and reverse-bias-stable perovskite solar cells,” *Nat. Mater.*, vol. 23, no. 6, pp. 810–817, 2024.

[222] K. Dey *et al.*, “Substitution of lead with tin suppresses ionic transport in halide perovskite optoelectronics,” *Energy Environ. Sci.*, vol. 17, no. 2, pp. 760–769, 2023.

[223] N. Li *et al.*, “Barrier reinforcement for enhanced perovskite solar cell stability under reverse bias,” *Nat. Energy*, vol. 9, 2024.

[224] F. Liu *et al.*, “Is Excess PbI_2 Beneficial for Perovskite Solar Cell Performance?” *Adv. Energy Mater.*, vol. 6, no. 7, p. 1502206, 2016.

[225] R. Ji *et al.*, “Thermally evaporated methylammonium-free perovskite solar cells,” *J. Mater. Chem. C*, vol. 8, no. 23, pp. 7725–7733, 2020.

[226] Y. Zhao *et al.*, “Effects of ion migration and improvement strategies for the operational stability of perovskite solar cells,” *Phys. Chem. Chem. Phys.*, vol. 23, no. 1, pp. 94–106, 2021.

[227] D. P. McMeekin *et al.*, “A mixed-cation lead mixed-halide perovskite absorber for tandem solar cells,” *Science*, vol. 351, no. 6269, pp. 151–155, 2016.

[228] T. Duong *et al.*, “High Efficiency Perovskite-Silicon Tandem Solar Cells: Effect of Surface Coating versus Bulk Incorporation of 2D Perovskite,” *Adv. Energy Mater.*, vol. 10, pp. 1903553, 2020.

[229] X. Yang *et al.*, “Superior Carrier Lifetimes Exceeding 6 μs in Polycrystalline Halide

Perovskites," *Adv. Mater.*, vol. 32, no. 39, pp. 6–13, 2020.

[230] K. Liu *et al.*, "Stress and Strain in Perovskite/Silicon Tandem Solar Cells," *Nano-Micro Lett.*, vol. 15, no. 1, pp. 1–5, 2023.

[231] K. A. Bush *et al.*, "Controlling Thin-Film Stress and Wrinkling during Perovskite Film Formation," *ACS Energy Lett.*, vol. 3, no. 6, pp. 1225–1232, 2018.

[232] G. Kim *et al.*, "Impact of strain relaxation on performance of a-formamidinium lead iodide perovskite solar cells," *Science*, vol. 370, no. 6512, pp. 108–112, 2020.

[233] Y. Cui *et al.*, "Correlating Hysteresis and Stability with Organic Cation Composition in the Two-Step Solution-Processed Perovskite Solar Cells," *ACS Appl. Mater. Interfaces*, vol. 12, no. 9, pp. 10588–10596, 2020.

[234] X. Zheng *et al.*, "The Controlling Mechanism for Potential Loss in $CH_3NH_3PbBr_3$ Hybrid Solar Cells," *ACS Energy Lett.*, vol. 1, no. 2, pp. 424–430, 2016.

[235] S. Shao *et al.*, "Efficient Perovskite Solar Cells over a Broad Temperature Window: The Role of the Charge Carrier Extraction," *Adv. Energy Mater.*, vol. 7, no. 22, p. 1701305, 2017.

[236] B. Roose *et al.*, "Critical Assessment of the Use of Excess Lead Iodide in Lead Halide Perovskite Solar Cells," *J. Phys. Chem. Lett.*, vol. 11, no. 16, pp. 6505–6512, 2020.

[237] J. Thiesbrummel *et al.*, "Universal Current Losses in Perovskite Solar Cells Due to Mobile Ions," *Adv. Energy Mater*, vol. 11, no. 34, p. 2101447, 2021.

[238] P. Caprioglio *et al.*, "Open-circuit and short-circuit loss management in wide-gap perovskite p-i-n solar cells," *Nat. Commun. 2023 141*, vol. 14, no. 1, pp. 1–13, 2023.

[239] E. A. Katz *et al.*, "Light intensity dependence of External Quantum Efficiency of fresh and degraded organic photovoltaics," *Sol. Energy Mater. Sol. Cells*, vol. 144, pp. 273–280, 2016.

[240] F. Huang *et al.*, "Fatigue behavior of planar $CH_3NH_3PbI_3$ perovskite solar cells revealed by light on/off diurnal cycling," *Nano Energy*, vol. 27, pp. 509–514, 2016.

[241] T. H. Y. Vu *et al.*, "Visualizing the Impact of Light Soaking on Morphological Domains in an Operational Cesium Lead Halide Perovskite Solar Cell," *J. Phys. Chem. Lett.*, vol. 11, no. 1, pp. 136–143, 2020.

[242] M. Prete *et al.*, "Bias-Dependent Dynamics of Degradation and Recovery in Perovskite Solar Cells," *ACS Appl. Energy Mater.*, vol. 4, no. 7, pp. 6562–6573, 2021.

[243] A. M. Soufiani *et al.*, "Electro- and photoluminescence imaging as fast screening technique of the layer uniformity and device degradation in planar perovskite solar cells," *J. Appl. Phys.*, vol. 120, no. 3, p. 35702, 2016.

[244] S. Bitton *et al.*, "Perovskite ionics – elucidating degradation mechanisms in perovskite solar cells via device modelling and iodine chemistry," *Energy Environ. Sci.*, vol. 16, no. 6, pp. 2621–2628, 2023.

[245] L. Jiang *et al.*, "Fatigue stability of $CH_3NH_3PbI_3$ based perovskite solar cells in day/night cycling," *Nano Energy*, vol. 58, pp. 687–694, 2019.

[246] N. Titan *et al.*, "Stability follows efficiency based on the analysis of a large perovskite solar cells ageing dataset," *Nat. Commun.*, vol. 14, p. 4869, 2023,.

[247] F. Laufer *et al.*, "Deep learning for augmented process monitoring of scalable perovskite thin-film fabrication," *Energy Environ. Sci.*, vol. 18, no. 4, pp. 1767–1782, 2025.

[248] U. Erdil *et al.*, "Mimicking Outdoor Ion Migration in Perovskite Solar Cells: A Forward Bias, No-Light Accelerated Aging Approach," *ACS Energy Lett.*, vol. 10, no. 3, pp. 1529–1537, 2025.

[249] F. U. Nitta *et al.*, "Transition metal dichalcogenide solar cells for indoor energy harvesting,"

Device, p. 100723, 2025.

[250] V. Paraskeva *et al.*, “Diurnal Changes and Machine Learning Analysis of Perovskite Modules Based on Two Years of Outdoor Monitoring,” *ACS Energy Lett.*, pp. 5081–5091, 2024.

[251] R. Pappenberger *et al.*, “Versatile Two-Step Process for Perovskite-Based Tandem Photovoltaics,” *Sol. RRL*, vol. 9, no. 13, pp. 202500193, 2025.

[252] A. Sinha *et al.*, “UV-induced degradation of high-efficiency silicon PV modules with different cell architectures,” *Prog. Photovoltaics Res. Appl.*, vol. 31, no. 1, pp. 36–51, 2023.

[253] G. E. Eperon *et al.*, “Metal halide perovskite tandem and multiple-junction photovoltaics,” *Nat. Rev. Chem.*, vol. 1, no. 12, p. 95, 2017.

[254] G. E. Arnaoutakis *et al.*, “Enhanced energy conversion of up-conversion solar cells by the integration of compound parabolic concentrating optics,” *Sol. Energy Mater. Sol. Cells*, vol. 140, pp. 217–223, 2015.

[255] X. Deng *et al.*, “Highly bright Li(Gd,Y)F_4:Yb,Er upconverting nanocrystals incorporated hole transport layer for efficient perovskite solar cells,” *Appl. Surf. Sci.*, vol. 485, pp. 332–341, 2019.

[256] R. Meng *et al.*, “Wide spectral response perovskite solar cells mixed with $NaGdF_4$:Yb^{3+}, Er^{3+}@$NaGdF_4$:Eu^{3+} core-shell rare earth nanoparticles,” *Opt. Mater.*, vol. 119, p. 111326, 2021.

[257] X. Lai *et al.*, “Broadband dye-sensitized upconverting nanocrystals enabled near-infrared planar perovskite solar cells,” *J. Power Sources*, vol. 372, pp. 125–133, 2017.

[258] M. S. Sebag *et al.*, “Microscopic Evidence of Upconversion-Induced Near-Infrared Light Harvest in Hybrid Perovskite Solar Cells,” *ACS Appl. Energy Mater.*, vol. 1, no. 8, pp. 3537–3543, 2018.

[259] A. Monguzzi *et al.*, “Upconversion-induced fluorescence in multicomponent systems: Steady-state excitation power threshold,” *Phys. Rev. B - Condens. Matter Mater. Phys.*, vol. 78, no. 19, p. 195112, 2008.

[260] S. Baluschev *et al.*, “Up-conversion fluorescence: Noncoherent excitation by sunlight,” *Phys. Rev. Lett.*, vol. 97, no. 14, p. 143903, 2006.

[261] D. Saleta Reig *et al.*, “Upconversion properties of SrF_2:Yb^{3+},Er^{3+} single crystals,” *J. Mater. Chem. C*, vol. 8, no. 12, pp. 4093–4101, Mar. 2020, doi: 10.1039/c9tc06591a.

[262] J. C. Boyer *et al.*, “Absolute quantum yield measurements of colloidal $NaYF_4$: Er^{3+},Yb^{3+} upconverting nanoparticles,” *Nanoscale*, vol. 2, no. 8, pp. 1417–1419, 2010

[263] I. Richman, “Longitudinal Optical Phonons in CaF_2, SrF_2, and BaF_2,” *J. Chem. Phys.*, vol. 41, no. 9, p. 2836, 2004.

[264] E. I. Madirov *et al.*, “An up-conversion luminophore with high quantum yield and brightness based on BaF_2:Yb^{3+},Er^{3+} single crystals,” *J. Mater. Chem. C*, vol. 9, no. 10, pp. 3493–3503, 2021.

[265] A. S. Bieber *et al.*, “Perovskite-Sensitized Upconversion under Operando Conditions,” *J. Phys. Chem. C*, vol. 127, no. 9, pp. 4773–4783, 2023.

[266] N. Irannejad *et al.*, “Upconversion graphene quantum dots incorporation in performance enhancement of p-i-n perovskite solar cells,” *J. Environ. Chem. Eng.*, vol. 9, no. 6, p. 106898, 2021.

[267] W. Sheng *et al.*, “Tremendously enhanced photocurrent enabled by triplet–triplet annihilation up-conversion for high-performance perovskite solar cells,” *Energy Environ. Sci.*, vol. 14, no. 6, pp. 3532–3541, 2021.

[268] N. Menyuk *et al.*, “$NaYF_4$: Yb,Er—an efficient upconversion phosphor,” *Appl. Phys. Lett*, vol. 21, no. 4, p. 159, 1972.

[269] J. F. Suyver *et al.*, “Highly efficient near-infrared to visible up-conversion process in $NaYF_4$:Er^{3+},Yb^{3+},” *J. Lumin.*, vol. 114, no. 1, pp. 53–59, 2005.

[270] S. Yang *et al.*, “Tm^{3+} doped α-$NaYF_4$ single crystal for 2 μm laser application,” *J. Alloys Compd.*, vol. 643, pp. 1–6, 2015.

[271] M. Schultes *et al.*, “Sputtered Transparent Electrodes (IO:H and IZO) with Low Parasitic Near-Infrared Absorption for Perovskite-Cu(In,Ga)Se_2 Tandem Solar Cells,” *ACS Appl. Energy Mater.*, vol. 2, no. 11, pp. 7823–7831, 2019.

[272] S. Gharibzadeh *et al.*, “Record Open-Circuit Voltage Wide-Bandgap Perovskite Solar Cells Utilizing 2D/3D Perovskite Heterostructure,” *Adv. Energy Mater.*, vol. 9, no. 21, pp. 1–10, 2019.

[273] S. Masi *et al.*, “Stabilization of Black Perovskite Phase in $FAPbI_3$ and $CsPbI_3$,” *ACS Energy Lett.*, vol. 5, no. 6, pp. 1974–1985, 2020.

[274] Z. Li *et al.*, “Stabilizing Perovskite Structures by Tuning Tolerance Factor: Formation of Formamidinium and Cesium Lead Iodide Solid-State Alloys,” *Chem. Mater.*, vol. 28, no. 1, pp. 284–292, 2016.

[275] B. Conings *et al.*, “Intrinsic Thermal Instability of Methylammonium Lead Trihalide Perovskite,” *Adv. Energy Mater.*, vol. 5, no. 15, p. 1500477, 2015.

[276] T. Leijtens *et al.*, “Tin-lead halide perovskites with improved thermal and air stability for efficient all-perovskite tandem solar cells,” *Sustain. Energy Fuels*, vol. 2, pp. 2450–2459, 2018.

[277] M. Stöhr *et al.*, “Measurement of 3D pore-scale flow in index-matched porous media,” *Exp. Fluids*, vol. 35, no. 2, pp. 159–166, 2003.

[278] I. H. Malitson, “Refractive Properties of Barium Fluoride,” *J. Opt. Soc. Am.*, vol. 54, no. 5, p. 628, 1964.

[279] R. Cao *et al.*, “Unveiling the Low-Temperature Pseudodegradation of Photovoltaic Performance in Planar Perovskite Solar Cell by Optoelectronic Observation,” *Adv. Energy Mater.*, vol. 6, no. 18, p. 1600814, 2016.

[280] J. G. Labram *et al.*, “Temperature-Dependent Polarization in Field-Effect Transport and Photovoltaic Measurements of Methylammonium Lead Iodide,” *J. Phys. Chem. Lett.*, vol. 6, no. 18, pp. 3565–3571, 2015.

[281] S. Meloni *et al.*, “Ionic polarization-induced current-voltage hysteresis in $CH_3NH_3PbX_3$ perovskite solar cells,” *Nat. Commun.*, vol. 7, no. 1, pp. 1–19, 2016.

[282] S. Kim *et al.*, “Relationship between ion migration and interfacial degradation of $CH_3NH_3PbI_3$ perovskite solar cells under thermal conditions,” *Sci. Reports 2017 71*, vol. 7, no. 1, pp. 1–9, 2017.

[283] M. A. Green, “General temperature dependence of solar cell performance and implications for device modelling,” *Prog. Photovoltaics Res. Appl.*, vol. 11, no. 5, pp. 333–340, 2003.

[284] P. Singh *et al.*, “Temperature dependence of solar cell performance—an analysis,” *Sol. Energy Mater. Sol. Cells*, vol. 101, pp. 36–45, 2012.

[285] A. Shalav *et al.*, “Luminescent layers for enhanced silicon solar cell performance: Up-conversion,” *Sol. Energy Mater. Sol. Cells*, vol. 91, no. 9, pp. 829–842, 2007.

[286] S. Fischer *et al.*, “Upconversion solar cell measurements under real sunlight,” *Opt. Mater.*, vol. 84, pp. 389–395, 2018.

[287] S. Fischer *et al.*, “Upconverter silicon solar cell devices for efficient utilization of sub-band-gap photons under concentrated solar radiation,” *IEEE J. Photovoltaics*, vol. 4, no. 1, pp. 183–189, 2014.

[288] A. Ghazy *et al.*, “Luminescent (Er,Ho)$_2$O$_3$ thin films by ALD to enhance the performance of silicon solar cells,” *Sol. Energy Mater. Sol. Cells*, vol. 219, p. 110787, 2021.

[289] B. S. Richards *et al.*, “Photon Upconversion for Photovoltaics and Photocatalysis: a Critical Review,” *Chem. Rev.*, vol. 121, no. 15, pp. 9165–9195, 2021.

[290] J. Christiansen *et al.*, “Analytical model for the intensity dependence of 1500 nm to 980 nm upconversion in Er^{3+}: A new tool for material characterization,” *J. Appl. Phys.*, vol. 125, no. 4, p. 43106, 2019.

[291] A. K. Jena *et al.*, “Severe Morphological Deformation of Spiro-OMeTAD in (CH$_3$NH$_3$)PbI$_3$ Solar Cells at High Temperature,” *ACS Energy Lett.*, vol. 2, no. 8, pp. 1760–1761, 2017.

[292] C. L. M. Hofmann *et al.*, “Experimental validation of a modeling framework for upconversion enhancement in 1D-photonic crystals,” *Nat. Commun.*, vol. 12, no. 1, pp. 1–10, 2021.

[293] A. Das *et al.*, “Over 1000-fold enhancement of upconversion luminescence using water-dispersible metal-insulator-metal nanostructures,” *Nat. Commun. 2018 91*, vol. 9, no. 1, pp. 1–11, 2018.

[294] A. Virtuani *et al.*, “Comparison of indoor and outdoor performance measurements of recent commercially available solar modules,” *Prog. Photovoltaics Res. Appl.*, vol. 19, no. 1, pp. 11–20, 2011.

[295] M. Remec *et al.*, “Seasonality in Perovskite Solar Cells: Insights from 4 Years of Outdoor Data,” *Adv. Energy Mater.*, vol. n/a, no. n/a, p. 2501906, 2025.

[296] R. Appels *et al.*, “Effect of soiling on photovoltaic modules,” *Sol. Energy*, vol. 96, pp. 283–291, 2013.

[297] B. Hüttl *et al.*, “Accurate performance rating of photovoltaic modules under outdoor test conditions,” *Sol. Energy*, vol. 177, pp. 737–745, 2019.

[298] E. Aydin *et al.*, “Interplay between temperature and bandgap energies on the outdoor performance of perovskite/silicon tandem solar cells,” *Nat. Energy*, vol. 5, no. 11, pp. 851–859, 2020.

[299] Q. Emery *et al.*, “Encapsulation and Outdoor Testing of Perovskite Solar Cells: Comparing Industrially Relevant Process with a Simplified Lab Procedure,” *ACS Appl. Mater. Interfaces*, vol. 14, no. 4, pp. 5159–5167, 2022.

[300] R. Cheacharoen *et al.*, “Design and understanding of encapsulated perovskite solar cells to withstand temperature cycling,” *Energy Environ. Sci.*, vol. 11, no. 1, pp. 144–150, 2018,.

[301] Q. Emery *et al.*, “Tips and Tricks for a Good Encapsulation for Perovskite-Based Solar Cells,” *Prog. Photovoltaics Res. Appl.*, vol. 33, no. 4, pp. 551–559, 2025.

[302] A. J. Pearson *et al.*, “Oxygen Degradation in Mesoporous Al$_2$O$_3$/CH$_3$NH$_3$PbI$_{3-x}$Cl$_x$ Perovskite Solar Cells: Kinetics and Mechanisms,” *Adv. Energy Mater.*, vol. 6, no. 13, 2016.

[303] R. Cheacharoen *et al.*, “Encapsulating perovskite solar cells to withstand damp heat and thermal cycling,” *Sustain. Energy Fuels*, vol. 2, no. 11, pp. 2398–2406, 2018a.

[304] N. Yantara and N. Mathews, “Toolsets for assessing ionic migration in halide perovskites,” *Joule*, vol. 8, no. 5, pp. 1239–1273, 2024.

[305] L. Wu *et al.*, “Resilience pathways for halide perovskite photovoltaics under temperature cycling,” *Nat. Rev. Mater.*, vol. 10, no. 7, pp. 536–549, 2025.

[306] E. Radziemska, “The effect of temperature on the power drop in crystalline silicon solar

cells," *Renew. Energy*, vol. 28, no. 1, pp. 1–12, 2003.

[307] J. H. Park *et al.*, "Sub-cell characterization of two-terminal perovskite/silicon tandem solar cells," *Cell Reports Phys. Sci.*, vol. 3, p. 101076, 2022.

[308] M. A. Sevillano-Bendezú *et al.*, "Predictability and interrelations of spectral indicators for PV performance in multiple latitudes and climates," *Sol. Energy*, vol. 259, pp. 174–187, 2023.

[309] M. Bonnet-Eymard *et al.*, "Optimized short-circuit current mismatch in multi-junction solar cells," *Sol. Energy Mater. Sol. Cells*, vol. 117, pp. 120–125, 2013.

[310] Y. Bao *et al.*, "Insights into efficiency deviation from current-mismatch for tandem photovoltaics," *Nano Energy*, vol. 120, p. 109165, 2024.

[311] A. A. B. Baloch *et al.*, "Impact of mixed perovskite composition based silicon tandem PV devices on efficiency limits and global performance," *Energy Reports*, vol. 8, pp. 504–510, 2022.

[312] D. L. Wang *et al.*, "Highly efficient light management for perovskite solar cells," *Sci. Rep.*, vol. 6, no. 1, p. 18922, 2016.

[313] G. Hou *et al.*, "High-low refractive index stacks for broadband antireflection coatings for multijunction solar cells," *Sol. Energy*, vol. 217, pp. 29–39, 2021

[314] H. Chen *et al.*, "Alleviating the Angular Dependence of Perovskite Solar Cells via Light-Harvesting Nanostructure," *Sol. RRL*, vol. 8, no. 12, p. 2400214, 2024.

[315] M. Jošt *et al.*, "Monolithic Perovskite Tandem Solar Cells: A Review of the Present Status and Advanced Characterization Methods Toward 30% Efficiency," *Adv. Energy Mater.*, vol. 10, no. 26, p. 1904102, 2020.

[316] M. Babics *et al.*, "One-year outdoor operation of monolithic perovskite/silicon tandem solar cells," *Cell Reports Phys. Sci.*, vol. 4, no. 2, p. 101280, 2023.

[317] A. J. Bett *et al.*, "Spectrometric Characterization of Monolithic Perovskite/Silicon Tandem Solar Cells," *Sol. RRL*, vol. 7, no. 2, p. 2200948, 2023.

[318] M. Jošt *et al.*, "Perovskite Solar Cells go Outdoors: Field Testing and Temperature Effects on Energy Yield," *Adv. Energy Mater.*, vol. 10, no. 25, p. 2000454, 2020.

[319] Y. Kim *et al.*, "Durable polyisobutylene edge sealants for organic electronics and electrochemical devices," *Sol. Energy Mater. Sol. Cells*, vol. 100, pp. 120–125, 2012.

[320] Y. Bai *et al.*, "Lower Levelized Cost of Energy Achievement of Silicon Heterojunction Solar Modules with Low Water Vapor Transmission Rate Encapsulants," *Energy Technol.*, vol. 11, no. 7, p. 2201466, 2023.

[321] S. Moghadamzadeh *et al.*, "Spontaneous enhancement of the stable power conversion efficiency in perovskite solar cells," *J. Mater. Chem. A*, vol. 8, no. 2, pp. 670–682, 2020.

[322] R. Breugelmans *et al.*, "Method to Study Potential-Induced Degradation of Perovskite Solar Cells and Modules in an Inert Environment," *Sol. RRL*, vol. 8, no. 11, pp. 2400046, 2024.

[323] A. Tong, "Improving the accuracy of temperature measurements," *Sens. Rev.*, vol. 21, no. 3, pp. 193–198, 2001.

[324] I. Galton, "Delta-sigma data conversion in wireless transceivers," *IEEE Trans. Microw. Theory Tech.*, vol. 50, no. 1, pp. 302–315, 2002.

[325] A. Özdemir *et al.*, "An application study about SMPS design and reduction of common mode noises," *International Conference on Electrical and Electronics Engineering - ELECO 2009*, pp. I-306-I–310, 2009.

[326] N. Muskinja *et al.*, "Use of TCP/IP protocol in industrial environment," in *IEEE International Conference on Industrial Technology, 2003*, vol. 2, pp. 896-900, 2003.

[327] N. Femia *et al.*, “Predictive & Adaptive MPPT Perturb and Observe Method,” *IEEE Trans. Aerosp. Electron. Syst.*, vol. 43, no. 3, pp. 934–950, 2007.

[328] Y. Yang *et al.*, “Adaptive perturb and observe maximum power point tracking with current predictive and decoupled power control for grid-connected photovoltaic inverters,” *J. Mod. Power Syst. Clean Energy*, vol. 7, no. 2, pp. 422–432, 2019.

[329] Y. Zhang *et al.*, “Tracing the Energy Losses in All-Perovskite Tandem Solar Cells From Opto-Electro-Thermal Perspectives,” *Adv. Funct. Mater.*, vol. n/a, no. n/a, p. 2503408, 2025.

[330] D. Di Girolamo *et al.*, “Silicon / Perovskite Tandem Solar Cells with Reverse Bias Stability down to −40 V. Unveiling the Role of Electrical and Optical Design,” *Adv. Sci.*, vol. 11, no. 31, pp. 2401175, 2024.

[331] D. Lan *et al.*, “Combatting temperature and reverse-bias challenges facing perovskite solar cells,” *Joule*, vol. 6, pp. 1782–1797, 2022.

[332] R. Prasanna *et al.*, “Design of low bandgap tin–lead halide perovskite solar cells to achieve thermal, atmospheric and operational stability,” *Nat. Energy*, vol. 4, no. 11, pp. 939–947, 2019.

[333] S. J. Yoon *et al.*, “Tracking Iodide and Bromide Ion Segregation in Mixed Halide Lead Perovskites during Photoirradiation,” *ACS Energy Lett.*, vol. 1, no. 1, pp. 290–296, 2016.

[334] D. J. Kubicki *et al.*, “Phase Segregation in Cs-, Rb- and K-Doped Mixed-Cation (MA)x(FA)1–xPbI3 Hybrid Perovskites from Solid-State NMR,” *J. Am. Chem. Soc.*, vol. 139, no. 40, pp. 14173–14180, 2017.

[335] R. Li *et al.*, “Reverse-bias challenges facing perovskite-silicon tandem solar cells under field conditions,” *Newton*, vol. 1, no. 1, 2025.

List of Figures

Figure 1.1: (a) Increasing trend in consumption of renewable energy sources (solar, wind, hydropower and others) over time and expected trends in the upcoming years. Adapted with permission from International Energy Agency. (b) Contribution of power generation among different photovoltaics technologies to meet the increasing demand of solar photovoltaics (estimated for 2023). Adapted with permission from Fraunhofer Institute for Solar Energy Systems.

Figure 1.2: (a) Record power conversion efficiency (PCE) reported for perovskite solar cells (PSCs) and perovskite-silicon tandem solar cells (TSCs) over the years [4]. Adapted with permission from National Renewable Energy Laboratory. (b) Estimated decrease in module manufacturing cost and minimum sustainable price (MSP) with increase in reported PCE of perovskite- silicon TSCs (based on production costs). Adapted with permission from Elsevier.

Figure 2.1: Crystal structure of a perovskite semiconductor depicting the position of A^+ cation (MA^+, FA^+ or Cs^+) and B^{2+} cation (Pb^{2+} or Sn^{2+}) alongside X^- anion (I^-, Br^- or Cl^-). Position of A^+ is in the center of the cubohederal with BX_6 octahedra at the corner.

Figure 2.2: (a) A schematic of perovskite solar cell consisting of front electrode, hole transport layer (HTL), perovskite absorber, electron transport layer (ETL) and back electrode. The light enters the solar cell from the front electrode (b) Energy band diagram of a perovskite solar cell under illumination showing electron accumulation in the conduction band (E_C) and hole accumulation in the valence band (E_V). The Fermi level splits into quasi-Fermi levels for electrons ($E_{F,e}$) and holes ($E_{F,h}$), generating a potential difference between the electrodes. Selective charge carriers, the electron transport layer (ETL) and the hole transport layer (HTL) facilitate efficient separation and extraction of charge carriers.

Figure 2.3: (a) One diode model of a solar cell represented by a current source, diode and shunt resistance (R_{sh}) in parallel and series resistances (R_s) in series. (b) Current density-voltage characteristics (J-V characteristics) of a solar cell with performance parameters: open-circuit voltage (V_{OC}), short-circuit current density (J_{SC}), maximum power point (P_m), voltage at maximum power point (V_m) and current at maximum power point (J_m).

Figure 2.4: Spectral irradiance of the air mass 1.5 global (AM1.5G) utilized by a perovskite solar cell of bandgap, E_G=1.57 eV (brown). The high-energy photons lose their excess energy as thermalization losses (light grey) and the low-energy photons are transmitted through the perovskite solar cell as transmission losses (dark grey). The low-energy photons are available to multi-junction solar cells or upconversion.

Figure 2.5: (a) Two-terminal (2T) and (b) four-terminal (4T) perovskite- Si tandem solar cells (TSCs). 2T TSCs are optically and electrically interconnected and 4T TSCs are optically interconnected but electrically isolated.

Figure 2.6: Schematic illustration of (a) Upconversion (b) Downconversion and (c) Downshifting. Upconversion is the annihilation of two low-energy photons into a high-energy photon. Downconversion is the splitting up of a high-energy photon into two low-energy photons. Downshifting is conversion of a high-energy photon into a low energy photon.

Figure 3.1: (a) positive-intrinsic-negative (p-i-n) and (b) negative-intrinsic-positive (n-i-p) architectures of perovskite solar cells (PSCs). The architecture depends on which charge transport layer is processed on the substrate first as the light is enters the solar cell through this front electrode. In semi-transparent devices, light can enter through both top and back electrode.

Figure 3.2: Absorptance spectra of a perovskite thin film of bandgap 1.57 eV. The transmittance and reflectance of the thin film was measured with ultraviolet-visible-near infrared (UV-VIS-NIR) spectroscopy. Absorptance was calculated as $A(\lambda) = 1 - T(\lambda) - R(\lambda)$.

Figure 3.3: X-ray diffraction (XRD) of a perovskite thin film exhibiting high degree of crystallinity with sharp perovskite PSK (100) peak at $2\theta = 14.2°$ alongside some unreacted lead iodide (PbI_2) at $2\theta = 12.7°$. PbI_2 is one of the precursors used for the fabrication of perovskite thin films.

Figure 3.4: Optical microscopy images of a perovskite thin film. Features on a macroscale such as crests (brighter areas) and troughs (darker areas) of the wrinkle formation are visible, giving a clear picture of the quality of the perovskite thin film.

Figure 3.5: Atomic Force Microscopy (AFM) images of a perovskite thin film depicting the inhomogeneity in the surface morphology. The heights appear brighter and the depths appear darker. Maximum root mean square surface roughness of the thin films measured is ~250 nm.

Figure 3.6: Scanning Electron Microscopy (SEM) images of a perovskite thin film. The morphology shows compact films with grain size of ~500 nm. Two types of grains are visible. The darker grains which are the perovskite grains and the brighter grains are the unreacted lead iodide (PbI_2), one of the precursors used for the fabrication of perovskite thin films.

Figure 3.7: Cathodoluminescence (CL) images of a perovskite thin film taken with (a) no filter (b) 550 nm filter (c) 800 nm filter. The filters eliminates the wavelengths that are longer than the wavelength of the filter. When using filter of 550 nm, only materials with wider bandgap are visible. Hence, only the bright spots of PbI_2 (E_G = 2.3 eV) are visible in (b). When a filter of 800 nm is used, low bandgap materials such as perovskite (E_G = 1.57 eV) are also visible in (c).

Figure 3.8: Surface profile and thickness measurement of a perovskite thin film. The measured depth of ~ 600nm is the thickness of the film.

Figure 3.9 (a) Hysteretic behavior between forward scan (scan direction: J_{SC} to V_{OC}) and reverse scan (scan direction: V_{OC} to J_{SC}) of a perovskite-based solar cell. (b) Maximum power output (P_m) extracted from a solar cell by tracking at maximum power point (MPP).

Figure 3.10: Suns-V_{OC} characterization of perovskite solar cell measured from 0.7 to 69.2 mW/cm^2 intensity. The fitting has a slope of 1.01. The ideality factor (n_{id}) = 1.01 represents radiative recombination is the dominant recombination mechanism.

Figure 3.11: External quantum efficiency (EQE) characterization and integrated J_{SC} calculated from EQE for a semi-transparent perovskite solar cell. An integrated J_{SC} of 20.3 mA/cm^2 was measured from the perovskite solar cell.

Figure 3.12: Electroluminescence (EL) characterization of a perovskite solar cell showing inhomogenieties like pinholes and edge effects.

Figure 3.13: (a) Delay time charge extraction by linearly increasing voltage (Delay-time CELIV) measurement of a perovskite solar cells. (b) Extracted charge carrier density vs. delay time plot.

Figure 4.1: (a) Statistical distribution of the power conversion efficiency (PCE) and (b) $J-V$ characteristics of the PSCs using an antisolvent quenching process. (c) Statistical distribution of PCE and (d) $J-V$ characteristics of the PSCs using a vacuum quenching process. Adapted with permission from American Chemical Society.

Figure 4.2: Statistical distribution of (a) open-circuit voltage (V_{OC}) (b) fill factor (FF) and (c) short-circuit current density (J_{SC}) of antisolvent-quenched devices with different molar ratios. Statistical

distribution of (d) V_{OC} (e) FF and (f) J_{SC} of vacuum-quenched devices with different molar ratios. Adapted with permission from American Chemical Society.

Figure 4.3: (a) External quantum efficiency (EQE) of devices with different molar ratios and (b) absorptance of films with different molar ratios quenched using antisolvent-quenching (ASQ) (c) EQE of devices with different molar ratios and (d) absorptance of films with different molar ratios quenched using vacuum-quenching (VQ). Adapted with permission from American Chemical Society.

Figure 4.4: (a) Derivative at inflection point of EQE of devices with different molar ratios and (b) Tauc plot from absorptance of films with different molar ratios quenched using ASQ (c) Derivative at inflection point of EQE of devices with different molar ratios and (d) Tauc plot from absorptance of films with different molar ratios quenched using VQ. Adapted with permission from American Chemical Society.

Figure 4.5: Scanning electron microscopy (SEM) images of perovskite thin films with molar ratios of (a) 1.2, (b) 1.1, and (c) 1.05 quenched using ASQ and molar ratios of (d) 1.2, (e) 1.1, and (f) 1.05 quenched using VQ. Adapted with permission from American Chemical Society.

Figure 4.6: Optical microscopy (OM) images of films (a) MR 1.2 (b) MR 1.1 (c) MR 1.05 quenched using ASQ. OM of films (d) MR 1.2 (e) MR 1.1 (f) MR 1.05 quenched using VQ. Adapted with permission from American Chemical Society.

Figure 4.7: X-ray diffraction (XRD) patterns with (a) molar ratios of 1.2, 1.1, and 1.05 quenched using ASQ. (b) Peak ratio of lead iodide PbI_2 (100) / perovskite PSK (100) with molar ratios of 1.2, 1.1, and 1.05 quenched using ASQ and aged for 500h under the mentioned stress factor. XRD patterns with (c) molar ratios of 1.2, 1.1, and 1.05 quenched using VQ. (d) Peak ratio of PbI_2 (100) / PSK (100) with molar ratios of 1.2, 1.1, and 1.05 quenched using VQ and aged for 500h under the mentioned stress factor. Adapted with permission from American Chemical Society.

Figure 4.8: Normalized (a) PCE, (b) V_{OC}, (c) J_{SC}, and (d) FF from $J-V$ characterization of ASQ devices of different stoichiometry under ISOS-D2I testing conditions (dark, 85 °C, intermittent $J-V$ characterization) for 500 h. Adapted with permission from American Chemical Society.

Figure 4.9: Comparison of J-V characterization of antisolvent-quenched devices of (a) MR 1.2 (b) MR 1.1 and (c) MR 1.05 measured before (initial) and after (final) ISOS-L1I test. Comparison of EQE of antisolvent-quenched devices of (d) MR 1.2 (e) MR 1.1 and (f) MR 1.05 measured before (initial) and after (final) ISOS-D2I test. Adapted with permission from American Chemical Society.

Figure 4.10: Normalized (a) power and (b) current density at the maximum power point (MPP) tracking of antisolvent-quenched devices of different stoichiometry under ISOS-L1I test conditions (100 mW/cm^2, 25 °C, MPP tracking) for 500 h. The power of MR 1.2, M.R. 1.1 and MR 1.0 were normalized with 18.33 % , 18.71 % and 17.95% respectively Adapted with permission from American Chemical Society.

Figure 4.11: Comparison of J-V characterization of antisolvent-quenched devices of (a) MR 1.2 (b) MR 1.1 and (c) MR 1.05 measured before (initial) and after (final) ISOS-L1I test. Comparison of EQE of antisolvent-quenched devices of (d) MR 1.2 (e) MR 1.1 and (f) MR 1.05 measured before (initial) and after (final) ISOS-L1I test. Adapted with permission from American Chemical Society.

Figure 4.12: Radar plot of the average PCE of devices with different stoichiometry aged under ISOS-D2I (yellow) and ISOS-L1I (green). Devices are measured by $J-V$ characterizations before the

accelerated stress testing (brown) and 24 h after the end of 500h of accelerated stress testing (purple) and 250 h (orange) of dark storage. Adapted with permission from American Chemical Society.

Figure 4.13: Radar plot of the average V_{OC} of devices with different stoichiometry aged under ISOS-D2I (yellow) and ISOS-L1I (green). Devices are measured by $J-V$ characterizations before the accelerated stress testing (brown) and 24 h after the end of 500h of accelerated stress testing (purple) and 250 h (orange) of dark storage. Adapted with permission from American Chemical Society.

Figure 4.14: Electroluminescence (EL) images of devices with (a) MR 1.2 and (b) MR 1.05 after dark storage of 250 h after ISOS-L1I testing. Extracted charge carrier density of devices with different stoichiometry aged under (c) ISOS-L1I and dark storage of 250 h along with (d) ISOS-D2I and dark storage of 250 h, measured by charge extraction by linearly increasing voltage (CELIV).

Figure 5.1: (a) Spectral irradiance of air mass 1.5 global (AM1.5G) and solar simulator alongside absorptance of the bifacial perovskite solar cells and BaF_2: Yb^{3+}, Er^{3+} upconversion (UC) crystal. The two or more low-energy photons are upconverted by the UC crystal and transferred to the bifacial solar cell which can absorb the high-energy photons. (b) Energy level diagrams of the Er^{3+} and Yb^{3+} ions along with the energy transfer (ET) UC mechanism. Adapted with permission from American Chemical Society.

Figure 6.2: (a) Change in upconversion quantum yield (ϕ_{UC}) and number of emitted photons observed as the thickness of upconversion (UC) crystal is varied up to 1cm (b) Absorption coefficient and normalized emission spectra of the UC crystal of thickness 1.7 mm. The emission was measured under 980 nm excitation. Adapted with permission from American Chemical Society.

Figure 5.3: Optical properties of a 0.23 mm thick BaF_2:Er^{3+},Yb^{3+} sample (a) Intensity dependence of the upconversion quantum yield (ϕ_{UC}) for green and red emission bands; (b) Absorptance spectrum and normalized emission spectra. Adapted with permission from American Chemical Society.

Figure 5.4: (a) Variation of number of emitted photons with the thickness of the crystal (b) The calculated emission spectra of samples with various thickness. Adapted with permission from American Chemical Society.

Figure 5.5: (a) Fraction of emitted light after the reabsorption. The dotted line shows the thickness of 1.7 mm used in the experiments. (b) Emission escape cone. The areas highlighted in green represent the emission angles from which photons can be harvested through the top surface of the crystal. Adapted with permission from American Chemical Society.

Figure 5.6: Variation in the number of emitted photons as a function of crystal thickness, accounting for reabsorption and escape cone effects. Adapted with permission from American Chemical Society.

Figure 5.7: (a) Power output (P_m) during maximum power point (MPP) tracking of bifacial perovskite solar cell (PSC). (b) Transmittance of the PSC device stack measured from the top (Indium Tin Oxide side) represented by green line and bottom (glass side) represented by yellow line. Adapted with permission from American Chemical Society.

Figure 5.8: (a) Schematic representation of the experimental setup used for the characterization of enhancement in J_{SC} and the overall influence of upconversion (UC) on the perovskite solar cell (PSC)-UC device. The UC crystal (pink) was placed at the backside of the PSC inside a stage (grey). The PSC-UC device was illuminated with a solar simulator (<850 nm) and laser (980nm) and current density-voltage (J-V) characterization was performed with Au probes (yellow). (b) Image of the experimental setup implementing PSC-UC device on the stage. Adapted with permission from American Chemical Society.

List of Tables

List of Publications and Contributions to Conferences

Peer-reviewed publications (first author)

R. Singh et. al., “Harvesting sub-bandgap photons via upconversion for perovskite solar cells,” ACS applied materials & interfaces, 13 (46), 54874–54883, 2021.

R. Singh et. al., “Danger in the Dark: Stability of Perovskite Solar Cells with Varied Stoichiometries and Morphologies Stressed at Various Conditions,” ACS applied materials & interfaces, 16 (21), 27450–27462, 2024.

Peer-reviewed publications (co-author)

S. Gharibzadeh et. al., “Two birds with one stone: dual grain-boundary and interface passivation enables >22% efficient inverted methylammonium-free perovskite solar cells,” Energy & environmental science, 14 (11), 5875–5893, 2021.

M. A. Ruiz-Preciado et. al., “Monolithic Two-Terminal Perovskite/CIS Tandem Solar Cells with Efficiency Approaching 25%,” ACS Energy Letters, 7 (7), 2273–2281, 2022.

B. A. Nejand et. al., “Scalable two-terminal all-perovskite tandem solar modules with a 19.1% efficiency,” Nature Energy, 7, 620–630, 2022.

I. M. Hossain et. al., “Four-terminal Perovskite/CIGS Tandem Solar Cells: Unveiling the Path to >27% in Power Conversion Efficiency,” Solar RRL, 6 (12), 2022.

A. Farag et. al., “Evaporated Self-Assembled Monolayer Hole Transport Layers: Lossless Interfaces in p-i-n Perovskite Solar Cells,” Advanced Energy Materials, 13 (8), 2023.

F. Schackmar et. al., “In Situ Process Monitoring and Multichannel Imaging for Vacuum-Assisted Growth Control of Inkjet-Printed and Blade-Coated Perovskite Thin-Films,” Advanced Materials Technologies, 8 (5), 2023.

H. Hu et. al., “Void-free buried interface for scalable processing of p-i-n-based $FAPbI_3$ perovskite solar modules,” Joule, 7 (7), 1574–1592, 2023.

Q. Jin et. al., “Inkjet-printed optical interference filters,” Nature Communications, 15 (1), 2024.

H. Hu et. al., “Triple-junction perovskite–perovskite–silicon solar cells with power conversion efficiency of 24.4%,” Energy & Environmental Science, 17 (8), 2800 – 2814, 2024.

D. O. Baumann et. al., “ Repeatable Perovskite Solar Cells through Fully Automated Spin-Coating and Quenching,” ACS Applied Materials & Interfaces, 16 (40), 54007–54016, 2024.

H. Hu et. al., “Laminated Two-Terminal All-Perovskite Tandem Solar Cells with Transparent Conductive Adhesives,” ACS Applied Materials and Interfaces, 17 (5), 7804–7810, 2025.

A. Diercks et. al., “Sequential Evaporation of Inverted $FAPbI_3$ Perovskite Solar Cells – Impact of Substrate on Crystallization and Film Formation,” ACS Energy Letters, 10 (3), 1165–1173, 2025.

R. Pappenberger et. al., “Versatile Two-Step Process for Perovskite-Based Tandem Photovoltaics,” Solar RRL, Volume 9, Issue 13 2500193, 2025.

Contributions to conferences

Roja Singh, Eduard Madirov, Dmitry Busko, Ihteaz M. Hossain, Vasilii A. Konyushkin, Andrey N. Nakladov, Sergey V. Kuznetsov, Amjad Farooq, Saba Gharibzadeh, Bryce S. Richards, Ulrich W. Paetzold, and Andrey Turshatov, “Upconversion for harvesting sub-bandgap photons in perovskite solar cells”, SPIE Photonics Europe, 2021, Strasbourg (France). Oral presentation.

Roja Singh, Motiur Rahman Khan, Saba Gharibzadeh, Fabian Schackmar, Thomas Feeney, Hang Hu, Alex Diercks, Paul Fassl, Ulrich Paetzold , “Enhancing long-term stability of perovskite solar cells using large cation additives”, 13th International Summit on Organic and Hybrid Photovoltaics Stability (ISOS-13), 2022, Sønderborg (Denmark). Poster Presentation.

Prize: Best Poster Award

Roja Singh, Hang Hu, Thomas Feeney, Alexander Diercks, Felix Laufer, Fabian Schackmar, Bahram Abdollahi Nejand and Ulrich W. Paetzold, “The determining factor contributing to degradation of PSC: material stoichiometry, quenching technique or stress factor?”, International Summit on Organic and Hybrid Photovoltaics Stability (ISOS-14) and Women Leaders in Solar Energy, 2023, Yokohoma (Japan).

Roja Singh, Hang Hu, Thomas Feeney, Alexander Diercks, Felix Laufer, Fabian Schackmar, Bahram Abdollahi Nejand and Ulrich W. Paetzold, “Stability of Perovskite Solar Cells with varied Stoichiometries and Morphologies under various Stress Conditions”, HOPV24 nanoGe International Conference on Hybrid and Organic Photovoltaics, 2024, Valencia (Spain).

Prize: The Rising Star

Roja Singh, Hang Hu, Thomas Feeney, Alexander Diercks, Felix Laufer, Yang Li, The Duong, Fabian Schackmar, Bahram Abdollahi Nejand and Ulrich W. Paetzold, “Impact of materials stoichiometry and surface morphology on stability of perovskite solar cells”, International Summit on Organic and Hybrid Photovoltaics Stability (ISOS-15), 2024, Berlin (Germany).

Nomination: Young Scientists Award

Supervised master theses

David Clement, “Lamination for Long-term Stability of Perovskite Solar Cells”, May 2021.

Keval Ashokbhai Tejani, Reliability Testing of Encapsulated Perovskite Solar Cells for Long Term Stability, May 2022 (in cooperation with Nordhausen University of Applied Sciences).

Acknowledgements

This PhD dissertation, along with the scientific work it covers, would not have been possible without the guidance and support of my supervisor, colleagues, collaborators, friends, and family.

My sincerest gratitude to Prof. Dr. Ulrich W. Paetzold for his guidance and support during my doctoral work at Karlsruhe Institute of Technology (KIT). I would also like to extend my heartfelt appreciation to Prof. Dr. Ulrich Lemmer and Prof. Dr. Bryce Richards for providing research facilities at Light Technology Institute (LTI) and Institute of Microstructure Technology (IMT). Many thanks to my colleagues at Perovskite Taskforce at KIT for their energy and valuable discussions during formal meetings or informal meetups.

I would like to thank my colleagues at IMT, Dr. Eduard Madirov, Dr. Dmitry Busko, Dr. Andrey Turshatov and Prof. Dr. Bryce Richards for their valuable input to the work incorporating upconversion crystals and perovskite solar cells. Their expertise in the field of upconversion elevated the work. Thanks to Dr. Bahram Abdollahi, Dr. Ihteaz Hossein, Dr. Saba Gharibzadeh, Dr. Fabian Schackmar and Dr. Hang Hu for their advice with the work studying the dark recovery of perovskite solar cells. Their feedback has made the work stronger. Finally, thanks to my masters students Mr. David Clement and Mr. Keval Tejani. The development they made with encapsulation along with the contribution of Dr. Lingyi Fang and Mr. Marc Schneider, has made the work based on the outdoor stability setup possible.

My gratitude to the staffs at LTI, Mr. Felix Geiselhöringer, Mr. Mario Sütsch, Mr. Hans Voegele, Mr. Christian Kayser, Mr. Reza Akbarzadeh Naseri and Mr. Julian Schickle for their support. Thanks to the staffs at IMT Dr. Alexandra Moritz, Mr. Achim Voigt and Mr. Marc Schneider for their assistance.

Special appreciation for Julie, Thomas, Hang and Felix. Their experience and suggestions has made my thesis-writing period less hectic. Thanks to Julie, Hang, Thomas, Alex, Lingyi, Joshua and Julian (Petry) for editing the chapters of this dissertation.

The past few years have shaped my life, both professionally and personally. Words fall short in capturing the depth of this experience. I am deeply grateful to everyone who has walked with me along the way.

Financial support:

The financial support of German Federal Ministry for Economic Affairs and Energy (CAPITANO, funding code 03EE1038B), the Initiating and Networking funding of the Helmholtz Association (HYIG of U.W.P., funding code VHNG1148), the Materials and Technologies for the Energy Transition Research Program, the Solar Technology Acceleration Platform (Project Zeitenwende and Solar TAP), the program-oriented funding IV of the Helmholtz Association (Materials and Technologies for the Energy Transition; Topic 1: Photovoltaics and Wind Energy, Code: 38.01.04), the German Federal Ministry for Economic Affairs and Climate Action (BMWK) through the projects 27Plus6 (03EE1056B) and SHAPE (03EE1123A) is gratefully acknowledged.

Co-authors contribution:

R.S. and E.M. have contributed equally to this work. U.W.P and A.T. conceived the idea; A.F. and D.B. performed initial investigation; R.S. fabricated and characterized the solar cells; S.G. developed the double cation perovskite, and I.H. contributed with device fabrication; V.A.K., A.N.N., and S.V.K. synthesized the $BaF_2:Yb^{3+}$, Er^{3+} upconversion single crystal. E.M. characterized the $BaF_2:Yb^{3+}$, Er^{3+} upconversion single crystal. R.S. and E.M. performed experimentation involving the $BaF_2:Yb^{3+}$, Er^{3+} upconversion single crystal and solar cell. R.S. wrote the manuscript. B.S.R. provided extensive guidance on the measurement approach of combining upconversion materials with the solar cells as well as developing a clear story for the manuscript. U.W.P and A.T. supervised the project.

R.S., F.S., U.W.P., and B.A. conceptualized the project; R.S. performed device fabrication and investigations; H.H. and T.F. contributed with device fabrication; A.D. performed SEM characterization; F.L. performed EL characterization; Y.L. performed AFM characterization; T.D. performed CL characterization; and U.W.P. supervised the project.